Defect Chemistry of Sodium Bismuth Titanate and its Solid Solutions

Dissertation
Zur Erlangung des akademischen Grades Doktor-Ingenieur (Dr.-Ing.) genehmigte Dissertation von M.Sc. Sebastian Andre Steiner aus Seeheim-Jugenheim
September 2019 – Darmstadt – D 17

TECHNISCHE UNIVERSITÄT DARMSTADT

Defect Chemistry of Sodium Bismuth Titanate and its Solid Solutions

Genehmigte Dissertation von M. Sc. Sebastian Andre Steiner aus Seeheim-Jugenheim

1. Gutachten: Dr. Till Frömling

2. Gutachten: Prof. Dr. Kyle Grant Webber

Tag der Einreichung: 09. September 2019

Tag der Prüfung: 20. November 2019

Fachbereich Material- und Geowissenschaften

September 2019 — Darmstadt — D 17

Thesis Statement pursuant to § 22 paragraph 7 and § 23 paragraph 7 of APB TU Darmstadt

I herewith formally declare that I, Sebastian Andre Steiner, have written the submitted thesis independently pursuant to § 22 paragraph 7 of APB TU Darmstadt. I did not use any outside support except for the quoted literature and other sources mentioned in the paper. I clearly marked and separately listed all of the literature and all of the other sources which I employed when producing this academic work, either literally or in content. This thesis has not been handed in or published before in the same or similar form.

In the submitted thesis the written copies and the electronic version for archiving are pursuant to § 23 paragraph 7 of APB identical in content.

Darmstadt, the 09th of September 2019

_____

(Sebastian Andre Steiner)

Content

Content I
List of Figures V
List of Tables XIII
List of Abbreviations XIV
List of Symbols XVI
Abstract XXI
1 Introduction 1
2 Theoretical Background 5
2.1 Dielectric Properties 6
2.2 Crystal Structure 10
2.3 Piezoelectric Properties 12
2.4 Pyroelectric Properties 13
2.5 Ferroelectric Properties 14
2.5.1 Relaxors 17
2.5.2 Dielectric Energy Storage 23
2.6 Defects in Solids 25
2.6.1 Intrinsic and Extrinsic Defects 26
2.6.2 Formation of Defect Complexes 29
2.7 Conduction Mechanisms 30
2.7.1 Electronic Conductivity 30
2.7.2 Ionic Conduction and Diffusion 33
2.8 Electromotive Force (EMF) 40
2.9 Electrochemical Impedance Spectroscopy (EIS) 41
2.10 Sodium Bismuth Titanate (NBT) 49
2.11 NBT-Based Solid Solutions 53
2.11.1 NBT-BT 53
2.11.2 NBT-ST 54
2.11.3 NBT-BT-CZ 56
3 Experimental 59
3.1 Powder Processing 59
3.2 Sample Preparation 63
3.3 Density 64
3.4 X-ray Diffraction (XRD) 64
3.5 Scanning Electron Microscopy (SEM) 65
3.6 Electrochemical Impedance Spectroscopy (EIS) 67
3.7 Dielectric Permittivity and Loss 68
3.8 Polarization and Strain Response 68
3.9 Electromotive Force (EMF) 70
3.10 Nuclear Magnetic Resonance (NMR) 70
3.11 Density Functional Theory (DFT) Calculations 71
4 Results and Discussion 73

4.1 Defect Chemistry of Acceptor Doped NBT 75
4.1.1 Acceptor Doped NBT: Microstructure 78
4.1.2 Acceptor Doped NBT: Electrical Properties 80
4.1.3 Mg-Doping: Analytical Model 87
4.1.4 Acceptor Doped NBT: Molecular Orbital Considerations 95
4.1.5 Defect Complexes in Al-doped NBT: NMR Analysis 101
4.1.6 Application Perspective: Grain Versus Grain Boundary 103
4.1.7 Defect Chemistry of Acceptor doped NBT: Summary 106
4.2 Defect Chemistry in NBT-Based Solid Solutions: NBT-6BT 109
4.2.1 A-Site Non-Stoichiometric NBT-6BT 109
4.2.2 A-Site Non-Stoichiometric NBT-6BT: Microstructure 111
4.2.3 A-Site Non-Stoichiometric NBT-6BT: Electrical Properties 114
4.2.4 A-Site Non-Stoichiometric NBT-6BT: Dielectric, Ferroelectric, and Piezoelectric Properties 117
4.2.5 A-Site Non-Stoichiometric NBT-6BT: Summary 122
4.2.6 B-Site Acceptor Doped NBT-6BT 123
4.2.7 B-Site Acceptor Doped NBT-6BT: Microstructure 125
4.2.8 B-Site Acceptor Doped NBT-6BT: Electrical Properties 128
4.2.9 B-Site Acceptor Doped NBT-6BT: Ferroelectric Hardening 132
4.2.10 B-Site Acceptor Doped NBT-6BT: Summary 134
4.3 Defect Chemistry in NBT-Based Solid Solutions: NBT-ST 135
4.3.1 Doped and A-site Non-Stoichiometric NBT-ST: Microstructure 138
4.3.2 Doped and A-site Non-Stoichiometric NBT-ST: Electrical Properties 144
4.3.3 Doped and A-site Non-Stoichiometric NBT-ST: Dielectric, Ferroelectric, and Piezoelectric Properties 147
4.3.4 Doped and A-site Non-Stoichiometric NBT-ST: Summary 155
4.4 Application of the Defect Chemistry to Develop High-Temperature Capacitors 157
4.4.1 The Solid Solution NB_xT-6BT-yCZ 157
4.4.2 NB_xT-6BT-yCZ: Microstructure 160
4.4.3 NB_xT-6BT-yCZ: Dielectric Properties 162
4.4.4 NB_xT-6BT-yCZ with BA Addition: Microstructure 165
4.4.5 NB_xT-6BT-yCZ with BA Addition: Dielectric Properties 167
4.4.6 NB_xT-6BT-yCZ with BA Addition: Electrical Properties 172
4.4.7 NB_xT-6BT-yCZ with BA Addition: Ferroelectric Energy Storage 174
4.4.8 NB_xT-6BT-yCZ with BA Addition: Summary 176
5 Conclusion and Outlook 179
Appendix 182
Acknowledgement 188
Bibliography 191
Curriculum Vitae 214

List of Figures

Figure 2.1.1: Microscopic polarization contributions with an applied electric field. Electronic, ionic, dipole orientation and space charges can be discriminated (redrawn after ref. [68]). 7

Figure 2.1.2: Frequency dependent responses of the real part (red) and the imaginary part (blue) of the permittivity (redrawn after ref. [68]). 8

Figure 2.1.3: All crystalline systems divided into subgroups: Dielectrics, piezoelectrics, pyroelectrics ferroelectrics and relaxors.[33] 9

Figure 2.2.1: Unit cell of the ABX_3 ideal cubic perovskite structure. The B-site atom (blue) occupies the center. The X-site atoms (red), typically oxygen, sit in the middle of each surface and form an octahedron around the center atom. The A-site atoms (black) are placed on the corners of the unit cell. 10

Figure 2.2.2: Unit cell of a perovskite with cubic (a), tetragonal (b) and rhombohedral (c) structure.. 11

Figure 2.5.1: Schematic illustration of a polarization (a) and strain hysteresis (b) with an applied electric field. The states (I) to (VI) represent the respective depicted domain state (redrawn after ref. [87]). 15

Figure 2.5.2: Comparison of a regular ferroelectric with a relaxor material with regards to the temperature dependent phase transition ((a) and (b)) and the temperature dependent permittivity response ((c) and (d)). The solid lines in (d) represent a canonical relaxor, the dashed lines represent a non-canonical relaxor with a spontaneous transition to a ferroelectric at T_{fr} (after ref. [90]). 17

Figure 2.5.3: Schematic illustration of a chemically ordered polar nano region (delimited by a red solid line) in a disordered, non-polar matrix for a $Pb(B^{2+}_{1/3}B^{5+}_{2/3})O_3$ perovskite (redrawn after ref. [93]). 18

Figure 2.5.4: Schematic illustration of the thermal evolution of high temperature (HT) and low temperature (LT) polar nano regions and the resulting permittivity responses with respect to PNR-concentration and -size effects in NBT-6BT-xKNN (redrawn after ref. [117]). 20

Figure 2.5.5: Polarization and strain hysteresis for an ergodic (ER) and non-ergodic (NR) canonical relaxor from the unpoled, virgin state. (a) depicts the polarization, (c) the strain response of an ergodic relaxor with (red line) and without (blue line) a reversible electric field-induced ferroelectric long-range order. (b) depicts the polarization, (d) the strain response of a non-ergodic relaxor with an irreversible electric field-induced ferroelectric long-range order (the grey line in (b) represents the response of a virgin sample) (adapted from ref. [10]). 21

Figure 2.5.6: Schematic illustration of hysteresis and energy storage density for (a) linear dielectrics, (b) ergodic relaxors and (c) regular ferroelectrics. The blue area depicts the recoverable energy storage density W_{rec}. The red area depicts the energy loss density (redrawn after ref. [125, 127]). 24

Figure 2.6.1: Schematic illustration of the formation of Schottky and Frenkel defect pairs in a crystal lattice. 26

Figure 2.6.2: Common Schottky pairs which can occur in a regular perovskite structure. Partial and full Schottky defects are depicted (orange and violet) as well as outgassing of oxygen (red) (redrawn after ref. [133]). 27

Figure 2.7.1: Diagram of the band structure of metals (left), intrinsic and extrinsic semiconductors (middle), and dielectrics or insulators (right). 31

Figure 2.7.2: Schematic illustration of an Arrhenius-type plot of the temperature-dependent conductivity. The here presented plot additionally displays a possible transition from extrinsic to intrinsic behavior. The dashed line accounts for a purely intrinsic behavior (after ref. [5])... 39

Figure 2.9.1: Schematic illustration of the phase shift φ (colored box) between the time-dependent sinusoidal input voltage signal $V(t)$ (blue curve) and the time dependent current response $I(t)$ (red curve) (after ref. [163]). 42

Figure 2.9.2: Impedance spectrum of a single RC-element with Z' as real part and $-Z''$ as imaginary part in the Nyquist representation. 44

Figure 2.9.3: (a) „Brick-Layer“ model of an idealized ceramic with bulk material (*b*) and grain boundaries (*gb*) between two metal electrodes (el). The equivalent circuit is represented for the corresponding bulk, grain boundary and electrode responses (redrawn after ref. [168]); (b) Schematic illustration of a typical impedance spectrum in the Nyquist representation with distinguishable bulk (black), grain boundary (red) and electrode (blue) responses. 45

Figure 2.9.4: (a) Schematic depiction for a blocking double-layer formation in Nyquist representation for an ion-conducting material resulting in a 45° at low frequencies; (b) Schematic depiction of a depressed semicircle concerning the corresponding α value of the CPE.[165] 47

Figure 2.10.1: Crystallographic phases and temperature dependent phase transitions of NBT processed with the help of the VESTA program. The phase transition temperatures are taken from ref. [176] 49

Figure 2.10.2: Bulk conductivity in Arrhenius representation for acceptor doped and A-site non-stoichiometric NBT. A characteristic kink is observable for the oxygen ionic conducting compositions. The temperature region where a phase coexistence was evidenced is

highlighted in blue. The bulk oxygen ionic conductivity of Mg-doped NBT is comparable to YSZ. (The Arrhenius plots, ionic transport numbers, as well as the comparison to commercial oxide ion conductors, are taken from ref. [48])....51

Figure 3.1.1: Powder processing steps....59

Figure 3.2.1: Processing steps for preparing the samples. 63

Figure 3.6.1: Schematic illustration of the measuring principle of an impedance spectroscopy setup (adapted from ref. [238]). 67

Figure 3.8.1: Schematic illustration of the home built Sawyer-Tower-Setup used for the temperature dependent polarization measurements. 69

Figure 3.9.1: Schematic illustration of a typical electromotive force (EMF) setup. 70

Figure 4.1.1: XRD-pattern of the Mg- (a), Al- (b), and Fe-doped (c) NBT compositions with doping contents between 0.1 mol% and 4.0 mol%. The peaks caused by the secondary phases are denoted with a star in the respective XRD-pattern. 78

Figure 4.1.2: SEM images of the 4.0 mol% doped Mg- (a), Fe- (b) and Al-NBT (c) in the BSE mode. The secondary phases are marked with red circles. 79

Figure 4.1.3: Impedance spectra of the Mg- ((a) to (c)), Fe- ((d) to (f)) and Al-doped ((g) to (i)) NBT compositions taken at 500 °C with a frequency range of 0.1 Hz to 3 MHz, shown for variable impedance ranges. 80

Figure 4.1.4: Arrhenius plots for the bulk conductivity σ_b of the Mg- (a), Al- (b) and Fe-doped (c) NBT compositions with varying doping contents between 0.1 mol% and 4.0 mol%. 82

Figure 4.1.5: Bulk conductivity as a function of the acceptor doping content taken at 500 °C for the Mg- (black), Fe- (red) and Al-doped (blue) NBT compositions. The three regions represent the electronic, mixed and ionic conduction region concerning the doping concentration. 85

Figure 4.1.6: Conductivity model for the 1.0 mol% Mg-doped NBT composition. The experimental data is represented by the filled bowls (cyan), the analytical model data (ΔH_{asso} = 0.45 eV) by empty circles (red). The horizontal black line illustrates the total Mg-doping concentration, the black crosses represent the free oxygen vacancy concentration vs. temperature. The background colors indicate the specific phase within the temperature range (R for rhombohedral, T for tetragonal, C for cubic). 89

Figure 4.1.7: Conductivity model for the 1.0 mol% Mg-doped NBT composition. The experimental data is represented by the filled bowls (cyan), the phase independent model data ($\Delta H_{asso,tet}$ = $\Delta H_{asso,rhom}$ = 0.45 eV) by empty circles (red) and the phase-dependent model data ($\Delta H_{asso,tet}$ = 0.1 eV and $\Delta H_{asso,rhom}$ = 0.45 eV) by empty circles (cyan). The horizontal black line illustrates the

total Mg-doping concentration, the black crosses represent the free oxygen vacancy concentration vs. temperature. The background colors indicate the specific phase within the temperature range (R for rhombohedral, T for tetragonal, C for cubic). 91

Figure 4.1.8: Phase dependent conductivity model (empty circles) with $\Delta H_{asso,tet}$ = 0 eV and $\Delta H_{asso,rhom}$ = 0.39 eV for the 1.5 mol% Mg-doped, $\Delta H_{asso,tet}$ = 0.1 eV and $\Delta H_{asso,rhom}$ = 0.45 eV for the 1.0 mol% Mg-doped and $\Delta H_{asso,tet}$ = 0.51 eV and $\Delta H_{asso,rhom}$ = 0.55 eV for the 0.5 mol% Mg-doped NBT directly compared with the experimental data (bowls). The background colors indicate the specific phase within the temperature range (R for rhombohedral, T for tetragonal, C for cubic). 92

Figure 4.1.9: Binding energy of a defect complex against the distance to another present Mg ion based on density functional theory calculations. The black, red and blue bowls represent the 1st, 2nd and 3rd nearest neighbor (NN) shell, respectively. 94

Figure 4.1.10: Calculated density of states for the Mg- (a), Al- (b) and Fe-doped NBT (c). The band gap is depicted in grey. Additional defect states within the band gap are highlighted with a red circle in the case of Fe-doped NBT in (c). 96

Figure 4.1.11: Calculated Crystal Orbital Hamiltonian Populations (COHPs) for Mg- (a), Al- (b) and Fe-doped (c) NBT. The colored boxes represent the bonding and antibonding states. The Fermi level is presented by the zero energy state. 98

Figure 4.1.12: Al-NMR spectra of Al-doped NBT with varying doping concentration. The AlO_x orientation is given by the resulting ^{27}Al chemical shifts (denoted with colored boxes at the x-axis). 101

Figure 4.1.13: Total Admittance Y (colored bowls) in direct comparison with the grain boundary admittance (empty circles) of the Mg- (a), Fe- (b) and al-doped (c) NBT compositions; only compositions which have featured a distinct grain boundary response are depicted. 103

Figure 4.1.14: Total conductivity and bulk conductivity of oxygen ionic conducting acceptor doped NBT compositions. The bulk conductivity values for YSZ (red) are extracted from ref.[48], the total conductivity values of polycrystalline YSZ (blue) are extracted from ref.[276] 104

Figure 4.2.1: XRD pattern of the A-site non-stoichiometric N_xB_yT-6BT samples with x= 0.50, 0.51, 0.52 and y= 0.49, 0.50. 0.51, 0.52 and 0.53 (a) and detailed scan (b); the stars denote additional peaks caused by secondary phases. 111

Figure 4.2.2: SEM images of A-site non-stoichiometric N_xB_yT-6BT compositions with (a) x= 0.50, y= 0.49; (b) x= 0.50, y= 0.50; (c) x= 0.50, y= 0.51; (d) x= 0.50, y= 0.52; (e) x= 0.50, y= 0.53 and (f) x= 0.51, y= 0.50 in secondary electron (SE) mode. 113

Figure 4.2.3: Impedance spectra of the Bi-varied (a) and Na-varied (b) N_xB_yT-6BT samples in Nyquist representation at 500 °C from 0.1 Hz to 3 MHz. 114

Figure 4.2.4: Arrhenius-type plots for the temperature dependent bulk conductivity of the A-site non-stoichiometric N_xB_yT-6BT compositions. 115

Figure 4.2.5: Temperature-dependent permittivity ε_r' and dielectric loss factor $\tan\delta$ for the Bi- non-stoichiometric N_xB_yT-6BT in the pre-poled state (3 $kVmm^{-1}$) ((a) to (e)) from 25 °C to 500 °C. The temperature of maximum permittivity T_m, as well as the depolarization temperature Td, are depicted with an arrow. The unpoled permittivity and loss response of the respective compositions (legend in (e) are compared concerning the Bi content in (f). 117

Figure 4.2.6: Temperature-dependent permittivity ε_r' and dielectric loss factor $\tan\delta$ for the Na- non-stoichiometric N_xB_yT-6BT samples after poling at 150°C with 3 $kVmm^{-1}$ from 25 °C to 500 °C ((a) to (c)). The temperature of maximum permittivity T_m, as well as the depolarization temperature Td, are depicted with an arrow. 118

Figure 4.2.7: Temperature-dependent polarization and strain responses for the N_xB_yT-6BT compositions below ((a) and (d)), near ((b) and (e)) and above ((c) and (f)) the depolarization temperature T_d. The measurements in (b) and (e) are taken at different temperatures which can be taken from the legend in (b). 119

Figure 4.2.8: Direct comparison of the remanent polarization P_{rem} (a), maximum strain ΔS_{max} (b), depolarization temperature T_d (c) and obtained grain size (d) concerning the Na/Bi ratio. ..120

Figure 4.2.9: XRD pattern of the Fe-doped and undoped NBT ((a) and (b)) as well as NBT-6BT ((c) and (d)) compositions with varying doping content. The additional peaks caused by secondary phases are denoted with a star. 125

Figure 4.2.10: SEM images of (a) pure NBT and (b) NBT-6BT in comparison to (c) 4.0 mol% Fe-doped NBT and (d) 4.0 mol% Fe-doped NBT-6BT in SE mode. The insets in (c) and (d) represent BSE images taken from the secondary phases in the respective composition in the same scale. 126

Figure 4.2.11: Grain size evolution with increasing Fe-doping content in NBT (black) and NBT-6BT (red). 127

Figure 4.2.12: Impedance spectra for Fe-doped and undoped NBT (a) and NBT-6BT (b) at 500 °C from 0.1 Hz to 3 MHz in Nyquist representation. The 1.0 mol% Fe-doped NBT and NBT-6BT composition are directly compared in (c). The peak frequencies are given for each respective bulk response. 128

Figure 4.2.13: Arrhenius-type plots of the bulk conductivity for the Fe-doped and undoped NBT (a) and NBT-6BT (b) compositions. The calculated activation energies are given within the figure. .129

Figure 4.2.14: Polarization vs. applied electric field for doped and undoped NBT (a) and NBT-6BT (b) at room temperature and 1 Hz. 132

Figure 4.3.1: XRD pattern of the A-site non-stoichiometric (a) and B-site doped NB_xT-25ST compositions (b). 138

Figure 4.3.2: SEM images for the undoped ((a) to (c)), 3.0 mol% Nb-((d) to (f)) and 3.0 mol% Fe-doped ((g) to (i)) and A-site non-stoichiometric NB_xT-25ST compositions in SE mode. 139

Figure 4.3.3: Calculated grain size of the doped (Fe-doped red and Nb-doped blue) and undoped (black) NB_xT-25ST compositions concerning A-site non-stoichiometry. 139

Figure 4.3.4: SEM images in BSE mode for the undoped ((a) to (c)), 3.0 mol% Nb-((d) to (f)) and 3.0 mol% Fe-doped ((g) to (i)) and A-site non-stoichiometric NB_xT-25ST compositions in BSE mode (core-shell structures are highlighted with red circles; secondary phases are denoted with blue circles). 141

Figure 4.3.5: Impedance spectra in the Nyquist representation for the A-site non-stoichiometric (a) and B-site Nb-doped (b) as well as Fe-doped NB_xT-25ST compositions (c) taken at 500 °C from 0.1 Hz to 3 MHz. 144

Figure 4.3.6: Arrhenius-type plots of the high-frequency process conductivity for the undoped (a) and doped (b), A-site non-stoichiometric NB_xT-25ST compositions. 145

Figure 4.3.7: Temperature and frequency-dependent permittivity ε_r' and dielectric loss $\tan\delta$ for the non-stoichiometric NB_xT-25ST compositions from 25 °C to 500 °C in the unpoled state ((a) to (e)). A direct comparison of the permittivity and loss responses concerning the Bi-variation if provided in (f) for 1 kHz. The temperature of maximum permittivity T_m is exemplarily denoted with an arrow in (b). 147

Figure 4.3.8: Frequency-dependent permittivity ε_r' and dielectric loss factor $\tan\delta$ for the Nb-doped ((a) to (c)) and Fe-doped and A-site non-stoichiometric NB_xT-25ST compositions ((d) to (f)); T_m is depicted with an arrow in (b) exemplarily. 148

Figure 4.3.9: Comparison of the maximum permittivity ε_{max} (a) and the temperature of maximum permittivity T_m (b) for the Fe-doped (red), Nb-doped (blue) and undoped NB_xT-25ST compositions (black) taken at 1 kHz concerning the A-site variation. 149

Figure 4.3.10: Polarization and strain responses of the A-site non-stoichiometric ((a) and (d)), Fe-doped ((b) and (e)) and Nb-doped (c and f) NB_xT-25ST compositions taken at 1 Hz and room temperature. 151

Figure 4.3.11: Comparison of the remanent polarization P_{rem}, the maximum polarization P_{max}, the maximum positive strain S_{pos} and the maximum negative strain S_{neg} concerning Fe- (red), Nb-doping (blue) and A-site non-stoichiometry black)of the NB_xT-25ST composition. 153

Figure 4.4.1: XRD-pattern of the A-site non-stoichiometric NB_xT-6BT-15CZ (magenta, red and violet) and NB_xT-6BT-20CZ (cyan, blue and dark blue) compositions (a). The peaks caused by secondary phases are denoted with a star. The respective region is shown in (b) in more detail. 160

Figure 4.4.2: Temperature and frequency-dependent permittivity ε_r' and dielectric loss factor $\tan\delta$ for the A-site non-stoichiometric NB_xT-6BT-15CZ ((a) to (c)) and the NB_xT-6BT-20CZ compositions ((d) to (f)). The two anomalies detected for the dielectric loss are denoted with arrows in (f). 162

Figure 4.4.3: XRD-pattern of the NBT-6BT-20CZ-xBA compositions with x= 0.0, 0.5, 1.0, 1.5, 2.0, 4.0 and 8.0 mol%. A full scan from 2θ = 20° to 2θ = 90° is provided in (a). The peaks caused by secondary phases are denoted with a star and are shown in detail in (b). 165

Figure 4.4.4: SEM-Images of pure NBT-6BT-20CZ after sintering (a) and an additional annealing at 750 °C for 12 h (b) compared to NBT-6BT-20CZ with 1.5 mol% BA addition after sintering (c) and an additional annealing step at 750 °C for 12 h (d) in the backscattered electron mode (BSE)..166

Figure 4.4.5: Temperature and frequency-dependent permittivity and dielectric loss factor for the NBT-6BT-20CZ-xBA compositions with x= 0.0 ((a) and (e)), 0.5 ((b) and (f)), 1.0 ((c) and (g)), and 1.5 ((d) and (h)) mol%. The frequency dispersion is depicted with an arrow in (a) and (e) exemplarily. The two local maxima in the dielectric loss are depicted with arrows in (f).....167

Figure 4.4.6: Temperature and frequency-dependent permittivity and dielectric loss factor for the NBT-6BT-20CZ-xBA compositions with x= 2.0 ((a) and (e)), 4.0 ((b) and (f)), 8.0 mol% ((c) and (g)), and a direct comparison for all processed compositions ((d) and (h)). 168

Figure 4.4.7: Comparison of $\Delta T(\varepsilon_r' \pm 15\ \%)$ (red dashed lines) and $\Delta T(\tan\delta \leq 0.02)$ (grey area) for the NBT-6BT-20CZ-xBA compositions (x= 0.0, 0.5, 1.0, 1.5 mol%). The orange arrows depict the temperature range in which both criteria are fulfilled simultaneously. 169

Figure 4.4.8: Comparison of $\Delta T(\varepsilon_r' \pm 15\ \%)$ (red dashed lines) and $\Delta T(\tan\delta \leq 0.02)$ (grey area) for the NBT-6BT-20CZ-xBA compositions (x= 2.0, 4.0, 8.0 mol%). The orange arrow depicts the temperature range in which both criteria are fulfilled simultaneously. 170

Figure 4.4.9: Comparison of $\Delta T(\varepsilon_r' \pm 15\ \%)$ (orange plot) and $\Delta T(\tan\delta \leq 0.02)$ (blue plot) for NBT-6BT-20CZ-xBA with respect to the BA content. The orange values represent ε_r'(150 °C). 171

Figure 4.4.10: Arrhenius-type plots for the bulk conductivity σ_b for the A-site non-stoichiometric NB_xT-6BT-yCZ (a) and the BA added NBT-6BT-20CZ-xBA compositions. 172

Figure 4.4.11: Polarization vs. Electric field for the different NB_xT-6BT-yCZ compositions ((a) and (d)) as well as temperature dependent polarization of the representative NB_xT-6BT-yCZ compositions ((b) and (e)) in comparison with the NBT-6BT-20CZ-xBA compositions ((c) and (f)) from room temperature to 150 °C. 174

List of Tables

Table 2.9-1: Impedance Phenomena and their capacitance range.[155] 46

Table 3.1-1: Drying temperatures and drying times for the used raw materials before weighing. 60

Table 4.1-1: Activation energies before and after the kink of the Mg-, Fe- and Al-doped samples. 82

Table 4.2-1: EDX analysis of the matrix and secondary phase found in Bi-excess ($N_{0.50}B_{0.53}$T-6BT) and Na-excess ($N_{0.51}B_{0.50}$T-6BT) compositions. 112

Table 4.2-2: Calculated activation energies of different N_xB_yT-6BT compositions below and above the temperature dependent transition. 115

Table 4.2-3: Oxygen ionic transport numbers of the investigated Fe-doped NBT and NBT-6BT compositions. 130

Table 4.4-1: Grain size, density, dielectric permittivity ε_r' at 1 kHz, temperature stability criteria for permittivity and dielectric loss $\tan\delta$ as well as recoverable energy W_{rec} and efficiency η of the NBxT-6BT-yCZ compositions. 163

Table 4.4-2: Relevant parameters for the processed NBT-6BT-20CZ-xBA compositions. 169

List of Abbreviations

AC	Alternating Current
b	Bulk
BA	$BiAlO_3$
BSE	Backscattered Electron
BT	$BaTiO_3$
CB	Conduction Band
COHP	Crystal Orbital Hamiltonian Population
COOP	Crystal Orbital Overlap Population
CPE	Constant Phase Element
CZ	$CaZrO_3$
DC	Direct Current
DFT	Density Functional Theory
DOS	Density of States
EDX	Energy Dispersive X-ray Spectroscopy
EIS	Electrochemical Impedance Spectroscopy
EMF	Electromotive Force
EPR	Electron Paramagnetic Resonance Spectroscopy
GDC	$Ce_{0.9}Gd_{0.1}O_{1.95}$
gb	Grain Boundary
HREM	High Resolution Electron Microscope
IS	Impedance Spectroscopy
KNN	$(K_{0.5}Na_{0.5})NbO_3$
LSGM	$La_{0.9}Sr_{0.1}Ga_{0.9}Mg_{0.1}O_{2.9}$
MO	Metal Oxide
NBT	$Na_{0.5}Bi_{0.5}TiO_3$
NBT-BT	$(1-x)(Na_{0.5}Bi_{0.5}TiO_3)$-$xBaTiO_3$
NBT-BT-CZ	$[(1-x)(1-y)(Na_{0.5}Bi_{0.5}TiO_3)$-$yBaTiO_3)]$-$xCaZrO_3$
NBT-6BT-20CZ-BA	$(1-x)(0.8[0.94Na_{0.5}Bi_{0.50}TiO_3$-$0.06BaTiO_3]$-$0.2(CaZrO_3))$-$xBiAlO_3$
NBT-BT-KNN	$x[y(Na_{0.5}Bi_{0.5}TiO_3)-(1-y)(BaTiO_3)]-(1-x)(K_{0.5}Na_{0.5}NbO_3)$
NBT-KBT-KNN	$x[y(Na_{0.5}Bi_{0.5}TiO_3)-(1-y)(K_{0.5}Bi_{0.5}TiO_3)]-(1-x)(K_{0.5}Na_{0.5}NbO_3)$
NBT-ST	$(1-x)(Na_{0.5}Bi_{0.5}TiO_3)$-$xSrTiO_3$

NMR	Nuclear Magnetic Resonance Spectroscopy
NN	Nearest Neighbor
NNN	Next Nearest Neighbor
PNR	Polar Nano Region
HT-PNR	High Temperature Polar Nano Region
LT-PNR	Low Temperature Polar Nano Region
PZT	$Pb(Zr_xTi_{1-x})O_3$
PLZT	$(Pb_{1-x}La_x)(Zr_{1-y}Ti_y)O_3$
PMN-PT	$(1-x)(Pb(Mg_{1/3}Nb_{2/3})O_3)–xPbTiO_3$
RT	Room Temperature
SC	Semiconductor
ST	$SrTiO_3$
SE	Secondary Electron
SEM	Scanning Electron Microscopy
SOFC	Solid Oxide Fuel Cell
VB	Valence Band
XRD	X-ray Diffraction
YSZ	$Zr_{0.92}Y_{0.08}O_{1.96}$

List of Symbols

A	Area
a	Lattice Constant
a_i	Chemical Activity of Species *i*
a_{O_2}	Oxygen Activity
α	Correlation Factor
C	Capacitance
C_b	Capacitance Bulk
C_{gb}	Capacitance Grain Boundary
C	Curie Constant
C_υ	Site Fraction of Vacancies
c	Concentration
D_i	Dielectric Displacement
D_s	Self-Diffusion Coefficient
D_v	Vacancy-Diffusion Coefficient
$\widetilde{D}$	Chemical Diffusion Coefficient
d	Distance
d_{ijk}	Tensor: Piezoelectric Coefficient
E	Electric Field
E_a	Activation Energy
E_{Acc}	Energetic State: Acceptor
E_c	Coercive Field
E_{Don}	Energetic State: Donor
E_g	Band Gap Energy
e	Elementary Charge
ε	Permittivity
ε_0	Vacuum Permittivity
ε_r	Relative Permittivity
$\varepsilon^*(\omega)$	Complex Frequency Dependent Permittivity
F	Faraday Constant
φ	Phase Shift
G	Gibbs Free Energy
G_{mig}	Free Migration Energy
ΔG^*	Total Free Enthalpy

ΔG_{mig}	Free Migration Enthalpy
ΔG_v^f	Free Vacancy Formation Enthalpy
Γ_d	Jump Rate
Γ_s	Specific Jump Rate
H	Enthalpy
ΔH^*	Activation Enthalpy
ΔH_{asso}	Association Enthalpy
ΔH_{mig}	Migration Enthalpy
h	Electron Hole
h, k, l	Miller Indices
I	Current
I_s	Sample Current
$I(t)$	Time Dependent Current
$I^*(\omega)$	Complex Frequency Dependent Current
J	Particle Flux
K	Equilibrium Constant
K_{asso}	Equilibrium Constant for Association
k_B	Boltzmann Constant
λ	Wavelength, Jump Distance
M	Modulus
$M^*(\omega)$	Complex Frequency Dependent Modulus
m	Slope
μ	Charge Carrier Mobility
N	Number of Lattice Sites
N_d	Number of Defect Lattice Sites
n	Number of Jumps
n_c	Electrons in Conduction Band
n_i	Number of Majority Charge Carriers
υ_i	Stoichiometric Factor for Species *i*
η	Energy Storage Efficiency
P	Macroscopic Polarization
P_{max}	Maximum Polarization
P_{rem}	Remanent Polarization
P_{sat}	Saturation Polarization

p	Dipole Moment
p_i	Pyroelectric Coefficient
$p_i(O_2)$	Oxygen Partial Pressure
p_v	Holes in Valence Band
q	Charge
R	Resistance
R_b	Bulk Resistance
R_{gb}	Grain Boundary Resistance
R_x	Variable Resistor
r_A	Ionic Radius A-site Atom
r_B	Ionic Radius B-site Atom
r_O	Ionic Radius X-site Atom
ρ	Density
ρ_{air}	Density of Air
ρ_{fl}	Temperature Dependent Density of Water
S	Entropy
ΔS^*	Entropy of Ionic Hopping
ΔS_{asso}	Association Entropy
ΔS_{mig}	Migration Entropy
σ	Conductivity
σ_b	Bulk Conductivity
σ_e	Electronic Conductivity
σ_{el}	Electrical Conductivity
σ_{gb}	Grain Boundary Conductivity
σ_i	Ionic Conductivity
σ_{jk}	Tensor: Mechanical Force
T	Temperature
T_B	Burns Temperature
T_C	Curie Temperature
T_{CW}	Curie-Weiss Temperature
T_d	Depolarization Temperature
T_{fr}	Freezing Temperature
T_m	Temperature of Maximum Permittivity
T_{VF}	Vogel-Fulcher Temperature

t	Time
$\tan\delta$	Dielectric Loss Factor
t_{GS}	Goldschmidt Tolerance Factor
t_{ion}	Ionic Transport Number
τ	Relaxation Time
θ	Scattering Angle
V	Voltage
$V(t)$	Time Dependent Voltage
$V^*(\omega)$	Complex Frequency Dependent Voltage
$V_O^{\bullet\bullet}$	Kröger-Vink Notation: Oxygen Vacancy
W	Energy Storage Density
W_{air}	Sample Weight in Air
W_{fl}	Sample Weight in Water
W_{rec}	Recoverable Energy Storage Density
W_{total}	Total Energy Storage Density
ω	Frequency
ω_0	Debye Frequency
ω_{max}	Peak Frequency
X	External Driving Force
χ_e	Susceptibility
x_{ij}	Inverse Piezoelectric Coefficient
Y	Admittance
$Y^*(\omega)$	Complex Frequency Dependent Admittance
Z	Impedance; Coordination Number
Z_0	Magnitude of Impedance
$Z^*(\omega)$	Complex Frequency Dependent Impedance
$Z'(\omega)$	Real Part of Complex Impedance
$iZ''(\omega)$	Imaginary Part of Complex Impedance
$Z_C^*(\omega)$	Complex Impedance for Capacitor
$Z_{CPE}^*(\omega)$	Complex Impedance for Constant Phase Element
$Z_R^*(\omega)$	Complex Impedance for Resistor
z	Charge Number
$'$	Kröger-Vink Notation: Negative Charge
$\bullet$	Kröger-Vink Notation: Positive Charge

Abstract

In this work, the perovskite structured system $Na_{0.5}Bi_{0.5}TiO_3$ (NBT) and its solid solutions (1-x)($Na_{0.5}Bi_{0.5}TiO_3$)-x$BaTiO_3$ (NBT-BT), (1-x)($Na_{0.5}Bi_{0.5}TiO_3$)-x$SrTiO_3$ (NBT-ST) and [(1-x)(1-y)($Na_{0.5}Bi_{0.5}TiO_3$)-y$BaTiO_3$)]-x$CaZrO_3$ (NBT-BT-CZ) have been investigated. In detail, the impact of A-site non-stoichiometry and B-site doping on the electrical, dielectric, ferroelectric and piezoelectric properties was discussed. The main aim was to reveal the defect chemical origin of extremely high oxygen ionic conductivity in NBT and to apply the gained knowledge to control and enhance the properties of NBT-based solid solutions. This could result in a large application range of NBT and its solid solutions from excellent solid ionic conductors to high-temperature dielectric materials.

High levels of oxygen ionic conductivity were rather unexpected in NBT and highlight that the already established defect chemical models for lead- or barium-based systems do not hold for this system. It was assumed that defect complexes form in NBT between a B-site defect and a generated oxygen vacancy, resulting in a non-linear increase of the effective oxygen vacancy concentration.

By performing temperature dependent impedance spectroscopy, the electrical properties of NBT have been investigated in more detail. With the help of density functional theory (DFT) calculations, an analytical model was established with regards to a possible defect complex formation in acceptor doped NBT. Further, the conducted work delivers proof that the association energy of the defect complex is dependent on the doping element (in particular mechanical contributions from the differing ionic radii, Coulomb interactions with concerning the valence state and covalent contributions), doping concentration and crystal phase. With a precise adjustment of the A-site and B-site defect chemistry, controllability of the ionic conductivity in NBT could be reached in such a way, that either high ionic conducting NBT or low, semiconducting NBT can be processed.

Based on the gained knowledge, the solid solution NBT-6BT was investigated for A-site non-stoichiometry and B-site acceptor doping to reveal similar defect chemical mechanisms as observed in NBT. B-site acceptor doping leads to similar electrical properties. The induction of high levels of oxygen ionic conductivity is, therefore, following the same mechanism in NBT-6BT. Based on this finding, acceptor doping was revealed to be not a valid approach to enhance the ferroelectric properties in NBT and NBT-based solid solutions. A-site non-stoichiometry featured a significant impact on the non-ergodic/ergodic relaxor transition on NBT-6BT which led to considerably different ferroelectric and piezoelectric properties at room temperature. Additionally, the presence of increased oxygen vacancy concentration is directly related to chemical diffusion during the processing.

This circumstance was utilized in the core-shell structured NBT-based solid solution NBT-25ST. In detail, B-site doping and A-site non-stoichiometry were simultaneously applied on NB_xT-25ST to elucidate the origin of forming this particular chemical inhomogeneity which could either be facilitated

by the occurrence of A-site vacancies or oxygen vacancies. With the help of a detailed SEM analysis, it could be confirmed that the oxygen vacancy concentration is mainly responsible for the formation of core-shell structures. Low oxygen vacancy concentration stabilized fine-grained, core-shell structures, larger concentrations result in grain growth and homogeneous elemental distribution. A remarkable impact on the resulting piezo- and ferroelectric properties could be revealed. As the NBT-rich core was attributed to being responsible for non-ergodic relaxor behavior, a core-shell structured composition should provide non-ergodic behavior. This assumption holds for A-site non-stoichiometry in NB_xT-25ST. Acceptor doping with Fe (high vacancy concentration), however, leads to non-ergodic relaxor behavior, Nb-donor doping (low vacancy concentration results in ergodic relaxor behavior at room temperature irrespective on additional A-site non-stoichiometry. This result confirms that, besides changing the occurrence of core-shell microstructures, the ferro- and piezoelectric responses of the NBT-rich cores themselves are affected by the doping. This results in ergodic behavior in the case of Nb-donor doping.

The feature of relaxor behavior was utilized to further enhance the application range of NBT. Therefore, the solid solution NB_xT-6BT-yCZ was investigated for its temperature-dependent dielectric properties. It could be confirmed that the stoichiometric NBT-6BT-20CZ composition exhibits an exceptionally large application temperature range where the criterion of temperature stable permittivity and low dielectric loss are fulfilled simultaneously. The almost temperature-independent permittivity was attributed to the presence and coexistence of two different kinds of polar nano regions, in the respective low temperature (LT) and high temperature (HT) form. The dielectric losses, however, limited the application range. By the addition of $BiAlO_3$ (BA), a further decrease of the dielectric losses could be achieved. This resulted in an excellent high-temperature dielectric material that can by far outperform commonly used high-temperature capacitors for the given operation temperature window in which the permittivity and loss criterion are fulfilled simultaneously.

The here presented results elucidate the defect chemical origin of oxygen ionic conductivity in NBT. By applying the gained defect chemical knowledge, oxygen vacancy formation can precisely be controlled and the application range of NBT and its solid solutions could be enlarged towards tunable piezo- and ferroelectric properties as well as excellent temperature stable dielectric properties.

1 Introduction

A class of materials, which is becoming increasingly important to address a growing demand on higher living standards, which needs to be covered by modern technologies, are ceramics. Ceramic materials are known for their excellent thermal insulation properties, high melting points, corrosion and wear resistance as well as low ductility and high hardness.[1]

Beyond that, functional ceramics exhibit excellent electrical, dielectric, optical and magnetic properties and are part of nearly every electronic device.[2]

A large group of functional ceramics originates from the discovery of piezoelectricity and ferroelectricity in Rochelle salt by Valasek in 1920[3, 4] which can be seen as the beginning of ceramic investigations not only from a structural material point of view but also a functional perspective. Materials that exhibit the piezoelectric effect allow for the conversion of electrical energy into mechanical strain and *vice versa*.[5, 6] This effect can be utilized wherever a coupling between mechanical and electrical energy is needed.

First and foremost, the family of lead-containing ceramics like lead zirconate titanate, $Pb(Zr_xTi_{1-x})O_3$ or short PZT, needs to be mentioned. PZT is even today one of the commercially most used functional ceramics. Those materials are vital for plenty of modern applications like transducers, sensors, actuators or micro-positioning systems.[5, 7-10]

As an example, the global market of piezoelectric actuators was estimated to be about 12 billion U.S. dollars in 2014.[2, 11, 12] The global market share of PZT as a piezoelectric material in 2014 was 96.5 %.[11]

Lead-based ceramics, however, evoke environmental as well as health concerns.[13] Lead is a cumulative toxic substance that causes a degeneration of the nervous system.[14, 15]

The production and use of PZT can cause a release of lead into the environment in various ways.[16, 17] Hence, the European Union started in 2003 to restrict the usage of lead and other hazardous elements by regulations like the “Restriction of the use of Hazardous Substances” (RoHS)[6] and the “Waste of Electrical and Electronic Equipment” (WEEE).[17]

Since the beginning of the 21st century, the emphasis of ceramic research has shifted towards lead-free alternatives for functional ceramics.[18-24]

With regards to actuator applications, three main solid solution systems have been recognized as the most promising candidates to replace PZT in the future.[25] These three systems are either based on potassium sodium niobate $(K_{0.5}Na_{0.5})NbO_3$ (KNN), barium titanate $BaTiO_3$ (BT) or sodium bismuth titanate $(Na_{0.5}Bi_{0.5})TiO_3$ (NBT). Amongst those, the lead-free ceramic NBT which was first reported by Smolenskii *et al.* in 1961[26], was seen as one of the most promising candidates for replacing its lead-containing counterparts concerning ferroelectric and piezoelectric applications.

Pure NBT, however, needs high poling fields due to its large coercive field (E_c = 7.3 kVmm^{-1}).[27, 28] This problem has been solved partially by forming solid solutions e.g. with barium titanate $BaTiO_3$ (BT).[29-31] The family of bismuth-based ceramics covers promising candidates for replacing PZT with regards to their dielectric, piezoelectric and ferroelectric properties.[32-43] NBT-based solid solutions can replace the lead-containing counterparts with regards to capacitor or actuator applications as they exhibit good piezoelectric and dielectric properties.[20, 24, 44-46] Even though, NBT-based solid solutions can outperform their lead-containing opponent for certain electromechanical properties[10, 47], the versatility to modify PZT with regards to the desired application is by far larger.[17] Therefore, the family of NBT-based systems cannot cover the same range of applications compared to PZT.

Aside from desirable electromechanical properties, the family of NBT and its solid solutions come along with some major inertia, impeding the utilization on an industrial scale. Pure NBT, for instance, exhibits high leakage currents making it less attractive for dielectric and ferroelectric applications. As the defect chemistry of NBT is rather complicated and not comparable to widely studied lead-based and other lead-free systems, the origin of the leakage current could not be clarified in detail. A better understanding of the defect chemical interactions in NBT is, therefore, kind of a bottleneck to further enhance the dielectric, electrical and electromechanical properties, as well. To address this impediment, the origin of this unexpected large leakage current in NBT was extensively investigated.

Li *et al.* revealed in 2014, that the high leakage current in NBT originates from an oxygen ionic transport mechanism.[48] The oxygen ionic conductivity in non-stoichiometric and acceptor doped NBT can even compete with commercially used oxide ion conductors like yttria-stabilized zirconia $Zr_{0.92}Y_{0.08}O_{1.96}$ (YSZ), $Ce_{0.9}Gd_{0.1}O_{1.95}$ (GDC) and $La_{0.9}Sr_{0.1}Ga_{0.9}Mg_{0.1}O_{2.9}$ (LSGM).[48]

This finding could potentially open a completely new field of application for NBT to function as a solid oxide ion conductor.[49, 50] NBT might be used as a ceramic membrane in a solid oxide fuel cell (SOFC). The ceramic membrane in SOFCs must feature high-temperature stability, as the working temperature is around 600 °C to 1000 °C. Furthermore, the material has to function as a good ionic conductor and an electronic insulator at the same time.[51-59]

This unexpected finding underlines the uniqueness of the defect chemistry in NBT compared to PZT or even lead-free BT-based systems. As the demand for lead-free, and possibly NBT-based, systems is rapidly growing, the lack of knowledge about the occurring leakage current and its defect chemical origin is highly detrimental. The inadequate knowledge of the defect chemistry in NBT and its solid solutions further results in a poor reproducibility which impedes the commercial use in large scales.

This work, therefore, shall elucidate the defect chemistry of NBT and, in the following, delivers proof that the here established concepts are also valid for more complex NBT-based solid solutions.

In detail, this work is focused on investigating the origin of extremely high oxygen ionic conductivity in NBT by taking the defect chemistry into account to achieve a deeper understanding of the defect chemical interactions which result in the oxygen ion transport and the electrical conductivity in general.[60, 61] The present oxygen ionic conductivity in NBT will be investigated with regards to a possible defect complex formation, the influence of coexisting phases, the concentration dependence, and the doping element choice experimentally and theoretically.

Furthermore, the obtained findings are used to derive a fundamental defect chemical model for NBT which is based on the possible defect complex formation in NBT. Additionally, the here derived model will be adapted to NBT-based solid solutions with BT to further enhance the dielectric, piezoelectric and ferroelectric properties.[62]

Beyond that, a solid solution of NBT with strontium titanate $SrTiO_3$ (ST) was investigated in more detail as it is known to exhibit a so-called core-shell structure.[63] The formation of a core-shell microstructure, a chemical inhomogeneity, results in a change of ferroelectric properties and strain enhancement and can directly be controlled by applying the here gained knowledge of the basic defect chemistry in NBT.[64]

Apart from oxygen ionic conductivity as well as ferroelectric and piezoelectric properties, NBT-based solid solutions with calcium zirconate $CaZrO_3$ (CZ) exhibit an almost temperature and frequency independent permittivity with low losses even at elevated temperatures.[65] By precise control of the defect chemistry, a further enhancement is expected to make this solid solution suitable to function as a high-temperature capacitor material.[66]

The field of application for NBT and its solid solutions, therefore, ranges from excellent oxide ion conductors on the one hand, to the best known high-temperature dielectric materials on the other. The knowledge of the unique defect chemistry of NBT allows for precise control and enhancement of the desired property.

2 Theoretical Background

In this chapter, the theoretical aspects which are necessary to understand the here presented work are highlighted. In the beginning, the class of dielectric materials and the related properties are discussed. Furthermore, a detailed look at the crystal structure of the investigated material sodium bismuth titanate $Na_{0.5}Bi_{0.5}TiO_3$ (NBT), the perovskite structure is provided. Alongside with the crystal structure, the resulting piezoelectric and ferroelectric properties are described.

The core of this work is to investigate the impact of defects, particularly point defects like vacancies in the A-site lattice or acceptor doping at the B-site and the simultaneously generated oxygen vacancies, on the material properties. Especially the effects on the electrical properties and enhancement of conductivity or piezo- and ferroelectricity by precise adaption of the defect chemistry are of major interest for bringing the investigated materials into an application. Therefore, the theoretical background provides detailed information about the formation of defects in a crystal as well as the basic principles of electronic and ionic conduction to the presence of such defects.

The technique of choice for the investigation of conduction mechanisms is the electrochemical impedance spectroscopy (EIS).

To highlight the potential of NBT and its solid solutions with regards to a variety of applications, a literature review will also be given for the basic system NBT and the here investigated NBT-based solid solutions $0.94(Na_{0.5}Bi_{0.5}TiO_3)$-$0.06BaTiO_3$ (NBT-6BT), $0.75(Na_{0.5}Bi_{0.5}TiO_3)$-$0.25SrTiO_3$ (NBT-25ST) and (1-x)$[0.94(Na_{0.5}Bi_{0.5}TiO_3)$-$0.06BaTiO_3]$-$xCaZrO_3$ (NBT-6BT-xCZ).

2.1 Dielectric Properties

To acquire knowledge about piezoelectrics and ferroelectrics, a basic description of the material class of dielectrics is necessary. The general description of dielectric-, piezoelectric- and ferroelectric properties is taken from the textbooks by A. J. Moulson and J. M. Herbert, B. Jaffe and H. Jaffe, M. E. Lines and A. M. Glass, and R. Waser and U. Böttger.[5, 9, 67, 68]

By its definition, a dielectric is an electrically insulating material that can be polarized by applying an external electric field. The macroscopically observable polarization P is directly related to the applied electric field E by the following relation:

$$P = \varepsilon_0 \cdot \chi_e \cdot E \,. \tag{2.1}$$

ε_0 is the vacuum permittivity and a physical constant ($8.854 \cdot 10^{-12}$ As V^{-1}m^{-1}). χ_e stands for the material-dependent susceptibility and is related to the relative permittivity ε_r:

$$\chi_e = \varepsilon_r - 1 \,. \tag{2.2}$$

The relative permittivity is dependent on the temperature, electric field and the frequency of the electric field. By applying an external electric field, a dielectric displacement D is generated which is also related to the polarization P:

$$D = \varepsilon_0 \cdot E + P = \varepsilon_0 \cdot \varepsilon_r \cdot E \,. \tag{2.3}$$

The macroscopically measurable polarization P is the sum of electronic, ionic, dipolar and space charge contributions which is schematically illustrated in Figure 2.1.1.

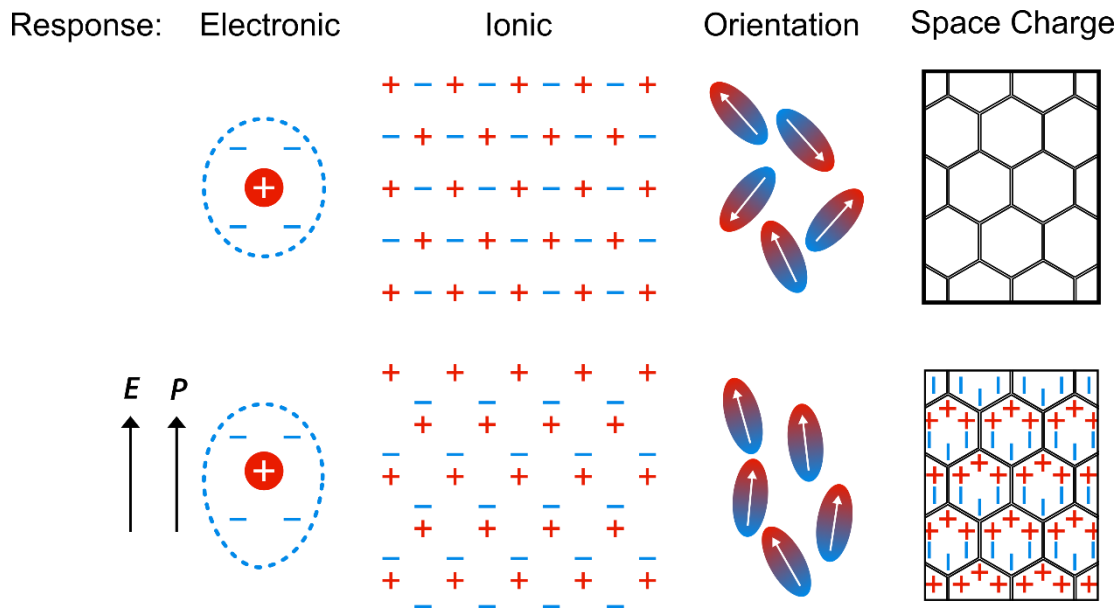

Figure 2.1.1: Microscopic polarization contributions with an applied electric field. Electronic, ionic, dipole orientation and space charges can be discriminated (redrawn after ref. [68]).

Around the positively charged nucleus, a negatively charged electron shell is present. By applying an electric field E, a deformation of the electron shell occurs and contributes to the polarization. This effect is present in all dielectric materials. Concerning an ionic crystal consisting of positively charged cation and negatively charged anion sublattices, the ionic contribution to the polarization occurs by the corresponding sublattice displacement when an electric field is applied. Whenever molecules or electrical dipoles are involved, an orientation-dependent polarization is evident. When exposed to an electric field, the electrical dipoles are enforced to align with the electric field. Besides electrical dipoles, mobile charge carriers like electrons, holes, and ions are also affected by an external electric field. In detail, a space charge contribution to the polarization is expected when the charge carrier distribution is inhomogeneous. Mobile ions and/or electrons are forced to move in a field gradient. A grain or phase boundary could act as a potential barrier leading to an accumulation of charge carriers building up a space charge.[68]

An ideal dielectric material would result in a capacitor free of conduction contributions to dielectric losses when introduced into an electrical circuit. The simple parallel-plate capacitor model suits for a description with a flat geometry of the dielectric material and represents the ideal relationship of the resulting capacitance C, the sample geometry (A for the area and d for the thickness) as well as the relative permittivity ε_r of the respective dielectric:

$$C = \varepsilon_r \cdot \varepsilon_0 \cdot \frac{A}{d}. \tag{2.4}$$

This, however, only describes the ideal case when the charge carriers can move instantaneously in the presence of an external electric field. In a more realistic scenario, there are several inertias. The previously discussed contributions to the polarization follow different mechanisms that occur in different time scales. When an alternating electric field is applied to a real dielectric, there will be a frequency dispersion of the permittivity. Figure 2.1.2 provides a schematic overview of the different contributions to the permittivity for the frequency region where the relaxation or resonance is expected.

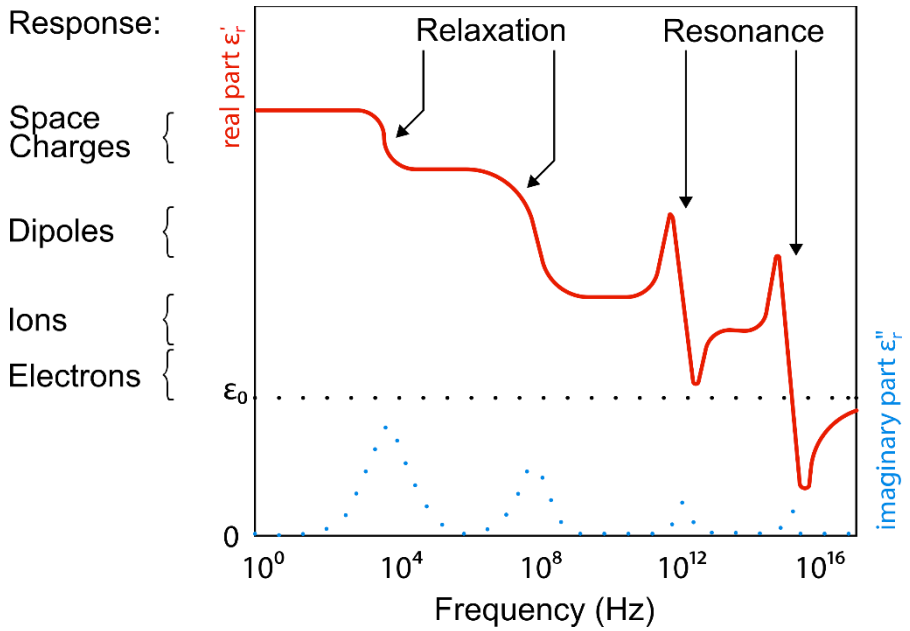

Figure 2.1.2: Frequency dependent responses of the real part (red) and the imaginary part (blue) of the permittivity (redrawn after ref. [68]).

Space charges and dipoles undergo relaxation. The space charge polarization results from a drift of mobile ions or electrons which are confined by interfaces like grain boundaries and can be found in a frequency range between mHz up to MHz depending on the local conductivity. Ions and electrons show resonance with molecular vibrations at frequencies in the THz region.[68] Those relaxations and resonances lead to a phase shift of the dielectric displacement D with regards to the electric field E. The frequency dependent dielectric permittivity can therefore be described as a complex function (ε_r^*) exhibiting a real part ε_r' and an imaginary part ε_r'' (see equation (2.5)):

$$\varepsilon_r^* = \varepsilon_r' - i\varepsilon_r'' \,. \tag{2.5}$$

The imaginary part of the permittivity ε_r'' results in losses. Those are dissipated as heat when the capacitor is utilized at the respective frequency where losses occur.

Aside from the ideal case, also resistive leakage and dielectric adsorption lead to an increase in the imaginary part. The resulting loss factor, or dielectric loss, $tan\delta$ is the quotient of the imaginary part ε_r'' and the real part of the permittivity ε_r':

$$\tan\delta = \frac{\varepsilon_r''}{\varepsilon_r'}. \tag{2.6}$$

The group of dielectrics can further be divided into certain subgroups concerning the material responses (see Figure 2.1.3).

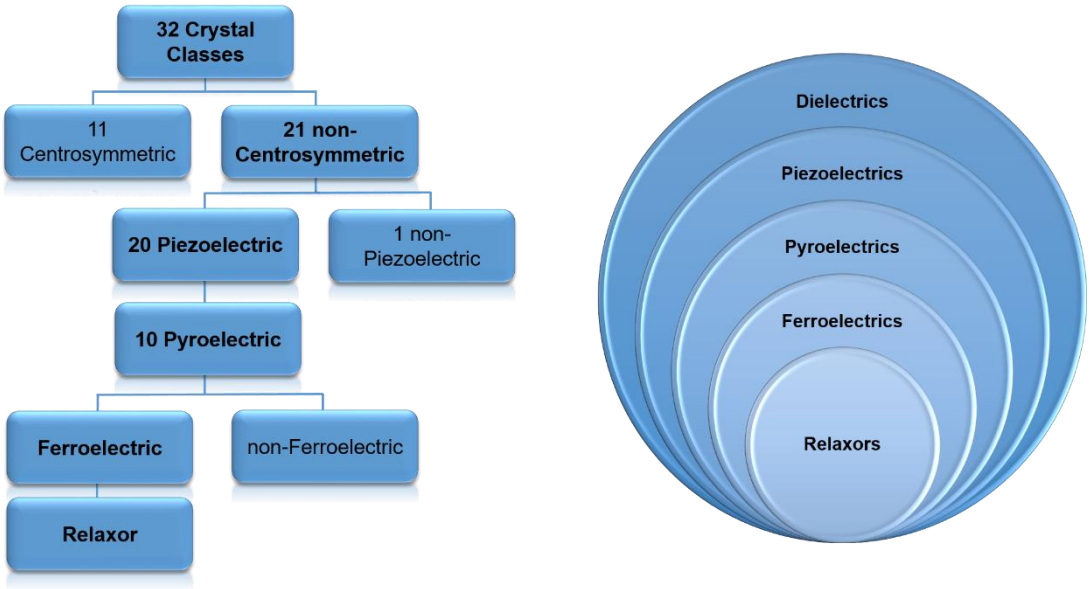

Figure 2.1.3: All crystalline systems divided into subgroups: Dielectrics, piezoelectrics, pyroelectrics ferroelectrics and relaxors.[33]

The occurrence of piezo-, pyro- and ferroelectricity originates from the inherent crystal structure which will be introduced in the following chapter.

2.2 Crystal Structure

The piezoelectric, pyroelectric and ferroelectric properties of a functional ceramic are directly related to its crystal structure. The vast majority of piezoelectric materials forms crystals that are related to the perovskite structure. The commercially most used perovskite material is lead zirconate titanate (PZT)[69] but there are also lead-free piezoelectrics like barium titanate (BT)[70], potassium sodium niobate (KNN)[71] and the system under investigation sodium bismuth titanate (NBT).[26] Especially the lead-free alternatives to PZT have drawn major interest during the past years. The name perovskite is derived from the mineral calcium titanate ($CaTiO_3$) which was named after the Russian mineralogist Count Lev Perovski and exhibits the general structure ABX_3.[72]

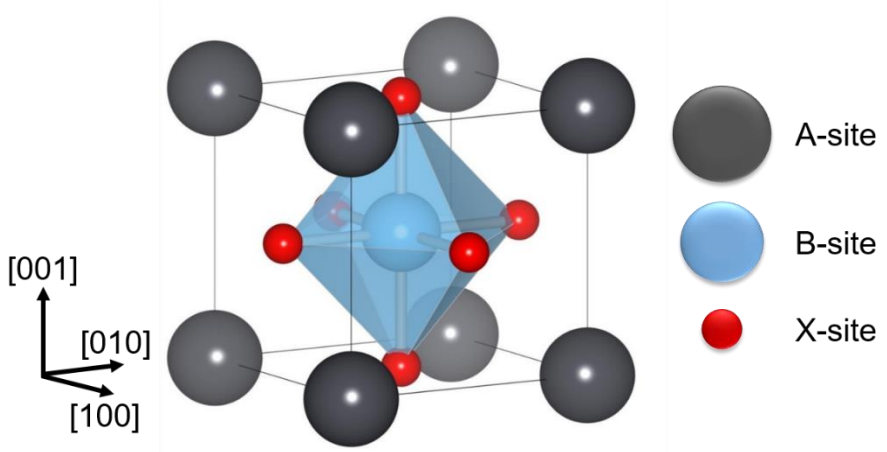

Figure 2.2.1: Unit cell of the ABX_3 ideal cubic perovskite structure. The B-site atom (blue) occupies the center. The X-site atoms (red), typically oxygen, sit in the middle of each surface and form an octahedron around the center atom. The A-site atoms (black) are placed on the corners of the unit cell.

Figure 2.2.1 depicts the general perovskite structure of the basic composition ABX_3 in a simple cubic case without any lattice distortions. The A-site is placed at the corners of the unit cell and is usually a cation from an alkali, alkaline earth or rare earth metal. The B-site is occupied by a smaller cation than the A-site which is usually a transition metal. The X-site is typically occupied by oxygen ions forming an octahedron around the center ion. It should be noted, that the X-site can also be occupied by fluorine, chlorine, carbon, sulfur, hydrogen or, in rare cases, nitrogen.[9, 67, 73-75] The resulting structure is a network of corner-linked oxygen octahedra with the smaller ion cation (B-site) filling the octahedra and the larger ions (A-site) filling the dodecahedral holes.[9] In the case of the system under investigation NBT, the Ti^{4+} ion forms the center (B-site) while the Na^{+}- and Bi^{3+} ions share the A-site on the edges with a ratio 1:1. The oxygen ions form an octahedron around the center ion. Victor Moritz Goldschmidt developed an empirically derived factor, the Goldschmidt's factor, in 1926.

Goldschmidt established two rules to judge whether the crystal structure is stable or not.[76] Cations and anions were considered to be rigid spheres.

The cation must be surrounded by as many anions as possible and further, the anions have to reside in the direct neighborhood of the cations. Hence, the anion-cation radius needs to be equal to the sum of the ionic radii of the respective ions. Equation (2.7) displays the relation of the ionic radii of the A-site cation (r_A), the oxygen anion at the X-site (r_O) and the B-site cation (r_B):

$$r_A + r_O = \sqrt{2} \cdot (r_B + r_O). \tag{2.7}$$

This equation describes the ideal behavior. Goldschmidt's tolerance factor t_{GS} forms based on the ideal case:[9]

$$t_{GS} = \frac{r_A + r_O}{\sqrt{2} \cdot (r_B + r_O)}. \tag{2.8}$$

The perovskite will only form when the tolerance factor is around 1. When t_{GS} equals 1, an ideal cubic perovskite will form. Small deviations from unity between $0.88 < t_{GS} < 1.09$ lead to a distorted, but still stable, perovskite structure. At tolerance factors above one, a tetragonal distortion along <001> is favored, below one rhombohedral distortion along <111> direction and orthorhombic distortions along <110> direction may occur.[77] Figure 2.2.2 provides a schematic of a cubic (a), as well as a tetragonal (b) and rhombohedral (c) unit cell.

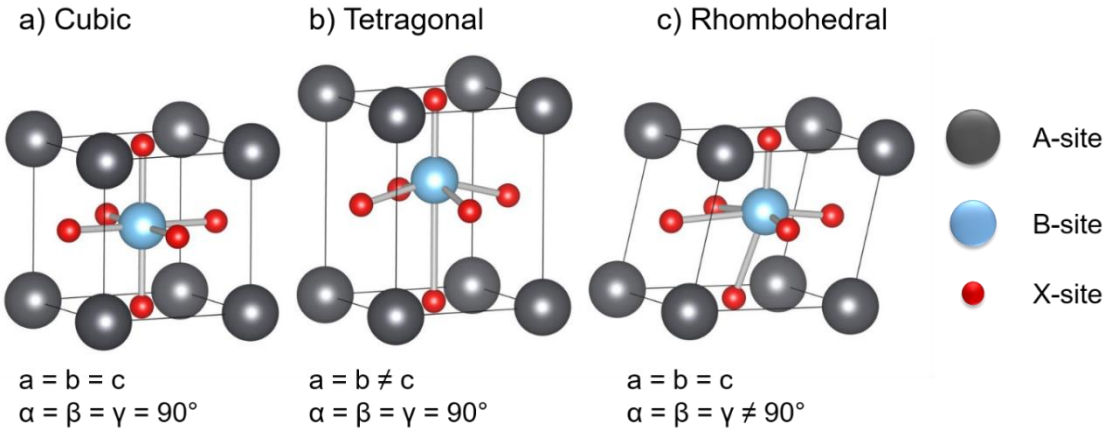

Figure 2.2.2: Unit cell of a perovskite with cubic (a), tetragonal (b) and rhombohedral (c) structure.

With regards to the occurring distortion, the positioning of the A-site center cation gets unstable which leads to spontaneous polarization.[17] The occurrence of spontaneous polarization and the evolution of piezoelectric, pyroelectric and ferroelectric properties will be described in chapter 2.3, 2.4, and 2.5 in more detail.

2.3 Piezoelectric Properties

Every apparent crystal structure can be described by one of 32 crystallographic point groups. Eleven of those point groups do not feature a centrosymmetric structure and hence, do not have an inversion center. 20 of the remaining 21 point groups exhibit piezoelectric responses. The application of a mechanical force σ leads to an electrical displacement in the material. The resulting polarization P_i is linearly dependent on the piezoelectric coefficient d_{ijk} (as a third rank tensor) and the applied mechanical force σ_{jk}.

$$P_i = d_{ijk} \cdot \sigma_{jk} \,. \tag{2.9}$$

This relationship is called the piezoelectric effect and was first introduced by Jacques Curie in 1880.[78] The application of an external force leads to a displacement of the polar species.[79]
Further, the application of an external electric field results in the formation of a measurable strain x. This effect is called the inverse piezoelectric effect and can be described by equation (2.10):[80, 81]

$$x_{ij} = d_{kij} \cdot E_k \,. \tag{2.10}$$

It should be noted, that electrostriction and piezoelectricity have to be distinguished. All dielectrics show electrostriction when an external electric field is applied.[82] The resulting strain features a quadratic dependence on the applied electric field making electrostrictive responses independent on the polar character of the applied electric field.[69] A piezoelectric response can only be observed when a dipole moment can be induced by an electric field and is therefore strictly dependent on the crystallographic structure.

2.4 Pyroelectric Properties

Ten groups from the remaining 20 piezoelectric crystallographic groups exhibit a unique polar axis in unstrained conditions. Those groups have a polar axis without an inversion center and show a spontaneous polarization. A spontaneous strain occurs due to electrostriction. The pyroelectric effect can be expressed as:[82]

$$\Delta P_i = p_i \cdot \Delta T \,. \tag{2.11}$$

p_i describes the pyroelectric coefficient. The magnitude of the resulting dipole moment is temperature-dependent and increases until the Curie temperature T_C is reached. The Curie temperature defines a crystallographic phase transition from a phase exhibiting a unique polar axis (e.g. tetragonal) towards a phase with a center of symmetry (e.g. cubic). Above T_C, the spontaneous polarization vanishes and the material becomes a regular paraelectric.[69] In the paraelectric, cubic phase, the dielectric permittivity (ε) can be described by the Curie-Weiss-law:[83]

$$\varepsilon = \varepsilon_0 + \frac{C}{T - T_{CW}} \approx \frac{C}{T - T_{CW}}. \tag{2.12}$$

The latter C is defined by the Curie constant, T_{CW} denotes the Curie-Weiss temperature and T the actual temperature. The Curie-Weiss temperature is equal to the Curie temperature for first-order phase transitions ($T_{CW} = T_C$). A first-order phase transition is characterized by discontinuous changes of the physical properties like the enthalpy resulting in the evolution of latent heat during the transformation.[80] For second-order phase transitions those two temperatures are similar but not equal ($T_{CW} < T_C$).[84] Second order phase transitions, for instance, are characterized by a continuous change of enthalpy. Hence, no latent heat is observable for second-order phase transitions.[80]

2.5 Ferroelectric Properties

A subgroup of pyroelectrics is characterized by the switchability of the polarization direction between crystallographically equivalent configurations when a sufficiently high external electric field is applied and was discovered in 1921[3] in the single crystal Rochelle salt and later in the 1940s for polycrystalline ceramics.[85, 86] Those materials are called ferroelectrics (in analogy to ferromagnetics). A ferroelectric material can be characterized by the possibility to change the direction of polarization by the presence of an external electric field.[33] As can be seen in Figure 2.1.3, only a small fraction of crystallographic point groups result in ferroelectric behavior. As a consequence of the spontaneous polarization, surface charges are generated which lead to the formation of a charge compensating depolarization field E_d. To reduce the consumed energy of the depolarization field, the crystal separates into regions with different polarization directions. Those regions are called domains. No macroscopic polarization establishes as the polarization vectors of domains cancel each other out.[69] All polarization vectors inside a single domain point towards the same direction. The polarization vectors of neighboring domains are usually antiparallel (180° domain walls) or perpendicular (90° domain walls) to avoid discontinuities in the polarization. The formation of domains is directly affected by the presence of vacancies, dislocations, dopants, elastic stress fields, and charge carriers which can counteract the domain formation process.[68]

By applying an electric field, the domains change their polarization direction, can shrink or grow, depending on the initial polarization direction of the corresponding domain concerning the applied electric field.

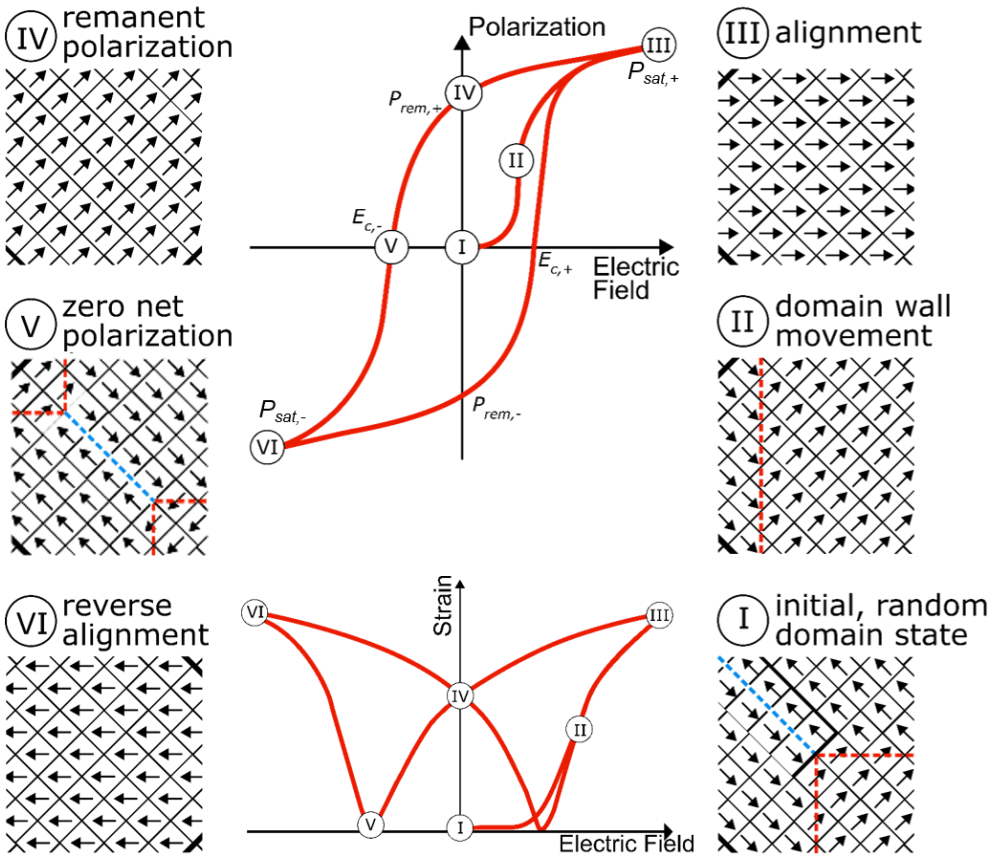

Figure 2.5.1: Schematic illustration of a polarization (a) and strain hysteresis (b) with an applied electric field. The states (I) to (VI) represent the respective depicted domain state (redrawn after ref. [87]).

Figure 2.5.1 depicts a schematic illustration of the polarization hysteresis with the respective evolution of domains of a normal ferroelectric material. In state (I), the virgin state, the sample was not exposed to an external electric field, yet. The domains within the material are randomly oriented and the respective polarization directions cancel each other out resulting in a zero net polarization. When the sample is exposed to an electric field, depicted as state (II), the domains with a polarization vector in the direction of the applied field start to grow. All other domains shrink simultaneously leading to an increase of the observable net polarization. In state (III), the present domains are aligned with the external electric field. Further increase of the electric field only activates intrinsic responses resulting in a linear rise of the polarization. It should be noted, that the saturated domain state does not result in a monodomain state due to the random orientation of grains in a polycrystalline material. Also, in single-crystalline samples stray energy, defects and/or stresses need to be considered which impede a monodomain state. A linear dependence of the applied electric field and the resulting polarization can be observed. The corresponding polarization response is called saturation polarization P_{sat}. By decreasing the electric field, the polarization decreases as well.

At zero electric field, a majority of the domains remain aligned and the domain state is therefore preserved resulting in the remanent polarization P_{rem} in state (IV). When an electric field is applied in the opposite direction, a back-switching to re-align the polarization vectors of the domains with the applied electric field is initiated. The macroscopic polarization decreases with an increasing field in the opposite direction until a zero net polarization is reached in state (V). The electric field which is necessary to decrease the macroscopic net polarization of the sample back to zero is called coercive field E_c. A further increase of the electric field leads to another reorientation of the domains in the respective direction, the polarization increases again until the negative saturation polarization P_{sat} is reached in state (VI).[9]

As known from the previous discussion on the classification of ferroelectrics, they also feature piezoelectric behavior. In detail, a sample that is exposed to an external electric field will show a macroscopic strain response. As the polarization undergoes a hysteresis, the strain response does as well (see Figure 2.5.1). A normal ferroelectric exhibits a butterfly-shaped bipolar strain hysteresis. The given states correspond to the states described for the ferroelectric polarization hysteresis. The strain is, for instance, caused by the alignment of the unit cells within the electric field which results in compression or elongation in the respective direction.

2.5.1 Relaxors

A subgroup of ferroelectric materials is the group of ferroelectric relaxors. Relaxors have first been mentioned by Smolenskii and Isupov in 1954.[88] Cross introduced the name relaxor ferroelectric in 1987.[89] In general, relaxors exhibit diffuse of even no phase transitions, as well as a differing dielectric, ferroelectric and piezoelectric responses when compared to regular ferroelectrics.

With regards to the dielectric permittivity, relaxors, therefore, exhibit remarkably different responses compared to a regular ferroelectric (see Figure 2.5.2).

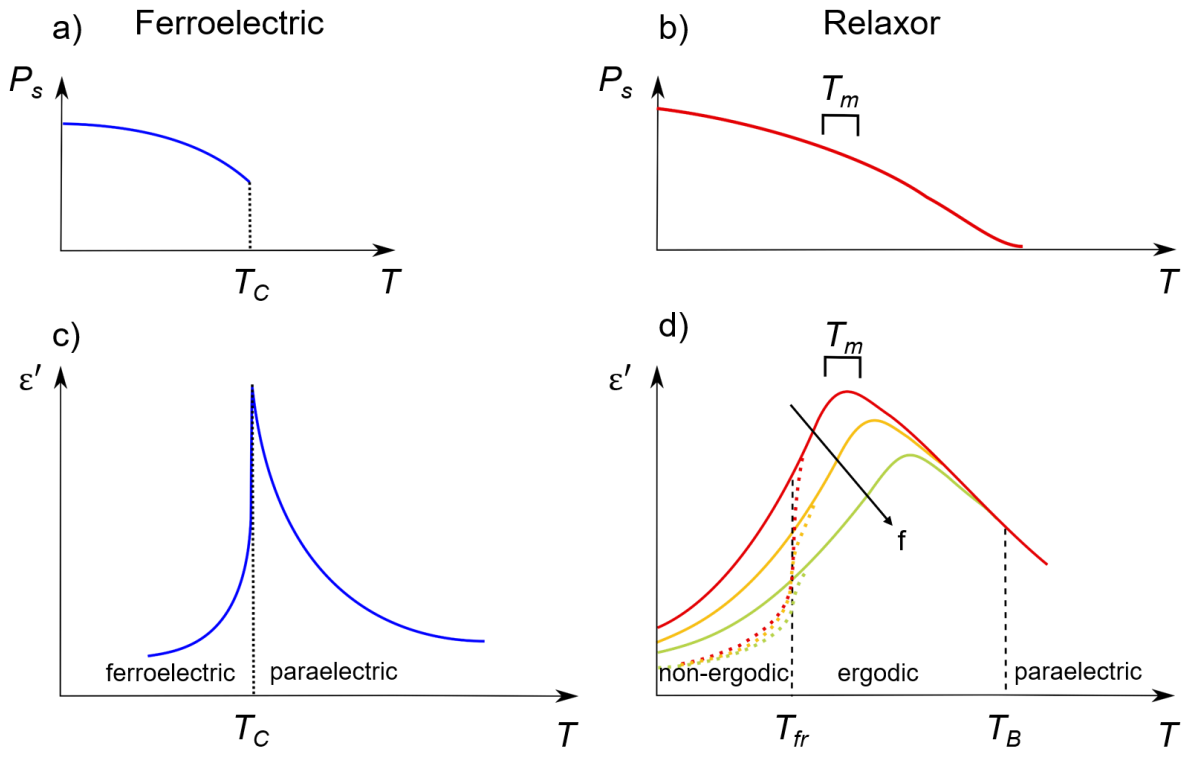

Figure 2.5.2: Comparison of a regular ferroelectric with a relaxor material with regards to the temperature dependent phase transition ((a) and (b)) and the temperature dependent permittivity response ((c) and (d)). The solid lines in (d) represent a canonical relaxor, the dashed lines represent a non-canonical relaxor with a spontaneous transition to a ferroelectric at T_{fr} (after ref. [90]).

At sufficiently high temperatures, relaxors, equivalently to regular ferroelectrics, exhibit a non-polar, paraelectric, cubic structure. By cooling down, the material properties start to differ. A ferroelectric material exhibits a sharp maximum in permittivity at the Curie temperature T_C, determined by a first or second-order phase transition. Relaxors exhibit a peak in permittivity at T_m (temperature of maximum permittivity) which is broader compared to a regular ferroelectric.

A regular ferroelectric shows a first-order or second-order phase transition at the Curie temperature T_C where a structural phase transition occurs from a paraelectric towards a ferroelectric crystal structure and the spontaneous polarization P_s establishes immediately. A relaxor exhibits a small fraction of macroscopic polarization even at temperatures far above the temperature of maximum permittivity T_m. Below T_B, the so-called Burns temperature, a non-zero polarization is evident in relaxors. [91, 92] To further discuss the similarities and differences of regular ferroelectrics and relaxors, the concept of polar nano regions will be introduced at this point. The presence of macroscopic polarization even above T_m is attributed to the formation of those ordered, nano-sized polar regions (polar nano regions, PNRs) exhibiting fluctuating dipole moments within an unordered, non-polar matrix. A schematic illustration of a PNR in a lead-based perovskite ($Pb(B^{2+}_{1/3}B^{5+}_{2/3})O_3$) is given in Figure 2.5.3.

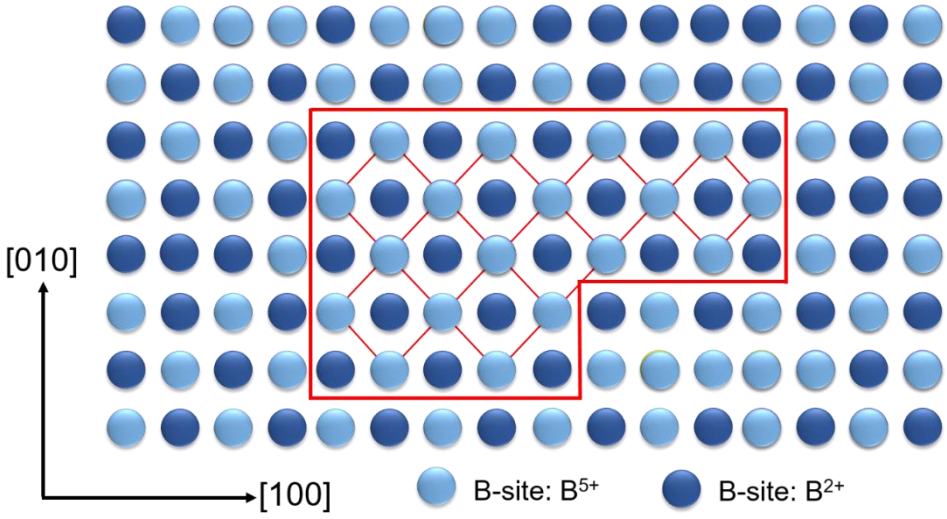

Figure 2.5.3: Schematic illustration of a chemically ordered polar nano region (delimited by a red solid line) in a disordered, non-polar matrix for a $Pb(B^{2+}_{1/3}B^{5+}_{2/3})O_3$ perovskite (redrawn after ref. [93]).

PNRs have been evidenced by neutron diffraction[94], Raman spectroscopy[95, 96] as well as nuclear magnetic resonance spectroscopy.[97, 98] Below T_B, the relaxor is in the so called ergodic state. In the ergodic state, the present PNRs exhibit an uncorrelated behavior. It needs to be mentioned, that the formation of PNRs does not lead to a change of the macroscopic crystal structure but leads to notable property changes.[89, 93] The broad permittivity peak can be attributed to the presence of PNRs. Different sizes of the PNRs and their interaction with each other lead to a broad permittivity peak which is, besides, strongly frequency-dependent.[90, 93, 99, 100] Due to varying relaxation times, lower measuring frequencies lead to larger permittivity values as well as a shift from T_m to lower temperatures as also larger PNRs (with higher relaxation times) contribute to the dielectric response.[101]

In the ergodic state (close to T_B), the existing PNRs do not interact with each other and they can switch the polarization between energetically equivalent crystallographic directions due to thermal fluctuations.[102] By decreasing the temperature, new PNRs are generated and start to grow resulting in a stronger interaction due to an increased correlation length.[94] When sufficiently low temperatures are reached, two different cases need to be considered. For a canonical relaxor, the thermal fluctuation of the PNRs can be decreased to a point where the PNRs "freeze", resulting in a reduced thermal motion of the majority of the PNRs. The temperature, at which the frozen in state of PNRs is reached is called freezing temperature T_{fr}. Below T_{fr}, the description of a glass like state is used to characterize relaxor behavior.[103] The freezing temperature T_{fr} is thus often related to be the Vogel-Fulcher temperature T_{VF}. The Vogel-Fulcher equation relates this transition temperature with the measuring frequency (ω) and the activation energy barrier (E_a) and was introduced by Vogel[104], Fulcher[105] and Tammann in the 1920's.[106]

$$\omega = \omega_0 \cdot \exp\left(\frac{E_a}{k_B \cdot (T - T_{VF})}\right). \tag{2.13}$$

The parameters ω_0, k_B and T_{VF} represent the Debye frequency, the Boltzmann constant, and the Vogel-Fulcher temperature, respectively. Below T_{fr}, a canonical relaxor shows non-ergodic behavior and is therefore called a non-ergodic relaxor.[93] Non-ergodic relaxors typically exhibit large relaxation times for the dielectric response.[107] The ferroelectric and piezoelectric responses are directly dependent on pre-treatment with either temperature, mechanical or electrical force.[108-111] A non-ergodic relaxor is characterized by an irreversible electric field-induced ferroelectric long-range order resulting in ferroelectric behavior. Some relaxors exhibit a thermally activated spontaneous transition to ferroelectric behavior at T_{fr} resulting from establishing a ferroelectric long-range order. Those relaxors are called non-canonical relaxors. Examples for non-canonical relaxors are (1-x)$Pb(Mg_{1/3}Nb_{2/3})O_3$-x$PbTiO_3$ (PMN-PT) [112-114] or $(Pb_{1-x}La_{(2/3)x})(Zr_yTi_{1-y})O_3$ (PLZT).[115, 116]

In certain cases, another anomaly is detectable in the dielectric responses of relaxors. NBT-based compositions like in x[y($Na_{0.5}Bi_{0.5}TiO_3$)-(1-y)($BaTiO_3$)]-(1-x)($CaZrO_3$), or short (NBT-BT-CZ)[65], x[y($Na_{0.5}Bi_{0.5}TiO_3$)-(1-y)($K_{0.5}Bi_{0.5}TiO_3$)]-(1-x)($K_{0.5}Na_{0.5}NbO_3$), or short (NBT-KBT-KNN)[33] and x[y($Na_{0.5}Bi_{0.5}TiO_3$)-(1-y)($BaTiO_3$)]-(1-x)($K_{0.5}Na_{0.5}NbO_3$), or short (NBT-BT-KNN)[117] feature the formation of a shoulder or a distinct second peak below the temperature of maximum permittivity T_m. The thermal evolution of the polar nano regions for NBT-6BT-xKNN is illustrated in Figure 2.5.4.[117]

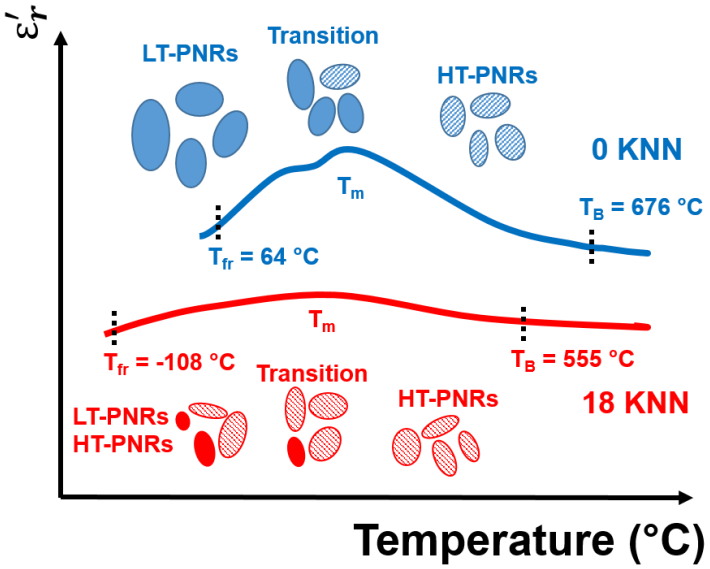

Figure 2.5.4: Schematic illustration of the thermal evolution of high temperature (HT) and low temperature (LT) polar nano regions and the resulting permittivity responses with respect to PNR-concentration and -size effects in NBT-6BT-xKNN (redrawn after ref. [117]).

In NBT-6BT-xKNN, two different kinds of polar nano regions are usually considered. At elevated temperatures only one kind of PNRs, the high-temperature PNRs (HT-PNRs), lead to the increased dielectric response around T_m. By decreasing the temperature, a fraction of the HT-PNRs transforms into more stable low-temperature PNRs (LT-PNRs) which are responsible for the additional shoulder in the temperature dependent permittivity plots. It is claimed in the literature that the transformation of HT-PNRs into LT-PNRs comes along with a distinct transition of the crystal structure of the respective PNRs. [33, 65, 117] The Burns temperature T_B and the freezing temperature T_{fr} shift significantly towards lower temperatures.

Beyond the dielectric responses, the ferroelectric and piezoelectric responses of relaxors also differ compared to a regular ferroelectric. A comparison of the polarization and strain responses of ergodic and non-ergodic relaxors is provided in Figure 2.5.5.

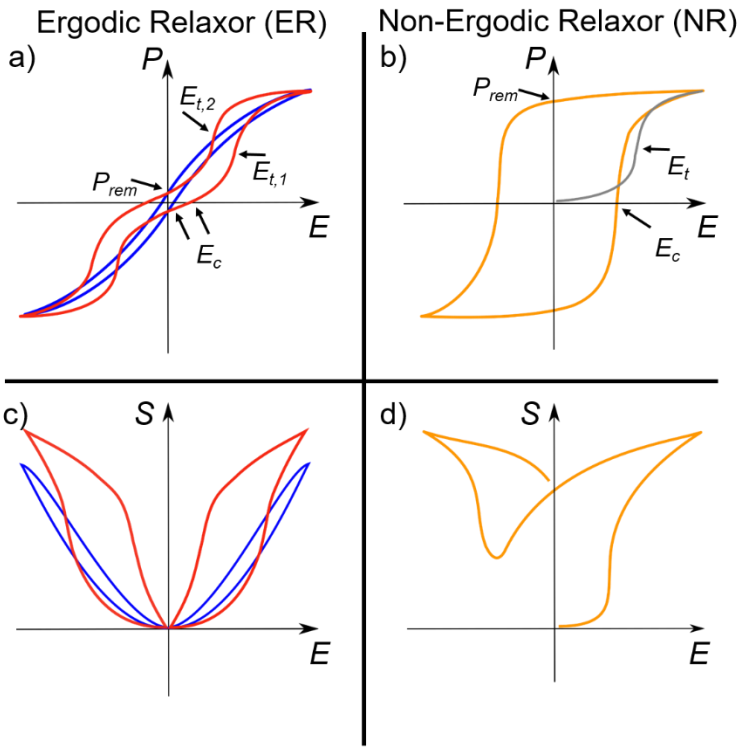

Figure 2.5.5: Polarization and strain hysteresis for an ergodic (ER) and non-ergodic (NR) canonical relaxor from the unpoled, virgin state. (a) depicts the polarization, (c) the strain response of an ergodic relaxor with (red line) and without (blue line) a reversible electric field-induced ferroelectric long-range order. (b) depicts the polarization, (d) the strain response of a non-ergodic relaxor with an irreversible electric field-induced ferroelectric long-range order (the grey line in (b) represents the response of a virgin sample) (adapted from ref. [10]).

When the relaxor is in the ergodic state (Figure 2.5.5 (a) blue line), the polarization response is not as pronounced as for a ferroelectric. The PNRs will align with the external electric field resulting in comparable polarization. Nevertheless, if the electric field is removed, the PNRs will not stay aligned resulting in low remanent polarization P_{rem}. The corresponding strain hysteresis exhibits a sprout shape with nearly vanishing strain at zero field condition (Figure 2.5.5 (c) blue line). Ergodic relaxors can also exhibit a reversible electric field-induced phase transition where ferroelectric long-range order establishes by a sufficiently high external electric field ($E_{t,1}$) resulting in a so called pinched polarization hysteresis (Figure 2.5.5 (a) red line). By removing the external field, the ferroelectric long-range is broken again (the electric field at which the ferroelectric long-range order collapses, $E_{t,2}$, is smaller than the electric field $E_{t,1}$ where ferroelectric long range order is introduced). The strain response still represents a sprout shape but with a broader hysteresis (Figure 2.5.5 (c) red line).

The resulting maximum strains are larger in those cases.[118-120] The formation of pinched polarization hysteresis due to electric field induced ferroelectric long-range order has been evidenced for the solid solution NBT-BT.[10] It should be noted, that pinched polarization loops cannot generally be attributed to an electric field induced ferroelectric long-range order. Chemical inhomogeneity can also result in pinched polarization loops e.g. due to a core-shell formation (a detailed discussion on the core-shell microstructure will be given in chapter 4.3). If a canonical relaxor is in the non-ergodic state, a ferroelectric long-range order can irreversibly be induced by an external electric field (Figure 2.5.5 (b) grey line). Once the PNRs are aligned in a non-ergodic relaxor, the polarization and strain response is similar to a regular ferroelectric resulting in large coercive fields E_c, high remanent polarization P_{rem} and butterfly shaped strain responses (orange line in Figure 2.5.5 (b) and (d)). According to Jo and Rödel, the electric field needed to induce ferroelectric long-range order in a non-ergodic relaxor is slightly higher than the coercive field after the transition ($E_t > E_c$).[121] A non-canonical relaxor, for instance, also exhibits ferroelectric behavior in the non-ergodic region as a temperature-induced spontaneous polarization occurs below the freezing temperature T_{fr}.

2.5.2 Dielectric Energy Storage

On a more application related basis, relaxors can be utilized as dielectric materials for capacitors. A capacitor accumulates charges when exposed to an external electric field. This charge is stored and can be released when needed.

The energy storage density W can be expressed as a function of the applied electric field E, and the polarization respective response P as follows:[122]

$$W = \int_0^{P_{max}} E(P)dP\,. \tag{2.14}$$

The recoverable energy W_{rec} can be calculated from extracting the remanent polarization P_{rem}, the coercive field E_c, and the maximum polarization P_{max} at maximum field E_{max} as follows:[122-124]

$$W_{rec} = \int_{P_{rem}}^{P_{max}} EdP\,. \tag{2.15}$$

The recoverable energy W_{rec} represents the energy that can be stored and recovered in a capacitor material.[125] The energy storage efficiency η is defined as the ratio between the recoverable energy W_{rec} and the energy needed for the charging/discharging of a capacitor, the total energy W_{total}:

$$W_{total} = \int_0^{P_{max}} EdP\,. \tag{2.16}$$

The energy storage efficiency can, therefore, be expressed as:[122, 126]

$$\eta = \frac{W_{rec}}{W_{total}} \cdot 100\%\,. \tag{2.17}$$

A schematic illustration of a polarization hysteresis is given in Figure 2.5.6 for a linear dielectric (a), an ergodic relaxor (b) and a regular ferroelectric (c). The colored areas depict the occurring energy losses (red) and the recoverable energy storage density (blue).

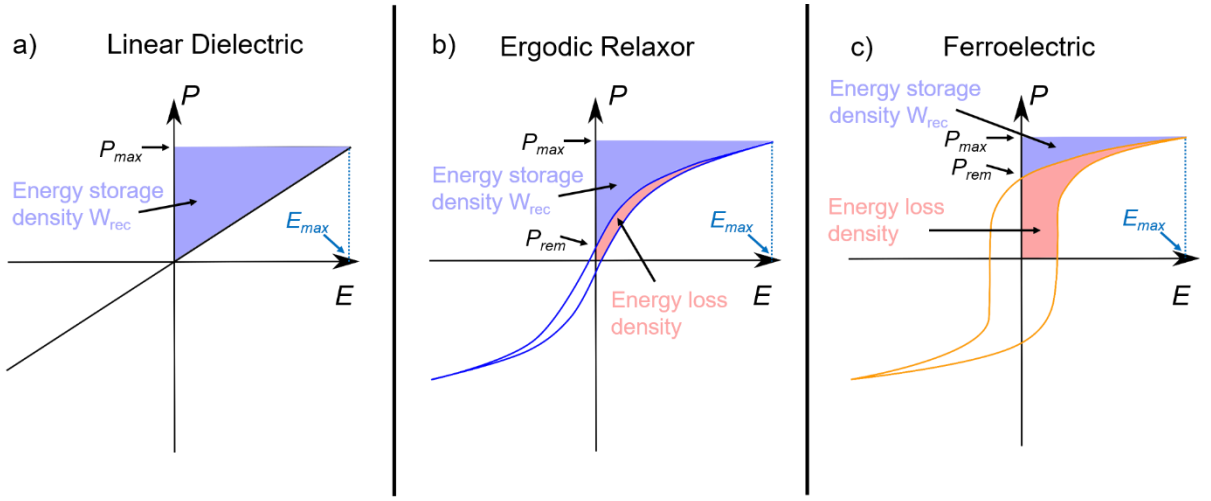

Figure 2.5.6: Schematic illustration of hysteresis and energy storage density for (a) linear dielectrics, (b) ergodic relaxors and (c) regular ferroelectrics. The blue area depicts the recoverable energy storage density W_{rec}. The red area depicts the energy loss density (redrawn after ref. [125, 127]).

An ideal linear dielectric (Figure 2.5.6 (a)) exhibits a linear polarization response with an increasing electric field. No polarization hysteresis and remanent polarization will be present at zero field condition. An ergodic relaxor (Figure 2.5.6 (b)) exhibits a slim polarization hysteresis resulting in low energy loss density (red area). P_{rem} is low in zero field conditions. In contrast, a regular ferroelectric (Figure 2.5.6 (c)) features a large P_{rem} at zero field conditions resulting in a high energy loss density. In a capacitor arrangement, the charging and discharging process can be described as follows:

By increasing the electric field up to the value E_{max}, the polarization simultaneously increases up to P_{max}. The total energy W_{total} which is consumed for the charging equals the sum of the red and blue areas. By decreasing the electric field, the capacitor undergoes a discharging process. The polarization decreases until the remanent polarization P_{rem} is reached at zero field. During the discharging, the recoverable energy W_{rec} is released (blue area) while the area inside the hysteresis loop represents the occurring losses which might be dissipated in heat (red area). To receive a high recoverable energy storage density W_{rec} paired with a high storage efficiency η, capacitors that can withstand high electric field with slim polarization loops and a low remanent polarization P_{rem} are most favorable.[125]

Apart from decreasing the polarization related losses, the reachable polarization at equal electric field is crucial for the storage capacity of a capacitor. Linear dielectrics exhibit orders of magnitude lower polarization compared to ferroelectrics or relaxors. Even though the storage efficiency could be higher in those cases, ergodic relaxors outperform linear dielectrics as they provide orders of magnitude larger polarization at equal electric fields.

2.6 Defects in Solids

It is essential to highlight the importance of defects as they feature a major impact on the material properties. Defects in a crystal can be classified concerning the dimensionality of the corresponding defect. Zero-dimensional defects, or point defects, are described by lattice defects on the atomic level. These could either be electrons, holes, impurities, interstitials or vacancies. Essentially this covers every defect on the atomic scale that deviates from the ideal crystal structure. One-dimensional defects, or line defects, are represented by dislocations which can extend infinitely along a line through the crystal. Two-dimensional defects are planar defects like grain boundaries, stacking faults or phase boundaries that do not have to be flat necessarily. Three-dimensional defects describe volume defects like voids, pores, cracks or inclusions.[128-131]

All of the here mentioned defects directly influence the resulting material properties. The main focus of this work is, however, to deliberately induce point defects to study the fundamental mechanisms of the defect chemistry in the material system NBT. The following discussion is based on textbooks by J. Maier, M. W. Barsoum and D. M. Smyth.[73, 129, 132]

2.6.1 Intrinsic and Extrinsic Defects

The occurring defects within a material can be divided into intrinsic and extrinsic defects. Intrinsic defects result from atom displacements within the host crystal structure. They are evident in each real crystal due to the thermal excitation and the entropy contribution. Extrinsic defects are caused by foreign atoms that are not part of the ideal crystal structure.[132] This could either be impurities or deliberately introduced dopants.

Defects will always form a defect pair with the compensating species in order not to violate the charge neutrality and the lattice conservation condition. On the one hand, an atom could leave its former position and occupy an interstitial lattice site leaving a vacancy behind. A so created defect pair is called a Frenkel defect. On the other hand, an atom could be extracted from the crystal creating a vacant lattice site. This vacancy is compensated by creating another vacancy with the opposite relative charge where the corresponding atom also vacates the crystal or will be built in at the surface. Such a defect pair is called a Schottky defect (see Figure 2.6.1).[9]

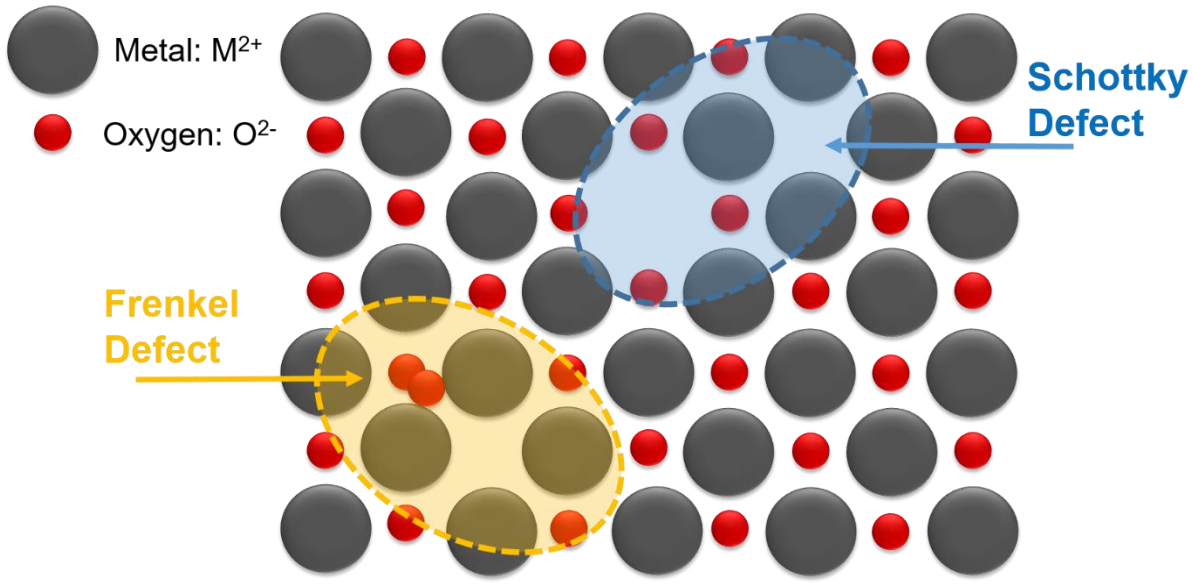

Figure 2.6.1: Schematic illustration of the formation of Schottky and Frenkel defect pairs in a crystal lattice.

Schottky defects can form in various ways depending on the atoms forming the crystal. Due to charge compensation, a Schottky pair may need to include more than just one atom and a corresponding vacancy in a perovskite structure (see Figure 2.6.2).

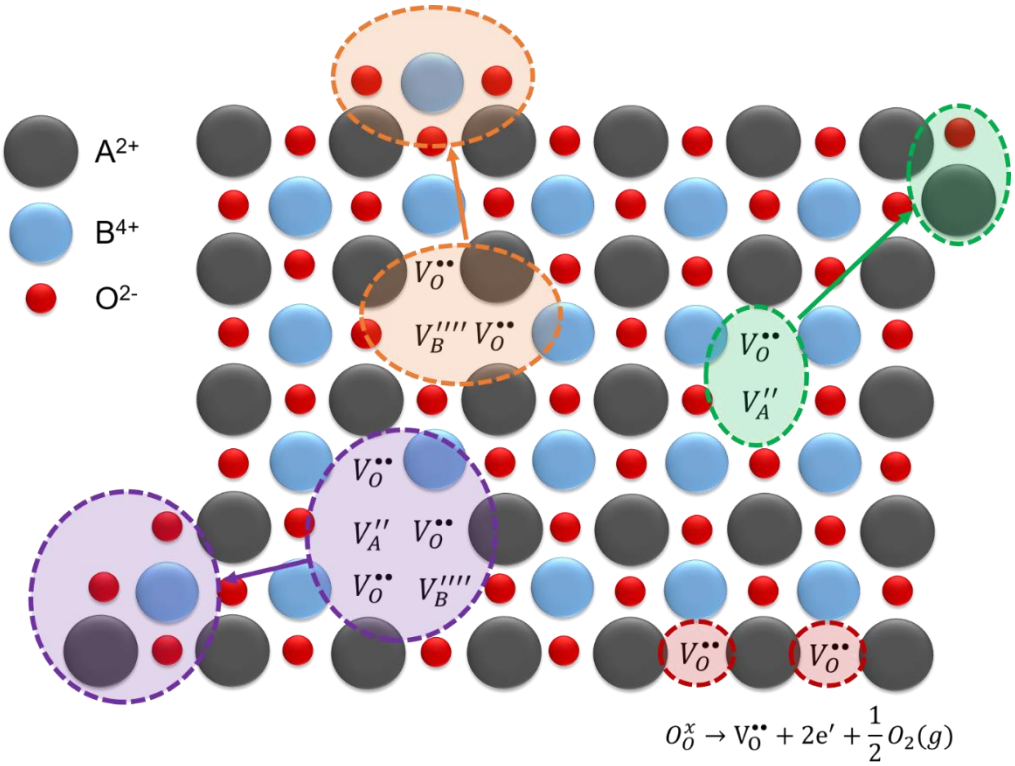

Figure 2.6.2: Common Schottky pairs which can occur in a regular perovskite structure. Partial and full Schottky defects are depicted (orange and violet) as well as outgassing of oxygen (red) (redrawn after ref. [133]).

The Kröger-Vink notation delivers a comprehensive way to express the resulting defect states and the corresponding relative charges on the present lattice sites. The Kröger-Vink notation is a set of conventions that are used to describe electric charges and lattice positions of 0-dimensional point defects for the investigated crystal structure.[1, 134]

$$M_S^C \ . \tag{2.18}$$

The letter M describes the species. This could either be atoms (Na, Bi, Ti, etc.), vacancies (denoted with V), interstitials (denoted as i), electrons (e) or holes (h). The subscript letter S displays the lattice site which is occupied by the species M. The superscript letter C stands for the relative electronic charge of the species concerning the lattice site which is occupied by the species. For a negative charge, the symbol "'" is used while for a positive charge the symbol "•" is used. In the case of NBT, intrinsic defects are caused by unintentional Bi-loss during the solid oxide synthesis.[49]

To get an impression of how the Kröger-Vink notation looks like, an example is provided for forming a full Schottky pair (see Figure 2.6.2 violet circles):

$$A_A^x + B_B^x + 3O_O^x \rightharpoonup V_A'' + V_B'''' + 3V_O^{\bullet\bullet} + ABO_3 \ . \tag{2.19}$$

Atom A and atom B, as well as O, occupy their respective lattice sites. Therefore, their relative charge is zero. In Kröger-Vink notation this will be denoted as a x in the superscript. After the reaction, one A-site vacancy (V_A'') and B-site vacancy (V_B'''') form which have a twofold and fourfold negative relative charge, denoted by "′′" and "′′′′", respectively. To charge compensate the two generated vacancies, three oxygen vacancies are created with a twofold positive relative charge denoted by "••".

Apart from intrinsic defects, extrinsic defects in NBT can either be caused by undesired, nearly uncontrollable, impurities of the starting reagents or deliberately introduced dopants which are capable to occupy the A-site or the B-site of the perovskite. An example which has already been discussed in the literature is the acceptor doping approach with magnesium at the B-site:[48, 50, 135]

$$MgO \rightharpoonup Mg_{Ti}'' + V_O^{\bullet\bullet} + O_O^x \,. \tag{2.20}$$

Each Mg ion which occupies a titanium B-site needs to be charge compensated by the generation of one additional oxygen vacancy. Thus, the oxygen vacancy concentration in B-site acceptor doped NBT is precisely adjustable by the incorporation of desired defects.

The generation of defects follows the fundamental law of mass conservation. First, a chemical reaction of reactant A with reactant B to the product C and D is assumed which all exhibit defined stoichiometric factors υ_A, υ_B, υ_C and υ_D respectively:

$$|\upsilon_A|A + |\upsilon_B|B \leftrightharpoons |\upsilon_C|C + |\upsilon_D|D \,. \tag{2.21}$$

An equilibrium constant K will adjust for the given reaction by taking the respective stoichiometric factors and activities a_i of the products and reactants into account (shown in equation (2.22)):

$$K = \frac{{a_{C,eq}}^{|\upsilon_C|} \cdot {a_{D,eq}}^{|\upsilon_D|}}{{a_{A,eq}}^{|\upsilon_A|} \cdot {a_{B,eq}}^{|\upsilon_B|}} \,. \tag{2.22}$$

For solid matter, the chemical activities are assumed to be one. So the equilibrium constant is dependent on the stoichiometric factors of reactants and products.

2.6.2 Formation of Defect Complexes

A defect complex can form between different kinds of point defects. Generally, the driving force for the formation of a defect complex could either be mechanical (relaxation of strain energy) or electrical (electrostatic interactions), or a combination of both.[136] The formation of defect complexes of an acceptor and a generated oxygen vacancy is already known from literature for lead-based and BT-based systems.[137-140] It is further assumed that defect complexes are present in the case of acceptor doped NBT. As an example, a defect pair of a divalent acceptor dopant A occupying the B-site (A_B'') and the corresponding oxygen vacancy $V_O^{\bullet\bullet}$ can form a defect complex:

$$A_B'' + V_O^{\bullet\bullet} \leftrightharpoons \{A_B'' V_O^{\bullet\bullet}\}^x \,. \tag{2.23}$$

The equilibrium constant of the association/dissociation reaction K_{asso} can be calculated[141, 142] as described in equation (2.24):

$$K_{asso} = \frac{[\{A_B'' V_O^{\bullet\bullet}\}^x]}{[A_B''] \cdot [V_O^{\bullet\bullet}]} = \frac{C - [V_O^{\bullet\bullet}]}{([V_O^{\bullet\bullet}])^2} = \exp\left(\frac{-\Delta H_{asso}}{k_B T} + \frac{\Delta S_{asso}}{k_B}\right). \tag{2.24}$$

With C as the constant doping concentration, k_B as the Boltzmann constant, ΔH_{asso} as the association enthalpy and ΔS_{asso} as the association entropy. The oxygen vacancy concentration is given by $[V_O^{\bullet\bullet}]$, the concentration of the divalent acceptor by $[A_B'']$.

The defect complex must be broken before an oxygen vacancy can migrate freely through the material. A direct relationship between the diffusion phenomena of ionic charge carriers and the properties is expected. Based on existing literature, oxygen vacancies which are bound in a defect complex can result in decreased domain wall mobility and, in consequence, to increased coercive fields. [137, 143, 144]

A detailed discussion on the formation of defect complexes in the B-site acceptor doped NBT will follow in chapter 4.1.3. The effects of possible defect complexes on the resulting ferroelectric properties of acceptor doped NBT and NBT-6BT are discussed in chapter 4.2.9.

2.7 Conduction Mechanisms

In general, a current is caused by the transport of charge carriers in an electric field. These charge carriers could either be electrons and holes or negatively and positively charged ions. If electrons and holes are the majority charge carriers, this results in electronic conductivity. When the charge is transferred by the migration of charged ions, this results in ionic conductivity. The mechanisms of those two conduction processes are fundamentally different and will be discussed in more detail in the following section taken from the textbooks by D. M. Smyth, J. Maier, A. J. Moulson and J. M. Herbert, and N. W. Ashcroft and N. D. Mermin.[5, 129, 132, 145] A deeper understanding of the conduction mechanisms is especially of major importance for the here investigated system NBT. Li *et al.* reported that, depending on the A-site non-stoichiometry or B-site doping, the conduction mechanism can change from intrinsic electronic towards oxygen ionic conductivity.[48]

2.7.1 Electronic Conductivity

Often materials are classified by their property to transfer charges. The three classifications are conductors like metals, semiconductors and electrical insulators which are all essential for modern technological applications.

In principle, there are several distinct energetic states for electrons or holes in atoms that are defined by their orbitals. Due to an overlap of orbitals in a crystal, the distinct energetic states degenerate and form energetic bands.[146] Electrons in a completely filled energetic band are not able to contribute to an electronic current.[83, 146] This is generally the case in an insulator where all bands are either completely occupied or unoccupied. Often insulators are characterized by the energy gap between highest occupied energy band, the valence band (VB) and lowest unoccupied energy band which is also called the conduction band (CB). This energy gap is called the band gap E_g. Without any thermal activation ($T = 0\ K$) every material which exhibits a band gap will be an insulator. By increasing the temperature, there is a certain probability to thermally excite an electron to overcome the band gap from the valence band into the conduction band. An electron-hole pair is formed by the excited electron in the CB and the remaining hole in the VB. Both are capable to contribute to the conductivity (electrons contribute to the n-type, holes to the p-type conductivity).[146] For the intrinsic case, two charge carriers are simultaneously created by exciting one electron. The energy which is needed to create one charge carrier, therefore, equals half of the band gap value $E_a = 1/2\, E_g$. The probability to thermally excite an electron is closely related to the band gap.

Materials that exhibit insulating properties at T = 0 K could become conductive at elevated temperatures depending on the band gap. Hence, solids, where conductivity is observable before the melting temperature is reached, are called semiconductors. Because of this, a sharp distinction between an insulator and a semiconductor is difficult. As a rule of thumb, solids that exhibit a band gap value larger than 3 eV are called dielectrics or insulators while lower band gap materials are called semiconductors. A schematic for the band structure of a conductor, semiconductor and insulator, or dielectric, is provided in Figure 2.7.1.

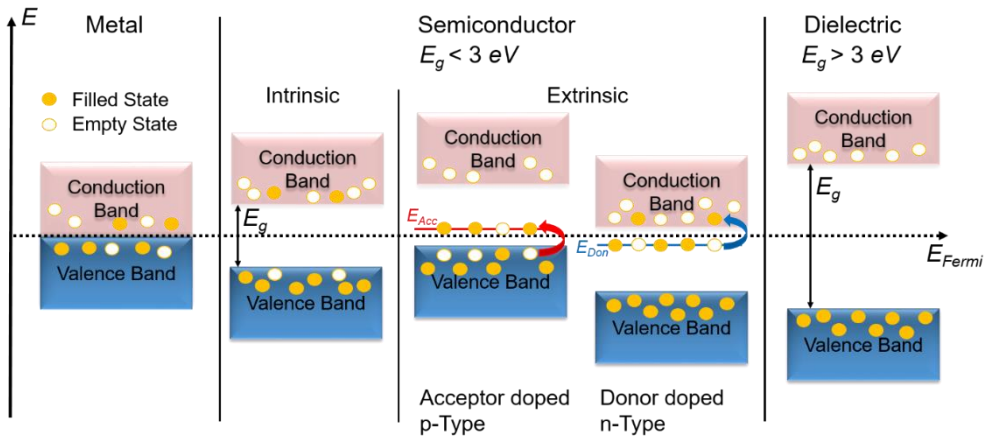

Figure 2.7.1: Diagram of the band structure of metals (left), intrinsic and extrinsic semiconductors (middle), and dielectrics or insulators (right).

The Fermi level E_{Fermi} is considered to be a hypothetical energy state where the probability is 50 % of being occupied by an electron at any given time in thermodynamic equilibrium and is regularly located within the band gap E_g.[83] For metallic conductors, the energy levels of VB and CB overlap resulting in a high concentration of charge carriers irrespective of the temperature (the band gap is zero in those cases).[5] A typical metallic conductor like copper exhibits a resistivity of $\rho = 1.68 \cdot 10^{-6}$ Ωcm at room temperature.[147] Increasing temperatures lead to a decrease of the mean free path before the charge carriers recombine resulting in a positive coefficient of resistance in metals.

Semiconductors usually exhibit resistivity values in the range of $10^{-3} - 10^{9}$ Ωcm at room temperature (RT).[145] The thermal excitation of electrons and the resulting electronic conductivity follows an Arrhenius relationship.[148] The Arrhenius equation can be expressed as:

$$\sigma_e = \sigma_0 \cdot \exp\left(-\frac{E_a}{k_B \cdot T}\right). \qquad (2.25)$$

The temperature-dependent electronic conductivity σ_e is exponentially related to $1/T$ and is therefore rapidly increasing with increasing temperature.

The Arrhenius relationship is also valid for the ionic conductivity and will be graphically utilized to extract the activation energy E_a of the respective conduction process in chapter 2.7.2. Also, increasing temperatures lead to a decrease of the mean free path before the charge carriers recombine in a semiconductor but this effect is by far overwhelmed by the additionally generated charge carriers resulting in an increase of the conductivity. Hence, semiconductors exhibit a negative coefficient of resistance.

Semiconductors can further be divided into intrinsic and extrinsic semiconductors. When all charge carriers contributing to the conductivity are generated by thermal excitation this is called intrinsic behavior. If impurities are responsible for the majority charge carrier concentration this behavior is called extrinsic. Deliberately introduced impurities are called dopants.[145] When the energy state of the dopant is close to the valence band or the conduction band, it will either act as an electron acceptor (energy state E_{Acc}) resulting in an increased hole concentration in the valence band (p-type conduction), or as an electron donor (energy state E_{Don}) resulting in an increased electron concentration in the valence band (n-type).

It should be highlighted that element semiconductors (like silicon) are very sensitive with regards to impurities and their effects on the conductivity. As an example, changing the impurity concentration by only a factor of 10^3 the resulting resistivity can be affected up to a factor of 10^{12}.[145] For ceramic-based compound semiconductors, the sensitivity towards impurities is much lower which discriminates compound and element semiconductors.[146]

So the temperature-dependent number of charge carriers per unit volume, electrons in the conduction band n_c or holes in the valence band p_v which are significantly affected by the presence of impurities, plays a vital role in every semiconducting material. For an intrinsic semiconductor the following condition holds:[146]

$$n_c(T) = p_v(T) \equiv n_i(T)\,. \tag{2.26}$$

The number of holes (p_v) and electrons (n_c) will be affected by impurities as shown in equation (2.27):

$$n_c - p_v = \Delta n \neq 0\,. \tag{2.27}$$

Hence, either holes or electrons will be the dominating charge carriers in the extrinsic case. This is why a semiconductor is called “n-type” or “p-type” regarding the dominant charge carrier species. Apart from the effects of doping on the electronic conductivity, the generation of oxygen vacancies leads to a change from semiconducting towards ionic conducting behavior in NBT.[48] Therefore, a deeper understanding of the ionic conduction mechanism is inevitable.

2.7.2 Ionic Conduction and Diffusion

Besides the electronic conduction and the classification of conductors, semiconductors, and insulators, the mechanism of ionic conductivity which can be seen as a directed diffusion of ionic charge carriers needs to be highlighted.

An ionic crystal exhibits electrical conductivity up to a certain degree even though the band gap is so large that theoretically no current should flow.[129] If the band gap is large enough, creating charge carriers by thermal excitation of an electron resulting in electronic conduction is impossible. The responsible charge carriers are therefore not electrons or holes, but the ions themselves. Conduction via the migration of ions is strongly dependent on vacancies in the lattice which are present in each real crystal as introduced in chapter 2.6.1 as well as the mobility.[132] As already seen for electronic conductivity, ionic conductivity is also a thermally activated process and follows an exponential relationship with $1/T$ (see equation (2.25)).

The ionic conduction process at small external fields can be described by a migration process of charged ions through the lattice. Besides the concentration of the charge carriers and the external field gradient, the mobility of the charge carriers plays a major role in the resulting migration process. In ionic conducting NBT, for instance, the charge carriers are oxygen ions that migrate over oxygen vacant sites through the lattice. In this case, the resulting ionic conductivity is the product of the oxygen vacancy concentration, the mobility, and the transferred charge:[132]

$$\sigma_i = ze \cdot [V_O^{\bullet\bullet}] \cdot \mu(T)\,. \tag{2.28}$$

Here ze represents the vacancy charge, $[V_O^{\bullet\bullet}]$ the oxygen vacancy concentration and $\mu(T)$ the temperature-dependent vacancy mobility. At this point, a closer look needs to be taken on a basic description of diffusion processes. Diffusion is defined as a thermally activated, statistically describable, kinetic process on an atomic scale.

An external driving force X for the diffusion could, for example, be a concentration or electric field gradient which affects, on the one hand, the mobility of charge carriers and on the other hand, leads to a directed migration of the charge carriers.[129] In general, it is very complex to describe the correlation of an external driving force X and the resulting mass fluxes J. Conditions need to be defined in which a linear relationship between those entities can be assumed.

Based on irreversible thermodynamics, the driving force-dependent mass flux $J(X)$ can be expressed as:[129]

$$J(X) = \alpha + \beta \cdot X + \gamma \cdot X^2 + \cdots \ . \tag{2.29}$$

The value for α equals zero when the external driving force X disappears. Further, the higher-order terms of the driving force can be neglected for conditions close to the equilibrium of the system. Based on those boundary conditions, the mass flux can be expressed as:

$$J(X) = \beta \cdot X \ . \tag{2.30}$$

As a prominent example of this condition, Fick's first law describes the diffusion which is governed by the existence of a concentration gradient at non-equilibrium conditions.[132]
Fick's first law (equation (2.31)) and the continuity equation (2.32) are further used to form Fick's second law (equation (2.33)) which describes the concentration change dC with the evolution of time t:[129]

$$J = -D_s \cdot \nabla C \ , \tag{2.31}$$

$$\frac{dC}{dt} + \nabla J = 0 \ , \tag{2.32}$$

$$\frac{dC}{dt} = \nabla (D_s \cdot \nabla C) \ . \tag{2.33}$$

Here, J represents the mass flux, ∇ the gradient operator, D_s is the self-diffusion coefficient and C the concentration of particles.
Another prominent example for a linear relationship between the particle flux J and the driving force X is Ohm's law of conduction which represents the linear relationship between the flux of charged particles i in the presence of an electric field:[132]

$$i = -\sigma \cdot \nabla \varphi \ . \tag{2.34}$$

Both, Fick's first law (equation (2.31)) and Ohm's law of conduction (equation (2.34)) are closely related to each other.[129]

This relationship becomes apparent by the fundamental transport equation where the particle flux J is a function of the electrochemical potential $\tilde{\mu}$:

$$J = -\beta \cdot \nabla\tilde{\mu} = j_D + j_E \,. \tag{2.35}$$

j_D represents the chemical gradient dependent particle flux density and j_E is the flux density resulting from an external electric field. If uncharged particles are considered or no external electric field is present, the process can be reduced to a pure diffusion ($\nabla\tilde{\mu} = \nabla\mu$):[129]

$$j_T = j_D \equiv j = -\beta_T \cdot \nabla\mu \,. \tag{2.36}$$

j_T represents the particle flux density of the transport process. In the dilute state ($\nabla\mu = RT\nabla C/C$), the particle flux density can be expressed by $j_T = -\beta_T RT\frac{\nabla C}{C}$. In comparison with Fick's first law (2.31), the pre-factor β_T can be expressed as:[129]

$$\beta_T = \frac{D_s \cdot C}{k_B \cdot T} \,. \tag{2.37}$$

If no noticeable changes in the chemical potential are observable, the electric field remains as the driving force:

$$j_T = j_E = -\beta_T \cdot z \cdot F \cdot \nabla\varphi \,. \tag{2.38}$$

After converting particle current densities in charge current densities (by applying $i = zFj_E$), the expression changes to:[129]

$$i = -\beta_T \cdot z^2 \cdot F^2 \cdot \nabla\varphi \,, \tag{2.39}$$

representing Ohm's law (see equation (2.34)). The pre-factor β_T corresponds to the electrical conductivity of the charge carriers σ, resulting in:

$$\sigma = \beta_T \cdot z^2 \cdot F^2 \,. \tag{2.40}$$

A comparison with equation (2.37), reveals that the self-diffusion D_s and the conductivity σ are related parameters resulting in the well-known Nernst-Einstein equation:[129]

$$D_s = \frac{\sigma \cdot k_B \cdot T}{z^2 \cdot F^2 \cdot C} = \frac{\sigma \cdot k_B \cdot T}{q^2 \cdot C} \ . \tag{2.41}$$

As can be extracted from the Nernst-Einstein equation, the self-diffusion D_s is a function of temperature T, the concentration C as well as the conductivity σ and the charge q. The self-diffusion is therefore not related to the external electric field. Based on the linear response theory, the diffusion at low external electric fields should be in a linear fashion.[149] If the field becomes sufficiently high, the self-diffusion coefficient of a charged ion is, nevertheless, expected to be influenced by the presence of the field.

The diffusion of ions can still be treated as a random walk of charge carriers in the case of very low excitation/driving forces. Thus, the diffusion coefficient does not depend on the driving force.[149] This model demonstrates a close relationship to the Debye-Onsager-Falkenhagen theory for liquids which was first reported in 1928.[150, 151] To get an impression on describing diffusion on the local scale, it is necessary to go one step back in the discussion.

Based on the random walk theory, the charge carrier migration is dependent on the jump distance λ, the number of jumps n and the jump rate Γ_d. In the case of self-diffusion (external forces are negligible), every jump of the charge carriers occurs with the same probability.[149] Though, the position change of a charge carrier with time will not be zero. The general Einstein-Smoluchowski relation represents the connection of Fick's second law (equation (2.33)) with the probability density as described in equation (2.42):[152]

$$D_s = \frac{1}{2 \cdot d} \cdot \Gamma_d \cdot \lambda^2 \ . \tag{2.42}$$

The dimension d is part of the Einstein-Smoluchowski relation. A possible anisotropy of the crystal structure can, therefore, result in an energetically favorable diffusion direction. For a 3-dimensional system, the Einstein-Smoluchowski-relation can be extended (see equation (2.43)).

$$D_s = \frac{1}{6} \cdot Z \cdot \Gamma_s \cdot \lambda^2 \ . \tag{2.43}$$

By using the specific jump rate $\Gamma_s = \Gamma_d/Z$, the coordination number comes into play. The coordination number Z which is also dependent on the crystal structure describes all possible places for the charge carrier to jump on.

The ions have to displace other ions while diffusing through the lattice. This results in elastic stress and can be described by the migration enthalpy ΔG_{mig}. The migration of oxygen ions in NBT follows a so-called vacancy migration mechanism. In this case, an oxygen ion exchanges its place with a neighboring oxygen vacancy. As the migration is only possible in the presence of vacancies, the vacancy concentration is one limiting factor of oxygen ionic conductivity. The potential barriers, however, significantly decrease, if an oxygen vacancy is in the nearest neighbor position representing the oxygen vacancy concentration dependence of ionic conductivity in NBT.

The total free enthalpy ΔG^* (equation (2.44)) of the formation and diffusion of a vacancy can be described as the sum of the enthalpy of the vacancy formation ΔG_v^f and the migration enthalpy of the generated vacancy ΔG_{mig}:[152]

$$\Delta G^* = \Delta G_v^f + \Delta G_{mig} \,. \tag{2.44}$$

Of course, this is only valid when the vacancy needs to be generated in advance. Hence, in the case of extrinsic contributions, ΔG_{mig} dominates. Taking the migration enthalpy, and the attempt jump rate Γ_0, into account, the temperature-dependent jump rate Γ of a vacancy can be expressed by equation (2.45):

$$\Gamma = \Gamma_0 \cdot \exp\left(-\frac{\Delta G_{mig}}{k_B \cdot T}\right). \tag{2.45}$$

In the given equation k_B represents the Boltzmann constant.

With the jump rate Γ expressed as a function of temperature, the temperature dependence of the resulting self-diffusion constant of a vacancy $D_{s,vac}$ (see equation (2.46)) can be expressed as:[152]

$$D_{s,vac} = \frac{1}{6} \cdot Z \cdot \lambda^2 \cdot \Gamma_0 \cdot \exp\left(-\frac{\Delta G_{mig}}{k_B \cdot T}\right). \tag{2.46}$$

Now as there is an expression for the self-diffusion constant of a vacancy, the activation enthalpy ΔH^* of the diffusion process can be extracted, if the temperature-dependent values of the diffusion coefficient are known. The total free enthalpy ΔG^* (see equation (2.47)) of the ionic hopping process can be expressed as:

$$\Delta G^* = \Delta H^* - T \cdot \Delta S^* . \tag{2.47}$$

By splitting the total free enthalpy into the enthalpy and the entropy, the factor $\gamma = \exp(\Delta S^*/k_B)$ can be determined.[153] By applying γ in equation (2.46), the calculation of the activation enthalpy ΔH^* of the diffusion of a vacancy becomes possible. The conductivity can therefore be expressed by equation (2.48):

$$\sigma = \sigma_0 \cdot \exp\left(-\frac{\Delta H^*}{k_B \cdot T}\right). \tag{2.48}$$

The given expression represents the exponential $1/T$ relationship of conductivity and is also valid for electronic conductivity in semiconductors, described in chapter 2.7.1. Applying the natural logarithm (see equation (2.49)) leads to the following expression:

$$\ln(\sigma) = \ln(\sigma_0) - \frac{\Delta H^*}{k_B} \cdot \left(\frac{1}{T}\right). \tag{2.49}$$

The Arrhenius representation (natural logarithm of conductivity against the reciprocal of temperature) the slope m (shown in equation (2.50)) of the resulting straight line can be expressed as:

$$m = -\frac{\Delta H^*}{k_B} = -\frac{E_a}{k_B}. \tag{2.50}$$

This allows to directly extract the activation energy E_a graphically from the Arrhenius representation. The activation energy E_a is typically given in electron volts (eV). The value of the Boltzmann constant is given as k_B = 8.617 · 10^{-5} eVK^{-1}. Figure 2.7.2 provides a schematic illustration of an Arrhenius-type plot that can be constructed e.g. from impedance data.

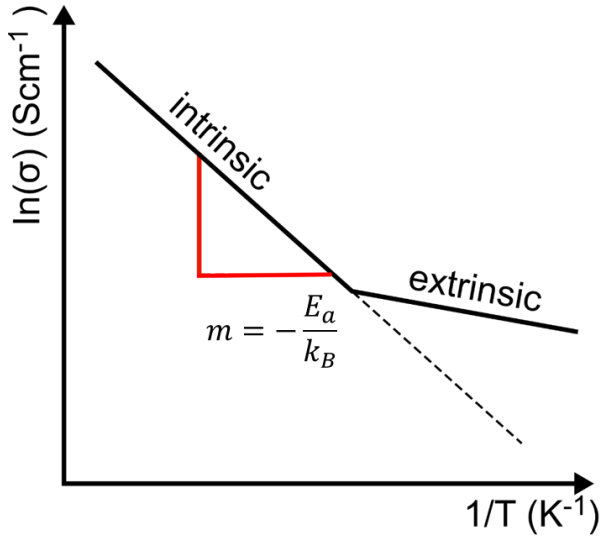

Figure 2.7.2: Schematic illustration of an Arrhenius-type plot of the temperature-dependent conductivity. The here presented plot additionally displays a possible transition from extrinsic to intrinsic behavior. The dashed line accounts for a purely intrinsic behavior (after ref. [5]).

Using temperature and frequency-dependent impedance spectroscopy (a detailed introduction to the measuring principles is provided in chapter 2.9) to express the thermal evolution of the conductivity and extracting the activation energies also allows to distinguish between different material responses e.g. bulk and grain boundary as they exhibit different relaxation times.[154] Further, it becomes possible to judge the conduction mechanism of the respective response with the help of the calculated activation energies. Judging the conduction mechanism only by the activation energies is ambiguous as the measured electrical conductivity σ_{el} is always the sum of electronic σ_e and ionic σ_i contributions ($\sigma_{el} = \sigma_e + \sigma_i$).

In most cases, there are either electronic or ionic contributions dominating which exhibit different activation energies. Based on this, it is possible to get at least indirect evidence, whether the electronic or ionic charge carriers are dominant in the material. To get direct, experimental, evidence for oxygen ionic conductivity, electromotive force (EMF) measurements need to be conducted by which the ionic transport number can be determined. [48, 49]

2.8 Electromotive Force (EMF)

By its definition, the electromotive force (EMF) is the electric potential generated by an electrochemical cell.[155] This could, for example, be a chemical gradient. By applying different oxygen partial pressures on each side of an oxygen ion conducting sample, an electric potential will establish across the sample. The resulting potential directly corresponds to the dissociation and recombination of the oxygen molecules such that O^{2-} ions can be formed at one electrode and converted to O_2 molecules at the other.[5] The electromotive force developed by such a cell can be expressed by the Nernst equation. The resulting Nernst potential can be expressed as seen in equation (2.51):[5, 129]

$$\Delta E = -\frac{\Delta G}{z \cdot F} \text{ with } \Delta G = \Delta G^0 + R \cdot T \cdot ln\left(\frac{p_{out}(O_2)}{p_{in}(O_2)}\right). \tag{2.51}$$

The forming electrochemical potential for a pure oxygen ionic conductor ΔE will only depend on the oxygen partial pressure differences at the top and the bottom of the sample ($p_{out}(O_2)$ and $p_{in}(O_2)$) as well as the charge z and the Faraday constant F.[5] When the forming electrochemical potential of a sample (ΔE_{sample}) is directly compared to the elctrochemical potential of a reference sample ($\Delta E_{reference}$) which exhibits pure oxygen ionic conductivity (this could for examples be yttria stabilized zirconia, YSZ), the ionic transport number t_{ion} can be calculated after equation (2.52):[129]

$$t_{ion} = \frac{\Delta E_{sample}}{\Delta E_{reference}}. \tag{2.52}$$

2.9 Electrochemical Impedance Spectroscopy (EIS)

As already mentioned, a vital part to gain a deeper understanding of the defect chemistry in NBT and NBT-based solid solutions is the investigation of the electrical conductivity as those systems exhibit a unique property evolution with regards to non-stoichiometry and/or doping.[45, 156-158]

Electrochemical impedance spectroscopy (EIS) is a powerful technique to investigate the mechanisms of electrochemical reactions as well as the dielectric and transport properties of a material in alternating current conditions.[154, 159]

As different material regions exhibit distinct relaxation times, a frequency-dependent analysis allows to discriminate between the corresponding regions and investigate them separately which is inevitable to achieve a better understanding of the respective defect chemical mechanisms. In general, the distinguishable regions and their related properties can be divided into the following groups. First and foremost, the intragranular, or bulk, properties are of major interest and enable an investigation of e.g. the oxygen ionic conductivity in the system under investigation NBT.[48] Secondly, it is possible to precisely investigate the grain boundary properties e.g. resistive grain boundary components like internal barrier layer capacitors.[160] Further, impedance spectroscopy provides insight into the properties of the sample/electrode interface region.[161]

Impedance spectroscopy, therefore, enables a detailed characterization of the electrical properties of a polycrystalline ceramic as a function of frequency.

In a classical direct current (DC) condition, the relationship between resistance R, voltage V and current I for an ideal resistor can be expressed by Ohm's law:

$$R = \frac{V}{I} \ . \tag{2.53}$$

The capacitive response of an ideal capacitor follows equation (2.4) in DC conditions. When an alternating current (AC) is applied, the material response becomes more complicated. The resistance for an alternating current condition is called impedance.[162] The impedance of an ideal resistor is frequency independent while the response of a capacitor differs. A closer look must, therefore, be taken on the capacitive material responses when AC is applied. Further discussion is based on small-signal measurements where the current/voltage relation follows a linear relationship. For small signals, the linear response exhibits a characteristic phase shift (see Figure 2.9.1).

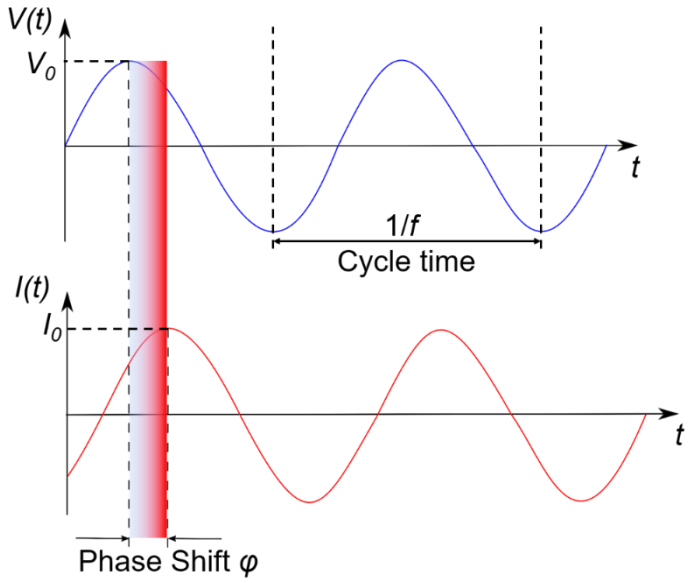

Figure 2.9.1: Schematic illustration of the phase shift φ (colored box) between the time-dependent sinusoidal input voltage signal $V(t)$ (blue curve) and the time dependent current response $I(t)$ (red curve) (after ref. [163]).

For an ideal capacitor, the voltage lags the current by 90°. The current/voltage signal is resulting in a function of time t. The excitation voltage $V(t)$ and the response current $I(t)$ can be expressed as:

$$V(t) = V_0 \cdot \sin(\omega t)\,, \tag{2.54}$$

$$I(t) = I_0 \cdot \sin(\omega t + \varphi). \tag{2.55}$$

With V_0 and I_0 representing the amplitude, ω the radial frequency ($\omega = 2\pi f$ with f as cycle time) and φ the phase shift of the response signal. The expression for the impedance Z is similar to Ohm's law:[163]

$$Z = \frac{V(t)}{I(t)} = \frac{V_0 \cdot \sin(\omega t)}{I_0 \cdot \sin(\omega t + \varphi)} = Z_0 \cdot \frac{\sin(\omega t)}{\sin(\omega t + \varphi)}\,. \tag{2.56}$$

The impedance is therefore expressed with the magnitude of the impedance Z_0 and the phase shift φ. It should be noted, that continuous time functions for alternating currents which are non-periodic or might differ from a sine- or cosine-type, result in very complicated differential equations in the time-dependent space.[164]

Based on this, a discussion of impedance results for the complex frequency-dependent, instead of the time-dependent space is more useful.

A simple reason for this is that in the complex frequency space, the frequency-dependent complex impedance $Z^*(\omega)$ follows the Kirchhoff rules and can easily be handled mathematically.[162]
Based on the Euler relationship, the impedance can be represented as a complex function:

$$\exp(i\varphi) = \cos\varphi + i\sin\varphi\,, \tag{2.57}$$

$$V(t) = V_0 \cdot \exp(i\omega t)\,, \tag{2.58}$$

$$I(t) = I_0 \cdot \exp(i\omega t - i\varphi)\,, \tag{2.59}$$

and for the complex frequency-dependent impedance $Z^*(\omega)$:[163]

$$Z^*(\omega) = \frac{V(t)}{I(t)} = \frac{V_0 \cdot \exp(i\omega t)}{I_0 \cdot \exp(i\omega t - i\varphi)} = Z_0(\cos\varphi + i\sin\varphi)\,. \tag{2.60}$$

The frequency-dependent impedance, therefore, consists of a real, or in phase, part and imaginary, or out of phase, part in the frequency space. Concerning the frequency-dependent complex current $I^*(\omega)$ and voltage $V^*(\omega)$, the frequency-dependent complex impedance $Z^*(\omega)$ can be calculated and divided into its real ($Z'(\omega)$) and imaginary ($iZ''(\omega)$) parts by:[165]

$$Z^*(\omega) = \frac{V^*(\omega)}{I^*(\omega)} = Z'(\omega) + iZ''(\omega)\,. \tag{2.61}$$

To describe a real dielectric system, a resistive term R and a capacitive term C need to be included to represent a possible polarization of the material under investigation.
A resistor with the resistance R and a capacitor with the capacitance C are therefore connected in parallel and are called “RC-element”.[166] The capacitance of the RC element can be calculated by assuming a simple plate capacitor which can be described by equation (2.4).
The complex frequency-dependent impedance $Z^*(\omega)$ of a resistor $Z_R^*(\omega)$ and a capacitor $Z_C^*(\omega)$ can be expressed by equation (2.62) and (2.63), respectively:

$$Z_R^*(\omega) = \frac{V^*(\omega)}{I^*(\omega)} = R\,, \tag{2.62}$$

$$Z_C^*(\omega) = \frac{V^*(\omega)}{I^*(\omega)} = \frac{1}{i\omega C}\,. \tag{2.63}$$

$V^*(\omega)$ describes the frequency-dependent voltage and $I^*(\omega)$ the current at the frequency ω. i is the complex number and C the capacitance. The impedance of a resistor Z_R^* is frequency independent, so the AC resistance results in R.

With the help of the Kirchhoff current law, the impedance of an RC-element connected in parallel can be expressed by the sum of the admittances $Y_R^*(\omega)$ and $Y_C^*(\omega)$ according to the frequency space:[165]

$$Z_{RC}^*(\omega) = (Y_R^*(\omega) + Y_C^*(\omega))^{-1} = \left(\frac{1}{R} + i\omega C\right)^{-1} = \frac{R}{(\omega RC)^2 + 1} - i\frac{\omega R^2 C}{(\omega RC)^2 + 1}. \qquad (2.64)$$

A commonly used way to express the complex impedance of an electrochemical system is using Cartesian coordinates as shown by equation (2.65):[165]

$$Z^*(\omega) = Z_{re} + iZ_{im}\,. \qquad (2.65)$$

Z_{re}, or Z' represents the real part, and Z_{im}, or Z'', the imaginary part of the impedance. Z' is often plotted against the negative of the imaginary part $-Z''$. This representation form is called Nyquist-plot. An RC-element results in a semicircle (equation (2.64)), as can be seen in Figure 2.9.2.

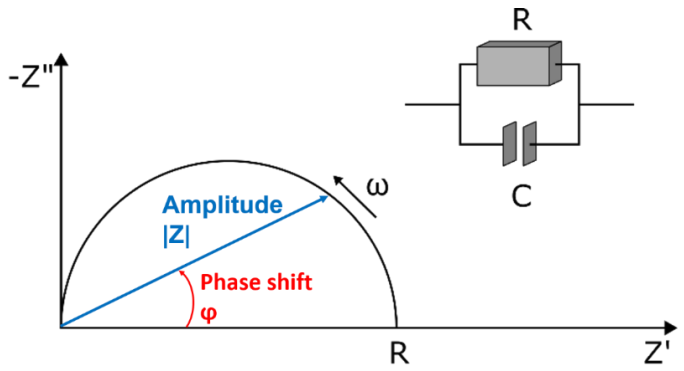

Figure 2.9.2: Impedance spectrum of a single RC-element with Z' as real part and $-Z''$ as imaginary part in the Nyquist representation.

At constant temperature, every single point on the semicircle represents the measured impedance (with amplitude $|Z|$ and phase shift φ) at the respective frequency ω. The frequency increases from right to left (as depicted by the arrow). At sufficiently low frequencies, the voltage drops at the resistive part, as the capacitive part exhibits blocking behavior. The intercept with the x-axis can, therefore, be seen as the DC-resistance of the respective process.[166]

The response exhibits a frequency at which the imaginary part of the impedance becomes maximum in the Nyquist representation. This frequency is called the peak frequency ω_{max} and is the inverse of the relaxation time τ of the process (equation (2.66)). The peak frequency equals one when multiplied by the resistance and the capacitance of the RC-element (equation (2.67)).

$$\omega_{max} = \frac{1}{\tau}\,, \qquad (2.66) \qquad\qquad \omega_{max} \cdot R \cdot C = 1\,. \qquad (2.67)$$

The capacitance of the response can be calculated with the help of equation (2.67) by determining the peak frequency (ω_{max}) and the resistance of the process.

With increasing frequency, the capacitive part becomes more and more conductive. If the measuring frequency is high enough, the capacitive part creates a shortcut resulting in a real and imaginary impedance of zero. The here presented relations describe the impedance response on a single, ideal RC-element. A polycrystalline material, however, exhibits a complex microstructure. If the relaxation times τ of the material region, e.g. the bulk and the grain boundary responses of a real polycrystalline ceramic exhibit a large enough difference, a discrimination of the material responses is possible.[166] Two semicircles form in the Nyquist representation which can both be represented by a particular RC-element. It is necessary to use a simplified model to resolve multiple material responses. Hence, the so-called "Brick-Layer" model is introduced which is based on an idealized ceramic with defined grains and grain boundaries (see Figure 2.9.3 (a)).[167] This allows considering the factors which determine the magnitude of capacitances for every single RC-element.[154]

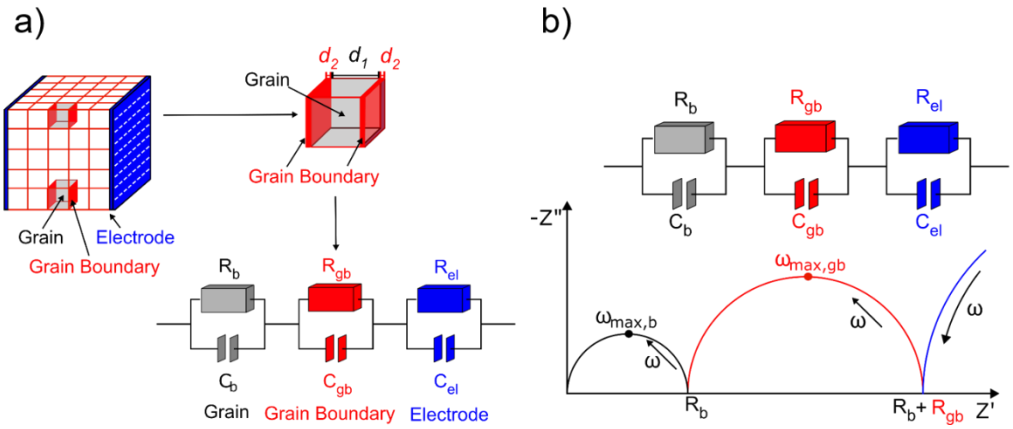

Figure 2.9.3: (a) „Brick-Layer" model of an idealized ceramic with bulk material (*b*) and grain boundaries (*gb*) between two metal electrodes (el). The equivalent circuit is represented for the corresponding bulk, grain boundary and electrode responses (redrawn after ref. [168]); (b) Schematic illustration of a typical impedance spectrum in the Nyquist representation with distinguishable bulk (black), grain boundary (red) and electrode (blue) responses.

In this simplification, the ceramic specimen is represented by cube-shaped grains. As the dielectric characteristics of different grains should ideally be equal in this model, they can be merged in the bulk response (b) and are described by a capacitor with the permittivity of the intragranular region (grey) and the distance d_1 (see Figure 2.9.3 (a)). The grain boundaries (gb) separate the grains and are characterized by a capacitor with a defined permittivity of the intergranular region (red) with distance d_2.[154] With regards to the capacitances of each element, the following relationship can be established:[154]

$$\frac{C_b}{C_{gb}} = \frac{d_2}{d_1}. \tag{2.68}$$

The thickness of the grain boundaries is naturally remarkably smaller than the actual grains which leads to $d_1 \gg d_2$. Based on this, the capacitance of the grain boundary must be considerably larger than that of the bulk ($C_{gb} \gg C_b$).[154] In most cases, the resulting capacitance of the grain boundaries is in the range of 10^{-11} F to 10^{-8} F.[154] It should be noted, that larger capacitances can be observed in well sintered, lower capacitances in poorly sintered ceramics as the quality of the grain boundary differs.[169] This effect was attributed to the effect of current constriction. The impact of the contact area of grain boundaries was confirmed with the help of finite element calculations by Fleig and Maier.[170]

Figure 2.9.3 (b) depicts a schematic of a Nyquist plot in connection with the resulting equivalent circuit for a bulk, grain boundary, and electrode process representing the capacitive and resistive responses of the corresponding regions.[171]

Typical capacitance values for different material responses are provided in Table 2.9-1.

Table 2.9-1: Impedance Phenomena and their capacitance range.[154]

Phenomenon	Capacitance (F)
Bulk	10^{-12}
Minor, second phase	10^{-11}
Grain boundary	10^{-11}-10^{-8}
Bulk ferroelectric	10^{-10}-10^{-9}
Surface layer	10^{-9}-10^{-7}
Sample-electrode interface	10^{-7}-10^{-5}
Electrochemical reactions	10^{-4}

Usually, the high-frequency semicircle exhibits a lower resistance and is related to the bulk response while the intermediate frequency semicircle can be assigned to the grain boundary response and exhibits a larger resistance. It should be noted, that the previous discussion is only valid for an ideal RC-element response. Real systems like polycrystalline materials might further exhibit chemical inhomogeneity resulting in differing dielectric behavior. This results in different relaxation times τ within the bulk of a real, polycrystalline, material.[172] An additional correction of the RC-element needs to be conducted. This is where the so-called constant phase element (CPE) comes into play. A CPE provides a correction factor α (see equation (2.69)).

$$Z^*_{CPE}(\omega) = A^{-1} \cdot (i\omega)^{-\alpha} . \tag{2.69}$$

The factor α can reach values between zero and unity ($0 \leq \alpha \leq 1$). A value of zero describes an ideal resistive, a value of one describes an ideal capacitive behavior.[165] The CPE will be included in the equivalent circuit replacing the capacitor C of the corresponding RC-element. Depending on the value of the correction factor α, the semicircle is shifted by $\alpha \cdot 90°$, resulting in a depressed semicircle (see Figure 2.9.4 (b)) emulating the variation of relaxation times τ. In contrast, a CPE in series with an RC-element additionally allows an evaluation of the sample/electrode interface. Especially for ionic conductors, this becomes important, as a charged double layer can establish due to charge separation by the migration of ions. This effect can be observed at low frequencies as the migration ions are partially blocked by a frequency-dependent formation of a potential barrier at the sample/electrode interface which is related to a Warburg-type diffusion process in the respective region.[154] The double-layer formation by Warburg-type diffusion shows a characteristic phase angle of 45° in the Nyquist representation of the frequency-dependent impedance response (see Figure 2.9.4 (a)).

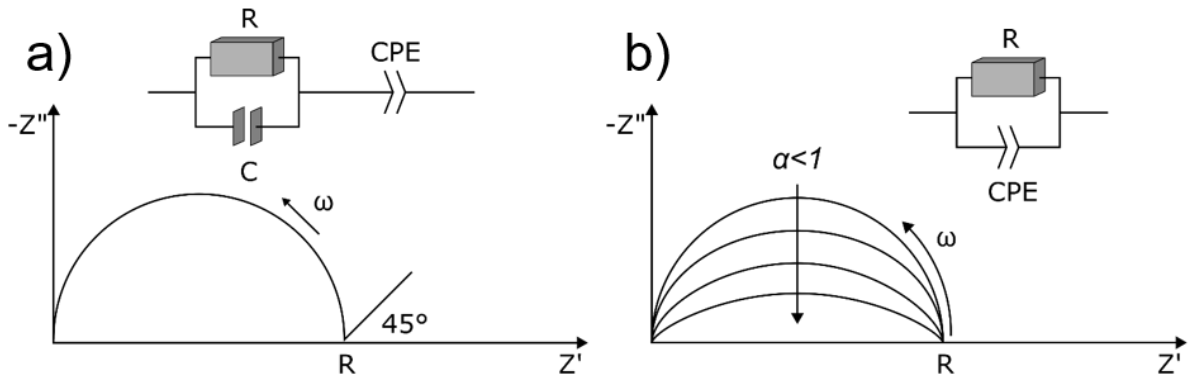

Figure 2.9.4: (a) Schematic depiction for a blocking double-layer formation in Nyquist representation for an ion-conducting material resulting in a 45° at low frequencies; (b) Schematic depiction of a depressed semicircle concerning the corresponding α value of the CPE.[165]

It should be noted that the CPE cannot resolve the complete Warburg-type diffusion.[163] At lower frequencies, the electrode might either represent ion blocking behavior (resulting in changes in the imaginary part of the impedance) or conductive behavior (resulting in a closed semicircle).
By taking the temperature evolution of the DC resistance into account e.g. by Arrhenius-type plots (see chapter 2.7.2), the DC resistance exhibits a strong temperature dependence.
For instance, also other frequency-dependent quantities like the admittance Y (equation (2.70)), the permittivity ε' (equation (2.71)) and the modulus M (equation (2.72)) can be extracted from the collected impedance data.

$$Y^*(\omega) = \frac{1}{Z^*(\omega)}, \tag{2.70}$$

$$\varepsilon'^*(\omega) = \frac{1}{i\omega C_0 \cdot Z^*(\omega)}, \tag{2.71}$$

$$M^*(\omega) = i\omega C_0 \cdot Z^*(\omega)\,. \tag{2.72}$$

This additional information is useful as it weighs the frequency-dependent material responses differently. While a high-frequency response might nearly vanish in the Nyquist representation of the impedance, it delivers the major contribution to the modulus. Therefore it is sometimes helpful to investigate the other quantities as well.
The conductivity follows a direct relationship with the admittance Y (equation (2.73)) and an inverse relationship with the impedance Z (equation (2.74)) and can be calculated by including the sample area A and thickness d:

$$\sigma^*(\omega) = Y^*(\omega) \cdot \frac{d}{A}, \tag{2.73}$$

$$\sigma^*(\omega) = \frac{1}{Z^*(\omega)} \cdot \frac{d}{A}. \tag{2.74}$$

Impedance spectroscopy, therefore, enables an investigation of all necessary parameters to describe the temperature dependent electrical properties and further allows for discrimination between the material regions. Especially with regards to the here investigated system NBT, this technique provides several advantages, as the bulk and the grain boundary responses need to be discussed separately.

2.10 Sodium Bismuth Titanate (NBT)

In this section, a literature review on the material system under investigation sodium bismuth titanate ($Na_{0.5}Bi_{0.5}TiO_3$), or short, NBT is provided. Each chapter of the results and discussion part also provides a more detailed description of the particular literature which is necessary for understanding the corresponding discussion.

NBT was first reported by Smolenskii *et al.* in 1961.[26] NBT is not only the base composition of a whole family of lead-free ferroelectric materials, but it also offers a large range of features. Smolenskii *et al.* reported NBT to be in a cubic structure via XRD with a lattice parameter of $3.88\,\text{Å}$ at room temperature[26] which was confirmed by Buhrer in 1962.[173] In 1985 neutron diffraction experiments revealed that NBT exhibits a rhombohedral phase at room temperature.[174] Actually, Levin and Reaney reported in 2012 that NBT exhibits a distorted ABO_3 perovskite structure with an extensive chemical, cation displacement, and octahedral tilt disorder.[175] Based on recent literature, Figure 2.10.1 summarizes the temperature-dependent phases of NBT.

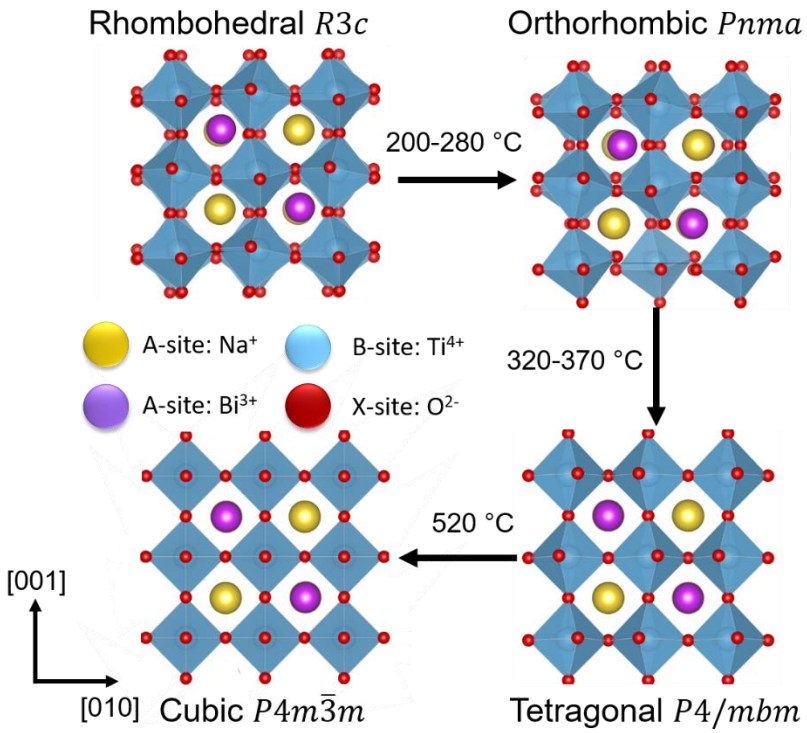

Figure 2.10.1: Crystallographic phases and temperature dependent phase transitions of NBT processed with the help of the VESTA program. The phase transition temperatures are taken from ref. [176]

The rhombohedral phase of the group $R3c$ is stable from room temperature up to 255 °C. In this phase, an anti-phase octahedral tilting and ionic displacement are evident along the <111> direction.[177] Octahedral tilting of the oxygen ions results from the lattice distortion as well as the variation of the A-site atoms Na and Bi.

According to recent studies, an orthorhombic phase with $Pnma$ symmetry which forms above 200°C was proven to be present in the rhombohedral $R3c$ symmetry as well.[178] A coexistence of the rhombohedral and the tetragonal phase between 280 °C and 320 °C could experimentally be evidenced by transmission electron microscopy which revealed tetragonal platelets embedded in a rhombohedral matrix.[179] Between 200 °C and 320 °C, NBT exhibits relaxor-like behavior[45, 180] with an electric field induced phase transition.[41] Above 370 °C, NBT exhibits a pure tetragonal phase of the space group $P4/mbm$.[176] Another phase transition can be observed at 520 °C to the paraelectric cubic phase of the space group $P4m\bar{3}m$.[174, 177] The precise temperature dependent phases and transition temperatures of NBT are, nevertheless, under debate.[175, 177, 178, 181-186]

The maximum permittivity is reported to be around 3000 at 320 °C.[187] The temperature-dependent permittivity further exhibits a large frequency dispersion resulting from the relaxor nature of NBT.[188] Additionally, the temperature of the maximum permittivity was reported to be uncorrelated with a structural phase transition. Thus, it was claimed that NBT provides some similarities to lead-based relaxor materials lead lanthanum zirconate titanate (PLZT) and lead magnesium niobate (PMN). This claim was supported by X-ray and neutron diffraction experiments where polar nano regions have been reported growing with decreasing temperatures.[174] Moreover, the frequency-dependent evolution of the permittivity was also attributed to the existence of PNRs.[189]

Takenaka *et al.* reported in 1990, that NBT exhibits a large coercive field of E_c ~ 7.3 kVmm^{-1} accompanied by a remanent polarization of P_{rem} = 0.48 Cm^{-2}.[29] By another publication from Takenaka in 1999, it turned out that the coercive field E_c and the remanent polarization P_{rem} can vary significantly. It was reported, that NBT exhibits a remanent polarization of P_{rem} = 0.17 Cm^{-2} and a coercive field of E_c = 3.0 kVmm^{-1}.[190] This underlines that the reproducibility of NBT is still an issue.

The maximum strain is rather low with S_{max} = 0.09 % at an applied field of 7.0 kVmm^{-1}.[32]

Apart from its ferroelectric and piezoelectric properties, NBT exhibits large temperature-dependent leakage current which is highly detrimental concerning a possible high-temperature dielectric, ferroelectric and/or piezoelectric application. Reducing the leakage current in NBT and NBT-based solid solutions is still a large field of research.[17] The strong sensitivity of NBT on possible A-site non-stoichiometry and the resulting properties gains more and more importance.

An elegant way to handle this “undesirable” drawback of the leakage current is to transform the drawback into an advantage. Non-stoichiometry, as well as deliberately introduced defects like A-site or B-site acceptor dopants, exhibit an unexpectedly large influence on the resulting conductivity.[48, 187, 191-193]

Li *et al.* reported, that Bi-deficiency, as well as B-site acceptor doping results in extraordinarily high levels of oxygen ionic conductivity (see Figure 2.10.2) making NBT competitive with commercially used solid oxide ion conductor materials like yttria, stabilized zirconia YSZ.[49] The information regarding the high levels of oxygen ionic conductivity is summarized in Figure 2.10.2.

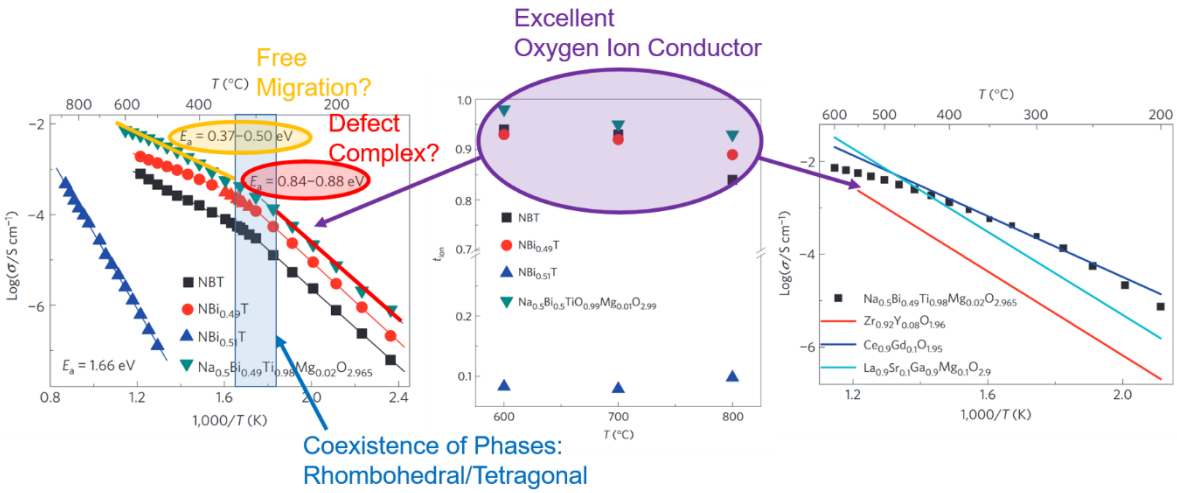

Figure 2.10.2: Bulk conductivity in Arrhenius representation for acceptor doped and A-site non-stoichiometric NBT. A characteristic kink is observable for the oxygen ionic conducting compositions. The temperature region where a phase coexistence was evidenced is highlighted in blue. The bulk oxygen ionic conductivity of Mg-doped NBT is comparable to YSZ. (The Arrhenius plots, ionic transport numbers, as well as the comparison to commercial oxide ion conductors, are taken from ref. [48]).

It needs to be highlighted, that this finding of high levels of oxygen ionic conductivity was completely unexpected. The bulk conductivity in acceptor doped NBT is about four orders of magnitude larger compared to Bi-excess NBT. Further, an abrupt change from semiconducting towards ionic conducting behavior could be evidenced.[48] The absolute values of oxygen ionic conductivity for solely 2.0 mol% Mg-acceptor doped NBT are comparable to YSZ. This finding impressively underlines the uniqueness of the defect chemistry in NBT compared to other well-studied lead-based and lead-free systems.[132, 142, 194, 195]

Furthermore, a kink, resulting from a temperature-dependent change of activation energies is observable in Arrhenius-type representation for Mg-acceptor doped NBT. The origin of the characteristic kink for the ion-conducting species is still not understood completely. The approach made within this work is a formation of defect complexes which results in a temperature-dependent change of the effective vacancy concentration.

At low temperatures, the defect complex needs to be broken before oxygen vacancies can contribute to the conductivity which results in larger activation energies including both, the defect association and oxygen vacancy migration (see Figure 2.10.2 red circle).

At elevated temperatures, all defect complexes are broken and the oxygen vacancies can migrate freely resulting in lower activation energies including only oxygen vacancy migration (see Figure 2.10.2 yellow circle). Based on this hypothesis, a temperature-dependent change from higher to lower activation energies could be explained. Elucidating the origin of the exceptionally high levels of oxygen ionic conductivity in NBT by only small compositional variations and the related defect chemistry is the main aim of this thesis.

The reported high levels of oxygen ionic conductivity already highlight the range of new applications of NBT. For certain applications like oxygen sensors or even solid electrolytes in solid oxide fuel cells (SOFCs), NBT could be a suitable candidate to replace commercially used counterparts. [51-56, 58, 196] Furthermore, it is reported that undesired Bi-loss during the processing also exhibits a major impact on the oxygen vacancy concentration and the resulting oxygen ionic conductivity.[197] This underlines the unexpected high sensitivity of NBT with regards to the A-site non-stoichiometry which might also be the reason for the poor reproducibility as well as the large range of reported dielectric, piezoelectric and ferroelectric properties of this system.[48, 187, 191-193, 197] Based on those findings, various reports have been published about the A-site and B-site substitution with different doping elements like Rb, Fe, Mg, and Nb, which are the most studied choices.[175, 191, 198-205] The strong influence of doping and non-stoichiometry in NBT provides a large set of possible design choices influencing various material properties.[156-158, 187] Precise control of the related defect chemistry is therefore inevitable in the case of NBT as small deviations can come along with unexpected large property changes.

Based on the obtained findings for the basic system NBT, the question needs to be addressed, whether such high levels of oxygen ionic conductivity can also be induced in more complex solid solutions. A general relationship between the defect chemistry in NBT and its solid solutions can, therefore, be derived. Concerning elucidating the similarities and differences of the defect chemistry in NBT and more complex NBT-based systems, the electrical properties of solid solutions of NBT with barium titanate (BT) or strontium titanate (ST) were investigated. The induction of high levels of oxygen ionic conductivity is highly detrimental with regards to ferroelectric and piezoelectric applications and needs to be discussed in more detail. So far, those effects have not been sufficiently discussed in the existing literature. Precise control of the defect chemistry was further utilized to enhance the dielectric, ferroelectric and piezoelectric properties. This might result in a large variety of properties and, in consequence, a large range of possible applications.

2.11 NBT-Based Solid Solutions

To further enhance the already promising properties of NBT which are, however, accompanied by notable "drawbacks" towards possible applications, numerous solid solutions have been fabricated and investigated during the last decades. Some of them are of major relevance with regards to the substitution of the lead-containing alternatives. The here discussed NBT-based solid solutions all provide superior properties within their respective fields of application.

2.11.1 NBT-BT

The system (1-x)$Na_{0.5}Bi_{0.5}TiO_3$-x$BaTiO_3$ or short NBT-BT is an intensively studied NBT-based solid solution which was first reported by Takenaka *et al.* in 1991.[34] Barium exhibits a $5p^6$ electron configuration with an ionic radius of 1.61 Å and is, therefore, larger compared to the regular bismuth (1.17 Å) and sodium ions (1.39 Å) which also occupy the A-site lattice.[206] The morphotropic phase boundary (MPB), a composition-dependent change of the crystal symmetry between rhombohedral and tetragonal structure, was reported to be between x= 0.06 and x= 0.07, derived by the dielectric and piezoelectric properties.[34] For those compositions, the highest piezo- and ferroelectric properties could be reached. The measured piezoelectric coefficient value (with an applied electric field parallel to the polarization direction, d_{33}) of the MPB was 125 pCN^{-1} paired with a relative permittivity of $\varepsilon_{r,33}$ = 580. At the MPB, a separation between the tetragonal and the rhombohedral phase is present. The authors claimed a relaxor behavior which could be caused by the mixed A-site.[34] However, only ferroelectric, relaxor and paraelectric phases could be evidenced. For a BT content of x= 0.05, a remanent polarization of P_{rem} = 0.2 Cm^{-2} decreasing to zero by increasing the temperature to 160 °C was observed. The electric field dependent polarization hysteresis featured a pinched double loop at this temperature.[34] Starting with this publication, the interest of the community on NBT-BT strongly increased over the following decade due to the useful electromechanical properties. With regards to the piezoelectric coefficient d_{33}, the composition NBT-6BT showed the highest values which, however, varied from 110 pCN^{-1} [207] up to 180 pCN^{-1} [208] and also the depolarization temperature ranged from T_d = 87 °C [209] to T_d = 150 °C.[34] Within the given range, several other publications report different values for these parameters.[35, 209] Ranjan *et al.* revealed by a powder XRD study, that the rhombohedral symmetry is evident until x= 0.055. NBT-6BT did not show any rhombohedral tilt angles.

Therefore, the structure was described to be nearly cubic as there was no clear evidence for a tetragonal peak splitting. An electric field-induced phase transition was reported by Daniels *et al.* in 2009 in NBT-7BT[118] by XRD analysis and could further be validated Simons *et al.* in 2011[120] by neutron diffraction experiments. Apart from detailed XRD and neutron diffraction analysis, various other techniques have been used to study the MPB in NBT-BT. With the help of Raman scattering, the MPB was located between x= 0.05 and x= 0.06.[210] Additionally, a change in the size of the domains was observed down to nanoscaled polar regions for NBT-7BT.[211] Jo *et al.* revealed by XRD and small-signal measurements that an electric field dependent MPB region is a better description where rhombohedral and tetragonal phase fractions coexist.[212] Concerning dielectric measurements, polar nano regions are claimed to be evident in NBT-BT systems near the MPB in both, the rhombohedral and the tetragonal symmetry.[213] An in-depth discussion on the influence of the defect chemistry on the electrical and electromechanical properties of NBT-6BT will be presented in chapter 4.2.

2.11.2 NBT-ST

Another NBT-based solid solution, which is of major interest, forms with strontium titanate $SrTiO_3$ (ST). ST itself exhibits a cubic ABO_3 perovskite structure at temperatures above -168 °C resulting in a lack of piezoelectricity.[214] Below a compositional fraction of x< 0.2, the resulting composition exhibits a rhombohedral structure at room temperature. For x= 0.2, the corresponding NBT-ST transforms into a pseudocubic (slightly tetragonal) distorted perovskite structure.[215] With ST ratios above x> 0.2, a gradual change from non-ergodic relaxor properties with ferroelectric polarization responses accompanied by butterfly strain hysteresis towards an ergodic relaxor state which comes along with slim polarization loops and sprout shaped strain responses can be detected. For x> 0.4, the solid solution becomes paraelectric.[216] With the addition of ST, a decrease of the coercive field can be observed with a simultaneous decrease of the temperature of maximum permittivity T_m from 340 °C for pure NBT close to room temperature for solid solutions with x= 0.5.[180] The maximum achievable strain at room temperature was reported for the x= 0.25 [216] or the x= 0.28 [217] NBT-xST compositions. The achievable strain in NBT-25ST is competitive with commercially used soft PZT at applied fields of 3 $kVmm^{-1}$.The occurrence of this large strain value was claimed to be a result of an electric field-induced phase transformation from rhombohedral to tetragonal phase.[217] The origin of the large strain is, however, part of ongoing research.

A publication by Krauss *et al.* suggests, that the strain originates from an antiferroelectric to ferroelectric phase transition [216] while a recent study by Acosta *et al.* from 2016 proposes that rotostriction might also influence the strain response.[218]

A key aspect that was claimed to be responsible for the large resulting strains is the formation of a so-called core-shell microstructure concerning the ST content where a strontium depleted core is covered by a strontium enriched shell in the solid solution NBT-ST. A variety of publications report such a core-shell formation[63, 64, 218, 219] while there are also numerous reports which do not see any core-shell formation at all.[220, 221] The circumstances which lead to either a core-shell formation or not are not completely understood, yet. Nevertheless, the solid solutions where core-shell microstructures have been found, provide evidence for the significant impact of this inhomogeneity in microstructure on the phase transition behavior and the electromechanical properties.[63] Furthermore, an increase of the reversible strain at reduced electric fields was reported for core-shell NBT-ST.[64, 222] Additionally, it was reported that not only the strain and polarization hysteresis are affected, but also a modification of the thermal stability and fatigue was observed.[63] It should be noted, that core-shell microstructures are also reported to enhance the piezoelectric properties of other NBT- as well as BT-based solid solutions underlining that the beneficial effects of the core-shell microstructure are not restricted to NBT-ST.[219]

It should be noted, that the reported electrical and electromechanical properties of NBT-25ST show some major deviations compared to each other due to poor reproducibility. A possible explanation of the large variety of the resulting properties could be different synthesis routes. The calcination temperature as well as one- or two-step calcination, leads to a variation of the maximum achievable strain by up to 35 %.[219] Additionally, the milling and sintering conditions affect the quality of the processed powders. Nevertheless, even similarly processed NBT-ST solid solutions showed notable differences in the respective material properties.[64, 219] This variety of resulting properties might be directly correlated to the formation of core-shell structures. There might be influencing parameters beyond the processing routes themselves resulting in core-shell formation. It has already been reported that A-site non-stoichiometry remarkably affects the properties of NBT and NBT-ST as well.[48, 49, 64, 156, 223, 224] Again, the A-site non-stoichiometry could be caused by unintentional Bi-loss during processing.[64, 225]

Precise control of core-shell microstructures can be utilized to further enhance the piezoelectric properties of systems that exhibit such structures. Furthermore, detailed knowledge of core-shell formation can also increase the reproducibility. It is known that the A-site non-stoichiometry is rather impactful with regards to a possible core-shell formation.[64]

So far, the basic defect chemical mechanisms which lead to the formation of core-shell structures is not completely understood as the defect chemistry is rather different compared to the well-established lead-containing counterparts like PZT. A general defect chemical consideration is therefore vital to gain additional information about the basic mechanisms of core-shell formation in NBT-based systems.

It could already be revealed that NBT-ST exhibits, rather comparable to the basic system NBT, a large sensitivity towards A-site non-stoichiometry. In NBT, the oxygen vacancy concentration is the dominating factor concerning the resulting electrical properties. An increased oxygen vacancy concentration could either be introduced by acceptor doping and deliberate Bi-deficiency or could be a result of unintentional Bi-loss during the processing due to charge compensation as Bi_2O_3 has a low melting point (817 °C) and boils at 1890 °C.[225] The basic effects of deliberately induced A-site off-stoichiometry, as well as B-site acceptor/donor doping on the microstructural evolution and the resulting electromechanical and especially the electrical properties, will be provided in chapter 4.3.

2.11.3 NBT-BT-CZ

As mentioned before, NBT-BT and its composition at the MPB gained large attention due to its useful properties with regards to several applications like actuators. Additional doping with calcium was reported by Yuan *et al.* to result in a significantly more stable temperature dependent permittivity where the variation was less than $\varepsilon_r'(T) \pm$ 15 % in a temperature range from 55 °C up 200 °C.[226] Song *et al.* further reported that the modification of NBT-BT with zirconium leads to an even more pronounced stabilization of ε_r' up to 600 °C.[227] Those findings made the system NBT-BT a viable candidate for high-temperature dielectric applications. Acosta *et al.* combined the effects of Ca and Zr doping on NBT-BT by investigating the ternary system (1-x)[0.94($Bi_{0.5}Na_{0.5}TiO_3$)-0.06($BaTiO_3$)]-x($CaZrO_3$) (NBT-6BT-xCZ) with CZ contents of x= 0.05, 0.10, 0.15 and x= 0.20.[65] For the higher CZ contents (x= 0.15 and x= 0.20), a secondary phase was observed which led to the assumption that the solubility limit of CZ in NBT-6BT is reached. The permittivity got decreased and further flattened by systematically increasing the CZ content to ε_r'(x= 0.05) ≈ 2300, ε_r'(x= 0.15) ≈ 900, and ε_r'(x= 0.20) ≈ 550 at 200 °C. Two local maxima could be evidenced which shifted towards lower temperatures with increasing CZ content. The occurrence of two local maxima was attributed to different kinds of polar nano regions (high-temperature HT and low-temperature LT PNRs) which coexist between the maxima resulting in a temperature-independent permittivity plateau (see also Figure 2.5.4).[117]

Based on a publication by Dai *et al.*, the random local field distribution is affected by the degree of lattice disorder which is influenced by substitution or doping[228] and results in a reduction of the correlation length of present polar nano regions due to the increased local random field strength.[228, 229] In consequence, the temperature-dependent anomalies of the permittivity decrease leading to a flattening of the dielectric response.[65, 230]

The Goldschmidt tolerance factor was calculated to be t_{GS} = 0.9677 for NBT-6BT-20CZ whereas NBT-6BT exhibits a t_{GS} = 0.982. According to Acosta *et al.*, the decrease of the tolerance factor results in increased local stress fields due to the variation of the ionic radii.[65] The processed NBT-6BT-xCZ compositions exhibit an exceptional operating temperature range of about 400 K with relative permittivity values between 470 and 2300, depending on the CZ content. Zang *et al.* were able to reproduce these values and further investigated the dielectric losses of NBT-6BT-xCZ compositions to enhance the material properties with regards to a possible application as high-temperature dielectrics. It was reported that two local maxima are evident for the temperature-dependent ε_r'' values at around 120 °C and 400 °C for a x= 0.05 composition which were related to low temperature and high temperature PNR responses, respectively.[231] Increased CZ contents also lead to a decrease of the local maxima observed for the imaginary part of the permittivity. Modulus plots of the imaginary part of the impedance against the frequency (M'' vs. $\log \omega$) revealed a shoulder in the high frequency region at temperatures above 300 °C which was attributed to a relaxation of polar nano regions.[213, 231] This shoulder formation is seen to be a feature of an additional relaxation process of relaxor materials.[117] In a publication from 2018, Höfling *et al*. have been able to show that, with respect to the CZ content as well as a precise adjustment of the A-site Na/Bi ratio, stable permittivity over a large temperature range can be achieved and the corresponding dielectric losses can be further reduced.[66] A detailed discussion of the impact of A-site non-stoichiometry on the high-temperature dielectric properties will be given in chapter 4.4.

3 Experimental

This chapter provides information about the processing of ceramics which have been investigated in this work. A general description of the powder and the sample processing with the corresponding processing parameters as well as a summary of the used characterization methods are provided and described.

3.1 Powder Processing

In this section, the general procedure of solid-state synthesis is described. Figure 3.1.1 depicts a schematic illustration of the conducted steps to produce high-quality powders which are necessary to further characterize the electrical, dielectric and electromechanical properties.

Figure 3.1.1: Powder processing steps.

It is known from the literature that the hygroscopic character of the used carbonates could falsify the stoichiometric weighing.[49] As NBT exhibits a high sensitivity towards non-stoichiometry, a pre-drying step is vital to receive stoichiometric, reproducible powders.
The different raw materials were dried in advance to the weighing with the corresponding parameters listed in Table 3.1-1 and have been conducted in a Nabertherm, HTC 08/15 oven.

Table 3.1-1: Drying temperatures and drying times for the used raw materials before weighing.

Powder	Drying temperature (°C)	Drying time (h)
Na_2CO_3	300	8
Bi_2O_3	180	8
TiO_2	800	8
MgO	1000	8
Al_2O_3	800	8
$SrCO_3$	180	8
Fe_2O_3	300	8
Nb_2O_5	180	8
$BaCO_3$	180	8
ZrO_2	800	8
$CaCO_3$	180	8

Afterwards, the powders have immediately been weighed in, before water could again be incorporated from air moisture. A regular batch size of the processed powders is 40 g. The weighed in raw materials got mixed in a home built nylon container using Y_2O_3-stabilized ZrO_2 milling balls (weight ratio of milling balls and the raw powder was set to 10:1; diameter 10 mm, Muehlmeier GmbH, Germany) with ethanol as a solvent. After the milling (planetary ball mill, Fritsch, Pulverisette 5, Idar-Oberstein, Germany), a calcination step in a covered alumina crucible followed (P320, Nabertherm GmbH, Germany) with a heating rate of 5 $Kmin^{-1}$. The respective temperatures deviate with regards to the processed compositions and are provided in the appendix (see Table A1 in the appendix). Most of the produced compositions underwent a two-step calcination procedure with an intermediate milling step to enable a complete chemical reaction of the raw materials. After each milling step, the powders have been dried in an oven at 90 °C to evaporate the solvent ethanol. Before each following processing step, the powders have been ground to break larger agglomerates which had formed during the ethanol evaporation step.

Powder processing of the acceptor doped NBT samples presented in chapter 4.1:

Powders of $Na_{0.5}Bi_{0.5}TiO_3$ (NBT), $Na_{0.5}Bi_{0.501}Mg_xTi_{1-x}O_3$ (x = 0.001, 0.002, 0.005, 0.01, 0.015, 0.02, 0.03 and 0.04) (Mg-doped NBT), $Na_{0.5}Bi_{0.501}Fe_xTi_{1-x}O_3$ (x = 0.001, 0.003, 0.01, 0.02, 0.03 and 0.04) (Fe-doped NBT) and $Na_{0.5}Bi_{0.501}Al_xTi_{1-x}O_3$ (x = 0.001, 0.003, 0.005, 0.01, 0.02 and 0.04) (Al-doped NBT) have been fabricated as described above with a two-step calcination procedure by a conventional solid oxide synthesis route.[232] The reagent oxides and carbonates (Alfa Aesar GmbH & Co. KG) Na_2CO_3 (99.5 %), Bi_2O_3 (99.975 %), TiO_2 (99.8 %), Al_2O_3 (99 %) MgO (99 %) and Fe_2O_3 (99.5 %) were used as raw materials. A small Bi-excess was chosen to avoid additionally introduced oxygen vacancies due to Bi-evaporation during the processing. The two-step calcination has been conducted at 800 °C for 2 h and 850 °C for 2 h.

Powder processing of the non-stoichiometric and acceptor doped NBT-6BT compositions presented in chapter 4.2:

Powders of the composition $0.94(Na_xBi_y)TiO_3$-$0.06BaTiO_3$ (N_xB_yT-6BT) (with x= 0.50, 0.51, 0.52 and y= 0.49, 0.50. 0.51, 0.52 and 0.53) have been fabricated with a single step calcination by a conventional solid oxide synthesis route (see chapter 4.2.1 to 4.2.5).[232] The reagent oxides and carbonates (Alfa Aesar GmbH & Co. KG, Karlsruhe, Germany). Na_2CO_3 (99.5 %), Bi_2O_3 (99.975 %), TiO_2 (99.6 %), $BaCO_3$ (99.8 %) have been pre-dried after Table 3.1-1, weighed and mixed for 24 h. After drying the powder mixture, a single calcination followed at 800°C for 3 h. Afterwards, the calcined powder was milled for 24 h. A deviation in the processing route for the powders of $0.94Na_{0.5}Bi_{0.501}Fe_xTi_{1-x}O_3$-$0.06BaTiO_3$ (x= 0.01, 0.02, 0.03, and 0.04) compositions compared to the previously processed non-stoichiometric NBT-6BT compositions was necessary in order to reach a direct comparability of the effects of acceptor doping on NBT and NBT-6BT (chapter 4.2.6 to 4.2.10). A variation of properties by the processing route could, therefore, be eliminated. The reagent oxides and carbonates (Alfa Aesar GmbH & Co. KG). Na_2CO_3 (99.5 %), Bi_2O_3 (99.975 %), TiO_2 (99.6 %), $BaCO_3$ (99.8 %) and Fe_2O_3 (99.5 %) were used as raw materials and have been pre-dried (see Table 3.1-1 for the respective drying parameters) before weighing to avoid non-stoichiometry caused by hygroscopic carbonates.[49] Furthermore, to avoid the formation of additional Bi vacancies and corresponding oxygen vacancies during the processing, all Fe-doped starting compositions exhibit a small Bi-excess of 0.1 mol% as the volatilization temperature of Bi_2O_3 (T> 825 °C) is considerably lower than for Na_2O (T>1132 °C).[233] After a regular milling step for 6 h, the dried powders were calcined in a covered alumina crucible at 800 °C for 2 h. To guarantee a homogeneous distribution, the calcined powders were ball milled again for 4 h and calcined a second time at 850 °C for 2 h followed by ball milling over 6 h to enable a full reaction of the raw materials.

Powder processing of the A-site non-stoichiometric and B-site doped NB_xT-25ST compositions presented in chapter 4.3:

The powders of the compositions $0.75(Na_{0.5}Bi_xTiO_3)$-$0.25SrTiO_3$ (with x= 0.49, 0.495, 0.5, 0.505 and 0.51), $0.75(Na_{0.5}Bi_xTi_{0.97}Fe_{0.03}O_3)$-$0.25SrTiO_3$ (with x= 0.49, 0.5 and 0.51) and 0.75 $Na_{0.5}Bi_xTi_{0.97}Nb_{0.03}O_3$-0.25 $SrTiO_3$ (with x= 0.49, 0.5 and 0.51) have been processed with the conventional solid oxide synthesis route.[232] The used reagent oxides and carbonates (Alfa Aesar GmbH & Co. KG, Karlsruhe, Germany). Na_2CO_3 (99.5 %), Bi_2O_3 (99.975 %), TiO_2 (99.6 %), Fe_2O_3 (99.5 %), Nb_2O_5 (99.9 %) and $SrCO_3$ (Sigma-Aldrich, 99.6 %) have been dried prior to weighing after the conditions listed in Table 3.1-1. All compositions underwent a two-step calcination (750 °C for 2 h and 850 °C for 2 h) with intermediate ball milling steps (250 rpm for 24 h each).

Powder processing of the non-stoichiometric and NB_xT-6BT-yCZ and the NBT-6BT-20CZ-xBA compositions presented in chapter 4.4:

The powders of the composition $(1-y)[0.94Na_{0.5}Bi_xTiO_3$-$0.06BaTiO_3]$-$y(CaZrO_3)$ (NB_xT-6BT-yCZ) were synthesized in the range of $0.49 \leq x \leq 0.51$ and with $0.15 \leq y \leq 0.20$.

The powder with $BiAlO_3$ addition of the composition $(1-x)(0.8[0.94Na_{0.5}Bi_xTiO_3$-$0.06BaTiO_3]$-$0.2(CaZrO_3))$-$xBiAlO_3$ (NBT-6BT-20CZ-xBA) were synthesized with a BA content of x= 0.0, 0.5, 1.0, 1.5, 2.0, 4.0, 8.0 mol%.

The raw materials Bi_2O_3 (99.975 %), ZrO_2 (99.5 %), TiO_2 (99.6 %), $CaCO_3$ (99.5 %), $BaCO_3$ (99.8 %), Na_2CO_3 (99.5 %), Al_2O_3 (99 %) (Alfa Aesar GmbH, Karlsruhe, Germany) have been dried with regards to the parameters provided in Table 3.1-1 due to their hygroscopic behavior and afterwards were mixed precisely according to the stoichiometric formula to realize the chosen A-site stoichiometry. The weighed powders have been ball-milled for 24 h at 250 rpm. After the drying to remove the solvent ethanol the dried powders were ground and calcined at 900 °*C* for 3h with a heating rate of 5 $Kmin^{-1}$ (P320, Nabertherm GmbH, Germany). Afterwards, the powders were ball-milled, dried and ground again with the same conditions as described above.

3.2 Sample Preparation

A general description of the sample processing steps is given schematically in Figure 3.1.1.

Figure 3.2.1: Processing steps for preparing the samples.

After the powders have been processed, green bodies of the powders with a diameter of 10 mm were fabricated by uniaxial pressing with a pressure of approximately 25 MPa followed by a cold isostatic pressing step at 382 MPa (750 kN) (Weber, KIP 100E). The so prepared green bodies have been sintered at different temperatures over different times with regards to their composition. The acceptor doped NBT samples (chapter4.1) have been sintered at 1150 °C for 2 h, except the Mg-doped compositions (2 h at 1050 °C) as Mg acts as a sintering aid.[48]

The non-stoichiometric NBT-6BT samples (starting from chapter 4.2.1) have been sintered for 4 h at 1160 °C while the Fe-doped NBT-6BT samples (starting from chapter 4.2.6) were sintered at 1150 °C for 2 h to keep the processing parameters equal to the directly compared Fe-doped NBT compositions. All A-site non-stoichiometric and acceptor/donor doped NB_xT-25ST samples (chapter 4.3) have been sintered at 1150 °C for 2 h. The NB_xT-6BT-yCZ samples (chapter 4.4) underwent a sintering procedure at 1100 °C for 2 h. The sintering of the green bodies was conducted in a covered alumina crucible with the use of sacrificial powder of the respective composition to avoid further evaporation of volatile reagents with a heating rate of 5 $Kmin^{-1}$ (Nabertherm, L16/14). The sintered samples have been ground on both sides to receive plain parallel surfaces. For the conducted electrical analysis, the so prepared samples have been electroded with Platinum (Pt) via sputter deposition (Argon plasma with $p(Ar)$ = 0.02 mbar; working current 40 mA; 8 minutes each side).

For the investigation of the sample topography, the samples have been thermally etched at 50 °C below the sintering temperature for 5 minutes.

3.3 Density

A high density of the processed samples is inevitable for a further electrical and electromechanical characterization as large pores would result in poor electrical stability. Hence, the density of the samples was determined by the Archimedes method. At first, the samples get weighed in air (W_{air}). The weight in water (W_{fl}) was determined after the samples were exposed to vacuum for 20 minutes in distilled water to suck the air out of the pores on the surface.

The density of air is assumed as ρ_{air} = 0.0012 gcm^{-3} and the temperature-dependent density of water as ρ_{fl} = 0.99768 gcm^{-3} at T = 22.5 °C. With equation (3.1) the density of the sample can be calculated:[234]

$$\rho = \frac{W_{air} \cdot (\rho_{fl} - \rho_{air})}{0.99983 \cdot (W_{air} - W_{fl})} + \rho_{air} \,. \tag{3.1}$$

3.4 X-ray Diffraction (XRD)

With the help of X-ray diffraction (XRD) measurements, the crystal structure, as well as the possible formation of secondary phases, can be investigated.

During an X-ray diffractogram is collected, an X-ray beam gets diffracted by the electron shells of the atoms within the crystal lattice. Destructive and/or constructive interference occurs between the diffracted X-rays.

The distance between the lattice planes d of the investigated crystal structure is directly related to the scattering angle θ of the incoming X-ray beam with the wavelength λ (by Bragg's equation):[145]

$$n \cdot \lambda = 2 \cdot d \cdot \sin(\theta) \,. \tag{3.2}$$

The corresponding lattice constants a, b, and c can further be calculated with the help of the Miller indices (denoted by h, k, and l) of a known crystallographic structure and the collected distances between the lattice planes d of the investigated material:

Cubic:
$$\frac{1}{d_{hkl}^2} = \frac{h^2 + k^2 + l^2}{a^2} \,. \tag{3.3}$$

The lattice constant a for the cubic case (see equation (3.4)) can be calculated by taking the equations (3.3) and (3.2) into account:

$$a = \frac{\lambda}{2 \cdot \sin(\theta)} \cdot \sqrt{(h^2 + k^2 + l^2)}\,. \tag{3.4}$$

For the XRD patterns presented in this work, a Bruker AXS D8 Advance diffractometer (Karlsruhe, Germany) was used where an X-ray beam was generated by a Copper source with a monochromatic wavelength of $\lambda\ (Cu_{K\alpha})$ = 0.15418 nm. The angular step size was θ = 0.02° with a measuring time of t = 5 s at each position.

3.5 Scanning Electron Microscopy (SEM)

With the help of scanning electron microscopy (SEM), images of the sample topography, as well as the possible formation of secondary phases, can be investigated on the micrometer or even nanometer scale. The following information is taken from the textbook by W. Göpel and C. Ziegler.[235]

A focused electron beam which is generated by an electron gun scans over the surface of the sample. Typically, the acceleration voltage of the electron gun is in the range between 0.2 kV and 40 kV.[235] The accelerated electrons penetrate the surface of the sample and interact with the atoms. By this interaction, different signals will be generated which can be collected and processed by variable detectors.

Secondary electrons (SE) occur when an in-elastic scattering of the primary electrons with the sample atoms takes place. Those electrons typically have an energy of around 10 eV. Hence, only secondary electrons close to the surface (up to fifty nanometers) are capable of leaving the sample and get collected by the detector. Therefore, secondary electron images are used to describe the sample topography. For the particular case of the investigated NBT and NBT-based compositions, a direct influence of the oxygen vacancy concentration on the shape and size of the grains could be observed.[156, 157, 236, 237]

Backscattered electrons (BSE), for instance, occur due to elastic scattering of the primary electrons with the sample atoms. The volume of interaction is deeper and broader than for the secondary electrons (about several hundreds of nanometers). The probability to generate backscattered electrons is directly related to the atomic mass of the sample atoms. Thus, backscattered electron images exhibit an atomic mass-dependent contrast and accordingly allow to investigate chemical inhomogeneity.

This is of major importance for an in-depth study of secondary phases which might not be detected by XRD due to the low resolution limit of > 5 % and, of course, the formation of core-shell structures in the particular case of NBT-ST (see chapter 4.3). Most SEMs provide an SE and BSE detector.

Additionally, the chemical composition of the samples was investigated with the help of energy-dispersive X-ray spectroscopy (EDX). While exposed to a highly energetic electron beam, electrons in discrete energy levels of the respective elements of the specimen get ejected leaving an electron hole behind. An electron of a higher energy level fills the hole emitting the energy difference in the form of an X-ray.[235] As the emitted X-rays are characteristic for each element, a qualitative and quantitative analysis of the chemical composition is possible on a local scale. The number and energy of the X-rays are collected by an EDX detector.

To avoid static charging at the surfaces, the samples need to be coated with a thin, conducting layer. Typically, a thin gold layer was sputtered onto the samples with a thickness of approx. 40 nm for the SE images and carbon for the BSE images.[235]

For the later shown SE and BSE images, two high-resolution electron microscopes (HREM) (Philips XL3000 FEG, FEI Company, Eindhoven, Netherlands; JEOL, Model JSM 7600F, Japan) were used. Additionally, an EDX analysis (Oxford Link ISIS, Oxford Instruments Ltd, Oxfordshire, UK) was conducted to evaluate the chemical composition of the occurring secondary phases.

3.6 Electrochemical Impedance Spectroscopy (EIS)

The EIS measurements were performed by a Novocontrol Alpha-A High-Performance Frequency Analyzer. The corresponding equivalent circuit is illustrated in Figure 3.6.1.

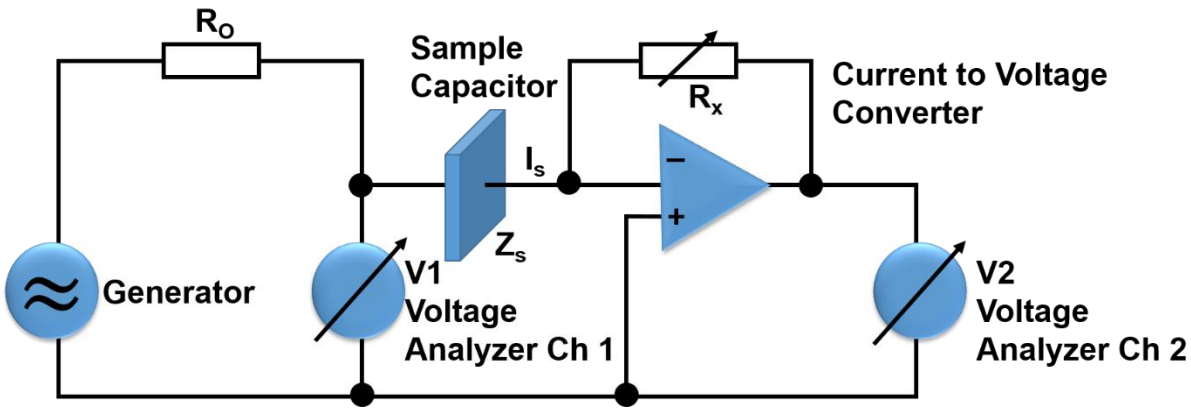

Figure 3.6.1: Schematic illustration of the measuring principle of an impedance spectroscopy setup (adapted from ref. [238]).

An AC voltage signal is created by the generator and is applied to the sample. The amplitude and phase of the response are measured in $V1$. If the impedance of the sample becomes too low during the measurement, the resistor R_O limits the sample current. The current signal of the sample I_s is fed into an operational amplifier (represented by the blue triangle which exhibits a variable resistor R_x in its feedback loop). The resistance of R_x is set by the Alpha A-impedance analyzer to result in an output voltage $V2$ such that the response of the operational amplifier is in good measurable range with the voltage input channel $V1$. The relationship for ideal components between the sample current I_s and to the voltage signal of the operational amplifier $V2$ can be expressed as:[238]

$$I_s = -\frac{V2}{R_x}. \tag{3.5}$$

For an ideal operational amplifier, the voltage at the sample current input (I_s) results in $0\,V$ with regards to ground. Hence, the voltage signal $V1$ equals the voltage over the sample. The sample impedance can, therefore, be expressed as a relationship between the input voltage signal $V1$, the output voltage signal $V2$ and the resistance of the variable resistor of the operational amplifier R_x:

$$Z_s = \frac{V1}{I_s} = -\frac{V1}{V2} \cdot R_x\,. \tag{3.6}$$

Based on Ref. [238], the response voltage $V2$ and current I_S of a sample capacitor (blue) to an applied sine wave signal $V1$ are measured in the so called gain phase mode. The measured voltage responses determine the corresponding Amplitude 1 (channel 1) and Amplitude 2 (channel 2). The advantage to measure to voltages instead of the sample current is a better signal to noise ratio.

If not mentioned otherwise explicitly, the regular impedance measurements have been conducted in a frequency range from 0.1 Hz to 3 MHz with a logarithmic factor of 1.3 (resulting in 67 measuring frequencies). The temperature span was set from 150 °C to 700 °C in 10 K steps to evaluate the temperature evolution of the conductivity in a regular tube furnace (control unit from HTM Reetz GmbH, Berlin, Germany). For the post-processing of the collected data, the RelaxIS software (rhd instruments, Darmstadt, Germany) was used.

3.7 Dielectric Permittivity and Loss

The dielectric responses of the samples have been measured with a simple parallel plate capacitor arrangement with plane parallel Pt electroded sample areas.

The temperature dependence of the dielectric permittivity has been investigated between room temperature (25 °C) and 600 °C with a constant heating rate of 2 $Kmin^{-1}$ (Nabertherm LE4/11/R6) with the help of an LCR meter (HP 4284A; Hewlett Packard Corporation, Palo Alto, USA). Accordingly, the measuring frequency was set to constant values of 100 Hz, 1 kHz, 10 kHz, 100 kHz, and 1 MHz.

3.8 Polarization and Strain Response

For the polarization and strain analysis, the samples have been exposed to an external electric field and the polarization and strain responses have been measured simultaneously. The polarization hysteresis has been measured using a Sawyer-Tower bridge.[239] As this is a home built set up, a schematic illustration is provided in Figure 3.8.1.

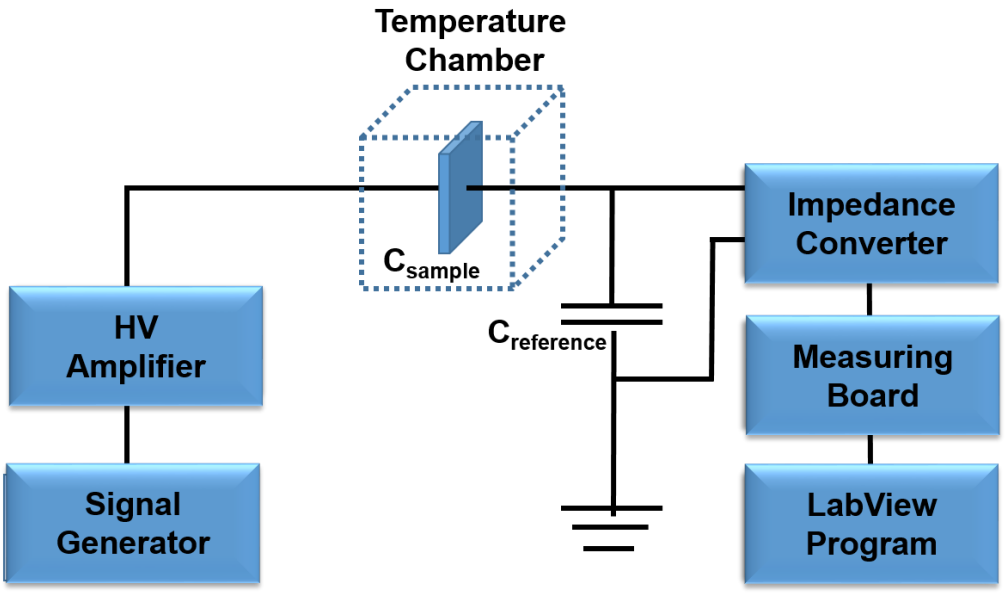

Figure 3.8.1: Schematic illustration of the home built Sawyer-Tower-Setup used for the temperature dependent polarization measurements.

A signal generator (33220A, Agilent, USA) created the DC voltage signal which was amplified by a high voltage generator (TREK model 20/20C, Trek Inc., USA). The displacement current measured at a reference capacitor (16.77 µF) is the same as for the sample as they are connected in series. Therefore, the same charge Q is accumulated at both capacitors. The relations for the reference capacitance $C_{reference}$ and voltage $V_{reference}$ and the measured sample capacitance C_{sample} and voltage V_{sample} are given in equation (3.7). The polarization P of the sample can be calculated after equation (3.8):

$$Q = C_{sample} \cdot V_{sample} = C_{reference} \cdot V_{reference}\,, \tag{3.7}$$

$$P = \frac{C_{reference} \cdot V_{reference}}{A_{sample}}\,. \tag{3.8}$$

A measuring board (National Instruments) was used to measure the voltage at the reference capacitor and was read out by a LabView program (written by Florian Schader, former PhD student at TU Darmstadt, FG NAW). The electric field was ramped with $8 \cdot 10^6$ V m^{-1} s^{-1}. For temperature-dependent measurements, the temperature was stabilized for 10 minutes before each measurement. To keep the errors small, the reference capacitor was chosen to have a much larger capacitance compared to the sample capacitances. The macroscopic strain was simultaneously measured by an optical displacement sensor LF356 from Texas Instruments.

3.9 Electromotive Force (EMF)

The oxygen ion transport numbers which are provided in chapter 4.2.8 for the Fe-doped NBT and NBT-6BT samples from electromotive force (EMF) measurements have been conducted by Dr. Ming Li, University of Nottingham, with the help of a ProboStat system (NorECs Norwegian Electro Ceramics AS, Oslo, Norway). A schematic illustration of the used setup is provided in Figure 3.9.1.

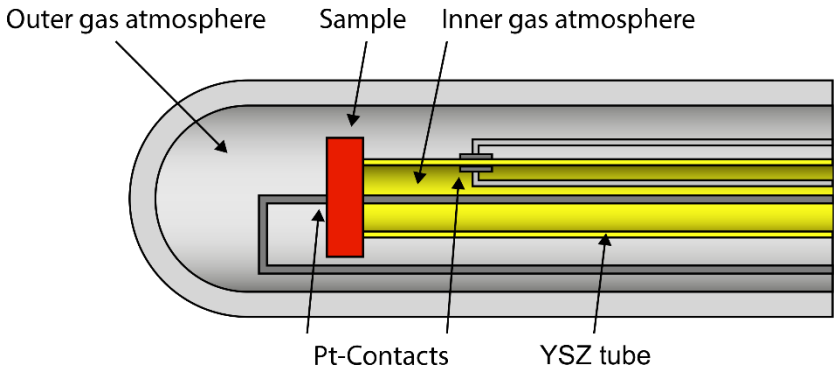

Figure 3.9.1: Schematic illustration of a typical electromotive force (EMF) setup.

The ceramic samples have been sealed onto a YSZ tube, serving as the reference, with a commercial glass frit. The YSZ tube was flooded by N_2 (inner gas atmosphere) while the top of the sample (outer gas atmosphere) remained in air to create an oxygen partial pressure ($p(O_2)$) across the sample. The partial pressure difference was measured by the voltage drop with the help of a Solartron Schlumberger 7150 digital multimeter across the YSZ tube and compared to the voltage drop across the sample to calculate the oxygen ionic transport numbers t_{ion}.

3.10 Nuclear Magnetic Resonance (NMR)

The here presented NMR results are based on measurements that were carried out by Dr. Pedro Groszewicz (Institute of Physical Chemistry, TU Darmstadt, Germany).

Solid-state ^{27}Al NMR spectra were recorded with a carrier frequency of 156.37 MHz. Ceramic pellets have been ground to powders and packed into 4 mm ZrO_2 rotors. Two dimensional ^{27}Al 3QMAS (or MQMAS) NMR spectra were acquired with a Z-filter pulse sequence.[240] The chemical shift scale was referenced to a 1M $AlCl_3$ aqueous solution (0 ppm).

3.11 Density Functional Theory (DFT) Calculations

The total energy calculations with regards to density functional theory (DFT) shown in chapter 4.1.3 have been conducted with the help of the Vienna Ab initio Simulation Package (VASP) [241, 242] by Leonie Koch from the Materials Modelling group at TU Darmstadt. Projector augmented waves[243, 244] in combination with the local density approximation (LDA) have been applied.[245]

A plane wave energy cut-off was set to be 600 eV with the following valence electron configuration: O: $2s^2 2p^4$, Na: $2p^6 3s^1$, Ti: $3s^2 3p^6 4s^2 3d^2$, Bi: $5d^{10} 6s^2 6p^3$ and Mg: $2p^6 3s^2$. The ionic positions were optimized in such a way that the forces between the ions have been reduced to less than 0.01 eV $Å^{-1}$. All relaxations were carried out with a single k-point and a supercell consisting of 319 atoms in total. Three different defect arrangements with two Mg substituting ions and one oxygen vacancy were chosen to mimic three different Mg-doping concentrations. The position of the oxygen vacancy was changed with regards to the closest Mg-dopant in each set respectively. Simultaneously, the distances between the two Mg-dopants were fixed. The distances between the two Mg substituents have been varied from the first nearest neighbor to the second nearest neighbor and the third nearest neighbor position which should resolve a varying Mg-dopant concentration. The here used defect complex $\{2\mathrm{Mg}''_{\mathrm{Ti}}\mathrm{V}_{\mathrm{O}}^{\bullet\bullet}\}''$ exhibits a relative charge of -2. Therefore, two additional electrons have been added to the simulation cell to achieve the correct ionic charges.

For the data presented in chapter 4.1.4, the generalized gradient approximation (GGA) in the Pardew-Burke-Ernzerhof parameterization to evaluate the exchange correlation energy functional was used.[246-248] In calculations where Fe is involved, additionally, a U value of 4 eV was applied to the d-orbitals.

Due to a rather large supercell size, all calculations are restricted to the Γ point. The influence of three different doping elements Mg, Al, and Fe was investigated. A more detailed description of the actual charge state of the dopant and the defect geometry will follow in the particular sections. The focus is set on the covalent bonding environment around the dopant and how a specific A-site ordering and extrinsic as well as intrinsic point defects affect the dopant-oxygen interaction. To reveal the difference in the temperature-dependent conductivity from a local perspective, the crystal orbital Hamiltonian population (COHP) method, as implemented in LOBSTER was considered.[249] This method has been proven effective as a post-processing tool for results from plane-wave codes. For detailed information on this method, the reader is referred to Ref.[250]

4 Results and Discussion

The results and discussion part is divided into four chapters. The first chapter will deal with the impact of the defect chemistry on the basic system NBT. It covers an experimental investigation of the electrical conductivity in B-site acceptor doped NBT which is further supported by theoretical considerations about the defect chemical mechanisms which lead to the extremely high oxygen ionic conductivity. A computational simulation-based analytical model (elaborated with the help of Leonie Koch from the Materials Modelling group, TU Darmstadt) was established to elucidate the influence of the doping element choice, the concentration dependence as well as the different occurring phases within the investigated temperature range. The here presented DFT calculations have been used to describe the experimental data based on the established model.

The second chapter will deal with the application of the defect chemical knowledge which was gained in the first chapter to the more complex solid solution NBT-6BT. It should also be seen as proof if the established model also holds for NBT-based systems with higher complexity. Therefore, A-site non-stoichiometric, as well as B-site acceptor doped in NBT-6BT, have been investigated in more detail. Besides the electrical conductivity, the focus was set on the dielectric, piezoelectric and ferroelectric properties with regards to adjusting the defect chemistry on the A- and the B-site to further enhance those properties.

The third chapter deals with the NBT-based solid solution with strontium titanate (ST), NBT-25ST. Here, core-shell microstructures have been observed which, in particular, are significantly affected by the diffusivity of Sr. The diffusivity, of course, features a strong relationship with the defect chemical circumstances. The mechanisms leading to the formation of chemical inhomogeneity such as core-shell microstructures is still under debate. The here conducted work should shed a light on the influence of the A-site and B-site defect chemistry on the diffusion properties in NBT-based systems like NBT-25ST. As the electromechanical properties of NBT-25ST are correlated to the occurrence of core-shell structures, a tuneability by precisely adjusting the regarding A-site and B-site defect chemistry is expected.

The fourth and last chapter of the results and discussion part provides a detailed study about extending the application range of NBT-based solid solutions. Apart from NBT as an excellent oxygen ionic conductor (discussed in chapter 4.1), solid solutions of NBT deliver exceptionally good piezo- and ferroelectric properties for actuators or transducers (discussed in chapter 4.2 and 4.3). Beyond that, there is a rather new field of research which has gained large interest since the last years, namely high-temperature dielectrics.

NBT-based ternary solid solutions like NBT-6BT with the addition of calcium zirconate (CZ) have been evidenced to exhibit superior properties referred to high-temperature dielectric applications. In detail, an almost temperature-independent permittivity plateau was reached over a temperature range beyond 300 K paired with an exceptionally low dielectric loss below $\tan\delta \leq 0.02$. By applying the gained knowledge about the fundamental defect chemical mechanisms in NBT, a further enhancement regarding the occurring dielectric losses, still seen as the bottleneck with regards to application, is expected. Therefore, the effects of A-site non-stoichiometry with a simultaneous variation of the CZ content was investigated in more detail. To further reduce the dielectric losses, bismuth aluminate $BiAlO_3$ (BA) was added to the ternary system.

Those four chapters should give a detailed view of the defect chemical interactions in the basic system NBT and the large applicability for more complex solid solutions. In connection with the enormous range of various properties NBT exhibits, this highlights the potential of NBT in multiple fields of application.

4.1 Defect Chemistry of Acceptor Doped NBT

Apart from the information already provided in chapter 2.10, the effects of A-site non-stoichiometry and B-site acceptor doping on the electrical properties of NBT need to be discussed in more detail.

Li et al. already delivered proof, that high levels of oxygen ionic conductivity can be established by A-site non-stoichiometry and B-site acceptor doping in NBT (see Figure 2.10.2).[48] The high levels of oxygen ionic conductivity were unexpected in NBT and are not comparable to widely studied lead-based and lead-free systems.[132, 142, 194, 195] The achieved ionic conductivity is competitive with YSZ.[48]

A kink, resulting from a temperature-dependent change of activation energies is observable in Arrhenius-type representation for Mg-acceptor doped NBT. The change of activation energies could be caused by a defect complex formation. At low temperatures, the defect complex needs to be broken before oxygen vacancies can contribute to the conductivity. Therefore, a temperature-dependent change from higher to lower activation energies could be explained.

This feature has been previously investigated by Schie *et al.* in $SrTiO_3$.[142] It was claimed that this kink, and the resulting change in the activation energies, is related to temperature and further a change in the free oxygen vacancy concentration. At high temperatures and low doping concentrations, oxygen vacancies can migrate almost freely through the sample. At sufficiently low temperatures or high doping concentrations, the oxygen vacancies might be trapped temporarily. Therefore, the actual conductivity could be estimated by including a suitable trapping factor which represents a temperature-dependent effective (free) vacancy concentration. This factor can be extracted by deriving a mass action law of the formed defect complex with not violating the charge neutrality condition.[141, 251-253] This effect is also evident in other perovskite-type structures apart from strontium titanate (ST), like $BaTiO_3$ (BT).[141, 142, 254]

It should be noted, that NBT undergoes a phase transition from rhombohedral to tetragonal between 280 °C and 320 °C. The coexistence of phases could be experimentally evidenced within this temperature region (see chapter 2.10).[179] The phase itself might also have an impact on the possible defect complex formation as well as on the oxygen ionic migration process.

Following questions regarding the defect chemistry in NBT need to be addressed:

- Why is the conductivity in acceptor doped NBT orders of magnitude higher?
- Is the change in activation energy explainable by a defect complex formation in acceptor doped NBT?
- What is the influence of acceptor dopant variation on a possible defect complex formation?
- What is the impact of the rhombohedral/tetragonal phase coexistence on the activation energy for oxygen ionic migration?
- Is oxygen ionic conductivity in acceptor doped NBT dependent on the doping element?
- What is the influence of modified doping concentration?
- Is there a solubility limit for acceptor doping in NBT and do secondary phases influence the electrical properties of the bulk and the grain boundary?
- Is NBT applicable as solid oxide ion conductor material?

To address the remaining questions about the defect chemistry of NBT, a B-site acceptor doping approach has been selected in this work. Three different acceptor dopants Mg, Fe, and Al have been chosen to further elucidate the defect chemical origin of the exceptionally high oxygen ionic conductivity and differences in possible defect association in NBT. The divalent Mg-acceptor should lead to a higher vacancy concentration as the trivalent acceptor Fe at the same doping level. Additionally, Al was chosen as it should, in principle, induce the same vacancy concentration than Fe concerning their valence state. The chosen dopants, however, exhibit different electron configurations and ionic radii which could further affect the resulting oxygen migration barrier height and/or the possible formation of defect complexes with the induced oxygen vacancies.

In this chapter, a systematic study about the electrical conductivity is provided for Mg-, Fe- and Al- B-site acceptor doping in NBT. The focus is set on elucidating the origin of extremely high levels of oxygen ionic conductivity based on a possible defect complex formation, concentration dependence, the impact of varying crystallographic phases on the oxygen ion migration as well as the tendency to form secondary phases in NBT. With the obtained findings, a new defect chemical model can be derived which might allow for precise controllability of the defect-related material properties in the basic system NBT.

The discussion starts with microstructural analysis with the help of XRD, SEM and EDX to investigate, where the solubility limit for acceptor doping in NBT is located concerning different acceptor dopants (chapter 4.1.1). Gaining a deeper knowledge about the solubility limit of the chosen dopants is crucial to further rationalize the obtained conductivity values. Subsequently, frequency-dependent impedance spectroscopy measurements were performed between 150 °C and 700 °C to investigate the doping element and concentration dependence of the oxygen ionic conductivity (chapter 4.1.2). Based on the experimental findings, a detailed, simulation supported discussion on the defect complex formation, the doping concentration as well as the coexistence of phases for the particular case of Mg-acceptor doping is provided in chapter 4.1.3. To clarify the origin of electronic conductivity for lower doping concentrations, a density of states (DOS) calculation based discussion on the effects of different acceptor doping on the band gap is given in chapter 4.1.4. Further, the covalent bonding contributions concerning the chosen doping element and the local oxygen coordination was investigated with the help of Crystal Orbital Hamiltonian Population calculations. The dopant dependent difference in the defect association could, therefore, be further elucidated. A nuclear magnetic resonance (NMR) study was carried out by Pedro Groszewicz to obtain information about possible defect formation in the particular case of Al-doped NBT (see chapter 4.1.5). To elucidate the applicability of acceptor doped NBT e.g. as a ceramic membrane in SOFCs, the concentration dependence of acceptor doping at grain boundaries and the resulting total oxygen ionic conductivity have been investigated in more detail in chapter 4.1.6.

The calculations presented in this chapter have been carried out by Leonie Koch from the Materials Modelling group at TU Darmstadt (in particular for chapter 4.1.3 and 4.1.4).

4.1.1 Acceptor Doped NBT: Microstructure

In this section, the microstructural analysis for the different acceptor doped NBT compositions is provided to clarify the doping element dependent solubility limit in NBT. The XRD pattern of Mg-, Fe- and Al-doped NBT with different dopant concentrations ranging between 0.1 mol% and 4.0 mol% are given in Figure 4.1.1.

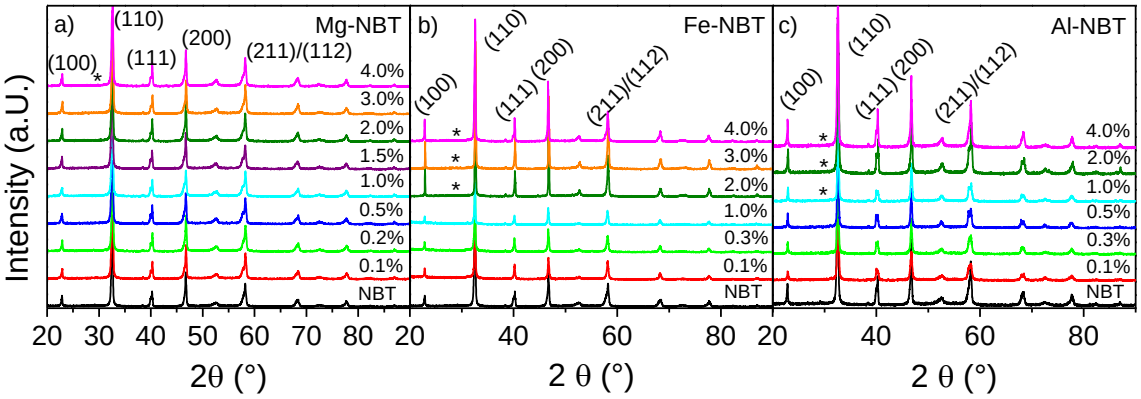

Figure 4.1.1: XRD-pattern of the Mg- (a), Al- (b), and Fe-doped (c) NBT compositions with doping contents between 0.1 mol% and 4.0 mol%. The peaks caused by the secondary phases are denoted with a star in the respective XRD-pattern.

As a general observation, all compositions exhibit the $R3c$ group perovskite structure at room temperature which is in good agreement with existing literature.[177, 178, 255, 256] The Mg-doped samples did not show any evidence for the formation of secondary phases within the resolution limit up to a doping content of 3.0 mol%. The solubility limit seems to be dependent on the doping element itself. For the Mg-doped case, no secondary phases can be detected until a doping content of 3.0 mol% is reached while in the case of Fe and Al-doping already at 2.0 mol% and 1.0 mol% an additional peak can be seen (denoted with a star).

To elucidate which secondary phases form, an SEM analysis in the BSE mode combined with a simultaneous EDX analysis of the matrix and secondary phase was performed.

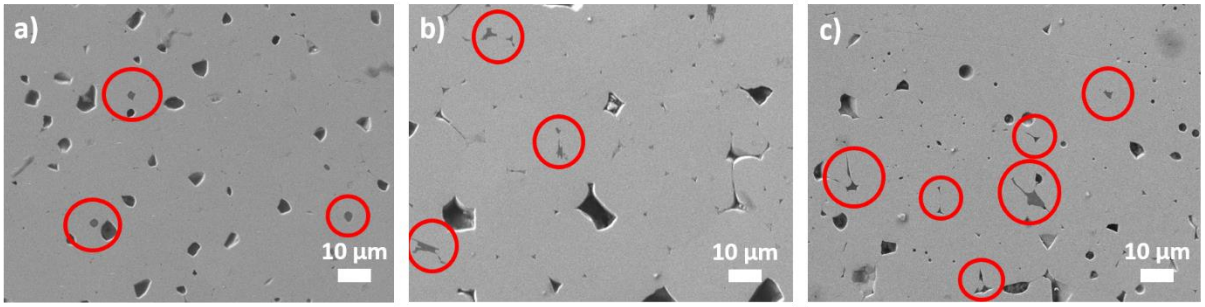

Figure 4.1.2: SEM images of the 4.0 mol% doped Mg- (a), Fe- (b) and Al-NBT (c) in the BSE mode. The secondary phases are marked with red circles.

A closer look at the microstructure reveals that secondary phases are evident in the differently doped NBT samples. Figure 4.1.2 depicts SEM images of the respective 4.0 mol% doped samples in the BSE mode. The Al-doped NBT samples exhibited the highest concentration of secondary phases at the grain boundaries compared to the Mg- and Fe-doped compositions at the same doping concentration. An EDX analysis of the corresponding phases proved the composition to be Ti- and either Mg-, Fe- or Al-rich as well as Bi-deficient, depending on the chosen dopant. It seems that the Ti-rich phase led to liquid phase sintering due to a lower melting point as the secondary phases could be located at the grain boundaries and, especially, at the triple points. The formation of secondary phases needs to be considered in the following discussion, as this could result in a lower concentration of induced oxygen vacancies than expected for the respective doping concentration. At this point, it can be concluded, that the solubility limit of acceptor dopants in NBT differs for each element. Based on the previous discussion, a solubility limit is dependent on the chosen dopant and ranges between 1.0 mol% for Al and 3.0 mol% for Mg-doping.

4.1.2 Acceptor Doped NBT: Electrical Properties

To address the question about the impact of different acceptor dopants with a varying concentration on the electrical conductivity, a detailed analysis of the frequency and temperature-dependent impedance responses has been conducted. The respective impedance spectra of Mg-, Fe- and Al-doped NBT compositions taken at 500 °C in a frequency range from 0.1 Hz to 3 MHz are illustrated in Figure 4.1.3. Only the Nyquist plots for the most relevant compositions are provided. The bulk, grain boundary and electrode responses are denoted with arrows.

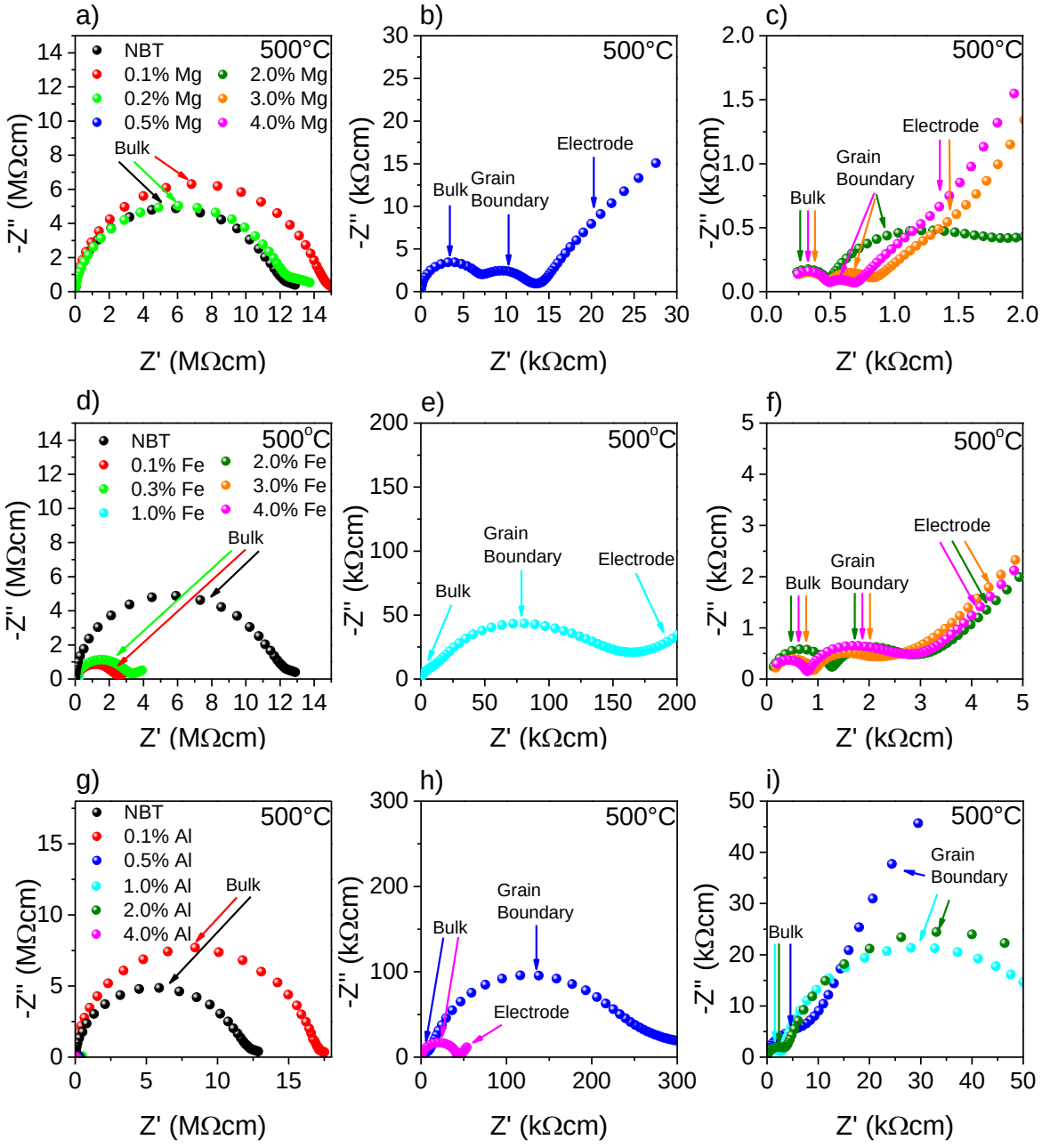

Figure 4.1.3: Impedance spectra of the Mg- ((a) to (c)), Fe- ((d) to (f)) and Al-doped ((g) to (i)) NBT compositions taken at 500 °C with a frequency range of 0.1 Hz to 3 MHz, shown for variable impedance ranges.

The 0.1 mol% doped compositions as well as undoped NBT all exhibit one semicircle which can be related to the bulk response of the respective samples ranging from R_b ~ 2.8 MΩcm (0.1 mol% Fe-doping (d)) to R_b ~ 17.5 MΩcm (0.1 mol% Al-doping (g)).[154] The obtained bulk resistivity values are in good agreement with existing literature presenting semiconducting behavior.[48] By further increasing the doping content, the obtained sample responses start to differ. While 0.2 mol% Mg-, 0.3 mol% Fe- and 0.1 mol% Al-doped NBT still exhibit one semicircle, the 0.5 mol% Mg and Al-doped specimens show an orders of magnitude lower resistivity and furthermore a formation of two semicircles representing the grain boundary (intermediate frequency) and bulk (high frequency) response (according to the "Brick-Layer" model, established in chapter 2.9). A direct relationship of oxygen ionic conductivity and the formation of two distinguishable semicircles and the electrode polarization at low frequencies have already been provided by Li et al. in acceptor doped NBT.[48] The low-frequency response displays a polarization of the electrode with an angle of about 45° in the Nyquist representation which is known from the literature to originate from a Warburg-type diffusion of oxygen ions at the sample/electrode interface and could be seen as a supporting evidence for oxygen ionic conductivity in those particular compositions.[257] The 1.0 mol% Fe-doped composition exhibits a bulk resistivity of R_b ~ 25 kΩcm. Fe-doped NBT has been proven to be oxygen ionically conducting by electromotive force measurements (t_{ion} > 0.9; a detailed discussion is provided in chapter 4.2.8). By further increasing the doping content, the obtained impedance spectra of the Mg-, Fe- and Al-doped NBT compositions represent a comparable shape. At a certain doping level, the impedance only changes slightly. For the Mg-doped compositions, no further change can be detected above 2.0 mol% doping with R_b ~ 0.5 kΩcm. The same accounts for the Fe-doped compositions with R_b ~ 0.8 kΩcm above 2.0 mol%. The 4.0 mol% Al-doped composition exhibit a significant increment in the resistivity compared to the lower doped species. This behavior might be explained by a formation of secondary phases which leads to a decreased oxygen vacancy concentration in the matrix.[135]

To further investigate the concentration dependence on temperature-dependent conductivity, Arrhenius-type plots of the bulk conductivity for the differently doped NBT compositions are provided in Figure 4.1.4.

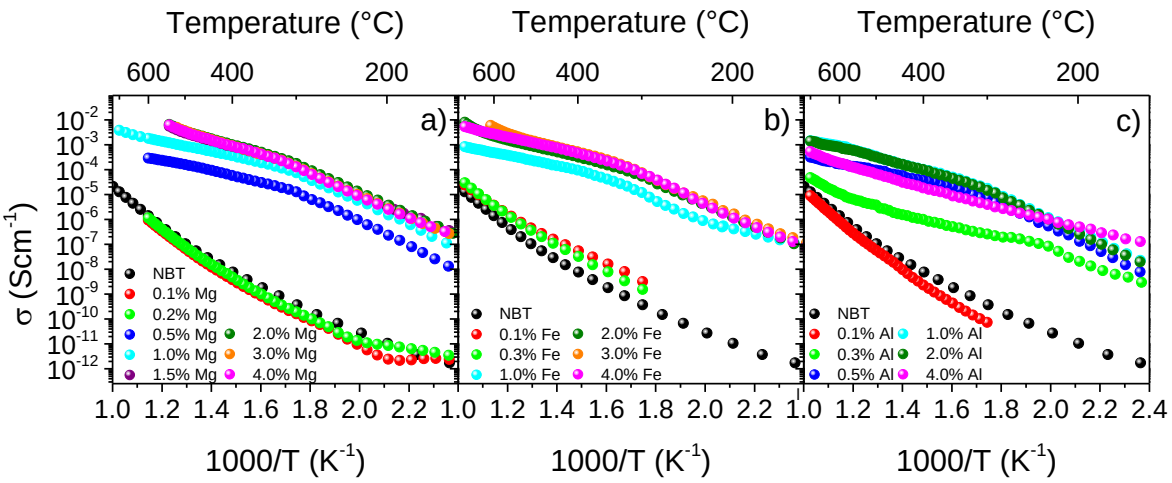

Figure 4.1.4: Arrhenius plots for the bulk conductivity σ_b of the Mg- (a), Al- (b) and Fe-doped (c) NBT compositions with varying doping contents between 0.1 mol% and 4.0 mol%.

A doping concentration-dependent change of the bulk conductivity is observable for all investigated acceptor dopants. Additionally, for all doped compositions two groups are forming depending on the respective doping concentration. This behavior is known from literature for A-site non-stoichiometric and B-site acceptor doped NBT where a change of the conduction mechanism from semiconducting towards oxygen ionic conducting behavior could be proven.[48, 49] The low doped as well as the undoped NBT represent the first group with low bulk conductivity paired with high activation energy values at temperatures above 320 °C (see Table 4.1-1).

Table 4.1-1: Activation energies before and after the kink of the Mg-, Fe- and Al-doped samples.

Composition	E_a below 280 °C (eV)	E_a above 320 °C (eV)
NBT	0.811	1.446
0.1 mol% Mg-NBT	0.986	1.410
0.2 mol% Mg-NBT	0.985	1.376
0.5 mol% Mg-NBT	0.952	0.442
1.0 mol% Mg-NBT	0.901	0.432
1.5 mol% Mg-NBT	0.871	0.553
2.0 mol% Mg-NBT	0.913	0.577
3.0 mol% Mg-NBT	0.851	0.609

4.0 mol% Mg-NBT	0.845	0.583
0.1 mol% Fe-NBT	-	1.113
0.3 mol% Fe-NBT	-	1.199
1.0 mol% Fe-NBT	0.738	0.439
2.0 mol% Fe-NBT	0.896	0.486
3.0 mol% Fe-NBT	0.831	0.533
4.0 mol% Fe-NBT	0.883	0.449
0.1 mol% Al-NBT	-	1.536
0.3 mol% Al-NBT	0.734	0.552
0.5 mol% Al-NBT	0.940	0.395
1.0 mol% Al-NBT	0.913	0.544
2.0 mol% Al-NBT	0.926	0.544
4.0 mol% Al-NBT	0.476	0.568

The thermal evolution reveals a transition from lower towards higher activation energies with increasing temperature in this particular group. This behavior is expected for a transition from extrinsic to intrinsic semiconducting behavior as the reached activation energies (E_a ~ 1.44 eV) are close to half of the band gap for NBT (E_g ~ 2.94 eV).[258] It should be highlighted, that "stoichiometric" NBT was claimed to be ionically conducting by Li *et al.*.[48, 49] The oxygen ionic conductivity was attributed to unintentional Bi-loss during the processing. The here presented results, however, represent a semiconducting, stoichiometric NBT. This impressively underlines the high sensitivity of NBT towards A-site non-stoichiometry. Revealing the origin of the difference in the reported "stoichiometric" NBT[48, 49] and the here presented stoichiometric NBT is part of ongoing research in collaboration with Prof. Dr. Derek C. Sinclair (University of Sheffield, UK) but is out of the scope of this work.

The second group is formed by the higher doped samples. Here, the bulk conductivity is about three orders of magnitude higher compared to the lower doped samples. Additionally, the activation energies are lower and undergo a transition in the opposite direction (from higher E_a = 0.73 eV – 0.95 eV to lower values of E_a = 0.39 eV – 0.58 eV). According to previous results, these compositions are very likely to be oxygen ionic conducting.[48, 50] For the Fe-doped samples, the oxygen ionic conductivity was evidenced by electromotive force measurements which are discussed in more detail in chapter 4.2.6. Also, the obtained activation energies are in accordance with the values found in the literature.[48, 142]

A transition from electronic conduction towards oxygen ionic conduction is therefore confirmed to be doping element and concentration-dependent. Even though, the Fe- and Al-doping should result in similar oxygen vacancy concentrations, the transition from electronic to ionic conduction could be observed for different doping contents (for Mg between 0.2 mol% and 0.5 mol%, Fe between 0.3 mol% and 1.0 mol%, and for Al between 0.1 mol% and 0.3 mol%). This already reveals that the plain concentration of induced oxygen vacancies is not the only factor to describe oxygen ionic conductivity in NBT. With the here presented results the question, if there is a doping element and concentration dependence for inducing oxygen ionic conductivity could already be answered:

Oxygen ionic conductivity is induced by all chosen acceptor dopants. A doping element and concentration dependence for the introduction as well as the resulting absolute values of oxygen ionic conductivity can be detected.

As already discussed in chapter 2.6.2, only free oxygen vacancies can contribute to the conductivity. The Coulomb and mechanical interactions, as well as the contribution of covalent bonding characteristics on the defect association, will be discussed in chapter 4.1.4 in more detail to elucidate the differences of the chosen dopants to each other. Experimentally, the difference could already be highlighted by the concentration dependence of inducing oxygen ionic conductivity. The effective vacancy concentration in Fe-doped NBT must be lower compared to the case of Al-doping resulting in oxygen ionic conductivity at higher doping concentrations. A detailed simulation-based discussion regarding the binding energies of the defect complexes between the dopant and the corresponding oxygen vacancy will be presented in chapter 4.1.4.

The position of the kink in the Arrhenius-type representation is located between 280 °C and 320 °C, independently on the doping element. It is known from the literature that within this temperature region, the rhombohedral and the tetragonal phase coexist.[48, 259] The influence of phases and the phase coexistence on the resulting oxygen ionic conductivity therefore also needs to be considered. The impact of phases on defect association and migration will be discussed in chapter 4.1.3 in more detail.

Another anomaly occurs for the 4.0 mol% Al-doped samples, as the bulk conductivity features no distinct kink in the Arrhenius representation and the obtained bulk conductivity decreases again compared to the lower doped specimens. This behavior can be explained by the formation of secondary phases which can reduce the effective vacancy concentration in the matrix.[135]

To get better comparability of the concentration and doping element dependent conductivity, the obtained bulk conductivities for Mg-, Fe- and Al- acceptor doped NBT compositions are plotted against the doping content at 500 °C (see Figure 4.1.5).

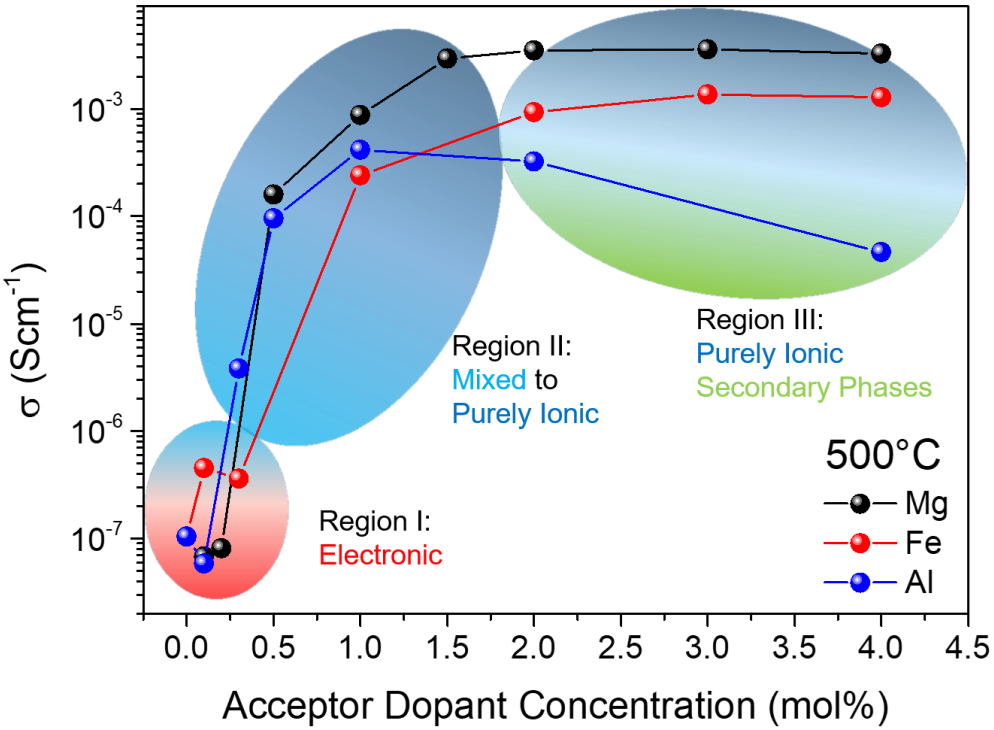

Figure 4.1.5: Bulk conductivity as a function of the acceptor doping content taken at 500 °C for the Mg- (black), Fe- (red) and Al-doped (blue) NBT compositions. The three regions represent the electronic, mixed and ionic conduction region concerning the doping concentration.

This temperature was chosen as it is sufficiently above the transition of the activation energies. The extracted conductivities can be divided into three regions. The first region (I) is represented by low doping contents and is governed by electronic conductivity (low bulk conductivity, activation energy close to half of the band gap value). Doping with Fe leads to an immediate increase in the conductivity which still might be electronic. Based on the presented impedance data (one semicircle, see Figure 4.1.3 (d)) and the calculated activation energies (see Table 4.1-1) this behavior can be attributed to semiconducting behavior in NBT.[48] A discussion on the effects of the different acceptor dopants on the electronic conductivity is provided in chapter 4.1.4 where the density of states for NBT with different doping elements is discussed.

In the intermediate region (II) (0.3 mol% up to 1.5 mol% doping), oxygen ionic conductivity is introduced leading to mixed electronic and finally pure ionic conductivity. A detailed discussion about the introduction of oxygen ionic conductivity for the particular case of Mg-doped NBT is provided in chapter 4.1.3.

In the third region (III), almost purely oxygen ionic conductivity is present which is not changing with higher concentrations of Mg- and Fe-doping in NBT.

The bulk conductivity in the ionic conducting region (III) is lower in the case of Fe-doped NBT. The association energy of the defect complex might, therefore, be higher compared to Mg and Al-acceptor doping (a detailed discussion is provided in chapter 4.1.4). As Mg is divalent while Al is trivalent, the small discrepancy in the absolute values can be explained by the different concentrations of induced oxygen vacancies. A further increase of the Mg-, Fe-doping content above 2.0 mol% does not affect the respective bulk conductivity significantly. Constant conductivity values might, therefore, be caused by the more and more favorable formation of secondary phases. This could directly be evidenced by BSE and EDX analysis for those compositions as the fraction of secondary phases is higher in the Al-doped compositions compared to the Mg- and Fe-doped specimens (see chapter 4.1.1). The secondary phases could also be responsible for the decrease in conductivity for the Al-doped compositions. It is known from the literature that the oxygen vacancy concentration in the matrix can be decreased when secondary phases form.[135]

Up to this point, a close relationship between acceptor doping concentration as well as doping element choice and the resulting oxygen ionic conductivity in NBT could clearly be confirmed experimentally. A suitable explanation of why there is an acceptor doping concentration-dependent jump could not be delivered, yet. Furthermore, the open questions regarding the origin of the kink in the Arrhenius-type plots of ionic conducting NBT concerning a defect complex formation and the coexistence of phases still need to be addressed. To elucidate the impact of defect complex formation and the rhombohedral/tetragonal phase coexistence in NBT, an analytical model is established and discussed in the following chapter which is discussed with the help of computational simulations.

4.1.3 Mg-Doping: Analytical Model

To gain a deeper understanding of the basic defect chemical mechanisms of defect complex formation and the resulting oxygen ion migration leading to the exceptionally high oxygen ionic conductivity in NBT, a theoretical discussion of the experimentally conducted results is essential. In the following, a detailed discussion of the oxygen ionic conductivity is provided for the simplest case of B-site acceptor doping with the divalent acceptor dopant Mg. As already mentioned, the acceptor doping with Mg on the Ti B-site leads to the formation of positively charged oxygen vacancies in order not to violate the charge neutrality condition. Apart from generating additional oxygen vacancies, it is assumed that the Mg dopant forms a defect complex with the respectively generated oxygen vacancy (see chapter 2.6.2). In consequence, the effective vacancy concentration of mobile vacancies will be reduced.[251]

The total vacancy concentration can further be divided into trapped (tr) and free (f) species. It should be highlighted, that only the free vacancies can contribute to the conductivity. The Mg-acceptor dopants are, for instance, considered to be immobile, whether they are trapping (Mg, tr) an oxygen vacancy or not (Mg, f). Trapped oxygen vacancies ($V_O^{\bullet\bullet}, tr$) are also considered to be immobile.

Hence, the total concentration of oxygen vacancies $[V_O^{\bullet\bullet}]_{tot}$ is constant and consists of either free or trapped oxygen vacancies (see equation (4.3)).[251, 253] However, the concentration of free vacancies $[V_O^{\bullet\bullet}]_f$ is a function of temperature.

It needs to be mentioned that, for the reduction of complexity, internal defect reactions are excluded. Apart from surface reactions, changing the oxidation state of oxygen vacancies as well as unintentional Bi loss are major concerns that might occur in reality. To avoid Bi-loss and the resulting additional generation of oxygen vacancies during processing, a slight Bi-excess was included in the starting powder. Furthermore, an electronic contribution by electron–hole pair formation has been excluded as well. Based on those boundary conditions, the defect concentrations can be expressed by the following equations:

$$[Mg_{Ti}'']_f = [V_O^{\bullet\bullet}]_f \,, \tag{4.1}$$

$$[Mg_{Ti}'']_{tr} = [V_O^{\bullet\bullet}]_{tr} \,, \tag{4.2}$$

$$[V_O^{\bullet\bullet}]_{tot} = [Mg_{Ti}'']_{tot} = [Mg_{Ti}'']_f + [\{Mg_{Ti}'' V_O^{\bullet\bullet}\}^x] = C \,. \tag{4.3}$$

As the formation of oxygen vacancies should follow the law of mass action, the equilibrium constant of the association K_{asso} can be determined and free oxygen vacancy concentration $[V_O^{\bullet\bullet}]_f$ can be calculated.[141, 142]

$$K_{asso} = \frac{[\{Mg'_{Ti}V_O^{\bullet\bullet}\}^x]}{[Mg'_{Ti}]_f \cdot [V_O^{\bullet\bullet}]_f} = \frac{C - [V_O^{\bullet\bullet}]_f}{([V_O^{\bullet\bullet}]_f)^2} = \exp\left[\frac{-\Delta H_{asso}}{k_B T} + \frac{\Delta S_{asso}}{k_B}\right]. \tag{4.4}$$

The dopant concentration is represented by C, the association enthalpy by ΔH_{asso}. The configuration entropy of the association ΔS_{asso} includes the six possible orientations of the defect complex. Based on this expression, the free oxygen vacancy concentration $[V_O^{\bullet\bullet}]_f$ can be derived:

$$[V_O^{\bullet\bullet}]_f = -\frac{1}{2 \cdot K_{asso}} \pm \sqrt{\frac{1 + 4 \cdot C}{4 \cdot K_{asso}}}. \tag{4.5}$$

To derive a complete expression of the ionic conductivity, the Nernst-Einstein equation needs to be considered (see also equation (2.41)):

$$\sigma = \frac{D_{V_O^{\bullet\bullet}} \cdot z^2 \cdot F^2 \cdot [V_O^{\bullet\bullet}]_f}{R \cdot T}, \tag{4.6}$$

which is dependent on the diffusion coefficient $D_{V_O^{\bullet\bullet},f}\ (T)$ for oxygen vacancy migration:

$$D_{V_O^{\bullet\bullet},f}\ (T) = \frac{1}{6} \cdot a^2 \cdot Z \cdot \upsilon_0 \cdot \exp\left(\frac{\Delta S_{mig}}{k_B}\right) \exp\left(\frac{-\Delta H_{mig}}{k_B \cdot T}\right). \tag{4.7}$$

The coordination number of an oxygen vacancy is Z = 8. The attempt frequency υ_0 is in the same order of magnitude as the Debye frequency ($\upsilon_0 = 1 \cdot 10^{12}$ Hz). The hopping distance ($a = 2.76$ Å) was determined by averaging the DFT calculations of the distances around the defect for different directions in the rhombohedral phase compared to the equilibrated rhombohedral DFT structure of NBT. The here presented calculations have been provided by Leonie Koch. ΔS_{mig} and ΔH_{mig} represent the migration entropy and enthalpy, respectively. The charge of the vacancies is given by zF where F corresponds to the Faraday constant. The migration entropy ΔS_{mig} was assumed to be negligible.

The migration enthalpy ΔH_{mig} was calculated by DFT calculations and averaged with regards to the possible paths of migration and was kept constant. The association entropy ΔS_{asso} is dependent on the eight-fold coordination of the vacancy and was also kept constant. The ionic conductivity calculated with the remaining, temperature independent, fitting parameter ΔH_{asso} (see equation (4.4)) is given in Figure 4.1.6.

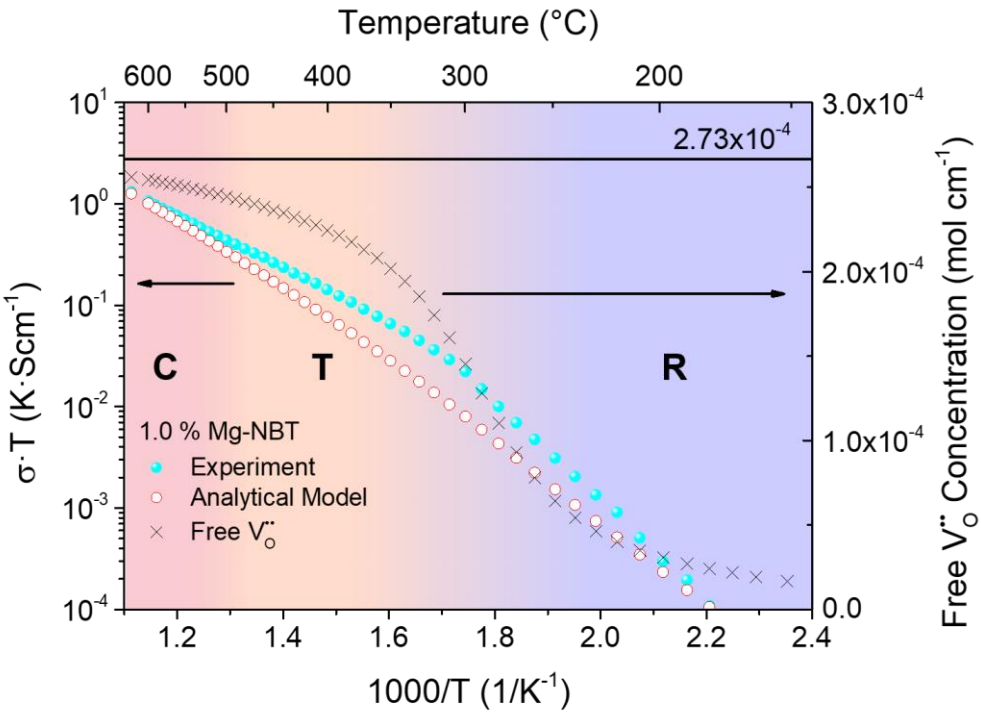

Figure 4.1.6: Conductivity model for the 1.0 mol% Mg-doped NBT composition. The experimental data is represented by the filled bowls (cyan), the analytical model data (ΔH_{asso} = 0.45 eV) by empty circles (red). The horizontal black line illustrates the total Mg-doping concentration, the black crosses represent the free oxygen vacancy concentration vs. temperature. The background colors indicate the specific phase within the temperature range (R for rhombohedral, T for tetragonal, C for cubic).

By calculating the ionic conductivity with constant parameters for ΔH_{mig}, ΔS_{asso} and a temperature-independent association enthalpy ΔH_{asso} of the defect complex (red empty circles), the kink, observed in the experimental data (cyan bowls), is not resolvable. This model, however, partly answers the question, if defect complexes are responsible for the change in activation energy. The defect complex formation and the resulting effective (free) oxygen vacancy concentration on its own is not sufficient to explain the kink in the Arrhenius-type plots. To address the question about the impact of the coexistence of rhombohedral and tetragonal phases[177] in the region where the kink in the Arrhenius plots could be located, a detailed discussion on the influence of different phases on the conductivity relevant parameters are provided in the following section.

4.1.3.1 Analytical Model: Phase Dependence of Ionic Conductivity

A possible explanation of why the applied model cannot resolve the experimental results is the fact that, so far, only a constant kinetic parameter was used which was independent of the crystal structure. Hence, the analytical model needs to be improved by including different kinetic parameters for the different occurring rhombohedral and tetragonal phases as well as the coexistence of phases.[177] To describe the phase coexistence, a probability function f is used to tune the impact of the specific phase dependent kinetics:

$$f\left(\frac{1}{T}\right) = \frac{1}{\exp\left(\frac{\left(\frac{1}{T}\right) - \mu}{k_B \cdot steepness}\right) + 1}. \tag{4.8}$$

The variables μ and $steepness$ were chosen as such, that this function was comparable to the experimentally measured phase fractions for the coexistence of phases, obtained by Jones et al. [177] The association enthalpy ΔH_{asso} can therefore be expressed as a fraction of the activation energies in the rhombohedral (ΔH_{rhom}) and the tetragonal (ΔH_{tet}) phase:

$$\Delta H_{asso} = \Delta H_{tet} + (\Delta H_{rhom} - \Delta H_{tet}) \cdot \left(1 - f\left(\frac{1}{T}\right)\right). \tag{4.9}$$

The probability function is here expressed by f. Four different parameters are used to describe the migration and association in the rhombohedral and the tetragonal phase $\Delta H_{mig,rhom}$, $\Delta H_{asso,rhom}$, $\Delta H_{mig,tet}$ and $\Delta H_{asso,tet}$, respectively. With regards to previous studies by Meyer and Albe, the averaged migration energies are almost independent on the phase with a value of $\Delta H_{mig,rhom}$ = $\Delta H_{mig,tet}$ = 0.5 eV.[259] This is only valid for averaging the migration enthalpies. Concerning the migration direction, those are, of course, different. According to DFT calculations, the association energies for $\Delta H_{asso,rhom}$ and $\Delta H_{asso,tet}$ are temperature (phase) dependent.

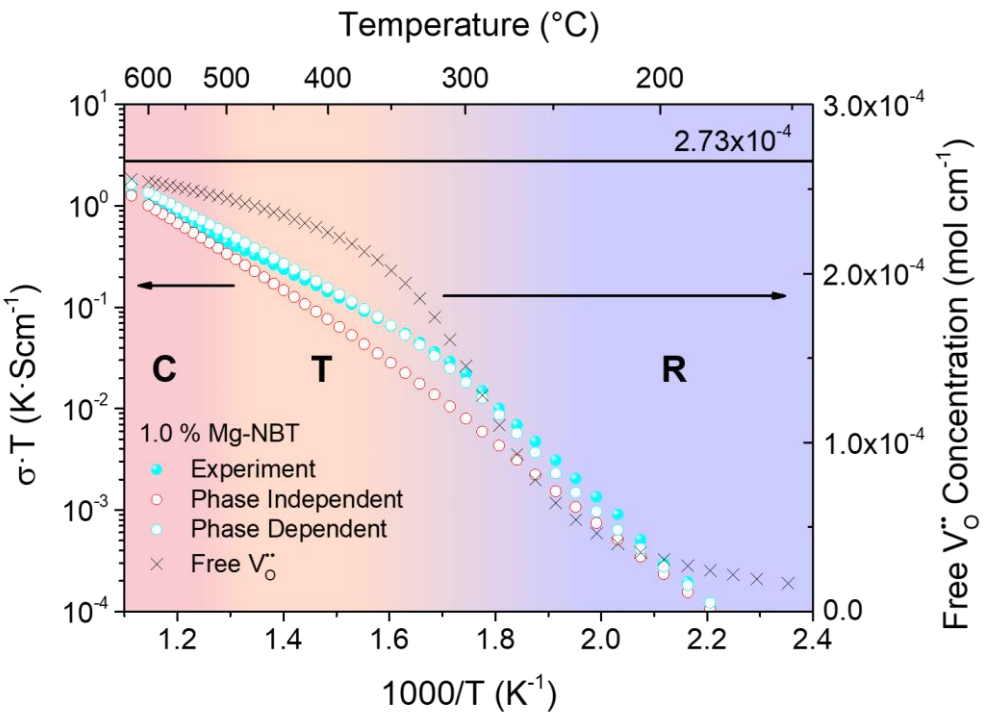

Figure 4.1.7: Conductivity model for the 1.0 mol% Mg-doped NBT composition. The experimental data is represented by the filled bowls (cyan), the phase independent model data ($\Delta H_{asso,tet}$ = $\Delta H_{asso,rhom}$ = 0.45 eV) by empty circles (red) and the phase-dependent model data ($\Delta H_{asso,tet}$ = 0.1 eV and $\Delta H_{asso,rhom}$ = 0.45 eV) by empty circles (cyan). The horizontal black line illustrates the total Mg-doping concentration, the black crosses represent the free oxygen vacancy concentration vs. temperature. The background colors indicate the specific phase within the temperature range (R for rhombohedral, T for tetragonal, C for cubic).

Fitting with the respective parameters $\Delta H_{asso,rhom}$ = 0.45 eV and $\Delta H_{asso,tet}$ = 0.1 eV delivered the best results and is in good agreement with the already reported DFT data by Meyer and Albe.[259] In Figure 4.1.6, the measured, as well as the calculated conductivities by the here presented model, are given. The calculated conductivities include the phase dependence for 1.0 mol% Mg B-site acceptor doped NBT (empty cyan circles). The enhanced model which includes the coexistence of phases and the resulting variation of association energies coincides well with the experimental data. Hence, the observed kink in the Arrhenius-type plot can be explained by the temperature, thus phase, dependent association energies. The still remaining deviations between the experimental and the model data could be explained by the averaging over local configurations. It is worth mentioning that, even at high temperatures, the free vacancy concentration never equals the acceptor dopant concentration. Hence, there is always a certain fraction of trapped vacancies present in the investigated temperature range. For the case of 1.0 mol% Mg-doping, this model delivers proof that defect complexes are forming in NBT between the acceptor and the corresponding oxygen vacancy.

4.1.3.2 Analytical Model: Doping Concentration Dependence of Ionic Conductivity

Aside from the coexistence of phases, the variation of acceptor doping concentration led to the largest change in oxygen ionic conductivity for oxygen conducting ceramics (see experimental data provided in chapter 4.1.2). This concentration dependence should also be resolvable with the here established model if the defect association is assumed to be independent on the acceptor doping concentration and further only depends on the changing free vacancy concentration $[V_O^{\bullet\bullet}]_f$. In order to elucidate, if the model also holds for different doping concentrations, it was attempted to reproduce the experimental data for the 0.5 mol% and 1.5 mol% Mg B-site acceptor doped NBT as well. The corresponding experimental and model data are given in Figure 4.1.8.

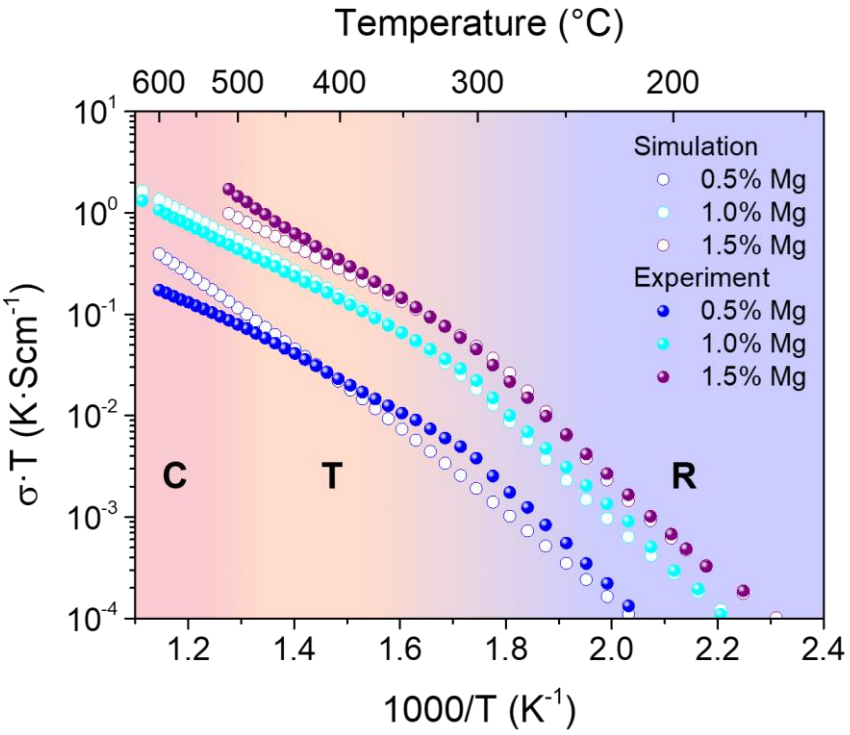

Figure 4.1.8: Phase dependent conductivity model (empty circles) with $\Delta H_{asso,tet}$ = 0 eV and $\Delta H_{asso,rhom}$ = 0.39 eV for the 1.5 mol% Mg-doped, $\Delta H_{asso,tet}$ = 0.1 eV and $\Delta H_{asso,rhom}$ = 0.45 eV for the 1.0 mol% Mg-doped and $\Delta H_{asso,tet}$ = 0.51 eV and $\Delta H_{asso,rhom}$ = 0.55 eV for the 0.5 mol% Mg-doped NBT directly compared with the experimental data (bowls). The background colors indicate the specific phase within the temperature range (R for rhombohedral, T for tetragonal, C for cubic).

The DFT calculations revealed, that the association energies decrease with increasing doping concentration. For the 1.5 mol% Mg-doped case the best fit was gained by setting the parameters $\Delta H_{asso,tet}$ = 0 eV and $\Delta H_{asso,rhom}$ = 0.39 eV. For the 0.5 mol% Mg-doped case, the parameters were set to $\Delta H_{asso,tet}$ = 0.51 eV and $\Delta H_{asso,rhom}$ = 0.55 eV. The model holds for sufficiently high dopant concentration. However, the high-temperature model data for the 0.5 mol% Mg-doped NBT varies notably from the experimentally obtained data.

This might be an indication that the plain phase transition could not sufficiently explain the concentration and temperature dependent ionic conductivity. Even though, the migration enthalpies ΔH_{mig} should exhibit a doping concentration dependence, the model reveals that the concentration-dependent association ΔH_{asso} delivers the major contribution to the resulting conductivity. Hence, the approximation of the average association energy is too drastic.

The association energy of the defect complex is therefore directly related to the acceptor dopant concentration. It should be highlighted, that the association energies for the rhombohedral and the tetragonal phase tend to align with decreasing the doping concentration. Additionally, those values are very sensitive concerning the choice of the corresponding migration energies. A distinct trend can be extracted: By increasing the dopant concentration, the association becomes weaker. This is the complete opposite behavior which would have been expected for other well-known ceramics.[142, 153, 260]

According to the concentration dependence of the association energies, it can be assumed that, apart from electrostatic interactions, also mechanical interactions like elastic strains and defect volume due to the size difference of the Mg ions and Ti ions might have a noticeable impact.

To receive a deeper insight, if the binding energy between the defects decreases by increasing the defect concentration, the binding energies of a magnesium ion and a corresponding oxygen vacancy with another present magnesium ion are provided in Figure 4.1.9. The values for the presented distance-dependent binding energies have been processed with the help of DFT calculations. As the number of atoms is restricted for a DFT calculation, the concentration dependence needs to be resolved by changing the distances and investigating the resulting interactions.

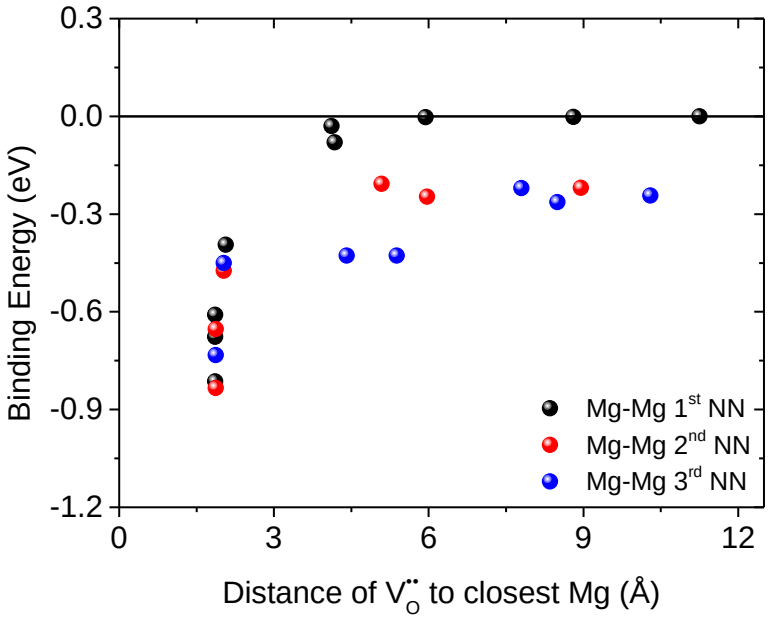

Figure 4.1.9: Binding energy of a defect complex against the distance to another present Mg ion based on density functional theory calculations. The black, red and blue bowls represent the 1st, 2nd and 3rd nearest neighbor (NN) shell, respectively.

The here given values display the results of ab initio calculations for different simulated Mg defect-vacancy arrangements by changing the Mg-Mg distances of the other present Mg ion at the first, second or third nearest neighbor (NN) position. The association enthalpy becomes more and more short-ranged with decreasing the distance between the two Mg ions (which is equivalent to increasing the doping concentration). Furthermore, a direct relationship between the defect concentrations and the effective diffusion properties have already been provided in literature where a defect lattice with a lattice constant of the mean defect-defect distance was proposed.[141, 261] The here presented calculations reveal that the dopant-oxygen association increases by increasing the distance between the dopants. The reduction of the association energy might occur due to an interplay of electrostatic and mechanical interactions. Concerning the concentration dependence, this equivalently means that increasing the acceptor doping concentration results in a weakening of the defect associate.

4.1.4 Acceptor Doped NBT: Molecular Orbital Considerations

The origin of a varying electronic conductivity for low doping concentrations (until 0.3 mol%, depending on the doping element) between the three investigated acceptor dopants Mg, Fe, and Al could not be resolved so far. Taking into account the here presented defect model (see chapter 4.1.3), the respective phase, as well as the association energy of the defect complex, are responsible for the change in mobility and effective concentration of oxygen vacancies resulting in a change of the observable oxygen ionic conductivity.

Nevertheless, Mg-, Al-and Fe-doped NBT differ in their electrical conductivity over the whole investigated concentration range (see chapter 4.1.2). According to the concept of formal charges, at least Fe and Al should behave similarly (trivalent dopants). The size difference of the ionic radii, resulting in elastic strains, and the consequences on the formation and strength of a defect dipole might also be crucial for a better understanding of the observed differences. Furthermore, the covalent bonding contribution could vary dependent on the doping element choice. The following considerations are utilized to derive a doping dependent hierarchy of covalent contributions, Coulomb interactions, as well as electrostatic and mechanical interactions.

The question remains: What is the difference between Mg, Al, and Fe with regards to their association with an oxygen vacancy? An approach to address this question includes the characteristics of the surrounding atoms in the bulk. The relaxation of the dopant due to the presence of an oxygen vacancy in its vicinity influences the covalent proportion as well as the stability of chemical bonds and is an essential factor concerning migration barrier calculations for different phases.

To analyze the covalent contribution of chemical bonding environments, the post-processing tool LOBSTER was used[249], allowing to investigate crystal orbital hamiltonian populations (COHPs) based on a plane-wave code calculation.

To describe the principle of constructing COHPs, the simple case of hydrogen atoms is considered in more detail.[262] In one crystallographic direction, the atoms can be seen as a linear chain. Each atom exhibits its characteristic atomic orbital within the chain. Those atomic orbitals overlap. In an ideal combination of e.g. 1s orbital overlaps, only bonding states (in-phase) e.g. by spin up configuration are present at low energies characterized by a positive overlap population. At higher energies, alternating spin up and spin down configurations might be present between neighboring atomic orbitals. This is characterized by antibonding (out-of-phase) combinations with a negative overlap population. A bonding indicator can, therefore, be easily be constructed by generating an overlap, population-weighted, density of states resulting in the so-called crystal orbital overlap population (COOP).

The COOP results from multiplying the density of states with the overlap population. This allows for partitioning the electron density into bonding, nonbonding and antibonding states. To go one step further, the DOS can not only be weighted by the overlap population, but also by the corresponding element of the Hamiltonian. This results in a partitioning of the band structure energy (for COHPs), instead of the electrons (COOP). It should be noted, that in the COHP consideration, positive values provide antibonding states and negative values bonding states, respectively.[262]

The here presented calculations have been prepared by Leonie Koch and are part of her dissertation. In the following, those results which highlight the effect of crystal orbital interactions between the acceptor dopant and the surrounding bulk atoms on the apparent electrical conductivity are summarized. For a more detailed discussion, the reader is referred to the work of Leonie Koch.

At first, the projected density of states (DOS) for all atoms of interest has been investigated in <111> direction for the rhombohedral symmetry (see Figure 4.1.10). The DOS calculations should provide useful information to elucidate possible electronic contributions by forming defect states within the band gap. The configuration of an oxygen vacancy which resides on the nearest neighbor position of the dopant will be used. The density of states for the corresponding dopant (black), bismuth (orange for the s orbital and red for the p orbital), titanium (green) and oxygen (blue) is provided. The contribution of sodium is almost identical in all configurations and does not impact the electronic conductivity notably. With the help of calculating DOS for the three different doping elements Mg, Fe, and Al, the electronic contribution of the dopants can be elucidated.

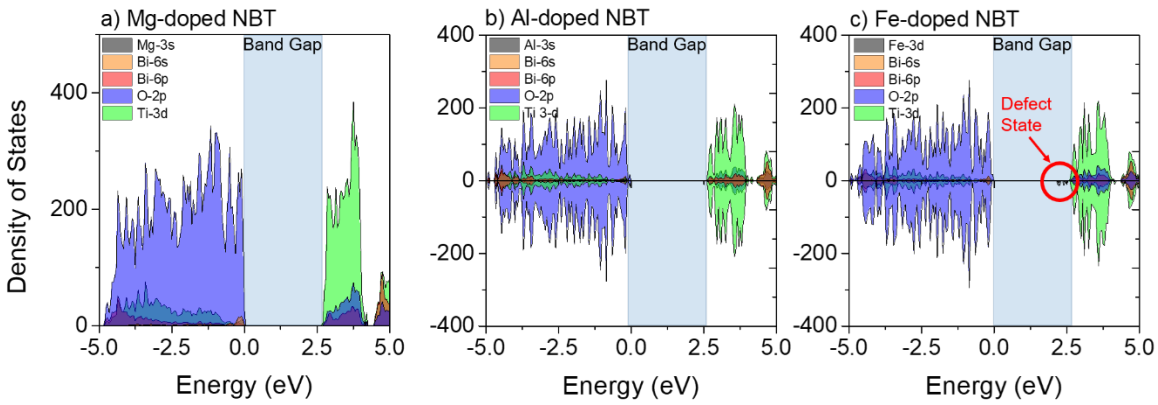

Figure 4.1.10: Calculated density of states for the Mg- (a), Al- (b) and Fe-doped NBT (c). The band gap is depicted in grey. Additional defect states within the band gap are highlighted with a red circle in the case of Fe-doped NBT in (c).

The density of states for the Mg-doped NBT (depicted in Figure 4.1.10 (a)) exhibits energy states which are far below or above the band gap. There is no change in the band gap with regards to the calculated value of pure NBT. The density of states calculated for Al-doped NBT reveal a similar distribution as for Mg-doped NBT. The band gap is not affected (depicted in Figure 4.1.10 (b)). The largest change occurs for the incorporation of a Fe dopant (depicted in Figure 4.1.10 (c)). Additional states are present in the band gap close to the conduction band edge between 2.2 eV and 2.5 eV resulting in a larger electron density in this region. In consequence, this efficiently leads to a change of the Fermi level and might be responsible for the experimentally observed increased electronic conductivity at low Fe-doping concentration (see chapter 4.1.2). The experimental data revealed an immediate increase of the conductivity only for the case of low Fe-doping concentrations which could additionally be attributed to electronic conductivity. The here presented DOS point in the same direction. Concerning the molecular orbitals of Mg (3s orbital), Al (3s orbital) and Fe (3d orbital), the largest overlap with the surrounding oxygen orbitals can be detected for the Fe-doped case. Fe exhibits the most comparable electronic configuration compared to the substituted Ti atom which also provides a d orbital. For the case of Mg and Al, a lower overlap could be observed which, in consequence, might disturb the electronic conductivity in those particular cases due to weaker interactions. The here presented results provide sufficient explanation to resolve the high levels of electronic contributions for the case of Fe-acceptor doping. The provided calculations on Mg- and Al-doping in NBT do not provide evidence for a detectable change of the density of states.

The investigation of the density of states can only be used to resolve the apparent changes in the acceptor dopant dependent electronic conductivity. With the help of COHP calculations, the specific chemical bonding environments can be investigated to derive the covalent contribution of defect association. The bond length distribution concerning the doping element choice directly affects the defect association resulting in different oxygen ionic conductivity.

The COHP calculations presented for the different electron spins (spin up in blue and spin down in red) in Figure 4.1.11 represent a dopant (either Mg (a), Al (b) or Fe (c)) residing on the Ti-site with five surrounding oxygen atoms (representing a defect complex with an oxygen vacancy in its nearest neighborhood). The difference in the oxygen bonds can be visualized by the COHPs itself. Bonding states lead to a stabilization of the dopant-oxygen bonds, antibonding states destabilize the dopant-oxygen bonds. This results in a lower association.

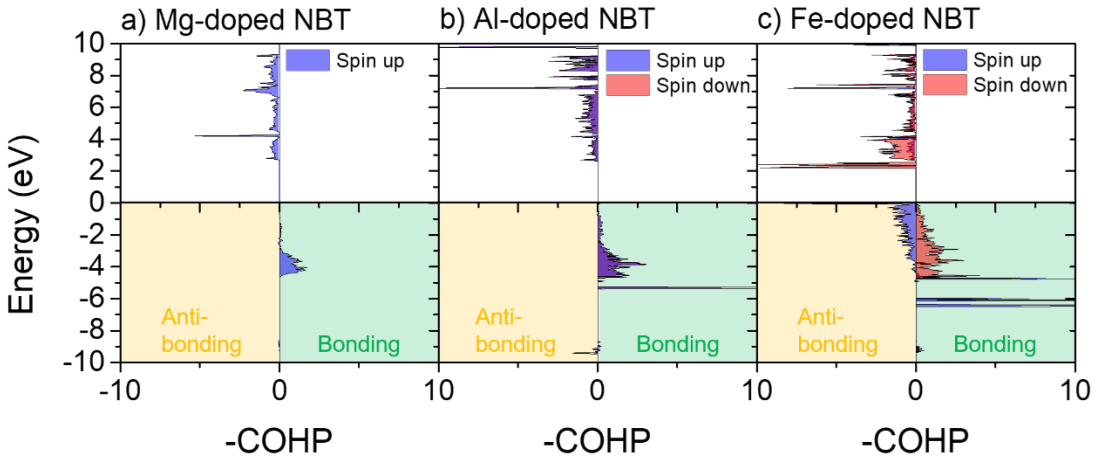

Figure 4.1.11: Calculated Crystal Orbital Hamiltonian Populations (COHPs) for Mg- (a), Al- (b) and Fe-doped (c) NBT. The colored boxes represent the bonding and antibonding states. The Fermi level is presented by the zero energy state.

The COHP calculations reveal that Mg exhibits a lower bonding contribution to the oxygen vacancy than Al with regards to bonding states (states within the green area). The largest contribution to bonding states can be detected in the case of Fe-doping. Mg- as well as Al-doping, do not provide evidence for large contributions of antibonding states (states within the yellow area). Fe-doping leads to a remarkably larger amount of antibonding states which are, also, close to the Fermi level. The first approximation of directly comparing the fraction of antibonding and bonding states is, however, misleading. For better comparability, the area of bonding and antibonding states can be integrated and subtracted from each other (resulting in integrated COHPs, iCOHP).

The integrated COHPs revealed that Mg exhibits the lowest contribution of bonding states (iCOHP value of -5), followed by Fe-doping (iCOHP value of -10). It turned out that Al exhibits the largest contribution of bonding states (iCOHP value of -22). Based on the so calculated iCOHPs, a hierarchy for the covalent contribution on the defect association for the different acceptor dopants can be estimated:

$$\boldsymbol{Covalent}: Al\ (iCOHP = -22) > Fe(iCOHP = -10) > Mg(iCOHP = -5)\ . \qquad (4.10)$$

If only the covalent contributions would be taken into account, Mg-doping would have resulted in a considerably larger oxygen ionic conductivity compared to the other dopants Al and Fe. The experimentally observed differences are, however, considerably low (see chapter 4.1.2). Besides covalent contributions, Coulomb interactions are expected between the dopant and the local oxygen coordination. The electrostatic interactions can easily be estimated by the relative formal charges of the dopant substituting the Ti-site. Based on the formal charges, the following hierarchy for defect association can be established:

$$\boldsymbol{Coulomb}: Mg^{2+} > Al^{3+} = Fe^{3+}\ . \qquad (4.11)$$

Magnesium is divalent which would in principle result in a larger Coulomb interaction with surrounding oxygens compared to the trivalent Al and Fe. If the electrostatic Coulomb interactions are also taken into account, the experimentally observed results can further be rationalized. Additionally, the ionic radii of the incorporated dopants differ from the substituted Ti. This results in elastic energy contributions which can, at least, not completely be neglected. For mechanical interactions following hierarchy can be assumed based to the ionic radii of the doping elements at the corresponding Ti-site (Mg = 72 pm, Fe = 64 pm, Al = 53 pm):[206]

$$\boldsymbol{Mechanical}: Mg(72\ pm) > Fe(64\ pm) > Al(53\ pm)\ . \qquad (4.12)$$

Those contributions could additionally influence the resulting defect association energy with different weighing. The experimentally observed oxygen ionic conductivities for the 0.5 mol% Mg-, 1.0 mol% Fe- and 1.0 mol% Al-doped NBT compositions (see chapter 4.1.2) are directly compared to each other. Please note that, due to charge compensation, the 0.5 mol% Mg-doped NBT should ideally result in the same oxygen vacancy concentration than the 1.0 mol% Fe- and Al-doped NBT compositions.

The doping concentration dependence of the association energy (see chapter 4.1.3.2) is neglected at this point but definitely provides another contribution. Based on these considerations following hierarchy can be established:

$$\boldsymbol{Experiment}: \sigma_b(Al) > \sigma_b(Fe) > \sigma_b(Mg)\,. \tag{4.13}$$

The defect association energy should, therefore, be the lowest for Mg, followed by Fe and Al.
The following weighting to the effective defect association between covalent, Coulomb and mechanical contributions can, therefore, be derived as follows:

$$\boldsymbol{Contribution\ Hierarchy}: Mechanical > Coulomb > Covalent\,. \tag{4.14}$$

This hierarchy is at least a qualitative approximation for the weighting of different contributions on the resulting defect association energy. It needs to be highlighted, that the previously discussed dopant concentration dependence was neglected which could also provide an additional contribution to the case of Mg-doping. The association energy for the 0.5 mol% Mg-doped NBT is considered to be larger compared to the 1.0 mol% (based on the discussion in chapter 4.1.3.2).
The here presented results of the calculated DOS can explain the electronic conductivity at low doping concentrations for the case of Fe-doping. The COHP calculations highlighted notable, doping element dependent differences in the bonding character of the defect complex. Electrostatic and mechanical interactions deliver an additional contribution to the association energy. Apart from the here presented contributions, a doping concentration dependence of the resulting association energy could also be confirmed in chapter4.1.3.2.

4.1.5 Defect Complexes in Al-doped NBT: NMR Analysis

To receive experimental evidence for the formation of defect complexes, Al-doped samples have been investigated with the help of nuclear magnetic resonance spectroscopy (NMR). The here presented results have been provided by Dr. Pedro Groszewicz who also performed all of the here presented NMR measurements. With the help of NMR analysis, the local coordination of the NMR active element (Al) can be derived. The ^{27}Al nucleus has a non-zero spin which is directly associated with a non-zero magnetic dipole moment and therefore is NMR active.[263-266] Whether an oxygen atom position is vacant in the nearest neighbor position, this results in a detectable chemical shift of the aluminum atom. The resulting peak shifts have been determined with the help of DFT calculations and compared to the experimental data. Besides detecting defect complexes between an Al dopant and a generated oxygen vacancy, the coordination number can be estimated. This allows for the detection of secondary phases (of the form AlO_4) on the one hand. On the other hand, NMR can deliver direct evidence, if the incorporated Al dopant resides on the A-site (12 fold coordination) or the B-site (6-fold coordination). In Figure 4.1.12, the NMR spectra for the here processed Al-doped NBT samples are depicted with varying doping concentrations.

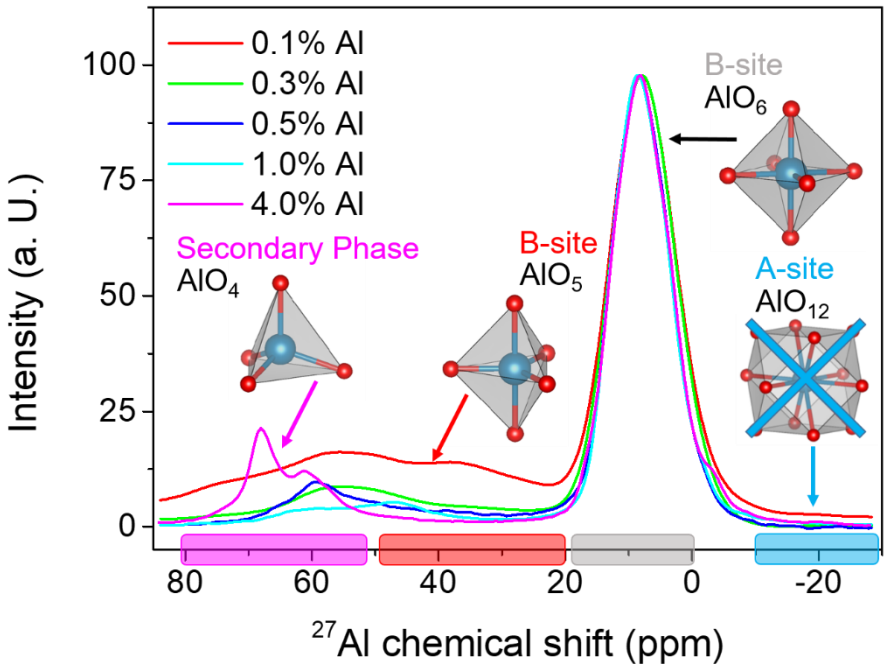

Figure 4.1.12: Al-NMR spectra of Al-doped NBT with varying doping concentration. The AlO_x orientation is given by the resulting ^{27}Al chemical shifts (denoted with colored boxes at the x-axis).

The characteristic chemical shifts resolving the different AlO_x configurations are illustrated with colored bars at the x-axis based on existing literature.[267-269] The presented spectra reveal, that the incorporated Al-dopants reside on the B-site as no chemical shift between -10 and -30 ppm can be detected (blue bar).[267-269] The highest intensity is reached at a chemical shift between 0 ppm and 20 ppm which can be attributed to Al with 6-fold oxygen coordination representing the B-site (grey bar). Unreacted Al_2O_3 can be excluded as the NMR signal would exhibit a peak at a chemical shift of 16 ppm.[270] Chemical shifts between 20 and 50 ppm are characteristic for 5-fold coordination, representing one vacant oxygen site (red bar).[269] This coordination is attributed to a defect complex between the Al-dopant and an oxygen vacancy. Especially, 0.1 mol% Al-doped NBT exhibits a large intensity and a broad peak in this range. Increased intensity is also observable for 0.3 mol%, 0.5 mol%, and 1.0 mol% but to a lesser extent. Chemical shifts between 50 ppm and 80 ppm are characteristic for Al with a 4-fold oxygen coordination and is attributed to a AlO_4 secondary phase (pink bar).[269] A peak with high intensity is detectable for the 4.0 mol% Al-doped composition. This finding coincides well with the already detected Al-rich secondary phases with the help of SEM and EDX analysis (see chapter 4.1.1). With the help of the here presented results, the following conclusions can be drawn. Al-doping results in effective B-site doping. A doping concentration-dependent formation of defect complexes could experimentally be evidenced what precisely represents the previously made assumptions (see also chapter 4.1.3.2). The exact ratio between trapped and free oxygen vacancies can, however, not be estimated exactly. For the case of completely trapped oxygen vacancies, the integrated area under the AlO_5 (20 to 50 ppm) and the AlO_6 (0 to 20 ppm) peak, must have been equal. This could not be resolved as the AlO_5 peak is too broad and overlaps with the peak for secondary phases of the form AlO_4 (50 to 80 ppm). Furthermore, a doping content of 4.0 mol% leads to the formation of secondary phases which can be supported by the previously provided results.

4.1.6 Application Perspective: Grain Versus Grain Boundary

As presented in chapter 4.1.1, secondary phases are apparent at the grain boundaries. This might have a significant effect on the defect chemistry of the respective material region, resulting in different electrical conductivity. Figure 4.1.13 depicts the Arrhenius-type representation of the concentration-dependent total admittance (bulk and grain boundary responses, represented by colored bowls) in direct comparison with the respective grain boundary admittance (represented by empty circles) for Mg-, Fe- and Al-acceptor doped NBT. The admittance Y was chosen for comparison reasons, as the conductivity needs to be normalized with the dimensions of the material region which is challenging to determine for a grain boundary.

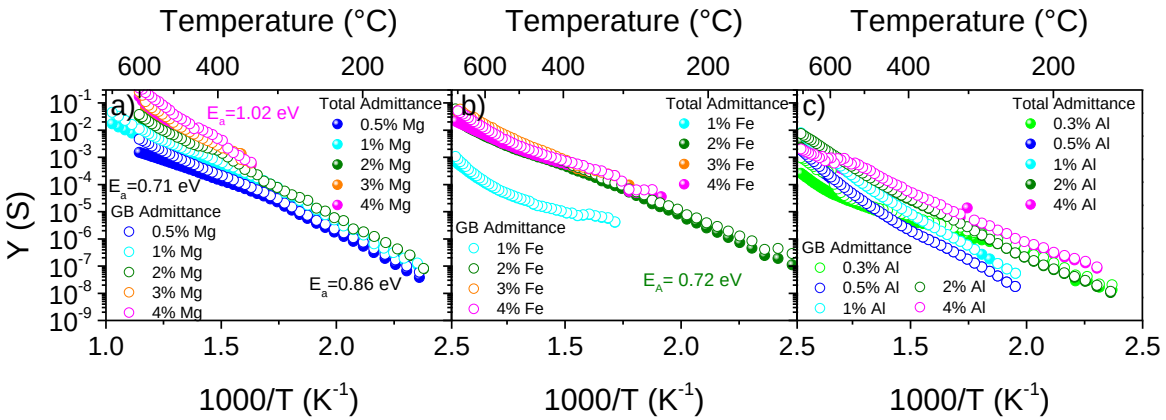

Figure 4.1.13: Total Admittance Y (colored bowls) in direct comparison with the grain boundary admittance (empty circles) of the Mg- (a), Fe- (b) and al-doped (c) NBT compositions; only compositions which have featured a distinct grain boundary response are depicted.

Not every acceptor doped composition exhibited a distinguishable bulk and grain boundary response. Therefore, only those compositions are depicted providing a clearly distinguishable grain boundary response at the corresponding temperature. It should be noted, that the evaluation of the grain boundary is particularly challenging, as an overlap with the bulk response (high frequency) as well as the electrode response (low frequency) might occur. An analysis in a more qualitative fashion should at least be possible.

The admittance of the grain boundary response and the total admittance are similar and, in certain cases, almost completely overlap. This is especially the case for highly doped Mg- and Al-doped NBT (see Figure 4.1.13 (a) and (b), respectively). Compared to the bulk conductivity, discussed in chapter 4.1.2, the Arrhenius plots do not present a very pronounced kink.

The resulting activation energies for Mg-doped NBT (Figure 4.1.13 (a)) range from E_a ~ 0.8 eV – 0.9 eV (for temperatures below 300 °C) to E_a ~ 1.0 eV for 4.0 mol% Mg-doped NBT (above 350 °C). The activation energies fit well to an oxygen ion migration process.[271] For Fe-doped NBT (Figure 4.1.13 (b)), the calculated activation energies are slightly lower (E_a = 0.72 eV for the 2.0 mol% Fe-doped NBT sample). For Al-doped NBT Figure 4.1.13 (c)), the total admittance and the grain boundary admittance almost completely overlap. This leads to the conclusion, that the grain boundary admittance is the governing factor for the charge carrier migration in the oxygen ionic conducting species.

No very pronounced kink can be detected for the grain boundary admittance, resulting in homogeneous activation energy over the whole investigated temperature range. The higher values could result from a larger migration barrier across the grain boundary.[152]

With regards to a possible application as ceramic membranes in SOFCs, the total conductivity is more relevant than the plain bulk conductivity.[53, 58] Grain boundaries are often seen as an impeding factor as the charge carrier mobility can be hindered by lower diffusion properties at grain boundaries.[272-275]

To get an impression, if the here presented acceptor doped NBT compositions are applicable e.g. as ceramic membranes in SOFCs, the total conductivities are plotted for the ionic conducting compositions and are directly compared to conductivity values for the commercially most relevant oxygen ion conductor yttria-stabilized zirconia $Zr_{0.92}Y_{0.08}O_{1.96}$ (YSZ) in Figure 4.1.14.[48]

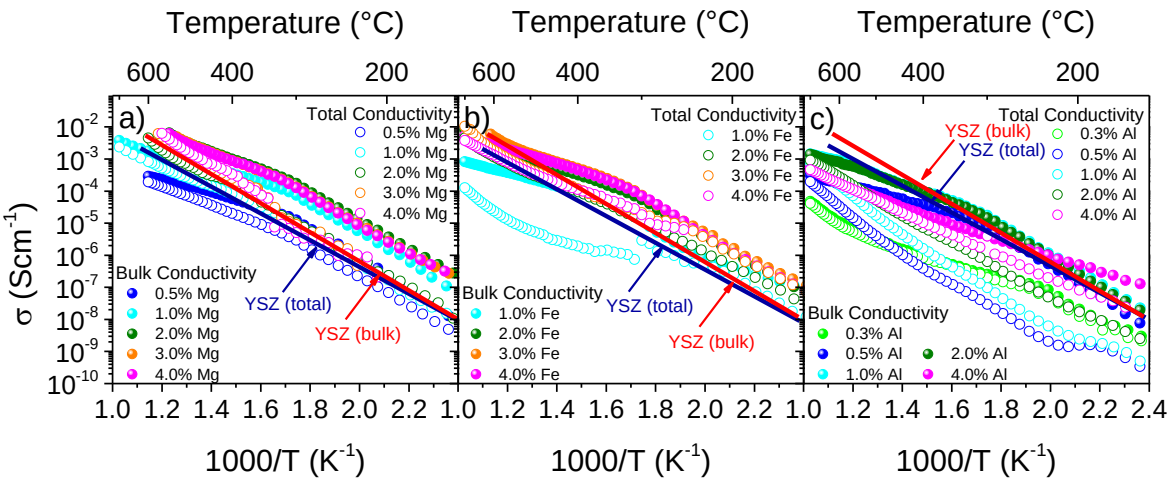

Figure 4.1.14: Total conductivity and bulk conductivity of oxygen ionic conducting acceptor doped NBT compositions. The bulk conductivity values for YSZ (red) are extracted from ref.[48], the total conductivity values of polycrystalline YSZ (blue) are extracted from ref.[276]

The bulk (colored bowls) and total conductivities (colored empty circles) of the acceptor doped NBT samples are overlapping for lower doping contents at large enough temperatures.

The observed kink for the bulk conductivity is, however, not as pronounced in the case of the total conductivities. The bulk conductivity of Mg-doped NBT above 1.0 mol% doping (see Figure 4.1.14 (a)) is one order of magnitude larger compared to YSZ in the observed temperature region. The values of the bulk oxygen ionic conductivity are already at the theoretical limit based on the oxygen-vacancy diffusion coefficient predicted in literature.[252] It should be noted, that the bulk and total conductivity of YSZ do not differ as much as observed for the acceptor doped NBT compositions.[48, 135, 276] The total conductivities are, nevertheless, in the same order of magnitude as YSZ for those compositions. 4.0 mol% Mg-doped NBT even exceeds the conductivity values reached for YSZ above 320 °C. [48, 196] The Fe-doped NBT samples (above 2.0 mol% doping content), presented in Figure 4.1.14 (b), feature higher total conductivities at low temperatures up to 280 °C. Concerning a possible application, those compositions exhibit the most interesting electrical properties. It needs to be mentioned, that Sr-doping at the A-site results in the highest reported oxygen ionic conductivity values.[135] From an application point of view, further enhancement can, therefore, be expected. Based on existing literature, acceptor doped NBT compositions can, thus, be considered as promising electrolyte materials for intermediate temperature SOFCs.[48, 135, 196] Al-doping in NBT results in lower total conductivities compared to Mg- or Fe-doping (see Figure 4.1.14 (c)). As already discussed, Al-doped NBT tends to form secondary phases for higher doping contents. At low doping contents, the total conductivity is about 3 orders of magnitude lower compared to the plain bulk conductivity. The grain boundaries therefore exhibit ion blocking properties.

Those results elucidate that the total conductivity needs to be considered concerning a possible application as the grain boundary conductivity is the governing parameter for oxygen ionic conductivity and could significantly differ from the bulk conductivity values. Further, it could be highlighted that, in the case of increased doping concentrations, the grain boundary conductivity can noticeably be enhanced even though the bulk conductivity stays nearly unaffected (see Figure 4.1.4 for comparison). It should be noted, that especially the grain boundary modification was not as extensively studied as the bulk conductivity modification, yet. Based on this, enhancing the total oxygen ionic conductivity of NBT can be expected by precise modification of the grain boundary properties in the future.

4.1.7 Defect Chemistry of Acceptor doped NBT: Summary

Temperature-dependent impedance analysis confirmed a doping concentration-dependent decrease of the bulk resistivity by about four orders of magnitude for all acceptor dopants (see chapter 4.1.2). The formation of two semicircles enables a distinction between bulk and grain boundary responses. Arrhenius-type representation of the bulk conductivity revealed that two different groups are forming, depending on the doping content. At low doping concentrations, semiconducting behavior with activation energies close to half of the band gap value and low bulk conductivity is apparent. At higher doping concentrations, oxygen ionic conductivity dominates paired with lower activation energies and high bulk conductivity. The transition from electronic towards oxygen ionic conductivity is dependent on both, the doping concentration and doping element itself. By comparing the doping element-specific bulk conductivities concerning the doping concentration, three different regions can be observed.

In the first (low doping concentration) region, electronic conductivity dominates. Compared to the undoped NBT composition, low doping contents with Fe result in an immediate increase of the conductivity while low doping concentrations with Mg and Al result in slightly lower conductivity. Based on DOS calculations, additional electronic states could be detected for the case of Fe-doping (see chapter 4.1.4) which affects the Fermi level. The second region defines the transition from electronic to oxygen ionic conductivity where the concentration, as well as the mobility of oxygen vacancies, is large enough to result in extremely high ionic conductivity.

The analytical model to resolve the oxygen ionic conductivity in the case of Mg-doped NBT confirmed the formation of defect complexes and their influence on the effective vacancy concentration. Furthermore, a phase, as well as concentration dependence of the defect association energy could be evidenced (see chapter 4.1.3). It should be highlighted, that the defect association energy decreases with increasing the doping concentration. This behavior is unique when compared to other well-studied lead-based and lead-free systems and underlines the uniqueness of the defect chemistry in NBT. ^{27}Al-NMR analysis of the Al-doped samples delivered experimental proof for the doping concentration-dependent formation of defect complexes. Effective B-site acceptor doping could also be confirmed as no Al was incorporated on the A-site (see chapter 4.1.5).

Depending on the acceptor dopant species, the values of oxygen ionic conductivity differ. The impact of covalent contributions, Coulomb and mechanical interactions on the association energy of the forming defect complex have been investigated.

The presented results, therefore, lead to the following conclusion (see chapter 4.1.4):

The largest covalent contribution to the defect association can be found for the case of Al-doping followed by Fe and Mg (based on integrated COHP calculations). The Coulomb interaction should be highest in the case of the divalent Mg and equal for the case of trivalent Fe- and Al-doping. Based on the ionic radii, the mechanical interactions are assumed to be highest for Mg, followed by Fe and Al. Concerning the experimental data, the following hierarchy for the impact on the resulting defect association could be derived: The mechanical interactions influence the association energy the most, followed by electrostatic Coulomb interactions and covalent contributions. At this point, the already confirmed concentration dependence of the defect association was neglected. This should further affect the resulting defect association.

The third region describes the saturation of oxygen ionic conductivity paired with a formation of secondary phases. In this region, the mobility and concentration of oxygen vacancies can be seen as constant in the bulk. The XRD analysis, combined with a detailed SEM and EDX investigation revealed the occurrence of secondary, liquid, phases forming in all acceptor doped NBT compositions. The solubility limit is directly dependent on the used doping element. While secondary phases form above 3.0 mol% in the case of Mg-doping, the Fe- and Al-doped samples already exhibit secondary phases at around 2.0 mol% and 1.0 mol%, respectively. With the help of EDX analysis, the secondary phases have been confirmed to be enriched with the respective doping element (see chapter 4.1.1).

The here presented results deliver proof for the concept of defect complex formation in acceptor doped NBT experimentally and theoretically. The origin of a concentration-dependent change from semiconducting towards ionic conducting behavior could be elucidated. Controlling the oxygen ionic conductivity is, therefore, possible by precisely adjusting either the acceptor dopant or its concentration.

Concerning a possible application as a ceramic membrane in SOFCs, the Fe-doped NBT provides the most suitable electrical properties (see chapter 4.1.6). It should be noted, that the total conductivity in all cases was mainly restricted by the decreased grain boundary conductivity. Increased doping concentrations lead to an increase of the total conductivity while the bulk conductivity stays nearly unaffected above the solubility limit of the respective dopant. Further enhancement of the total conductivity can be expected especially by the grain boundary modulation of acceptor doped NBT as this circumstance was not studied in more detail so far.

4.2 Defect Chemistry in NBT-Based Solid Solutions: NBT-6BT

4.2.1 A-Site Non-Stoichiometric NBT-6BT

Besides acceptor doping on the B-site (see chapter 4.1), it is known from literature that A-site non-stoichiometry has a tremendous effect on the occurring electrical conductivity in NBT.[48, 49] Bismuth vacancies, either created deliberately by A-site non-stoichiometry or by Bi-loss during the processing, act as acceptors resulting in a notable increase of oxygen vacancy concentration in NBT ($2Bi_{Bi}^{x} + 3O_{O}^{x} \leftrightharpoons 2V_{Bi}^{'''} + 3V_{O}^{\bullet\bullet} + Bi_2O_3 \uparrow$).[48] Already minor changes around 1.0 mol% are sufficient to completely change the conduction mechanism from semiconducting towards oxygen ionic conducting behavior resulting in orders of magnitude higher bulk conductivity.[49]

Apart from the impact of A-site non-stoichiometry on the electrical properties, other studies more focus on the microstructural development combined with the resulting electromechanical properties. In these studies, NBT-based ceramics are investigated concerning an increased oxygen vacancy concentration which might be introduced due to not violating the charge neutrality condition when negatively charged Bi-vacancies are present.[27, 156-158, 223, 233, 277, 278] Based on these findings, it is vital to get a better understanding regarding the defect chemistry in NBT-based ceramics to control and enhance the dielectric as well as piezoelectric and ferroelectric properties.

With regards to ferroelectric and piezoelectric applications, the solid solution (1-x)($Na_{0.5}Bi_{0.5}$)TiO_3-x$BaTiO_3$ (NBT-xBT) is one of the best choices as it has already been widely studied and exhibits excellent electromechanical properties at the morphotropic phase boundary (MPB) between x= 0.06 and x= 0.07.[34, 41, 207, 212, 279-281] The general features of NBT-BT have already been described in chapter 2.11.1. A better understanding of the defect chemical interactions in such systems could result in an increased tunability and reproducibility. The impact of A-site non-stoichiometry on the electrical, ferroelectric and piezoelectric properties has already been discussed in the literature.[28, 282-285] Qiao and Chen *et al.* reported that oxygen vacancies which are introduced by A-site non-stoichiometry in NBT-6BT influence the dielectric loss as well as the ferroelectric and piezoelectric properties notably.[284, 285] The effects are, however, not as drastic as for the basic system NBT. Especially the impact of oxygen vacancies on the conductivity as well as the ferroelectric and piezoelectric properties has not been understood sufficiently so far. While NBT is highly sensitive towards A-site non-stoichiometry, this seems not to be the case for NBT-6BT.[48, 49]

A-site non-stoichiometry could be utilized to further enhance the ferroelectric and piezoelectric properties, as long as no high levels of oxygen ionic conductivity will be introduced with this approach. Otherwise, NBT-6BT would not be a favorable ferroelectric material anymore. The questions which should be addressed in this chapter are:

- What is the impact of A-site non-stoichiometry on the electrical properties NBT-6BT?
- How high is the change of the dielectric, ferroelectric and piezoelectric properties with A-site non-stoichiometry?
- Is the phase purity and microstructure of NBT-6BT significantly affected by A-site non-stoichiometry?

To fill this gap of knowledge, this chapter will provide a detailed discussion about the systematic change in A-site non-stoichiometry in the NBT-6BT, MPB solid solution with regards to phase purity, microstructure, electrical conductivity, dielectric, ferroelectric and piezoelectric properties. The following work was done in close collaboration with Dr. In-Tae Seo and has already been published as a Journal of the American Ceramic Society feature article.[62]

In detail, the effects of A-site non-stoichiometry on the microstructure of NBT-6BT have been investigated covering XRD to check the phase purity, SEM in the SE and BSE mode to investigate the grain morphology and the possible occurrence of secondary phases combined with an EDX analysis of occurring secondary phases. The electrical properties have been investigated with the help of temperature-dependent impedance spectroscopy. Furthermore, the resulting dielectric properties have been investigated with the help of temperature dependent permittivity measurements. Additionally, the ferroelectric and piezoelectric properties are presented to address the previously stated questions.

4.2.2 A-Site Non-Stoichiometric NBT-6BT: Microstructure

N_xB_yT-6BT samples with different variations of the Na/Bi ratio at the A-site were processed and investigated concerning their phase purity with the help of XRD to address the question if the phase purity is affected by A-site non-stoichiometry.

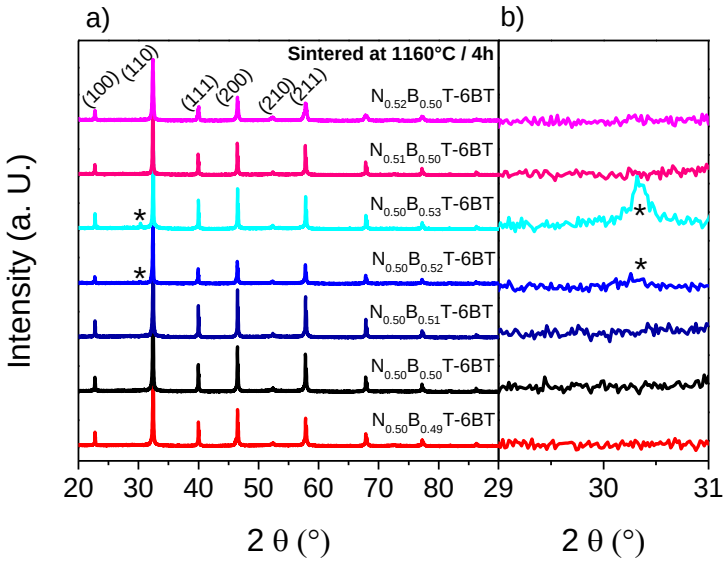

Figure 4.2.1: XRD pattern of the A-site non-stoichiometric N_xB_yT-6BT samples with x= 0.50, 0.51, 0.52 and y= 0.49, 0.50. 0.51, 0.52 and 0.53 (a) and detailed scan (b); the stars denote additional peaks caused by secondary phases.

The XRD pattern (see Figure 4.2.1) illustrates that the $R3c$-group perovskite structure could be obtained for all processed specimens at room temperature.[177, 178, 255, 256] A small amount of secondary phases could, however, be detected in the $N_{0.50}B_{0.52}T$-6BT which further evolves for the $N_{0.50}B_{0.53}T$-6BT composition (denoted with a star). This secondary phase can be attributed to a Bi-rich composition which exhibits a layer type structure such as $Na_{0.5}Bi_{4.5}Ti_4O_{15}$ or $BaBi_4Ti_4O_{15}$.[286, 287] This finding will be supported later in this chapter by EDX analysis of the secondary phases.

During processing, an undeliberate loss of Bi_2O_3 and Na_2O is expected for elevated temperatures during the calcination and sintering leading to a formation of Bi and Na vacancies. Because of this, a Bi-excess in the starting powder should compensate for the Bi_2O_3 losses during the processing. It should be noted, that the formation of Bi vacancies might be favored because of Bi_2O_3 exhibits a lower evaporation temperature (above 825 °C) than Na_2O (above 1132 °C).[233, 288]

As the samples were sintered at temperatures only slightly above the evaporation temperature of Na_2O (the samples were sintered at 1160 °C), the Bi evaporation is assumed to be by far more pronounced in terms of introducing vacancies which will be compensated by the formation of oxygen vacancies. A formation of secondary phases is initiated when the Bi addition exceeds a value of 2.0 mol%.

For the basic system NBT, it is already known that the addition of Na_2O to the starting powder results in a, in total, Bi-deficient ceramic exhibiting high levels of oxygen ionic conductivity combined with the formation of Na-rich secondary phases.[49] For the here processed compositions, a Na-rich phase could be detected via EDX analysis which was not registered by the XRD pattern of compositions with Na-excess in the starting powders. To get a deeper insight into which secondary phases have formed concerning either Na- or Bi-excess starting powders, Table 4.2-1 provides the EDX analysis results performed for the matrix and occurring secondary phases for the $N_{0.50}B_{0.53}$T-6BT and the $N_{0.51}B_{0.50}$T-6BT compositions.

Table 4.2-1: EDX analysis of the matrix and secondary phase found in Bi-excess ($N_{0.50}B_{0.53}$T-6BT) and Na-excess ($N_{0.51}B_{0.50}$T-6BT) compositions.

	$N_{0.50}B_{0.53}$T-6BT		**$N_{0.51}B_{0.50}$T-6BT**	
	Matrix (at%)	Secondary Phase (at%)	Matrix (at%)	Secondary Phase (at%)
Bi	25.47	47.86	25.46	19.16
Na	26.41	6.74	26.63	48.42
Ti	44.90	40.63	43.95	29.05
Ba	3.22	4.78	3.96	3.37
Total	100	100	100	100

In the case of 3.0 mol% Bi-excess, a secondary phase with a larger Bi content compared to the matrix composition could be evidenced validating the already made assumption that Bi_2O_3 which has not reacted during the processing leads to the formation of secondary phases. Furthermore, a Na-rich secondary phase could be observed in the 1.0 mol% Na-excess starting composition. To address the question regarding phase purity in A-site non-stoichiometric N_xB_yT-6BT, these results reveal a large sensitivity towards an off-stoichiometry in the starting compositions.

To further investigate the impact of A-site non-stoichiometry on the microstructure, a detailed SEM analysis was carried out.

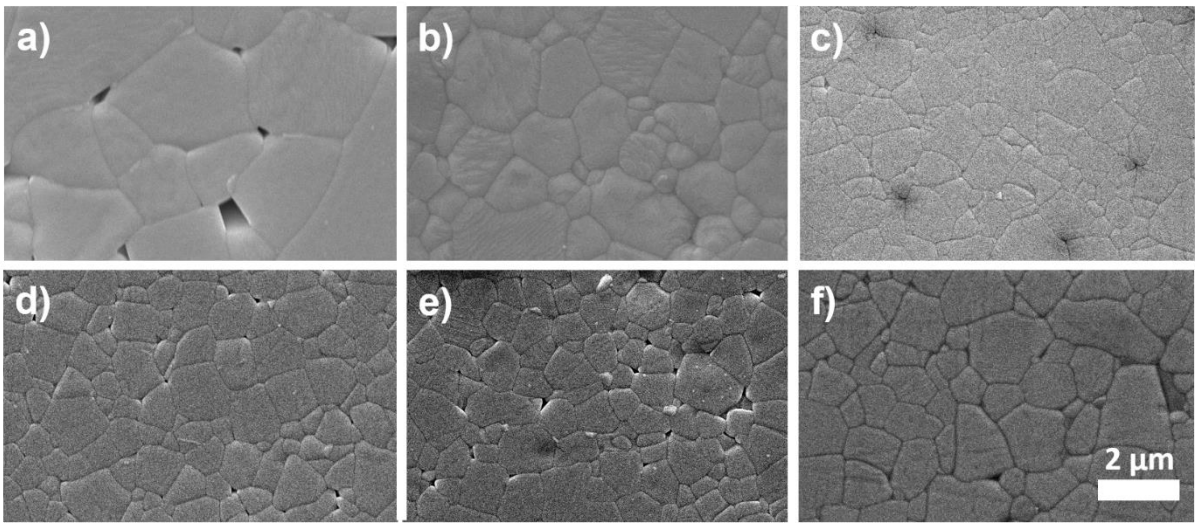

Figure 4.2.2: SEM images of A-site non-stoichiometric N_xB_yT-6BT compositions with (a) x= 0.50, y= 0.49; (b) x= 0.50, y= 0.50; (c) x= 0.50, y= 0.51; (d) x= 0.50, y= 0.52; (e) x= 0.50, y= 0.53 and (f) x= 0.51, y= 0.50 in secondary electron (SE) mode.

Figure 4.2.2 depicts the SEM images of different N_xB_yT-6BT ceramics in SE mode. It should be noted, that all processed ceramics exhibit a relative density of about 96 % or higher. Bi-excess leads to a homogeneous, fine-grained microstructure (grain size ~ 1.2 µm) while Bi-deficiency leads to grain coarsening with an average grain size of about 2.5 µm. This finding reveals a direct relationship between grain size and A-site non-stoichiometry. A possible explanation is provided by literature where a grain boundary roughening leads to a higher grain boundary mobility resulting in increased grain growth.[223] The oxygen vacancy concentration seems to be the responsible factor as Bi-deficiency should be compensated by the generation of additional oxygen vacancies.

It is reported for BT, that the morphology of grain boundaries changes from faceted to rough.[236, 289] Subsequently, the compositions with Bi-excess, presumably resulting in a lower oxygen vacancy concentration, exhibit a lower driving force for grain boundary movement and hence exhibit a smaller grain size. Na-excess however, which was expected to feature roughly the same behavior than the Bi-deficiency, as reported for NBT with regards to the conductivity, does not provide a very pronounced effect on the grain size evolution compared to the stoichiometric composition.[49] This hints towards a low or almost negligible impact of Na-excess in NBT-6BT. The SEM analysis in BSE mode combined with EDX provided evidence that secondary phases are already present with a rather small Na-excess of 1.0 mol%. According to Li *et al.*, Na-excess in NBT also leads to the formation of secondary phases but additionally, the matrix remains Bi-deficient and exhibits high levels of oxygen ionic conductivity.[49] From this point of view, the minor impact of Na-excess is rather unexpected in NBT-6BT.

4.2.3 A-Site Non-Stoichiometric NBT-6BT: Electrical Properties

To further elucidate the impact of non-stoichiometry on the electrical properties a detailed impedance analysis has been conducted. Figure 4.2.3 represents the impedance spectra in Nyquist representation for the Bi- and Na-variation at 500 °C measured from 0.1 Hz to 3 MHz. In Figure 4.2.3 (a), the effect of Bi non-stoichiometry is illustrated, in (b) the Na non-stoichiometric samples are given.

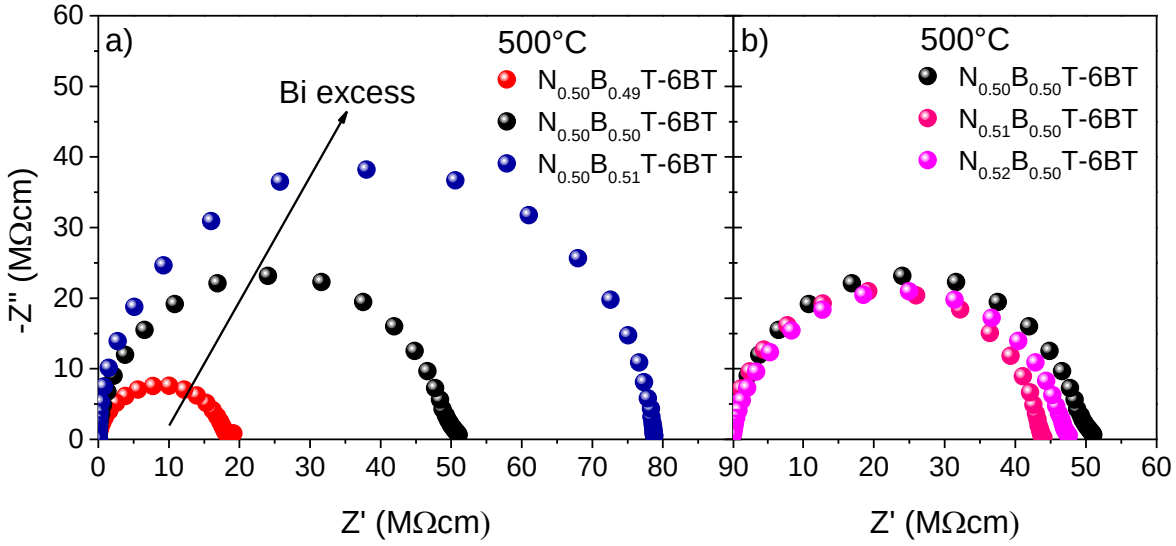

Figure 4.2.3: Impedance spectra of the Bi-varied (a) and Na-varied (b) N_xB_yT-6BT samples in Nyquist representation at 500 °C from 0.1 Hz to 3 MHz.

Only one semicircle can be detected for all processed compositions which could be attributed to the bulk response of each composition, respectively. Semiconducting behavior can be expected (see also chapter 4.1.2). Bi-excess leads to an increase in the resistivity by a factor of 1.5 to a value of R_b ~ 78 MΩcm. Bi-deficiency leads to a decrease of the bulk resistivity to R_b ~ 18 MΩcm with respect to the stoichiometric NBT-6BT composition (R_b ~ 51 MΩcm). The Na variation does not exhibit such a pronounced effect. Furthermore, 1.0 mol% Na-excess should have led to similar results than a 1.0 mol% Bi-depletion with respect to NBT which is not the case for NBT-6BT.[49] Li *et al.* reported for the basic system NBT, that a Bi-deficiency, as well as a Na-excess of about 1.0 mol%, leads to a three orders of magnitude higher conductivity at 500 °C.[49] Additionally, two semicircles could be observed, representing a change from semiconducting towards ionic conducting behavior. Moreover, an electrode polarization response, typical for oxygen ionic conductors, could also not be detected for low measuring frequencies which would have been an indication of an ionic migration mechanism.[257]

This finding is rather unexpected but reveals a considerably lower sensitivity towards A-site non-stoichiometry on the electrical properties. A detailed discussion of the activation energies is necessary to elucidate if the conduction mechanisms have changed in N_xB_yT-6BT similarly to the NBT system.

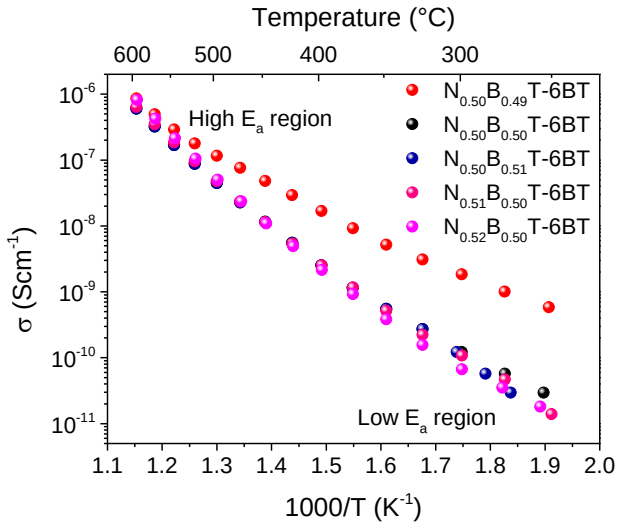

Figure 4.2.4: Arrhenius-type plots for the temperature dependent bulk conductivity of the A-site non-stoichiometric N_xB_yT-6BT compositions.

Arrhenius-type plots of the previously presented compositions are provided in Figure 4.2.4 to evaluate the temperature evolution of the bulk conductivity and to calculate the respective activation energies. A change in the slopes can be detected for all depicted compositions at ~ 375 °C. The transition from lower towards higher activation energies has already been seen for the semiconducting NBT species and represents a change from extrinsic to intrinsic semiconducting behavior (see chapter 4.1). In Table 4.2-2 the corresponding activation energies are given.

Table 4.2-2: Calculated activation energies of different N_xB_yT-6BT compositions below and above the temperature dependent transition.

Composition	E_a (below 375 °C)	E_a (above 375 °C)
$N_{0.50}B_{0.49}T$-6BT	0.63	0.97
$N_{0.50}B_{0.50}T$-6BT	0.88	1.39
$N_{0.50}B_{0.51}T$-6BT	1.08	1.39
$N_{0.51}B_{0.50}T$-6BT	0.94	1.41
$N_{0.52}B_{0.50}T$-6BT	0.98	1.51

Almost no change in the activation energies concerning the Na/Bi ratio variation could be observed. As already assumed by the grain size analysis, the contribution of Na-excess is also negligible with regards to the resulting conductivity. The only composition showing a noticeable deviation is $N_{0.50}B_{0.49}$T-6BT. The activation energy gets remarkably lowered to E_a ~ 0.97 eV compared to E_a ~ 1.39 eV for the stoichiometric composition at elevated temperatures. The calculated activation energies for the other processed compositions are in the range of E_a ~ 1.39 eV – 1.51 eV beyond the transition which represents roughly half of the bandgap value reported in the literature for NBT-6BT obtained from ultraviolet-visible spectroscopy analysis.[258]

Therefore, it can be concluded that intrinsic semiconducting behavior is evident at elevated temperatures for those compositions. Before the transition, for instance, the activation energies are lower with about 0.9 eV. This value is attributed to the oxygen vacancy movement in ionic crystals.[257, 271] Nonetheless, an increase of the oxygen vacancy concentration should not result in such low activation energy observed for the $N_{0.50}B_{0.49}$T-6BT (~ 0.63 eV). Based on those findings, an extrinsic, semiconducting behavior is more probable to be the corresponding conduction mechanism. Defect states seem to be present within the bandgap of the material which behaves as donors and/or acceptors influencing the Fermi level of the material (see chapter 2.7.1).

For the case of the Bi-deficiency, a minor contribution of oxygen ionic conductivity cannot be ruled out completely as the activation energy at elevated temperatures is significantly below the intrinsic value. This composition can possibly be seen as a mixed electronic/ionic conductor.

The presented Arrhenius plots deliver proof, that the impact of Na/Bi variation on the electrical conductivity of the solid solution NBT-6BT is by far less prominent as it could have been observed in the basic system NBT.[49] A minor change in the conductivity is detectable for Bi-deficient samples.

4.2.4 A-Site Non-Stoichiometric NBT-6BT: Dielectric, Ferroelectric, and Piezoelectric Properties

The effective concentration of oxygen vacancies is not large enough to result in oxygen ionic conductivity. However, the oxygen vacancy concentration is, indeed, changing concerning A-site non-stoichiometry, as already presented by the grain coarsening effects in chapter 4.2.2. Those oxygen vacancies might affect the dielectric and electromechanical properties, even though extreme oxygen ionic conductivity cannot be induced. The temperature-dependent dielectric permittivity and loss for poled Bi non-stoichiometric N_xB_yT-6BT samples ((a) to (e)) are provided in Figure 4.2.5.

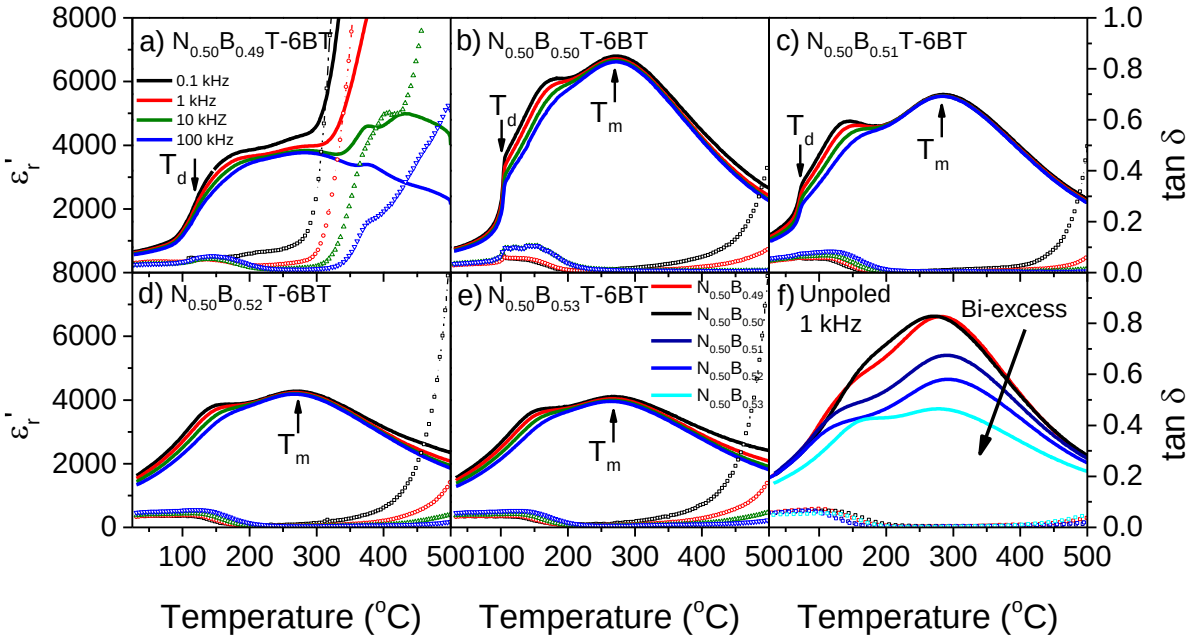

Figure 4.2.5: Temperature-dependent permittivity ε_r' and dielectric loss factor $\tan\delta$ for the Bi- non-stoichiometric N_xB_yT-6BT in the pre-poled state (3 $kVmm^{-1}$) ((a) to (e)) from 25 °C to 500 °C. The temperature of maximum permittivity T_m, as well as the depolarization temperature Td, are depicted with an arrow. The unpoled permittivity and loss response of the respective compositions (legend in (e) are compared concerning the Bi content in (f).

All investigated samples exhibit two dielectric anomalies, the depolarization temperature T_d and the temperature of maximum permittivity T_m. Furthermore, a frequency dispersion can be detected above T_d, resulting from the relaxor properties of NBT-6BT.[290] Below T_d, the induced ferroelectric long range order by poling is observable for $N_{0.50}B_yT$-6BT with y= 0.49, 0.50, 0.51 resembling the non-ergodic relaxor state. Above T_d, the ergodic state is reached as the induced ferroelectric long-range order collapsed. The depolarization temperature is in this case closely related to the freezing temperature T_{fr} which is defined as the temperature where the material properties transform from the ergodic to the non-ergodic state.[10, 290-293]

Compared to the other processed compositions, $N_{0.50}B_{0.49}$T-6BT exhibits the highest T_d with about 119 °C. With increasing the Bi content, T_d shifts towards lower temperatures and could not even be resolved for the $N_{0.50}B_{0.52}$T-6BT and the $N_{0.50}B_{0.53}$T-6BT specimens as it shifted below room temperature.

Previous reports attribute this behavior to an interaction of PNRs with oxygen vacancies.[285] In detail, the depolarization is inhibited by the presence of oxygen vacancies and, as a result, the transformation from a non-ergodic/ferroelectric to an ergodic relaxor behavior occurs at increased temperatures. A direct relationship between the induced oxygen vacancy concentration and the resulting relaxor behavior could, therefore, be confirmed in NBT-6BT. In contrast, a decreased oxygen vacancy concentration should shift T_d towards lower temperatures. This behavior can precisely be observed for the present compositions and further supports the hypothesis of a variation of the oxygen vacancy concentration concerning Na/Bi variation. As a consequence, the dielectric response and the present PNRs in NBT-6BT are more sensitive towards an A-site non-stoichiometry and the resulting increase of oxygen vacancies than the electrical conductivity. This can further be supported by the $N_{0.50}B_{0.50}$T-6BT and $N_{0.51}B_{0.50}$T-6BT compositions, as both exhibit the similar electrical conductivity and activation energies but show a distinguishable dielectric response (see Figure 4.2.6)

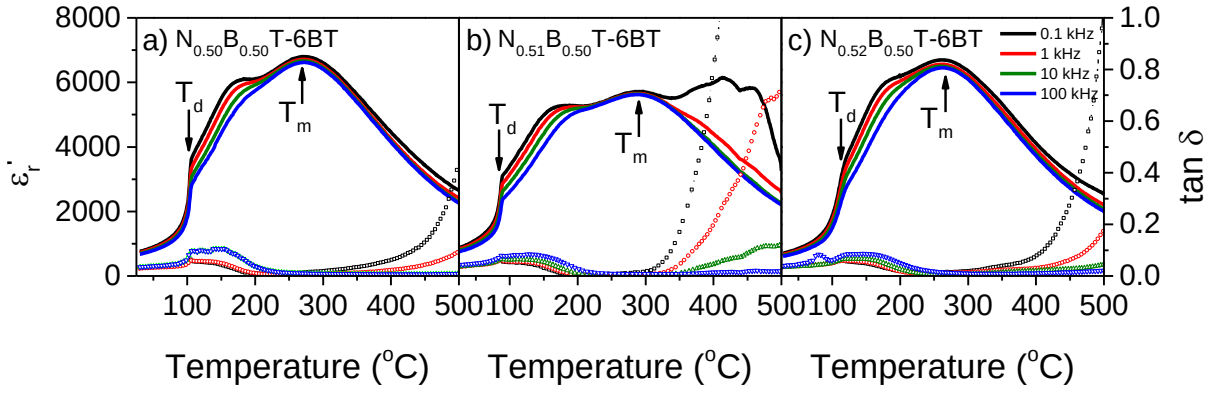

Figure 4.2.6: Temperature-dependent permittivity ε_r' and dielectric loss factor $\tan\delta$ for the Na- non-stoichiometric N_xB_yT-6BT samples after poling at 150°C with 3 kVmm^{-1} from 25 °C to 500 °C ((a) to (c)). The temperature of maximum permittivity T_m, as well as the depolarization temperature Td, are depicted with an arrow.

With the here presented results, a strong correlation between the A-site non-stoichiometry induced oxygen vacancies and the relaxor nature of NBT-6BT could be evidenced.

The changing depolarization temperature already hints towards a different large signal response with regards to A-site variation. A noticeable effect on the temperature-dependent polarization and strain responses is expected.

Figure 4.2.7 depicts the polarization and strain response of the processed N_xB_yT-6BT compositions at room temperature ((a) and (d)), near the depolarization temperature ((b) and (e)) as well as above the depolarization temperature ((c) and (f)) at a maximum applied field of 6 kVmm^{-1}.

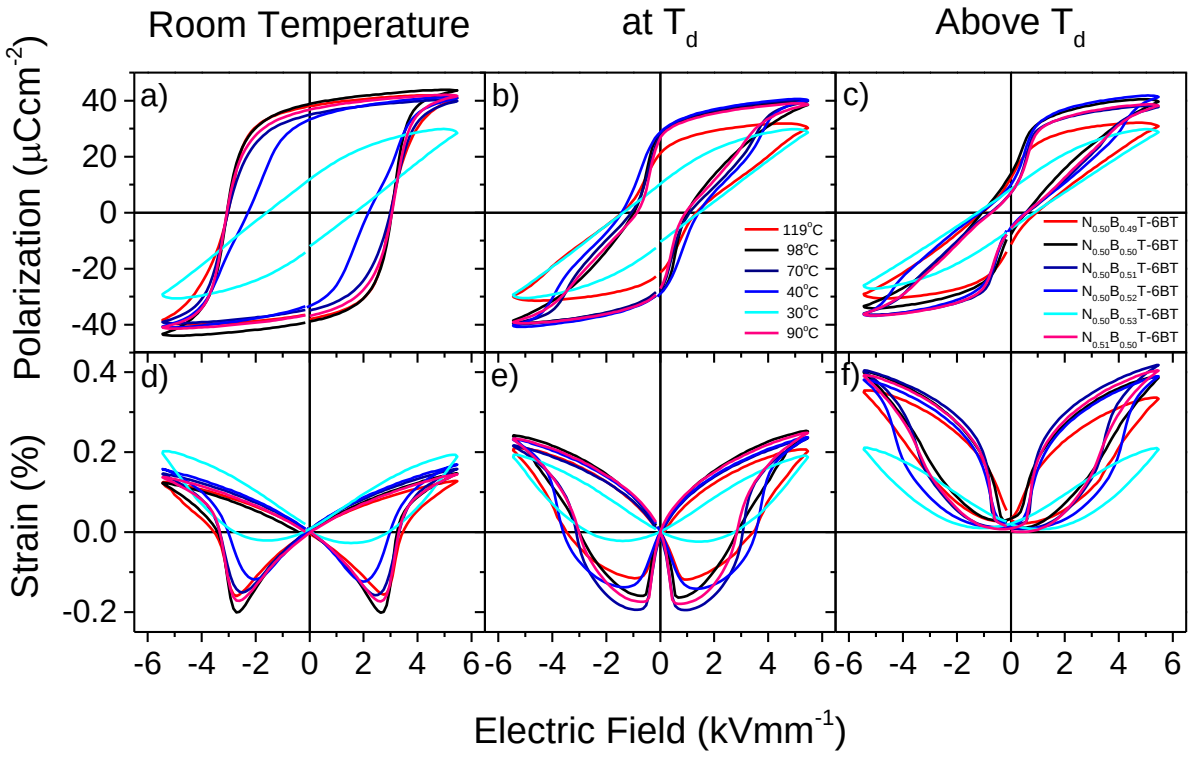

Figure 4.2.7: Temperature-dependent polarization and strain responses for the N_xB_yT-6BT compositions below ((a) and (d)), near ((b) and (e)) and above ((c) and (f)) the depolarization temperature T_d. The measurements in (b) and (e) are taken at different temperatures which can be taken from the legend in (b).

At room temperature, all samples, except $N_{0.50}B_{0.53}T$-6BT, exhibit a typical ferroelectric polarization and strain response resulting in a high remanent polarization and a butterfly-shaped strain hysteresis resembling non-ergodic relaxor behavior. The coercive field, however, decreases with increasing Bi content. Additionally, the negative strain of those compositions decreases and the strain curves change from a butterfly towards a sprout shape. Near T_d (please find the corresponding temperatures in the legend in (b), as T_d differs for each composition), the shape of the polarization response shifts towards a pinched loop while the strain curve shows a more sprout shaped hysteresis. This can be explained by a collapse of the ferroelectric long-range order, irreversibly induced by the electric field in the non-ergodic state, into the ergodic state with increasing temperatures. As a consequence, pinched polarization loops caused by a reversible electric field-induced phase transition as well as completely sprout shape strain responses without any negative strain are evident above T_d.

Those results impressively show the strong interaction of oxygen vacancies, induced by A-site non-stoichiometry, with the existing PNRs in NBT-6BT leading to a shift of the non-ergodic/ergodic relaxor transition temperature.

To obtain a better overview of the impact of Na/Bi variation in NBT-6BT, a direct comparison of the extracted microstructural, dielectric, ferroelectric and piezoelectric properties is provided in Figure 4.2.8.

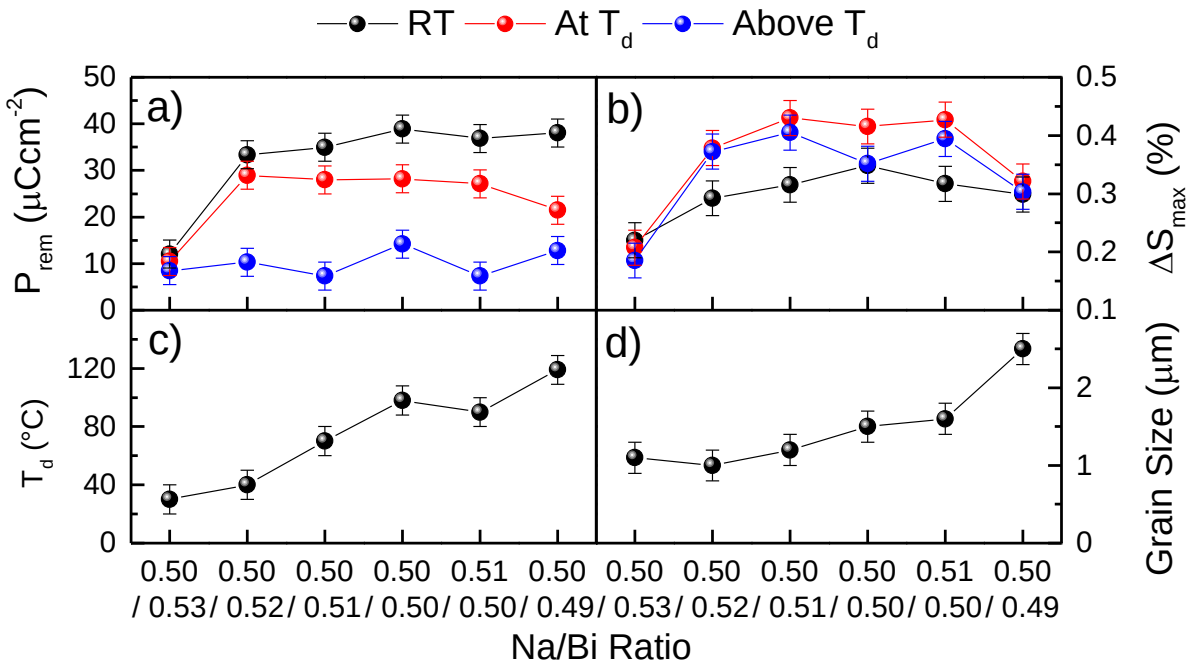

Figure 4.2.8: Direct comparison of the remanent polarization P_{rem} (a), maximum strain ΔS_{max} (b), depolarization temperature T_d (c) and obtained grain size (d) concerning the Na/Bi ratio.

As already discussed, a variation of the Na/Bi ratio has a major impact on the ferroelectric and piezoelectric properties P_{rem} and ΔS_{max} (Figure 4.2.8 (a) and (b), respectively). The stoichiometric composition exhibits a remanent polarization of 38.9 µCcm^{-2} and a ΔS_{max} of about 0.35 %. The introduced oxygen vacancies are influencing the domain wall motion (domain wall pinning), resulting in an enhancement of the ferroelectric properties. The $N_{0.50}B_{0.51}$T-6BT composition displays a minor decrease in the obtained P_{rem} and ΔS_{max} values compared to stoichiometric NBT-6BT. Furthermore, the Bi-deficient composition $N_{0.50}B_{0.49}$T-6BT which should have a significantly higher oxygen vacancy concentration did not exhibit a noticeable variation of the polarization and strain responses. Besides oxygen vacancies in the bulk, grain boundaries are also known to influence the domain wall mobility.[156, 294] The application of a high field could have led to a non-linear migration and segregation of charge carriers at the grain boundaries.[156, 294]

Based on this, the domain wall mobility might be decreased by the grain boundaries during the measurement. This would mean that on the one hand oxygen vacancies and on the other hand grain size effects could competitively influence the ferroelectric responses of the material. Keeping this in mind, the slightly different P_{rem} and ΔS_{max} values for $N_{0.50}B_{0.49}$T-6BT and $N_{0.50}B_{0.51}$T-6BT could be explained by the counteracting effect of increased vacancy concentration against an increment of the grain size and is therefore not much different compared to the stoichiometric NBT-6BT composition. By taking a closer look at the compositions with a higher Bi-excess ($N_{0.50}B_{0.52}$T-6BT and $N_{0.50}B_{0.53}$T-6BT), the obtained values for the maximum strain ΔS_{max} and the remanent polarization P_{rem} are smaller. This could be explained by the fact that those compositions exhibit a depolarization temperature close to room temperature. Accordingly, $N_{0.50}B_{0.53}$T-6BT is in the ergodic relaxor state or could at least be transformed during the measurement. No long-range ferroelectric order can be established during the poling which leads, in consequence, to a small remanent polarization.

4.2.5 A-Site Non-Stoichiometric NBT-6BT: Summary

To summarize the obtained findings, the effects of A-site non-stoichiometry in N_xB_yT-6BT are different compared to what was expected from previous findings in NBT.[49]

Temperature-dependent impedance analysis combined with the calculation of the activation energies of conductivity revealed minor sensitivity towards A-site non-stoichiometry of the electrical properties. High levels of oxygen ionic conductivity could not be induced by A-site variation. The effective oxygen vacancy concentration remains too low to result in oxygen ionic conductivity (see chapter 4.2.3). This hints towards a decisive change in defect chemistry by the formation of a solid solution with 6.0 mol% BT.

The dielectric responses of poled samples revealed a shift of the depolarization temperature from 120 °C down to almost room temperature by a systematic increase of the Bi content. Further, the maximum permittivity decreased from values around 7000 for the stoichiometric composition to values around 4000 for Bi-excess. Increased dielectric losses could be observed for the Bi-deficient samples. The polarization and strain responses for temperatures below, at and above the depolarization temperature revealed a shift from non-ergodic towards ergodic relaxor behavior resulting in a change from butterfly towards sprout shaped strain responses paired with a decrease in the remanent polarization with a systematic increase of the Bi content. Above T_d, pinched polarization hysteresis is observable, indicating a reversible field-induced phase transition. A direct relationship between oxygen vacancies and the PNRs and the resulting piezoelectric and ferroelectric properties could be evidenced in NBT-6BT (see chapter 4.2.4).

Microstructural analysis with the help of XRD, SEM, and EDX revealed the formation of secondary phases for a Bi-excess above 2.0 mol% and Na-excess above 1.0 mol%. A grain coarsening occurred for Bi-deficient compositions (see chapter 4.2.2).

4.2.6 B-Site Acceptor Doped NBT-6BT

The differences in the electrical properties in NBT-6BT and NBT concerning A-site non-stoichiometry could clearly be evidenced in the previous chapter. As already described earlier in chapter 4.2.3, the sensitivity of the electrical properties in NBT-6BT with regards to A-site non-stoichiometry is rather low compared to NBT.[49] The impact on the piezoelectric and ferroelectric properties is by far more pronounced (see chapter 4.2.4).

Even though high levels of oxygen ionic conductivity cannot be induced with A-site variation, B-site acceptor doping could result in oxygen ionic conductivity, if NBT-6BT follows comparable defect chemical mechanisms than NBT.

In pure NBT, acceptor doping even at low levels leads to highly mobile oxygen vacancies and as a result excellent high oxygen ionic conductivity.[48, 49] Evidence has been provided that a defect complex is forming which is strongly affected by the acceptor dopant choice as well as the doping concentration (see also chapter 4.1.2).[48-50, 135, 191]

In contrast, several reports about acceptor doping can be found in the literature claiming that a ferroelectric hardening might occur to acceptor dope a ferroelectric material. [295-298] In the case of Fe-doping, a Fe^{3+} ion occupies the Ti^{4+} lattice sites e.g. in PZT or BT perovskites due to the similar ionic radii of the respective ions. As a result, an immobile defect dipole forms between the Fe'_{Ti} and the charge compensating $V_O^{\bullet\bullet}$.[137-139] The so formed defect dipoles induce a time-dependent clamping of the domain wall motion and therefore lead to the ferroelectric hardening effect.[137, 143, 144] In PZT and BT, $(Fe'_{Ti} - V_O^{\bullet\bullet})^{\bullet}$ charged complexes form resulting in immobile oxygen vacancies.

On the one hand, Prasertpalichat *et al.* already provided evidence of high ionic conductivity in off stoichiometric NBT-BT caused by mobile oxygen vacancies.[299] Sapper *et al.*, on the other hand, reported that ferroelectric hardening can be induced to NBT-6BT by Fe-acceptor doping which might be caused by immobile oxygen vacancies .[300] Furthermore, it was shown that A-site acceptor doping induced by A-site non-stoichiometry could also lead to a hardening effect.[301] The observed hardening effect was, nevertheless, not as significant as it was expected from the knowledge about lead-based ceramics. So far, there is also no possibility to make predictions about the degradation behavior and fatigue based on the yet available knowledge.[302] Especially, the influence of oxygen vacancies on the degradation and fatigue of NBT and NBT-6BT are part of ongoing research in the NAW working group but are out of the scope of this work.

This chapter should, therefore, address the following questions:

- What is the reason for the reported ferroelectric hardening on the one hand and oxygen ionic conductivity on the other hand?
- Is the defect chemistry of NBT-6BT comparable to NBT based on the here established model?
- Is acceptor doping a valuable approach to induce ferroelectric hardening in NBT-6BT?

To address the still remaining questions about the differences and similarities of NBT-6BT and NBT, the effects of B-site Fe-acceptor doping in NBT-6BT are discussed. To clarify, whether there is an oxygen vacancy concentration-dependent change of the properties from ferroelectric hardening towards ionic conductivity, a systematic increase of the acceptor doping concentration was performed. The electrical properties of NBT and NBT-6BT are presented and directly compared to study, if oxygen ionic conductivity can be induced and if it follows the same concentration dependence proposed for NBT in chapter 4.1.2. Even though the variation of A-site non-stoichiometry did not display the expected impact on the electrical properties, the Fe-acceptor doping will be able to prove the applicability of the gained knowledge about the effects of acceptor doping in NBT on the technologically more relevant, concerning ferroelectric applications, solid solutions like NBT-6BT. The main focus was to investigate the relation between oxygen vacancies induced by acceptor doping and their effect on the electrical conductivity. To elucidate, if ferroelectric hardening is present and if acceptor doping in NBT-6BT is a valuable approach to enhance the ferroelectric properties, the polarization responses for Fe-doped NBT and NBT-6BT are provided and compared.

4.2.7 B-Site Acceptor Doped NBT-6BT: Microstructure

The impact of Fe-acceptor doping on the properties of NBT has already been provided in chapter 4.1. For a direct comparison, however, a short repetition of the already presented results for Fe-doped NBT is inevitable. Figure 4.2.9 depicts the XRD pattern taken for the Fe-doped NBT ((a) and (b)) and NBT-6BT compositions ((c) and (d)).

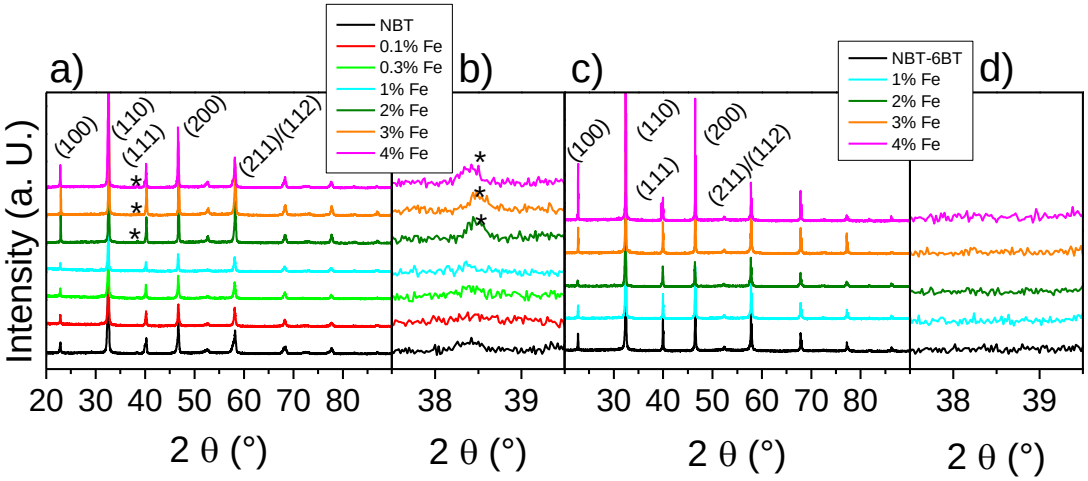

Figure 4.2.9: XRD pattern of the Fe-doped and undoped NBT ((a) and (b)) as well as NBT-6BT ((c) and (d)) compositions with varying doping content. The additional peaks caused by secondary phases are denoted with a star.

All processed ceramics exhibit the $R3c$-group perovskite structure at room temperature.[177, 178, 255, 256] By taking a closer look at the diffraction pattern around 38°, an additional peak can be found for compositions with higher Fe-doping contents. In detail, the additional peak can already be observed for 2.0 mol% doped NBT. For the NBT-6BT system, a related peak cannot be detected up to the 4.0 mol% doped composition with the XRD analysis. EDX analysis revealed that a Fe-, Ti-rich and Bi-deficient secondary phase is evident in the Fe-doped NBT samples above 1.0 mol% doping content as well as in the 4.0 mol% Fe-doped NBT-6BT which is located at the grain boundaries. As previously discussed in 4.1.1, a liquid phase might have formed exhibiting a lower melting point and solidified at the grain boundaries. This finding reveals that the solubility limit of Fe for NBT is between 1.0 mol% and 2.0 mol% and between 3.0 mol% and 4.0 mol% for the NBT-6BT system. As a noticeable impact of induced oxygen vacancies on the microstructure in A-site non-stoichiometric NBT-6BT could be observed (see chapter 4.2.2), SEM analysis was carried out to receive information about the grain size evolution (SE mode) and the formation of the secondary phases (BSE mode).

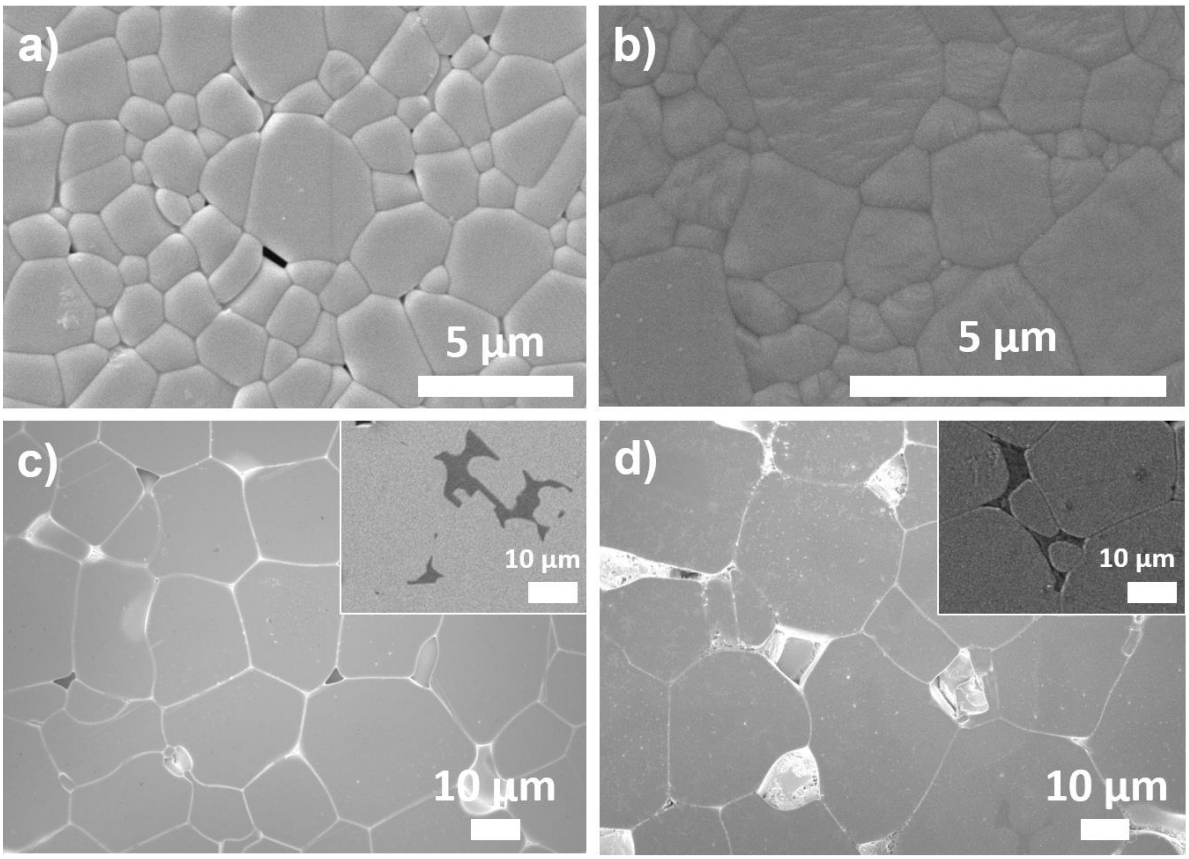

Figure 4.2.10: SEM images of (a) pure NBT and (b) NBT-6BT in comparison to (c) 4.0 mol% Fe-doped NBT and (d) 4.0 mol% Fe-doped NBT-6BT in SE mode. The insets in (c) and (d) represent BSE images taken from the secondary phases in the respective composition in the same scale.

Figure 4.2.10 illustrates the SEM images for pure NBT (a) and NBT-6BT (b) as well as the 4.0 mol% Fe-doped compositions ((c) and (d)) taken in the SE mode. The insets in (c) and (d) provide the corresponding BSE images which include the observed secondary phases at the grain boundaries (the SEM images for the other compositions can be found in Figure A1 in the appendix).

Both, NBT and NBT-6BT exhibit increased grain growth concerning Fe-acceptor doping. This effect was expected as grain coarsening was already attributed to the presence of an increased oxygen vacancy concentration.[27, 62, 156, 285, 303] Figure 4.2.11 represents the grain size evolution concerning the Fe-acceptor doping content.

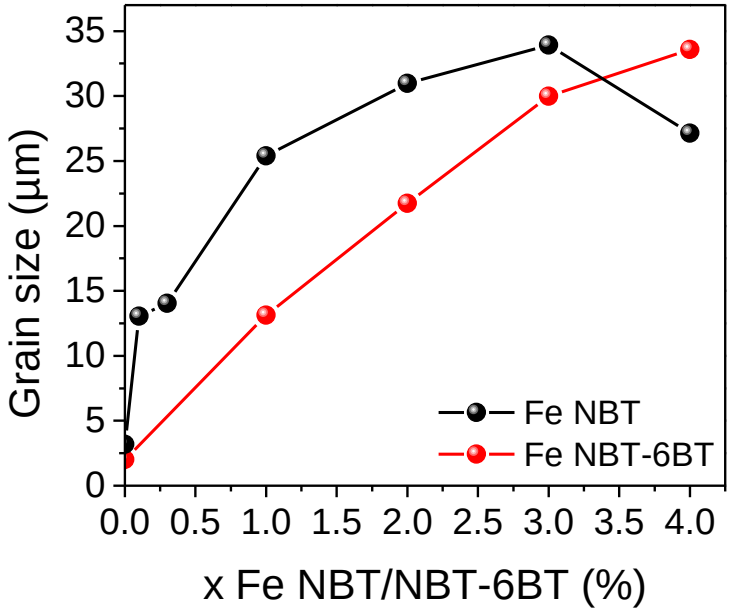

Figure 4.2.11: Grain size evolution with increasing Fe-doping content in NBT (black) and NBT-6BT (red).

The undoped compositions exhibit a comparable grain size (pure NBT ~3 µm, pure NBT-6BT ~2 µm). Doping with 0.1 mol% Fe already results in a tremendous increase of the grain size by about 400 % in NBT. By reaching a doping level of 1.0 mol%, Fe-doping causes a grain growth of about 800 % concerning the starting composition. The grain coarsening in NBT-6BT is also remarkable but not as pronounced as for the NBT compositions when compared to the same doping concentration. In NBT, the maximum grain size is reached at about 3.0 mol% Fe-doping. Above this doping content, the average grain size decreases again. This phenomenon could be explained by the formation of secondary phases as the oxygen vacancy concentration in the matrix might be reduced resulting in a decreased grain boundary mobility and therefore a smaller grain size.[304] Besides the fact that both NBT and NBT-6BT exhibit a grain coarsening, the formation of a solid solution with $BaTiO_3$ seems to buffer against grain coarsening in NBT-6BT as the occurring grain growth is delayed concerning the doping level. It is known from the literature that especially immobile oxygen vacancies are attributed to reducing the grain boundary mobility.[236, 289]

4.2.8 B-Site Acceptor Doped NBT-6BT: Electrical Properties

It could be qualitatively evidenced, that defect complexes of the form $(Fe'_{Ti} - V_O^{\bullet\bullet})^{\bullet}$ are present in the case of Fe-acceptor doped NBT as well as NBT-6BT by electron paramagnetic resonance spectroscopy (EPR) (see Figure A2 in the appendix for a detailed discussion). The EPR measurements have been performed by Dr. David Keeble (University of Dundee, UK). The impact of Fe-acceptor doping on the resulting concentration-dependent conductivity will be elucidated with the help of temperature-dependent impedance spectroscopy. Figure 4.2.12 provides impedance spectra in the Nyquist representation for the Fe-acceptor doped NBT (a) and NBT-6BT compositions (b) at 500 °C from 0.1 Hz to 3 MHz.

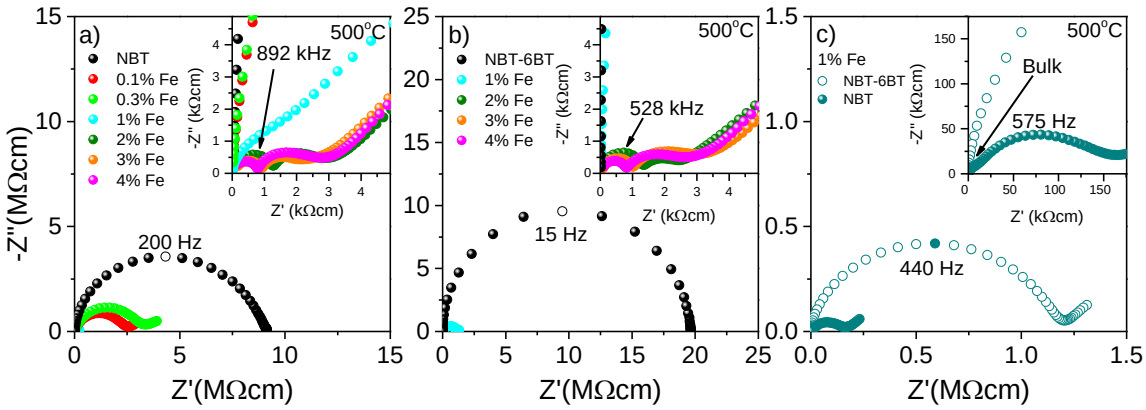

Figure 4.2.12: Impedance spectra for Fe-doped and undoped NBT (a) and NBT-6BT (b) at 500 °C from 0.1 Hz to 3 MHz in Nyquist representation. The 1.0 mol% Fe-doped NBT and NBT-6BT composition are directly compared in (c). The peak frequencies are given for each respective bulk response.

As already discussed in chapter 4.1.2, the 0.1 mol% and 0.3 mol% Fe-doped NBT compositions display only one semicircle. For the pure as well as 1.0 mol% Fe-doped NBT-6BT also only one conduction process can be observed which is attributed to the bulk conductivity of the sample (R_b ~ 1.2 MΩcm at 500 °C for the 1.0 mol% Fe-doped NBT-6BT).[154] This behavior has already been observed for A-site non-stoichiometric NB-6BT and can be attributed to semiconducting behavior (see chapter 4.2.3). A non-linear decrease of the resistivity can be observed for an increased doping concentration to 1.0 mol% and 2.0 mol% for NBT and NBT-6BT, respectively. For those compositions, two semicircles form. The high-frequency arc represents the bulk (R_b ~ 1.0 kΩcm at 500 °C) while the intermediate frequency semicircle is related to the grain boundary response (R_{gb} ~ 2.5 kΩcm at 500 °C) of each sample. The low frequency response can again be described by a Warburg-type diffusion of ions at the sample/electrode interface.[257] This already leads to the conclusion that high levels of ionic conductivity can be induced in NBT-6BT as well.

It should be noted, that the bulk resistivity of NBT decreases by another order of magnitude between 1.0 mol% and 2.0 mol% doping and stays constant afterwards, irrespective of further increase of the doping content. This finding can also be supported by the findings of chapter 4.1 as well as by literature on acceptor doped NBT.[135]

NBT-6BT behaves similarly compared to NBT. Concerning the observed resistivity, there is also a clear transition evident when the doping level increases. The 1.0 mol% Fe-doped sample still exhibits relatively high resistivity with only one distinct semicircle observable in the Nyquist plots. At 2.0 mol% and higher, two semicircles start to develop with a, by orders of magnitude, lower resistivity. This result highlights the similarity of both systems, NBT and NBT-6BT, with regards to the B-site acceptor doping approach and the resulting electrical properties. The only apparent difference is the sensitivity towards the presence of oxygen vacancies.

The temperature evolution of the bulk conductivity was investigated to address the question regarding the doping concentration dependence of electrical conductivity and if ionic conductivity can also be induced to NBT-6BT by B-site doping. To obtain the activation energies for the bulk response, Arrhenius-type plots are provided in Figure 4.2.13.

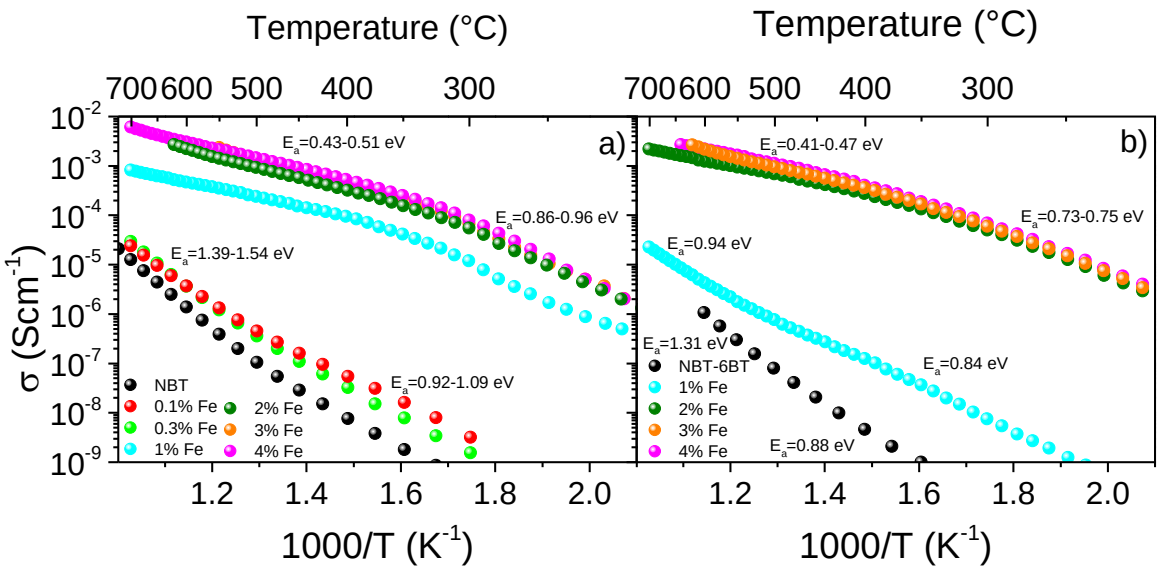

Figure 4.2.13: Arrhenius-type plots of the bulk conductivity for the Fe-doped and undoped NBT (a) and NBT-6BT (b) compositions. The calculated activation energies are given within the figure.

The Arrhenius-type plots for NBT have already been discussed in detail in chapter 4.1.2. In direct comparison to Fe-doped NBT, NBT-6BT reveals similar trends in the temperature and doping concentration dependence of the conductivity. The 1.0 mol% Fe-doped NBT-6BT sample exhibits an increase of the bulk conductivity and lower activation energy (E_a = 0.94 eV above 320 °C) compared to the semiconducting pure NBT-6BT (E_a = 1.31 eV above 320 °C).

With a content of at least 2.0 mol% Fe-acceptor doping, the obtained bulk conductivity is about three orders of magnitude higher. Moreover, a concentration-independent bulk conductivity can be observed for doping contents of 3.0 mol% and 4.0 mol% Fe. The 2.0 mol%, 3.0 mol% and 4.0 mol% acceptor doped samples all represent a change from higher towards lower activation energy. Furthermore, the activation energies of the bulk process fit well to what was already seen for the acceptor doped NBT samples featuring oxygen ionic conductivity (see chapter 4.1.2). Based on those findings, a concentration-dependent transition from semiconducting towards oxygen ionic conducting behavior in NBT-6BT due to acceptor doping becomes more and more probable. As already proposed for the grain coarsening effect, the formation of a solid solution with $BaTiO_3$ buffers against the impact of induced oxygen vacancies in direct comparison to NBT with the expected same oxygen vacancy concentration. Complete suppression of the effect of oxygen vacancy concentration-dependent behavior could, however not be obtained. The here presented results deliver proof for a large concentration of induced oxygen vacancies in both, NBT and NBT-6BT. With regards to recent simulations reported by Zhang *et al.*, a high level of cation conductivity can be neglected in NBT.[305]
To provide direct evidence for the change from semiconducting to oxygen ionic conducting behavior, electromotive force (EMF) measurements were conducted by Dr. Ming Li (University of Nottingham, UK) to calculate the oxygen ionic transport numbers t_{ion} (see Table 4.2-3). The ionic transport number provides the fraction of ionic conductivity concerning ideally oxygen ionic conducting behavior.

Table 4.2-3: Oxygen ionic transport numbers of the investigated Fe-doped NBT and NBT-6BT compositions.

Composition	t_{ion} at 700 °C	t_{ion} at 800 °C
1.0 mol% Fe NBT	0.93	0.90
2.0 mol% Fe NBT	0.89	0.90
1.0 mol% Fe NBT-6BT	0.07	0.07
2.0 mol% Fe NBT-6BT	0.83	0.84
3.0 mol% Fe-NBT-6BT	0.83	0.83

The calculated ionic transport numbers for the acceptor doped NBT samples clearly illustrate the expected change from semiconducting to almost purely oxygen ionic conducting behavior concerning Fe-acceptor doping.

1.0 mol% and 2.0 mol% Fe-doped NBT exhibits values of t_{ion} ~ 0.90 at 800 °C. The 1.0 mol% Fe-doped NBT-6BT sample still features a low ionic contribution to the observed conductivity (t_{ion} ~ 0.07 at 700 °C and 800 °C).

Additionally induced defects, therefore, may lead to extrinsic electronic behavior.[306, 307] The 2.0 mol% and 3.0 mol% Fe-doped NBT-6BT compositions exhibit ionic transport numbers of t_{ion} ~ 0.83 which proves those compositions to be oxygen ionic conducting. Although evidence has been provided that oxygen ionic conductivity can be induced by Fe-acceptor doping in NBT and NBT-6BT, the oxygen vacancy concentration, needed for a change of the conduction mechanism, differs. A certain threshold value needs to be exceeded before oxygen ionic conductivity can be induced. For the case of Fe-doping, the threshold value is between 1.0 mol% and 2.0 mol%. As long as the induced oxygen vacancy concentration is considered to be low enough, this could result in ferroelectric hardening as reported in the literature (see also chapter 4.2.9). [138, 139, 300] A-site non-stoichiometry does not result in increased oxygen ionic conductivity at all (see chapter 4.2.3). Thus, reports about high levels of ionic conductivity in NBT-6BT are comparably rare.[299] Simple A-site non-stoichiometry cannot induce a high enough vacancy concentration to change the conduction mechanism. Instead, secondary phases form which impede an increased vacancy concentration in the matrix. Moreover, the introduced Ba^{2+} ions in the lattice change the potential barriers for migration which leads to lower mobility of the induced oxygen vacancies.[308] Sapper *et al.* reported a ferroelectric hardening effect in Fe-acceptor doped NBT-6BT which underlines the rather immobile character of oxygen vacancies in this system.[300]

The apparent similarities in the variation of the structure, microstructure and phase in NBT and NBT-6BT with regards to the Fe-doping approach lead to the suggestion that the pronounced decrease in the sensitivity of oxygen ionic conductivity might be caused by the differences in the A-site cation lattice. The incorporation of a small fraction of at least 6.0 mol% Ba^{2+} ions at the A-site is the only difference in NBT and NBT-6BT. The activation energy for oxygen ionic migration in $BaTiO_3$ was reported to be in the range of 1.0 eV – 1.1 eV.[309-311] The migration of oxygen ions could be hindered by the difference in the bond strength of Bi-O and Ba-O bonds.[308] At this point it should be highlighted, that the 1.0 mol% Fe-doped NBT-6BT composition provided nearly vanishing amounts of ionic conductivity while the equivalent NBT composition features oxygen ionic transport numbers of around 0.9. Based on the here presented results, the initial question regarding the possibility to induce oxygen ionic conductivity in NBT-6BT and if it follows similar defect chemistry could, therefore, be answered.

4.2.9 B-Site Acceptor Doped NBT-6BT: Ferroelectric Hardening

It is possible to induce oxygen ionic conductivity in NBT-6BT by B-site acceptor doping while it was not possible for A-site variation. This might be caused by an increased concentration of oxygen vacancies in the case of B-site acceptor doping. The ferroelectric properties of Fe-doped NBT-6BT are of major interest to address the question regarding the mobility and concentration dependence on oxygen vacancies in this system. Ferroelectric hardening should be observable by a decrease of the remanent polarization P_{rem} and an increasing coercive field E_c. [137-139] Figure 4.2.14 depicts the obtained polarization curves taken at room temperature and 1 Hz for the most important NBT (a) and NBT-6BT compositions (b) with regards to their Fe-doping content.

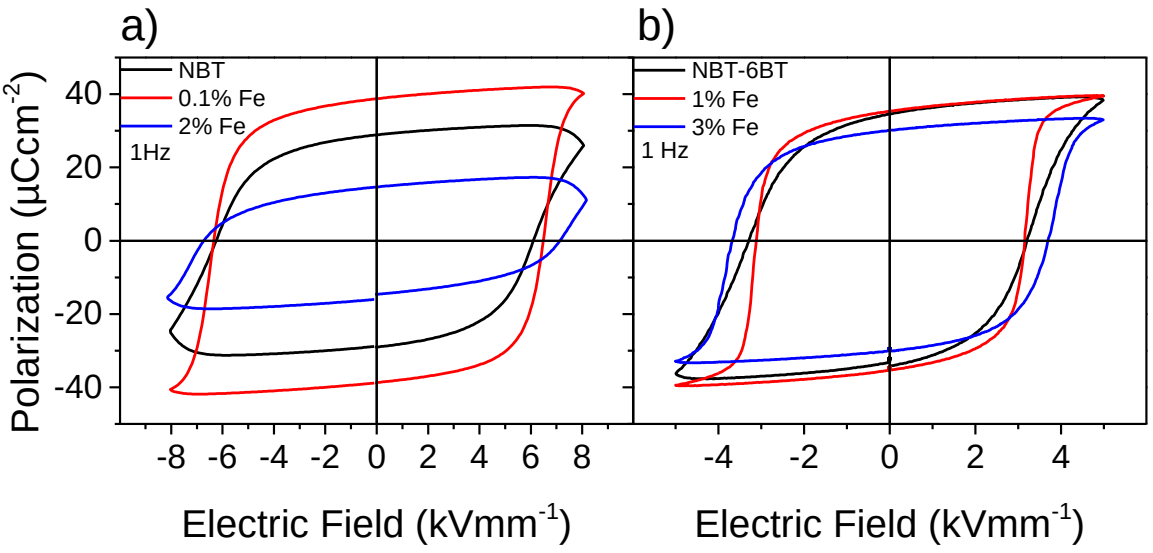

Figure 4.2.14: Polarization vs. applied electric field for doped and undoped NBT (a) and NBT-6BT (b) at room temperature and 1 Hz.

For all illustrated compositions, irrespectively of their doping content, regular ferroelectric polarization behavior is evident at room temperature. According to previous reports about non-stoichiometry, NBT suffers high losses and therefore shows a bulky and lossy loop.[312] It can be concluded that the low-temperature resistance is high enough that ferroelectric polarization switching is still possible. At low temperatures (e.g. room temperature), the induced oxygen vacancies are considered to be less mobile compared to high temperatures where oxygen ionic conductivity is regularly investigated (temperatures beyond 300 °C). Therefore, ferroelectric hardening is observable. It should be mentioned, that the 2.0 mol% Fe-doped NBT sample always suffered electrical breakdown after the first polarization loop which hints towards a non-linear contribution of an increased oxygen vacancy concentration to the degradation behavior of NBT.

This result confirms that acceptor doping might not be the right approach to enhance the ferroelectric properties of NBT-based solid solutions. For low doping contents of 0.1 mol% Fe-doping, the coercive field stays almost constant, while there is a noticeable increase in the remanent polarization. This behavior could be compared with a donor or at least isovalent doping with Zr which leads to a stabilization of the ferroelectric long-range order in NBT-6BT.[313] With increased doping concentration, a ferroelectric hardening effect can be achieved. This result is in good agreement with the previously presented results. In detail, no ferroelectric hardening can be observed in semiconducting NBT compositions (0.1 mol% Fe-doping) while a higher concentration of oxygen vacancies contributes to an observable, but small, hardening in the ionic conducting compositions (2.0 mol% Fe-doping). Taking advantage of the considerably small hardening is, at least, questionable as this effect is overwhelmed by the detrimental non-linearly increasing effects of increased loss and electro-degradation due to the presence of the highly mobile defects. A similar effect is also evident for the doped NBT-6BT compositions. It should be noted, that the reduction of P_{rem} as well as E_c is not as pronounced as for the doped NBT system. The coercive field of NBT-6BT is significantly lower compared to the NBT compositions which is in agreement with existing literature.[118, 212, 213] The here presented results address the question about ferroelectric hardening by Fe-acceptor doping in NBT and NBT-6BT. Ferroelectric hardening can be achieved but the minor beneficial effects on the ferroelectric properties vanish due to the increased leakage by highly mobile oxygen vacancies. It should be highlighted, that acceptor doping is therefore not a valuable approach to enhance ferroelectric properties in NBT-based solid solutions.

4.2.10 B-Site Acceptor Doped NBT-6BT: Summary

Temperature-dependent impedance analysis combined with an investigation of the activation energies obtained by Arrhenius-type plots revealed similar behavior of NBT-6BT to the basic system NBT by B-site acceptor doping. The bulk resistivity decreases by up to four orders of magnitude concerning acceptor doping. In combination with EMF measurements, the oxygen ionic transport numbers experimentally confirmed a dopant concentration-dependent change from semiconducting towards oxygen ionic conducting behavior in both systems (see chapter 4.2.8). Inducing oxygen ionic conductivity by acceptor doping is, therefore, possible for both systems, NBT-6BT and NBT. This leads to the conclusion that the oxygen vacancy concentration and mobility, as well as the formation of defect complexes, follows similar defect chemistry as the same characteristic kink is also observable for the oxygen ionic conducting NBT-6BT compositions. This strong relationship between the conduction mechanism and the oxygen vacancy concentration is already a first hint that the findings made for the B-site defect chemistry in NBT are applicable to more complex NBT-based solid solutions. The only difference which could be observed is the varying doping content at which oxygen ionic conductivity is induced. As long as the doping content becomes high enough, the defect chemical behavior follows the same mechanisms. Forming a solid solution with 6.0 mol% BT buffers against the effects of increased oxygen vacancy concentration to a certain threshold value.

The low-temperature resistivity is still high enough to obtain ferroelectric switching (see chapter 4.2.9). EPR analysis qualitatively confirmed the presence of $(Fe'_{Ti} - V_O^{\bullet\bullet})^{\bullet}$ defect complexes in Fe-doped NBT and NBT-6BT (see Figure A2 in the appendix). The observed minor ferroelectric hardening effect can be attributed to the rather unusual behavior of oxygen vacancies in NBT-based systems. Based on those findings, it can be expected that the point defect dependent electrical degradation and fatigue in NBT will be different from what is known for lead based-systems. Enhancing the ferroelectric properties by acceptor doping is not a valuable approach for NBT-based systems as the detrimental effects of highly mobile vacancies overwhelm the beneficial effects by far.

With the help of XRD and a detailed microstructural analysis by SEM and EDX, liquid, Fe-rich secondary phases could be evidenced in Fe-doped NBT and NBT-6BT as well. The solubility limit differs from 2.0 mol% to 3.0 mol% for NBT and 3.0 mol% to 4.0 mol% for NBT-6BT. A grain coarsening effect could be observed for both systems resulting in up to 800 % larger grains compared to the undoped systems (see chapter 4.2.7).

4.3 Defect Chemistry in NBT-Based Solid Solutions: NBT-ST

Another very promising NBT-based candidate that exhibits superior piezoelectric properties is the solid solution NBT-25ST. The large strains that could be achieved by these solid solutions were attributed to the occurrence of core-shell microstructures.[119, 217, 219, 259, 314] A general overview for NBT-ST is provided in chapter 2.11.2. Core-shell microstructures result from chemical inhomogeneity forming a depleted core, surrounded by an enriched shell with regards to a compositional atom. With the knowledge gained about doping and A-site non-stoichiometry on the microstructural evolution in NBT and NBT-6BT (see chapter 4.1.1, 4.2.2 and 4.2.7), further enhancement could be achieved concerning a possible core-shell formation and its beneficial effects on electromechanical properties.[315] Frömling *et al.* reported, in a publication from 2018, a strong influence of A-site non-stoichiometry on the microstructure and furthermore a close relationship between the core-shell formation and the resulting electrical, piezoelectric and ferroelectric properties.[64]

In detail, a systematic study of bismuth variation was performed which led to the conclusion that the formation of core-shell structures can either be stabilized or suppressed by Bi-excess or -deficiency, respectively. Moreover, the ferroelectric and piezoelectric properties are remarkably affected by A-site non-stoichiometry. Those results highlight that the formation and control of core-shell structures, which are strongly affected by the A-site related defect chemistry, open a new field of research for tailoring electrical, dielectric, piezoelectric and ferroelectric properties of NBT-based systems.[63, 64, 219]

As the reproducibility of lead-free functional ceramics is still a major issue[25], a precise knowledge of the defect chemistry and basic mechanisms leading to the formation of a core-shell structure are inevitable for further enhancement in this field of research. It should be noted, that core-shell microstructure has also been evidenced in other systems. The impact is, however, not completely revealed, yet.[66]

As already presented for the NBT-6BT solid solution, not only the A-site non-stoichiometry (see chapter 4.2.1 and following), but also B-site doping (see chapter 4.2.6 and following), significantly influence the oxygen vacancy concentration. To further elucidate the effects of oxygen vacancies on the core-shell formation and the resulting properties of NBT-25ST, Fe was chosen as an acceptor substituting the Ti^{4+} ion at the B-site. This should lead to the formation of additional oxygen vacancies.[316] Fe-acceptor doping further allows for a direct comparison with the previously discussed Fe-doped NBT and NBT-6BT compositions. Donor doping should, for instance, lead to a decreased oxygen vacancy concentration.

Niobium was chosen to function as a donor, again substituting the Ti^{4+} ion at the B-site:[317, 318]

$$Nb_2O_5 + 2Ti_{Ti}^{x} + V_O^{\bullet\bullet} \rightharpoonup 2TiO_2 + 2Nb_{Ti}^{\bullet} + O_O^{x} \,. \tag{4.15}$$

A low oxygen vacancy concentration should facilitate the formation of a small-grained, core-shell microstructure (see also chapter 4.2.7).[64] This finding highlights that the defect concentration in NBT-25ST is directly related to the present chemical diffusion phenomena and the core-shell formation. Based on this, a deeper look at the occurring diffusion phenomena must be taken to understand the defect chemical mechanisms resulting in a formation and stabilization of a core-shell structure.

It has been found in previous studies, that the solid-state reaction NBT and ST performs in two steps deviating in their respective formation temperature. During the calcination, NBT cores start to form at around 410 °C which will then be covered by an ST shell at around 610 °C by a chemical diffusion of Sr into the NBT phase.[219] Those core-shell structures exhibit a Sr-depleted core and a Sr-rich shell resulting in a large Sr concentration gradient within the grains.[63, 219] The concentration gradient of Sr between the core and the shell will, therefore, result in a diffusion of Sr in the opposite direction of the concentration gradient. When the diffusivity is considered to be large enough, the core-shell microstructure will vanish and Sr will be distributed homogeneously. In contrast, if the diffusivity is low, this will result in a core-shell structure. In the case of Sr diffusing from the shell towards the NBT core during the sintering, the chemical diffusion coefficient is dependent on the diffusion kinetics of bismuth, sodium as well as oxygen vacancies. The total diffusion is, however, determined by the slowest diffusing species. The diffusion of Sr from the shell to the core region can be described by a chemical diffusion with the respective diffusion constant $\widetilde{D}$.[319] According to Frömling *et al.*, the chemical diffusion $\widetilde{D}$ can be expressed by the diffusion coefficient of strontium D_{Sr} as well as the effective diffusion coefficient of sodium and bismuth $D_{Na/Bi}$ as follows:[64]

$$\widetilde{D} = \frac{D_{Sr} \cdot D_{Na/Bi}}{D_{Sr} + D_{Na/Bi}} \approx D_{Sr} \,. \tag{4.16}$$

As the formation of NBT starts roughly 200 °C below the starting temperature of ST formation, the effective diffusion coefficient for $D_{Na/Bi}$ has to be much larger compared to the respective diffusion coefficient of strontium D_{Sr}.[219] Hence, D_{Sr} is seen to be the limiting factor.[64, 219] The formation and stability of core-shell microstructures can be influenced by several approaches. It could have been shown, that elongation of the sintering time leads to a decreased occurrence of grains establishing a core-shell structure.[219, 222] Furthermore, doping as well as A-site non-stoichiometry directly influence the formation of core-shell structures.

Especially the A-site non-stoichiometry was proven to either stabilize, by Bi-excess, or suppress, by Bi-deficiency, the development of such chemical inhomogeneity.[64] Frömling *et al.* stated that the A-site vacancy concentration (bismuth vacancies) determines the corresponding strontium diffusion. In contrast, Cho *et al.* have recently reported that Fe-acceptor doping in NBT-23ST leads to a suppression of core-shell formation and the development of ergodic relaxor characteristics compared to the undoped counterpart showing non-ergodic relaxor behavior at room temperature.[316] In contrast to Frömling *et al.*, it was claimed that the increased oxygen vacancy concentration might be responsible for the increased strontium diffusion.[64] Up to this point, the available literature is kind of contradictive, as it is still under debate, whether the diffusion of Sr is governed by the occurrence of either A-site (Bi) vacancies or oxygen vacancies. The following questions will, therefore, be addressed in this chapter:

- Is the core-shell formation in NBT-25ST more affected by B-site acceptor/donor doping or A-site non-stoichiometry and can it directly be controlled?
- Is the electrical conductivity in NBT-25ST comparable to NBT concerning A-site non-stoichiometry and B-site acceptor doping?
- Do core-shell microstructures correlate with the dielectric, ferroelectric and piezoelectric properties?
- Is the defect chemistry comparable to NBT?

This chapter will, therefore, deal with a systematic study of the A-site non-stoichiometry and B-site doping dependent formation of core-shell structures. The influence of A-site variation and B-site acceptor/donor-doping on the electrical, dielectric, ferroelectric and piezoelectric properties concerning the present microstructure will be discussed in more detail. The aim is to address the still unanswered questions about the basic defect chemical interactions in the NBT-based solid solution NBT-25ST and further to clarify which lattice site vacancies result in the formation or annihilation of the core-shell structure. The main focus is set on the interplay of A-site and B-site defects. A doping content of 3.0 mol% for the acceptor Fe (Fe'_{Ti}) and the donor Nb ($Nb^{\bullet}_{Ti}$), occupying the titanium B-sites, was chosen as this should generate or annihilate an equal amount of oxygen vacancies than for 1.0 mol% Bi-deficiency ($2Bi^{x}_{Bi} + 3O^{x}_{O} \leftrightharpoons 2V'''_{Bi} + 3V^{\bullet\bullet}_{O} + Bi_2O_3 \uparrow$) or -excess. By comparing the effects of doping which directly influence the oxygen vacancy concentration and A-site non-stoichiometry generating A-site vacancies should elucidate which defects are of major importance concerning the strontium diffusivity in NBT-25ST and all related properties. The here presented results have been elaborated in close collaboration with Jonas Heldt and are part of his Master's Thesis.[320]

4.3.1 Doped and A-site Non-Stoichiometric NBT-ST: Microstructure

To investigate the crystal structure and a possible occurrence of secondary phases, the XRD pattern of A-site non-stoichiometric (a) and B-site doped NB_xT-25ST compositions (b) is illustrated in Figure 4.3.1.

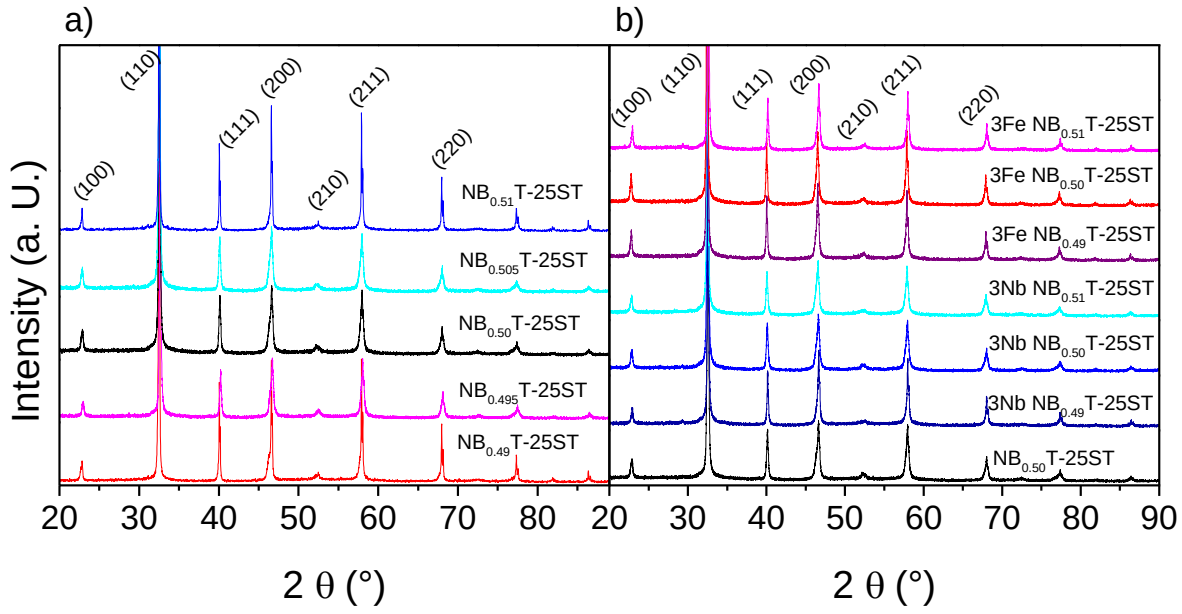

Figure 4.3.1: XRD pattern of the A-site non-stoichiometric (a) and B-site doped NB_xT-25ST compositions (b).

All processed compositions exhibit an ABO_3 typical pseudo-cubic crystal structure without evidence for additional secondary phases at room temperature. The results for the extracted lattice parameters are in good agreement with literature for the $Pm\bar{3}m$ space group.[26, 63, 119, 216, 321, 322] It should be noted, that some studies claim NBT-25ST to exhibit a small tetragonal distortion.[322, 323] A closer look at the (111) peaks reveals some irregularities. A peak splitting would indicate the presence of a rhombohedral phase.[215] However, this irregularity cannot be investigated in more detail due to the resolution limit of the given diffractogram. A detailed investigation of the evolution of the crystal structure in NBT-xST is part of ongoing research but out of the scope of this work. The here presented results suggest that A-site non-stoichiometry and B-site doping do not lead to an observable change in the crystal structure at room temperature.

Besides XRD analysis, an SEM investigation was performed to evaluate not only the morphology (SE mode) but also the formation of possible secondary phases and core-shell structure (BSE mode). SEM images in SE mode are given in Figure 4.3.2 to investigate the grain size and morphology.

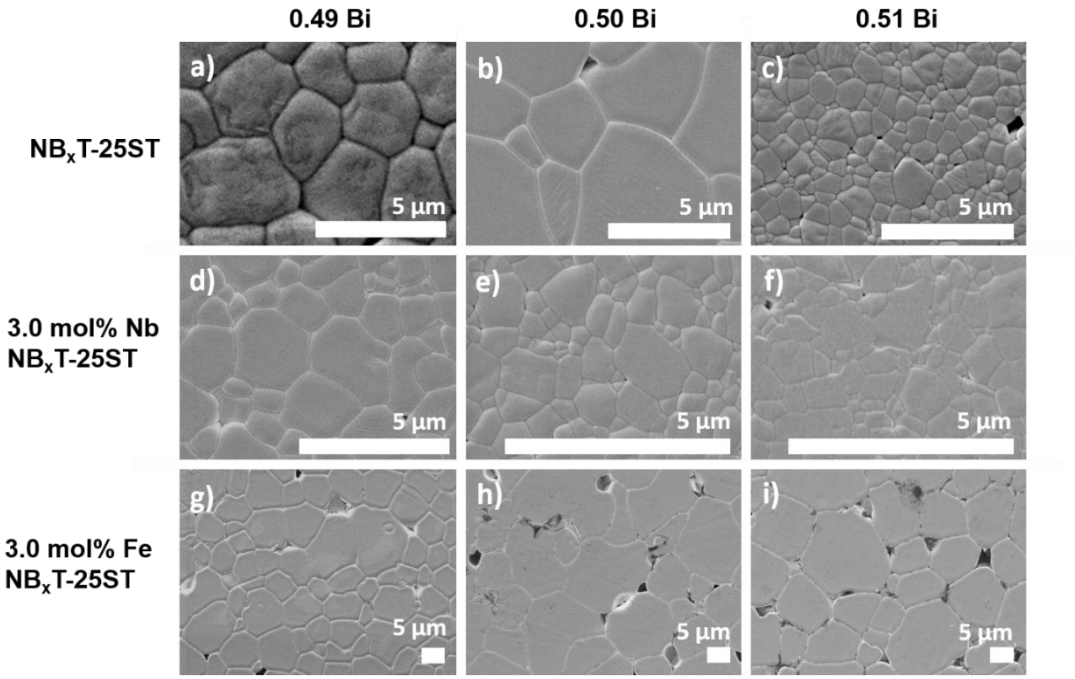

Figure 4.3.2: SEM images for the undoped ((a) to (c)), 3.0 mol% Nb-((d) to (f)) and 3.0 mol% Fe-doped ((g) to (i)) and A-site non-stoichiometric NB_xT-25ST compositions in SE mode.

The stoichiometric NBT-25ST composition exhibits an average grain size of about 4.71 µm with round-shaped grains (see Figure 4.3.2 (b)). However, a broad grain size distribution is present ranging from small grains with about 2 µm up to grains with 10 µm and beyond. A close relationship between A-site non-stoichiometry and the resulting grain size can be observed (see Figure 4.3.2 (a) to(c)). Bi-deficiency leads to a grain coarsening while smaller grains develop in the Bi-excess compositions. Apart from Bi-deficiency, acceptor doping with Fe leads to a grain coarsening (see Figure 4.3.3).

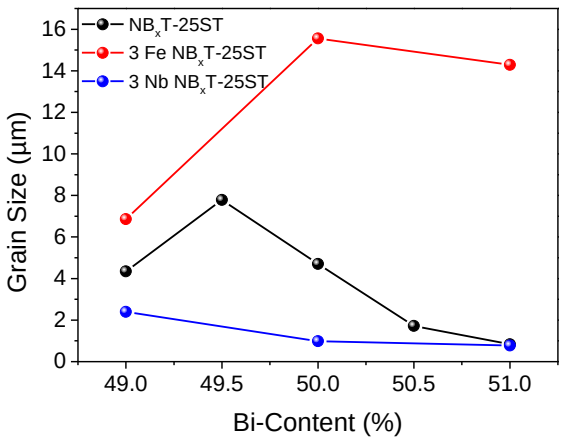

Figure 4.3.3: Calculated grain size of the doped (Fe-doped red and Nb-doped blue) and undoped (black) NB_xT-25ST compositions concerning A-site non-stoichiometry.

Irrespective of the A-site non-stoichiometry, Fe-acceptor doped NB_xT-25ST (red) always exhibits a larger grain size compared to the undoped compositions ranging from ~ 6.9 µm up to ~15.5 µm. Nb-doping (blue), for instance, always leads to a smaller grain size between ~ 2.5 µm and ~ 1 µm. Nevertheless, A-site non-stoichiometry can be seen as an additive effect also influencing the grain size but gets overwhelmed by the effects of acceptor doping.

It should be noted, that the 3.0 mol% Fe-doped $NB_{0.51}T$-ST composition exhibits an unexpected shrinkage compared to the stoichiometric acceptor doped composition. Secondary phases can be detected at the grain boundaries (see Figure 4.3.4). Those secondary phases can influence the defect chemistry at the grain boundary and, as a consequence, the grain boundary mobility during the sintering. The grain size variation by doping and A-site non-stoichiometry can be attributed to the induced oxygen vacancy concentration. Oxygen vacancies, generated by Fe-acceptor doping and/or A-site Bi-deficiency, lead to grain coarsening as already discussed in the previous chapters. A similar effect can be found in literature as an increased oxygen vacancy concentration can change the grain boundary structure from faceted to rough which results in a differing grain boundary mobility and, in consequence, to a change in grain size.[62, 64, 66, 236, 324]

To address the question regarding the impact of A-site and B-site defect chemistry on the core-shell formation, SEM images in the backscattered electron mode (BSE) for doped and undoped non-stoichiometric NB_xT-25ST compositions are provided in Figure 4.3.4.

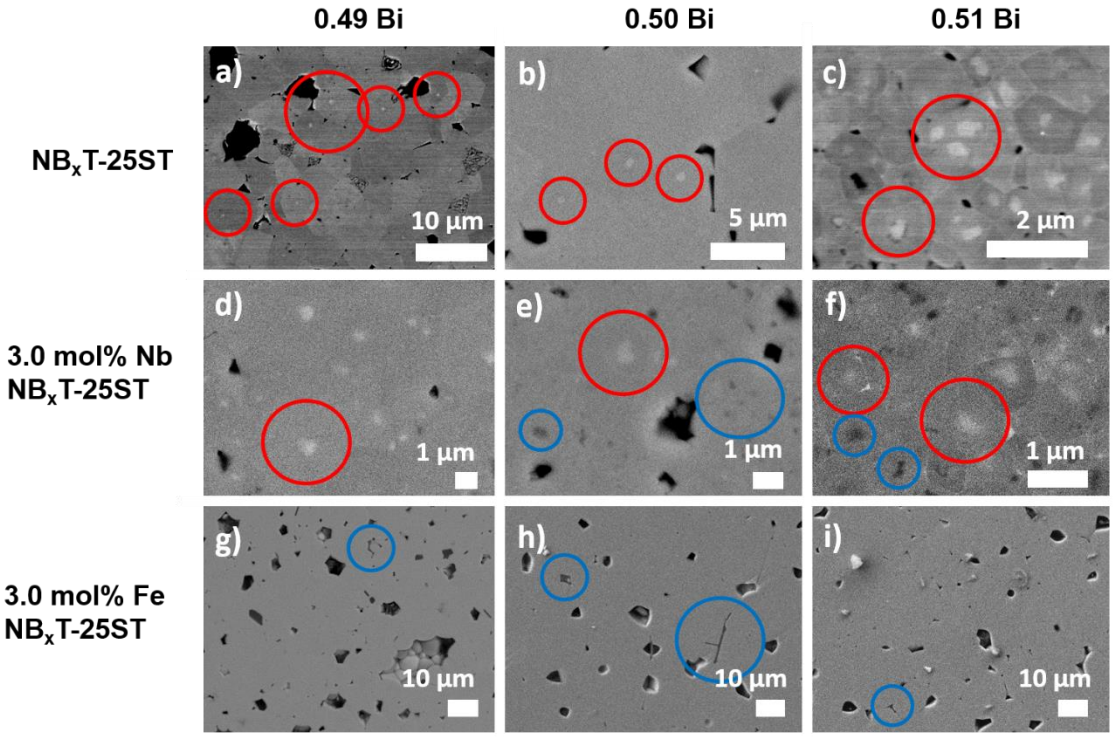

Figure 4.3.4: SEM images in BSE mode for the undoped ((a) to (c)), 3.0 mol% Nb-((d) to (f)) and 3.0 mol% Fe-doped ((g) to (i)) and A-site non-stoichiometric NB_xT-25ST compositions in BSE mode (core-shell structures are highlighted with red circles; secondary phases are denoted with blue circles).

The bright dots centered inside the grains are attributed to the NBT cores of the core-shell structure (red circles). The increased amount of the heavy element Bi inside the core appears brighter as the lighter element Sr which partly substitutes Bi in the shell region. Heavier elements have a higher probability to backscatter electrons compared to lighter elements. The observed NBT cores are roughly 400 nm in diameter. A formation of the core-shell structure is validated to be strongly affected by both, the A-site variation as well as the B-site doping. In detail, $NB_{0.49}T$-25ST exhibits only a rather low concentration of cores while almost every grain in $NB_{0.51}T$-ST exhibits a core-shell structure. These findings agree with literature.[64]

Aside from the A-site non-stoichiometry, acceptor/donor doping reveals an even stronger effect on the core-shell formation. All donor doped NB_xT-25ST compositions provide a high concentration of core-shell structures. In contrast, not even one acceptor doped composition provides evidence for core-shell formation. Additionally, it can be seen that Bi-excess in the Nb-doped NB_xT-25ST further increases the core-shell concentration. The core size in the doped compositions is in the range of 300 nm to 500 nm which is comparable to the core size of the undoped compositions. The size of the cores themselves seems neither to be affected by A-site non-stoichiometry, nor by doping.

It should be noted, that the provided SEM images only represent a cross-section through the samples. As the core always exhibits the same size but the grain size increases, the probability of finding a core decreases simultaneously. Furthermore, the doping with either 3.0 mol% Fe or 3.0 mol% Nb seems to be above the solubility limit as secondary phases can also be detected with the BSE images (see blue circles in Figure 4.3.2).

EDX analysis of the corresponding areas revealed a secondary phase consisting of Na (approx. 45 %), Sr (approx. 40 %) and Ti (approx. 8 %) in the Nb-doped compositions and a secondary phase consisting of Ti (approx. 60 %), Na (approx. 20 %) and Fe (approx. 15 %) for the Fe-doped compositions.

To get better controllability of the core-shell related properties, the first and foremost goal is to understand the formation of such structures concerning the diffusion properties and what might influence the formation. The formation of a Sr-depleted core with a Sr-enriched shell is mainly driven by the chemical diffusion of Sr in the NBT matrix. It has been claimed by Frömling *et al.*, that Sr diffusion in NBT-25ST is mainly occurring via an A-site vacancy mechanism.[64] Therefore, an increase of the Bi vacancy concentration (Bi-deficiency) should be beneficial for the Sr diffusion and, hence, should lead to a less pronounced core-shell concentration. Besides, the introduced oxygen vacancies might also play a role concerning the Sr diffusion.[316] Aside from Bi-deficiency, Fe-acceptor doping leads to an increment in the oxygen vacancy concentration in the material while Bi-excess as well as Nb-donor doping results in a decrease the oxygen vacancy concentration.

A change in the A-site non-stoichiometry which is strongly affecting the oxygen vacancy concentration significantly influences the formation of core-shell microstructures. To address the question, if bismuth A-site vacancies or oxygen vacancies have a higher impact on the chemical diffusion of Sr, a closer look should be taken on the B-site doped compositions. Nb-donor doping, for instance, leads to a high concentration of core-shell structure independent of A-site variation while Fe-acceptor doping leads to an almost vanishing concentration of the core-shell structure. As both, acceptor and donor doped NB_xT-25ST compositions should exhibit the same amount of Bi vacancies, the introduced oxygen vacancy concentration determines whether a core-shell structure forms or not. This becomes even more obvious when the 3.0 mol% Nb-doped $NB_{0.49}T$-25ST is directly compared with the 3.0 mol% Fe-doped $NB_{0.51}T$-25ST. While the donor doped, Bi-depleted, species still displays a relatively high concentration of core-shell structures (Figure 4.3.4 (d)), the acceptor doped Bi-excess species (Figure 4.3.4 (i)) shows no evidence for inhomogeneity in the microstructure at all.

This leads to the conclusion, that the B-site doping and the variation of oxygen vacancy concentration exhibits a much more pronounced effect on the Sr diffusivity and the related core-shell formation than the A-site variation and the change of the Bi vacancy concentration.

It should be noted, that the concentration change of the oxygen vacancies by 1.0 mol% Bi variation should ideally be equal to the changes with 3.0 mol% acceptor and donor doping. Those counteracting effects, however, do not annihilate each other in reality (see 3.0 mol% Fe-doped $NB_{0.51}$T-25ST in Figure 4.3.4 (i) and 3.0 mol% Nb-doped $NB_{0.49}$T-25ST in Figure 4.3.4 (d)). The reason for this is that the 1.0 mol% Bi-excess might not completely be incorporated into the system as there are not enough A-site vacancies to be occupied by the additional bismuth. Hence, the formation of secondary phases becomes more favorable (observed in the doped compositions) which also changes the actual A-site non-stoichiometry. Na and Sr-rich secondary phases could be found in the Nb-doped compositions via EDX analysis which should lead to a decrease of Bi-deficiency in the matrix phase. The 3.0 mol% Fe-doped $NB_{0.51}$T-25ST also showed secondary phases at the grain boundaries which might lead to a decrease of the actual Bi-excess in this composition. Keeping this in mind, a precise determination of the actual oxygen vacancy concentration is challenging. But at least a qualitative statement is possibly representing the trend that B-site acceptor doping exhibits a larger impact than A-site vacancies on chemical diffusion and hence the formation of a core-shell structure.

4.3.2 Doped and A-site Non-Stoichiometric NBT-ST: Electrical Properties

A-site non-stoichiometry and B-site doping should have a noticeable effect on the electrical properties if NBT-25ST follows the same defect chemical mechanisms as NBT. Thus, impedance spectroscopy analysis has been conducted for the processed compositions.

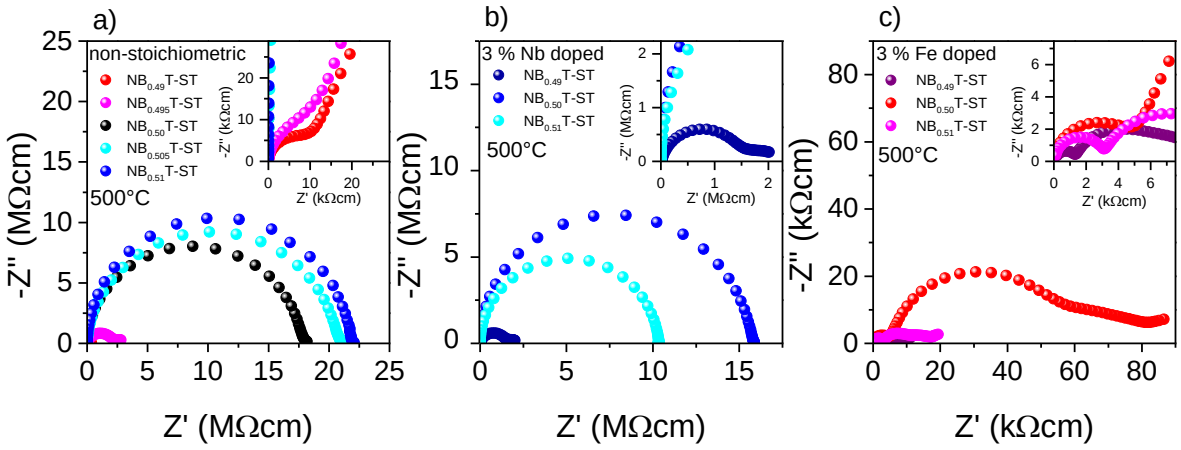

Figure 4.3.5: Impedance spectra in the Nyquist representation for the A-site non-stoichiometric (a) and B-site Nb-doped (b) as well as Fe-doped NB_xT-25ST compositions (c) taken at 500 °C from 0.1 Hz to 3 MHz.

Figure 4.3.5 depicts the impedance plots in Nyquist representation measured at 500 °C from 0.1 Hz to 3 MHz. Firstly, the A-site non-stoichiometric NB_xT-25ST was investigated (see Figure 4.3.5 (a)). The resistivity undergoes notable changes concerning the Bi content. $NB_{0.505}T$-25ST and $NB_{0.51}T$-25ST exhibit only one semicircle. This behavior is directly comparable to the semiconducting NBT (see chapter 4.1.2) as well as NBT-6BT (see chapters 4.2.3 and 4.2.8) compositions. These compositions do not differ significantly from the stoichiometric composition $NB_{0.50}T$-25ST with regards to the obtained resistivity. The Bi-deficient compositions reveal orders of magnitude lower resistivity. Additionally, two semicircles form with Bi-deficiency. This behavior has previously been observed for oxygen ionic conducting compositions (see chapter 4.1.2, 4.2.3 and 4.2.8). The high frequency, low resistivity arc represents one process with a distinct relaxation time τ, the intermediate frequency, higher resistivity arc represents another process with a different relaxation time τ. This behavior is very similar to non-stoichiometric NBT compositions discussed in lithe terature.[49]

For the Nb-doped, non-stoichiometric species (see Figure 4.3.5 (b)), only one semicircle is observable independent from the A-site variation. Nonetheless, the resistivity decreases for Bi-deficiency.

It should be noted, that the effect is by far not as drastic as for the undoped compositions. The resistivity slightly decreases for the Nb-doped $NB_{0.51}$T-25ST composition (R_b ~ 10.5 MΩcm) compared to the Nb-doped stoichiometric composition (R_b ~ 16 MΩcm).

The Fe-doped NB_xT-25ST compositions, however, exhibit orders of magnitude lower resistivity (R_b ~ 1.5 MΩcm – 7.5 MΩcm) compared to the undoped, stoichiometric composition (see Figure 4.3.5 (c)). Furthermore, two semicircles are evident. In direct comparison between A-site non-stoichiometry and B-site doping, it becomes obvious that the doping features a much more pronounced impact on the resistivity than the Bi-variation.

To get a better view of how the temperature-dependent conductivity is affected by B-site doping and A-site non-stoichiometry, Arrhenius-type plots are provided in Figure 4.3.6.

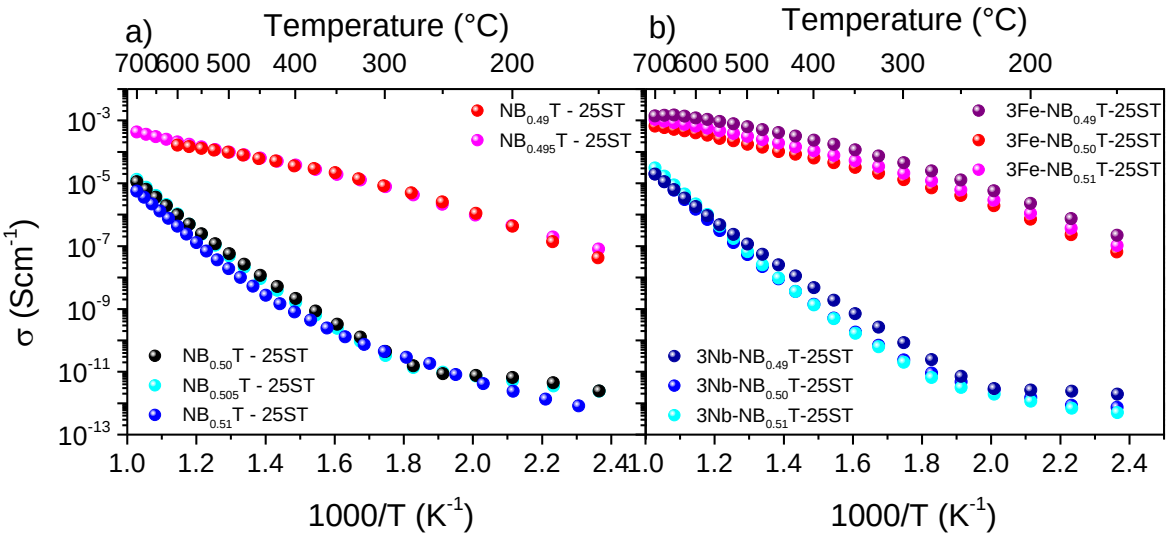

Figure 4.3.6: Arrhenius-type plots of the high-frequency process conductivity for the undoped (a) and doped (b), A-site non-stoichiometric NB_xT-25ST compositions.

Two different groups can be discriminated. On the one hand, the low conductivity, high activation energy group is represented by stoichiometric NBT-25ST as well as Bi-excess NB_xT-25ST (Figure 4.3.6 (a)) and the entire Nb-donor doped NB_xT-25ST compositions (Figure 4.3.6 (b). On the other hand, Bi-deficient, as well as all Fe-doped NBxT-25ST compositions, form the second group providing orders of magnitude higher conductivity paired with low activation energies.

The low conducting species represent a transition from low activation energy towards higher activation energy with increasing the temperature. The highly conducting species, in contrast, reveal a transition from high activation energy towards lower activation energy concerning an increasing temperature. It should be noted, that for the highly conductive samples the high-frequency process is taken into account to resolve the Arrhenius-type plots.

For the lower conducting species, however, only one process is evident which was used to represent the temperature-dependent conductivity. The here presented electrical conductivities display the entirely same behavior when compared to the previously provided results for acceptor doped NBT as well as NBT-6BT including also the kink at the same temperature in the presumably ionic conducting compositions (see also chapter 4.1.2 and 4.2.8).

The activation energies for the low conductive species were calculated to be in the range of 1.47 eV and 1.87 eV for temperatures above 325 °C. It can be assumed that those compositions exhibit intrinsic semiconducting behavior. The activation energy for an intrinsic semiconductor can be determined by half of the bandgap value.[146] The bandgap of pure NBT is 2.94 eV [258] and 3.25 eV for ST.[325] The here processed NBT-25ST compositions should, therefore, exhibit a bandgap value in between. An approximated band gap of around 3 eV is in good agreement with the calculated values. The fact that the activation energies are lower at lower temperatures can be explained by defect states within the bandgap which could act as a donor and/or acceptor states influencing the Fermi level (as presented by the DOS calculations for Fe-doped NBT, see chapter 4.1.4). At temperatures below 275 °C, those materials behave like extrinsic semiconductors.

In contrast, the activation energies of the Fe-doped and Bi-deficient samples representing the highly conductive species show the opposite trend. The transition from higher to lower activation energies takes place gradually in a temperature region between 275 °C and 325 °C. The presence of two distinct semicircles and electrode polarization in Nyquist representation and the calculated activation energies for the high-frequency process lead to the assumption that the conduction process changed from intrinsic/extrinsic semiconducting towards oxygen ionic conducting behavior (see also chapters 4.1.2 and 4.2.8).[50, 304, 326] The calculated activation energies change from E_a = 0.65 eV (between 150 °C and 275 °C) for $NB_{0.495}$T-25ST and around E_a = 0.75 eV for Fe-doped NB_xT-25ST to about E_a = 0.46 eV (above 325 °C) irrespective of the A-site non-stoichiometry. This change in the activation energy fits well with the previously presented results for acceptor doping in NBT as well as NBT-6BT (see chapters 4.1.2 and 4.2.8) and can be corroborated with already existing literature for Mg-doped NBT[50], NBT [187] and $NB_{0.49}$T.[135]

By a detailed discussion of the provided impedance spectra and Arrhenius plots, a significant impact of the A-site and B-site defect chemistry on the conductivity up to an entire change of the conductivity mechanism paired with orders of magnitude different conductivity could have been evidenced for doped and undoped NB_xT-25ST. These results deliver proof that NBT-25ST follows similar defect chemical mechanisms than the basic system NBT.

4.3.3 Doped and A-site Non-Stoichiometric NBT-ST: Dielectric, Ferroelectric, and Piezoelectric Properties

As already discussed for non-stoichiometric NBT-6BT in chapter 4.2.4, the A-site and B-site defect chemistry might also have a major influence on the dielectric, ferroelectric and piezoelectric properties. To address the question of how the A-site defect chemistry affects the dielectric properties, the permittivity and loss for the A-site non-stoichiometric NB_xT-25ST compositions are given in Figure 4.3.7.

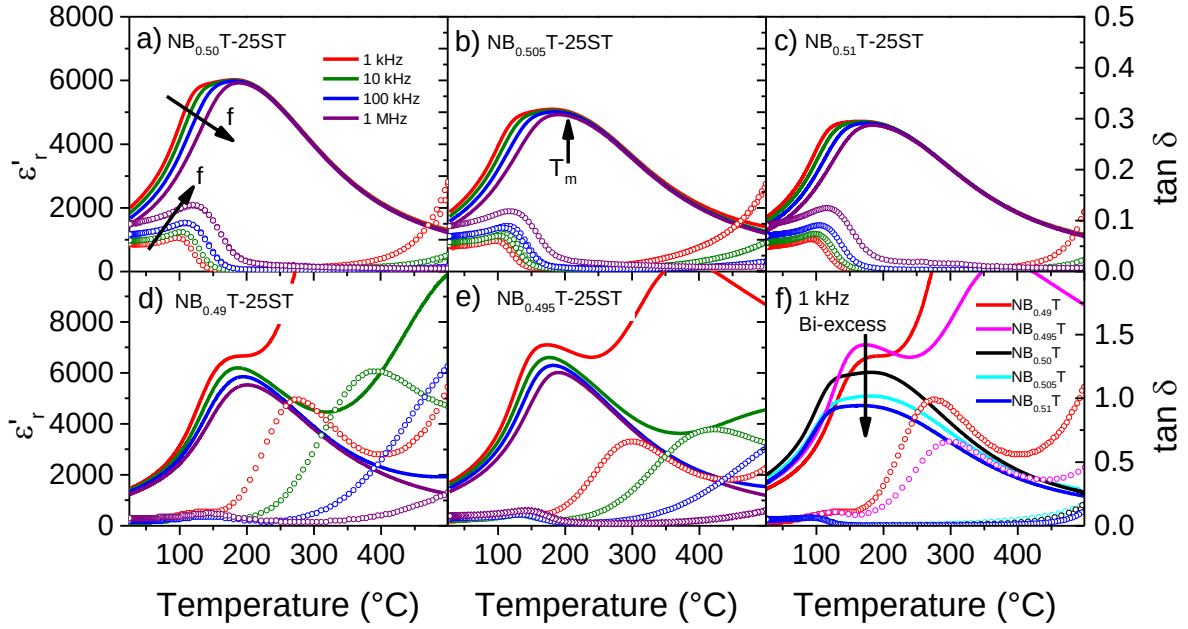

Figure 4.3.7: Temperature and frequency-dependent permittivity ε_r' and dielectric loss $\tan\delta$ for the non-stoichiometric NB_xT-25ST compositions from 25 °C to 500 °C in the unpoled state ((a) to (e)). A direct comparison of the permittivity and loss responses concerning the Bi-variation if provided in (f) for 1 kHz. The temperature of maximum permittivity T_m is exemplarily denoted with an arrow in (b).

A notable frequency dispersion is evident below the temperature of maximum permittivity T_m. A broad peak at T_m can be detected at 182 °C for $NB_{0.50}T$-25ST (Figure 4.3.7 (a)) exhibiting a maximum permittivity ε_{max} of 6023 at 1 kHz. The dielectric loss factor shows a peak value of 0.065 at 100 °C and decreases with increasing temperature up to 300 °C.

By increasing the Bi content, different effects can be observed. While T_m stays almost constant concerning the Bi content, a peak broadening with a simultaneous decrease of ε_{max} can be detected. Bi-depleted NB_xT-25ST (see Figure 4.3.7 (d) and (e)) exhibits a smaller T_m of around 174 °C which comes along with an increase of ε_{max}. The most significant effect, however, can be observed in the dielectric loss. At 250 °C, the loss reaches a value of about 0.5 already indicating a high level of electrical conductivity in those compositions.

The temperature-dependent permittivity, as well as the dielectric loss of stoichiometric and Bi-excess NBxT-25ST compositions, exhibit a second peak at around 120 °C. This second peak is attributed to a conversion of PNRs from their high temperature (HT) towards their low temperature (LT) state (see chapter 2.5.1).[33, 65, 231] The here provided permittivity and loss results fit well to the findings reported in the literature on Bi non-stoichiometry in NB_xT-ST.[64]

Apart from the impact of non-stoichiometry on the dielectric properties in NB_xT-25ST, the effects of B-site doping might elucidate, if NBT-25ST follows comparable mechanisms as NBT-6BT. Figure 4.3.8 ((a) to (c)) therefore illustrates the permittivity and loss for the Nb-doped and Fe-doped NB_xT-25ST compositions ((d) to (f)).

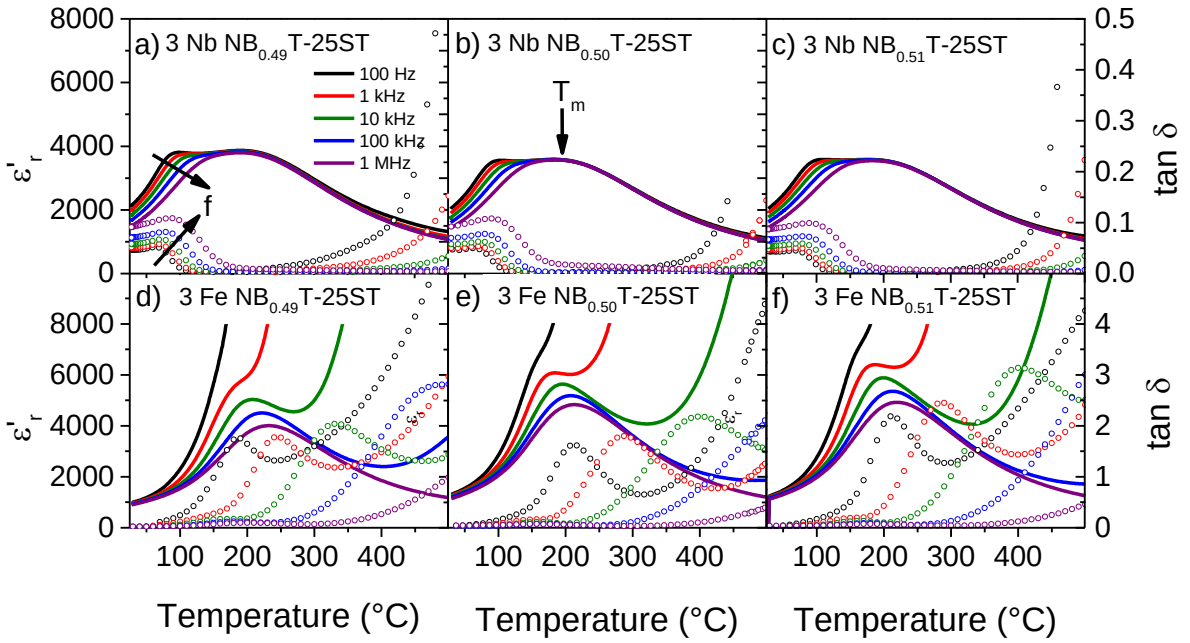

Figure 4.3.8: Frequency-dependent permittivity ε_r' and dielectric loss factor $\tan\delta$ for the Nb-doped ((a) to (c)) and Fe-doped and A-site non-stoichiometric NB_xT-25ST compositions ((d) to (f)); T_m is depicted with an arrow in (b) exemplarily.

T_m appears not to be affected in 3.0 mol% Nb-doped $NB_{0.50}T$-25ST as is stays the same value as for undoped, stoichiometric $NB_{0.50}T$-25ST (182 °C).

Nevertheless, ε_{max} is notably lower compared to undoped compositions with the same stoichiometry (ε_{max} ~ 3582). By adding Bi-excess, ε_{max} stays constant but T_m is going to be slightly decreased (from 182 °C in 3.0 mol% Nb-doped $NB_{0.50}T$-25ST to 176 °C in 3.0 mol% Nb-doped $NB_{0.51}T$-25ST). Bi-deficiency reveals the opposite effect on T_m (increases to 189 °C) while ε_{max} increases to 3847. The effect of Bi-variation on the temperature dependent permittivity is comparable between the Nb-doped and undoped compositions. However, the dielectric loss is significantly reduced for the Nb-doped, Bi-deficient composition with regards to the undoped $NB_{0.49}T$-25ST equivalent. Nb-doping therefore efficiently decreases occurring leakage currents.

Furthermore, the low dielectric loss is detectable, independently on the A-site variation. As already seen for the undoped, non-stoichiometric compositions, a shoulder (in permittivity) and a peak (in dielectric loss) are detectable which are slightly shifted towards lower temperatures (110 °C). This results in a broader temperature window in which the permittivity is rather temperature and frequency independent.

Fe-doping, for instance, leads to an increased permittivity (ε_{max} ~ 6080) and a slightly higher T_m (186 °C) paired with a remarkable increase in the dielectric loss (see Figure 4.3.8 (d) to (f)). The variation of the Bi content leads to an increase of ε_{max} up to 6400 with Bi-excess and a decreases to 5525 with Bi-deficiency while the dielectric loss exceeds unity irrespective of the Bi content. The obtained permittivity values are therefore rather inaccurate above 250 °C.

For comparison reasons, an overview of the maximum permittivity ε_{max} and its corresponding temperature T_m at 1 kHz is given in Figure 4.3.9.

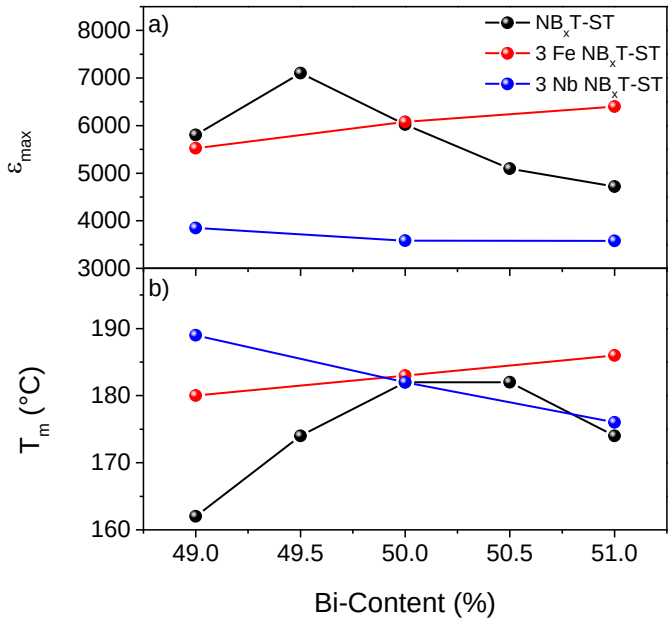

Figure 4.3.9: Comparison of the maximum permittivity ε_{max} (a) and the temperature of maximum permittivity T_m (b) for the Fe-doped (red), Nb-doped (blue) and undoped NB$_x$T-25ST compositions (black) taken at 1 kHz concerning the A-site variation.

Taking the effects of A-site non-stoichiometry and B-site doping into account, it can be concluded that the effects of doping are far more pronounced as the effects of A-site non-stoichiometry as already stated for the microstructure (see chapter 4.3.1) and the electrical properties (see chapter 4.3.2).

Acceptor or donor doping results in a decreasing sensitivity towards A-site non-stoichiometry. The expected effects concerning the increased oxygen vacancy concentration can be seen for the A-site non-stoichiometric compositions as well but doping overwhelms those effects.

In more detail, acceptor doping with Fe leads to a significant increase of the dielectric losses while Nb-doping leads to a decrease and stabilization of the dielectric loss paired with a decrease in the maximum permittivity. The shoulder in the temperature-dependent permittivity is present for all compositions featuring a core-shell structure and could, therefore, be directly related to the chemical inhomogeneity or could also result from the phase transition from LT-PNRs to HT-PNRs.[33, 65, 231] $NB_{0.49}$T-25ST and $NB_{0.495}$T-25ST, however, do not exhibit a shoulder in permittivity even though a small fraction of core-shell structure could be observed via SEM (see Figure 4.3.4). A possible explanation might be that the fraction of core-shell structures is too low to result in a distinct shoulder in the permittivity plots. Several studies on the transition of LT-PNRs to HT-PNRs exist for other NBT-based solid solutions e.g. $x(Na_{0.5}Bi_{0.5}TiO_3)$-$(1-x)(CaZrO_3)$ NBT-CZ[65], $x[y(Na_{0.5}Bi_{0.5}TiO_3)$-$(1-y)(BaTiO_3)]$-$(1-x)(K_{0.5}Na_{0.5}NbO_3)$ NBT-BT-KNN[231], $x[y(Na_{0.5}Bi_{0.5}TiO_3)$-$(1-y)(SrTiO_3)]$-$(1-x)(BaTiO_3)$ NBT-ST-BT[327] and $x[y(Na_{0.5}Bi_{0.5}TiO_3)$-$(1-y)(K_{0.5}Bi_{0.5}TiO_3)]$-$(1-x)(K_{0.5}Na_{0.5}NbO_3)$ NBT-KBT-KNN[33] where the formation of a chemical inhomogeneity by the presence of core-shell structures can at least be assumed. They have, unfortunately, never been investigated towards the direction of possible core-shell formation. A direct relationship between the occurrence of core-shell microstructures and the influence on the PNRs could therefore not be evidenced.

To further address the question regarding the correlation between core-shell structures and the ferroelectric and piezoelectric properties, polarization and strain hysteresis loops under electric field were taken for all processed compositions at room temperature (see Figure 4.3.10). A relaxor can be divided into an ergodic and a non-ergodic state (see chapter 2.5.1). NBT-25ST should contain a mixture of both, an ergodic (shell) as well as a non-ergodic (core) relaxor state at room temperature caused by chemical inhomogeneity. For direct comparability, all specimens were measured under a maximum electric field of 6 $kVmm^{-1}$. The strain values at zero electric field have been normalized to zero for better comparability.

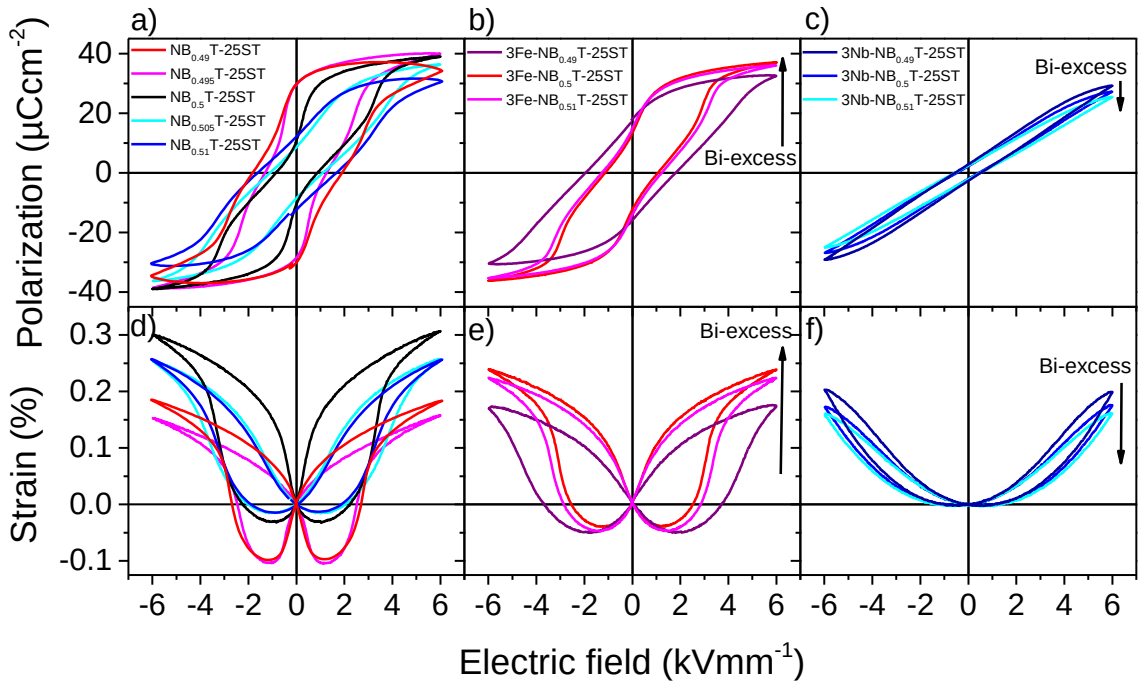

Figure 4.3.10: Polarization and strain responses of the A-site non-stoichiometric ((a) and (d)), Fe-doped ((b) and (e)) and Nb-doped (c and f) NB_xT-25ST compositions taken at 1 Hz and room temperature.

The polarization (a) and strain hysteresis loops (d) for A-site non-stoichiometric NB_xT-25ST compositions are given. Stoichiometric NBT-25ST exhibits a pinched polarization hysteresis with a saturation polarization P_{sat} of 39.13 µCcm^{-2} and a remanent polarization P_{rem} of 10.43 µCcm^{-2}. Acosta *et al.* also reported a pinched polarization loop and a similar strain response for NBT-25ST.[63] The pinched polarization loops have been attributed to the presence of core-shell structures.[63] Additionally, comparable results have already been reported for NBT-BT-KNN which did not provide evidence for core-shell mircostructures.[41, 63, 328]

The pinched hysteresis was claimed to be caused by a reversible electric field-induced phase transition between a long-range ferroelectric order and a mixed ergodic relaxor state.[63] The reversible electric field-induced ferroelectric long-range order results in a pinched polarization hysteresis (see also chapter 2.5.1).

Additionally, the switching dynamics might be influenced by nucleation processes at the core-shell interfaces. Furthermore, the volumetric core/shell ratio results in a different strain response.[63] These phenomena lead to an increased strain contributing to the total measured strain response.[118-120] Hence, a maximum positive strain of 0.307 % could be reached for stoichiometric NBT-25ST. $NB_{0.50}$T-25ST, for instance, features a mixture between a butterfly-shaped strain response typical for a ferroelectric, non-ergodic relaxor, material and a sprout shaped loop, typical for an ergodic relaxor.

By taking a closer look on the non-stoichiometric compositions, Bi-excess leads to a decreased remanent polarization paired with a slimmer hysteresis loop and a slightly more sprout shape strain response with a maximum positive strain of about 0.257 % and a nearly vanishing negative strain of about 0.016 % (see Figure 4.3.10 (d)). Based on these findings, it can be concluded that Bi-excess stabilizes the ergodic relaxor response in NBT-25ST. It should be noted, that the saturation polarization for $NB_{0.51}$T-25ST decreases while the strain hysteresis stays nearly unaffected.

Bi-deficiency leads to a larger remanent polarization of 29.4 µCcm^{-2} and a broader hysteresis. The strain hysteresis shifts towards negative direction leading to a decrease in the maximum positive strain to 0.158 % but a far more pronounced maximum negative strain of about 0.105 %. Based on this, Bi-deficiency leads to an almost complete transformation into a non-ergodic relaxor resembling a ferroelectric response. With regards to the previous discussion about the impact of Bi-excess, the A-site non-stoichiometry influences the fraction of ergodic and non-ergodic relaxor states. This finding can be supported by recent work by Frömling *et al.*.[64]

The polarization and strain responses of Fe-doped NB_xT-25ST compositions are presented in Figure 4.3.10 (b) and (e). Acceptor doping features a significant impact on the remanent polarization which is in the range of the Bi-deficient, undoped NB_xT-25ST compositions. Additionally, the strain response shifts towards the negative direction with a maximum positive strain of 0.239 % and a negative strain of 0.039 % exhibiting non-ergodic relaxor behavior. Bi-excess only features a minor impact on polarization (a shift from P_{rem} = 17.05 µCcm^{-2} to P_{rem} = 13.86 µCcm^{-2} with increasing Bi content) as well as strain responses (a shift from S_{pos} = 0.17 % to S_{pos} = 0.24 % with increasing Bi content). Bi-deficiency, for instance, results in a broader polarization and strain response paired with a decreased saturation polarization which might be caused by an increased leakage current.

Nb-doping always leads to a slim, non-pinched polarization hysteresis (see Figure 4.3.10 (c)). The maximum polarization is 27.21 µCcm^{-2}. Additionally, the remanent polarization decreases to a value of 2.01 µCcm^{-2}. A sprout shape strain response can be detected with no negative strain and a quadratic increase to a maximum positive strain of 0.176 % at 6 kVmm^{-1} (see Figure 4.3.10 (f)). With regards to the occurrence of core-shell microstructures and the influence on the piezoelectric and ferroelectric properties, it should be noted that a mixed ergodic/non-ergodic relaxor behavior was assumed as Nb-doping leads to a stabilization of core-shell microstructure (see chapter 4.3.1). This is, however, not the case for Nb-doping. The presented results of ergodic relaxor behavior can be explained by a change of the relaxor behavior of the NBT core itself from non-ergodic towards ergodic behavior. The behavior could be characterized by electrostriction (see Figure A3 in the appendix).

It should be highlighted, that, comparable to the Fe-doped NB_xT-25ST compositions, additional A-site variation does not provide such a pronounced impact the polarization and strain response compared to the undoped compositions. Nevertheless, Bi-excess leads to a decrease of the maximum polarization paired with a decrease of the maximum strain. Bi-deficiency exhibits the opposite trend. For comparison reasons, Figure 4.3.11 summarizes the extracted polarization and strain values for all undoped and doped NB_xT-25ST compositions.

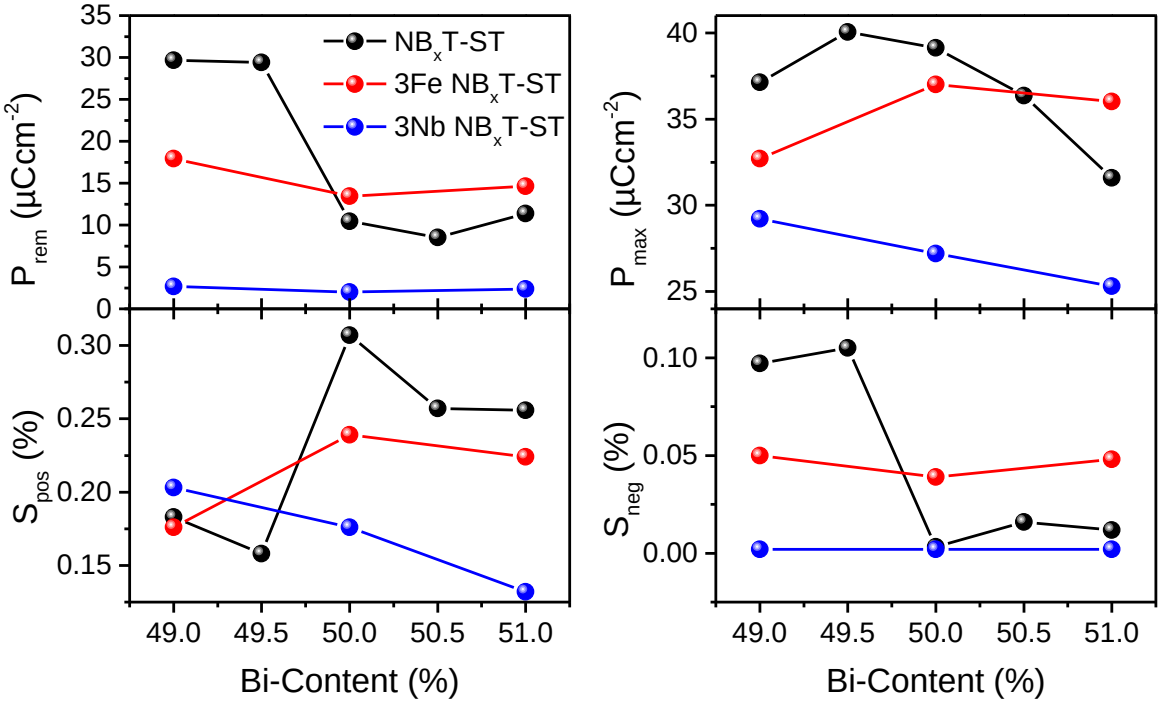

Figure 4.3.11: Comparison of the remanent polarization P_{rem}, the maximum polarization P_{max}, the maximum positive strain S_{pos} and the maximum negative strain S_{neg} concerning Fe- (red), Nb-doping (blue) and A-site non-stoichiometry black)of the NB_xT-25ST composition.

It is known from the literature that the present core-shell microstructure influences the ferroelectric and piezoelectric properties.[63, 222] It could already be proven that the Sr-depleted core, which mainly consists of NBT, exhibits a non-ergodic relaxor state at RT while the Sr-enriched shell is in an ergodic relaxor state.[63, 222]

The here presented results deliver proof that the microstructural modulation by A-site non-stoichiometry and B-site doping significantly impact the ergodic/non-ergodic polarization and strain responses in NB_xT-25ST. In detail, Bi-depletion leads to a remarkable reduction of the core-shell concentration. With regards to the obtained polarization and strain responses, it can be concluded that there is a close relationship between the detectable fraction of core-shell structures and the ferroelectric responses. Decreasing the fraction of core-shell structures shifts the ferroelectric responses at room temperature from an ergodic towards a non-ergodic behavior. For the B-site doped compositions, a similar picture can be drawn. Donor doping with Nb leads to a high core-shell concentration, independent on A-site variation. Those compositions, however, show ergodic relaxor behavior. This leads to the conclusion that additional doping could also affect the particular ergodic relaxor behavior of the core and shell region resulting in ergodic relaxor behavior even though core-shell microstructures could be evidenced. Fe-acceptor doped compositions, which have been proven to exhibit a noticeably lower core-shell concentration, provide non-ergodic responses.

4.3.4 Doped and A-site Non-Stoichiometric NBT-ST: Summary

Concerning the discussed impedance spectra and Arrhenius plots, it should be highlighted, that all compositions with core-shell microstructure feature semiconducting behavior while all compositions featuring high electrical conductivity do not provide a detectable core-shell structure, except for the $NB_{0.495}$T-25ST composition. This composition exhibits at least a minor fraction of core-shell structures but therefore also shows a lower electrical conductivity compared to the Fe-doped NB_xT-25ST and the $NB_{0.49}$T-25ST compositions. The Arrhenius plots highlight a similar change from low, semiconducting, towards high, ionic conducting, behavior with regards to A-site non-stoichiometry and acceptor doping, proving that the solid solution NBT-25ST follows the same defect chemistry as NBT (see chapter 4.3.2).

By a detailed analysis of the temperature dependent dielectric properties, a shoulder in the permittivity below T_m could be observed for compositions that exhibit core-shell structures. A composition-dependent shift of the shoulder could be detected which could either be attributed to the occurrence of core-shell structures or the transition from HT-PNRs to LT-PNRs. A frequency dispersion is present for all investigated NB_xT-25ST compositions confirming the relaxor nature of this system. The dielectric losses notably increase with Bi-deficiency as well as Fe-acceptor doping and decrease for Bi-excess and Nb-doping.

The piezo- and ferroelectric properties reveal a mixed ergodic/non-ergodic behavior, shifting from non-ergodic towards ergodic relaxor behavior by a systematic increase of the Bi content at room temperature. Pinched polarization loops are present for the Bi-excess compositions which have exhibited a higher fraction of core-shell structures. Acceptor doping with Fe also leads to pinched polarization loops paired with butterfly strain hysteresis. Donor doping with Nb features ergodic behavior resulting in slim polarization loops combined with sprout shape strain responses which are attributed to the change of the relaxor nature of the NBT core from non-ergodic towards ergodic behavior due to donor doping (see chapter 4.3.3). Concerning the microstructural analysis, a strong correlation between the formation and presence of core-shell structures and the resulting dielectric and ferroelectric properties can be concluded especially for the undoped, non-stoichiometric cases. It should be highlighted, that B-site doping overwhelms the effects of additional A-site non-stoichiometry. While a shift between non-ergodic and ergodic behavior could be observed by A-site non-stoichiometry, B-site doping leads to either completely non-ergodic (Fe-acceptor doping) or completely ergodic behavior (Nb-donor doping).

The microstructural analysis of B-site doped, A-site non-stoichiometric NB_xT-25ST by XRD, SEM, and EDX revealed the occurrence of core-shell microstructures and the formation of secondary phases related to B-site doping.

By direct comparison of A-site non-stoichiometry and B-site acceptor doping, a larger effect of doping on the resulting microstructure could be confirmed, overwhelming the apparent effects of A-site non-stoichiometry (see chapter 4.3.1). Based on these findings, it can be stated that high oxygen vacancy concentration and/or mobility suppresses the formation of a chemical inhomogeneity such as core-shell structures while decreasing the oxygen vacancy concentration and/or mobility leads to the stabilization of such structures due to a decrease of the Sr diffusion. This is indirect evidence that the impact of oxygen vacancies is larger compared to generating Bi A-site vacancies when it comes to Sr diffusivity and the resulting core-shell formation.

4.4 Application of the Defect Chemistry to Develop High-Temperature Capacitors

4.4.1 The Solid Solution NB_xT-6BT-yCZ

With the application of the gained knowledge about property related effects of defect chemistry in NBT and NBT-based solid solutions, it should be possible to further extend the application range of the respective systems. As could have been shown in the previous chapters, that the A-site, as well as the B-site defect chemistry, features a significant impact not only on the ferroelectric and piezoelectric, but also the electrical conductivity and the dielectric properties.

Concerning application as a dielectric material for capacitors, the dielectric losses need to be small. This becomes even more crucial for harsh conditions like high environmental temperatures. During the past decade, the worldwide demand for high-temperature capacitor materials has steadily increased.[329] Capacitors that can handle harsh conditions are mandatory for monitoring systems for automotive, aviation and aerospace applications. The implemented dielectrics have to function reliably at temperatures between -55 °C up to 300 °C with a sufficiently high capacitance.[329-333]

High band gap materials like SiC which can withstand drastic heat generation due to high power pulses lead to a growing demand for increasing high-temperature performance of other components like capacitors placed in their vicinity.[334] Commercially established capacitor materials are not able to fulfill those requirements, yet. Hence, high-temperature capacitors are seen as kind of a bottleneck to further enhance the field of high-temperature electronics. This is where ceramic capacitors come into play. As ceramics can withstand high temperatures without degradation or decomposition, these are under the most promising candidates to fill the gap of suitable high-temperature capacitor materials.[329, 335]

A major impediment of ceramic capacitors based on ferroelectric materials is the fact, that, even though high absolute values for the permittivity can be reached, it is not temperature stable. Above T_C, ferroelectrics become paraelectric (see also chapter 2.5). Relaxors, which exhibit a broader temperature of maximum permittivity peak, are therefore much more attractive. As discussed by Figure 2.5.4, the presence and coexistence of LT- and HT-PNRs further results in an almost temperature-independent permittivity.[65, 117, 231, 336] This is crucial for the utilization as a high-temperature dielectric material. The typically used benchmark temperature for high-temperature capacitors is 150 °C.[333] For a so-called ferroelectric type II capacitor, the permittivity and so the capacitance must not vary more than ±15 % compared to the benchmark value (at 150 °C) and further defines the temperature range of application which should be from -55 °C to +125 °C.[65, 226, 329, 337]

Besides the temperature stability of the permittivity, microelectronics that cover high capacitance, as well as energy/power density, are also of major interest (see also chapter 2.5.2). Zeb and Milne recently provided a summary of the most promising lead-free high-temperature dielectrics focusing on BT-based[338-340], NBT-based[65, 341] and KNN-based dielectrics.[329]

(1-x)[0.94$Na_{0.5}Bi_{0.5}TiO_3$-0.06$BaTiO_3$]-x($CaZrO_3$) (NBT-6BT-xCZ), for instance, is reported to be an excellent candidate for high-temperature capacitor materials according to an almost temperature-independent high permittivity plateau (variations of ε_r'(150 °C) ± 15 %) and low dielectric loss factors $\tan\delta \leq 0.02$ over an exceptional temperature range.[65, 329, 341, 342] Systematically increasing the Zr content results in a broader temperature range with stable permittivity down to lower temperatures.[65, 343] The desired temperature window between -55 °C and 300 °C could not be reached by NBT-BT-CZ as the dielectric losses do, in contrast to the exceptionally stable permittivity, not stay in the desired region of $\tan\delta \leq 0.02$ within the given temperature range. Based on the here presented results and also recent studies, the modulation of the A-site stoichiometry strongly affects the electrical properties as well as the microstructure in NBT and NBT-based systems.[48, 49, 62, 156, 157, 187, 285, 344, 345] Beuerlein *et al.* reported, that BT based compositions behave similarly to NBT-based compositions concerning an occurring A-site non-stoichiometry.[346] Additionally, Qiao *et al.* claimed that Bi-deficiency leads to the formation of space charges which generally influence the permittivity and dielectric loss.[345] Up to which degree the so introduced Bi and corresponding oxygen vacancies affect the dielectric properties, depends on the respective solid solution. For NBT-6BT, the effects on the dielectric properties have already been presented (see chapter 4.2.3). NBT-25ST evidenced a rather strong sensitivity on the A-site non-stoichiometry comparable with the basic system NBT (see chapter4.3.3). Hence, a notable impact on the dielectric properties can be expected for the high-temperature dielectric material NB_xT-6BT-yCZ. Concerning solving the problem of increasing dielectric losses at high temperatures, another approach by Yang *et al.* where a solid solution of NBT was formed with $BiAlO_3$ (BA) is taken into account.[347] The formation of a solid solution with BA resulted in notably decreased dielectric losses at elevated temperatures in NBT. This effect was attributed to additional trap states for oxygen vacancies by forming a solid solution with $BiAlO_3$ without increasing the oxygen vacancy concentration due to acceptor doping effects.

The following questions shall, therefore, be addressed in this chapter:

- Does the NBT-based system NB_xT-6BT-yCZ exhibit the same sensitivity towards A-site non-stoichiometry like NBT, NBT-6BT, and NBT-25ST?
- Can the operating range with temperature-independent permittivity and low dielectric losses be extended by applying the gained defect chemical knowledge?
- Does a compositional tuning with $BiAlO_3$ result in an enhancement of the temperature dependent dielectric properties?
- Do the compositional changes result in sufficiently large dielectric energy storage density and efficiency?

To answer the remaining questions, a detailed discussion on the effects of A-site non-stoichiometry as well as the CZ content variation in NB_xT-6BT-yCZ is provided. Furthermore, those results are used to determine the composition which covers the most promising properties concerning temperature stable permittivity and low dielectric losses. The here presented results about the effects of A-site non-stoichiometry in combination with a variation of the CZ content on the system NB_xT-6BT-yCZ have already been published as a Journal of Materials Chemistry C article in close collaboration with Marion Höfling.[66]

To further enhance the temperature-dependent dielectric properties of the so determined NBT-BT-CZ composition, another approach to reduce the dielectric losses at elevated temperatures will be taken into account, based on a recent publication by Yang *et al.* where a solid solution of NBT was formed with $BiAlO_3$ (BA).[347] This approach led to almost complete suppression of oxygen ionic conductivity and significantly reduced dielectric losses at high temperatures still being a major issue for the here investigated NB_xT-6BT-yCZ system. The aim of this chapter is to highlight the possible extension of the application range of NBT and its solid solutions by precise control of the defect chemistry.

4.4.2 NB_xT-6BT-yCZ: Microstructure

The phase purity and the crystal structure of NB_xT-6BT-yCZ are investigated with the help of XRD. It is known from the literature, that the variation of the CZ content in NBT-6BT-xCZ results in the formation of secondary phases.[65] To resolve, if A-site non-stoichiometry affects the tendency to form secondary phases in this system, the XRD pattern taken for NB_xT-6BT-yCZ compositions is given in Figure 4.4.1.

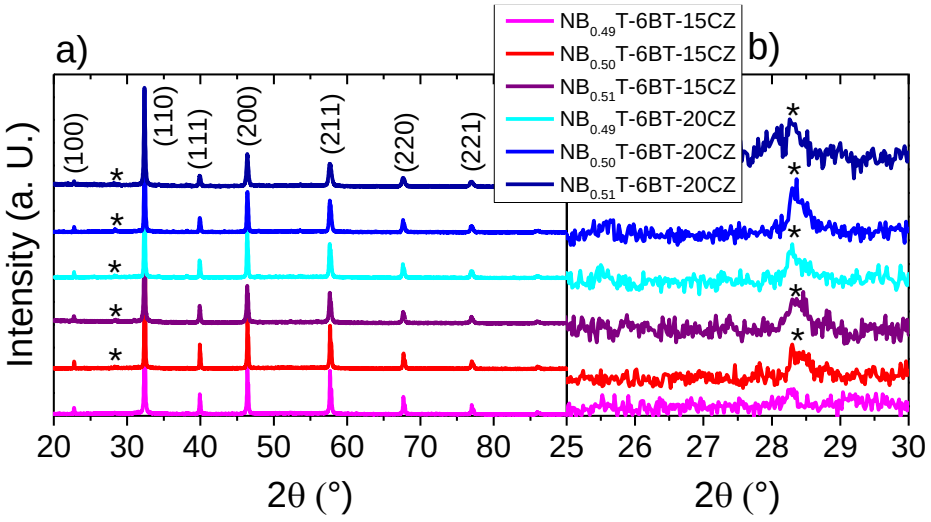

Figure 4.4.1: XRD-pattern of the A-site non-stoichiometric NB_xT-6BT-15CZ (magenta, red and violet) and NB_xT-6BT-20CZ (cyan, blue and dark blue) compositions (a). The peaks caused by secondary phases are denoted with a star. The respective region is shown in (b) in more detail.

A pseudo-cubic structure is evident at room temperature which is consistent with literature reported for other NBT-based solid solutions.[62, 65, 342, 348] A secondary phase starts to form for the Bi-enriched and stoichiometric NB_xT-6BT-15CZ as well as NB_xT-6BT-20CZ compositions (denoted with a star). The Bi-deficient $NB_{0.49}T$-6BT-15CZ was the only composition where no secondary phases have been evidenced by XRD. A general statement on the effect of A-site non-stoichiometry on phase purity in NB_xT-6BT-yCZ can therefore not be given at this point. It should be noted, that NBT-6BT-15CZ was confirmed to exhibit a core-shell microstructure representing occurring chemical inhomogeneity concerning the CZ content.[66]

The presence of mobile defects like oxygen vacancies is also presented to significantly affect the grain size (see chapter 4.2.7). In Table 4.4-1, the grain sizes of the particular A-site non-stoichiometric NB_xT-6BT-yCZ compositions are listed. The strong correlation of the Bi content and the resulting grain size can also be supported by several publications for example by Qiao *et al.*[345] and Sung *et al.*.[156] Additional Bi-excess does not seem to have any effects on the grain size in the NBT-6BT-yCZ system.

This coincides well with the assumption that excess Bi is only capable to counteract the formation of additional Bi vacancies during the processing.

The remaining Bi tends to form secondary phases. Bi-deficiency, for instance, leads to the generation of oxygen vacancies due to charge compensation. The generated oxygen vacancies are attributed to be responsible for the deviation in the microstructure.[27, 156-158, 236, 289] Based on existing literature, increased oxygen vacancy concentration could be the reason for a change from faceted to rough grain boundaries.[62] This affects the driving force for grain boundary movement and, in consequence, the grain growth.[236, 289]

4.4.3 NB_xT-6BT-yCZ: Dielectric Properties

To reveal the effect of A-site non-stoichiometry and CZ content variation on the temperature dependent dielectric permittivity and loss, Figure 4.4.2 presents ε_r' and $\tan\delta$ of the A-site non-stoichiometric and CZ content varied NB_xT-6BT-yCZ compositions. The aim is to find the most suitable composition for further investigations with the $BiAlO_3$ addition approach.

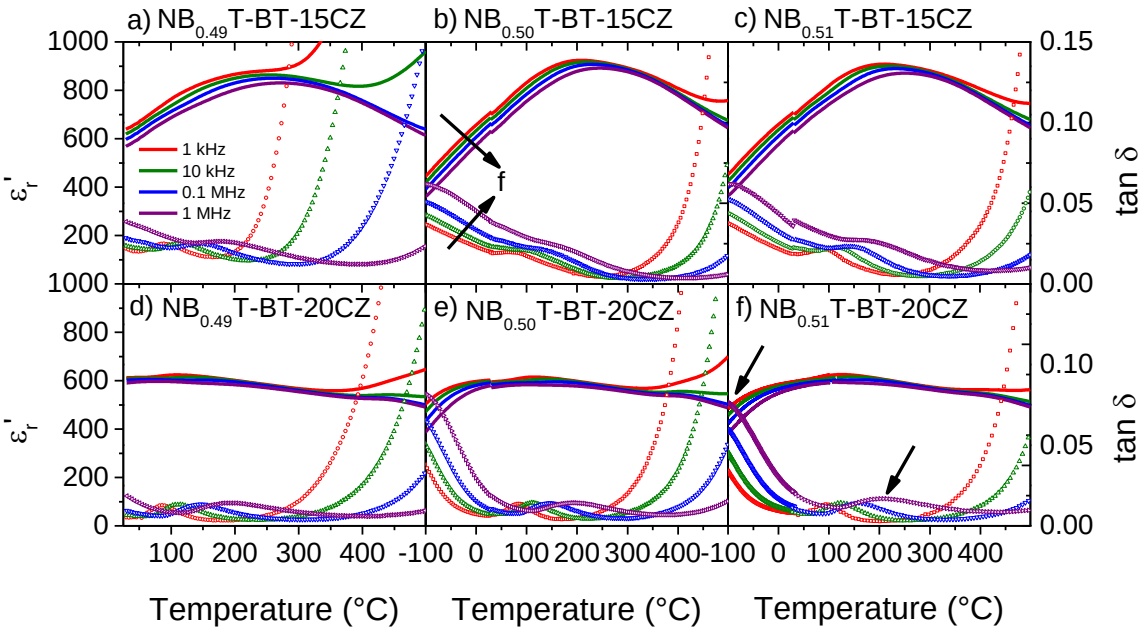

Figure 4.4.2: Temperature and frequency-dependent permittivity ε_r' and dielectric loss factor $\tan\delta$ for the A-site non-stoichiometric NB_xT-6BT-15CZ ((a) to (c)) and the NB_xT-6BT-20CZ compositions ((d) to (f)). The two anomalies detected for the dielectric loss are denoted with arrows in (f).

A frequency dispersion is evident for all illustrated compositions (exemplary depicted with arrows in Figure 4.4.2 (b)). The frequency dispersion decreases with increasing Bi content. A decrease of the frequency dispersion is related to a change of the dynamic fluctuation[211] which is strongly affected by a lower concentration of charged defects due to Bi-excess.[157] Moreover, increasing the CZ content also leads to a decrease of the frequency dispersion over the investigated temperature range (see Figure 4.4.2 (d) to (f)). Additional changes of the A-site non-stoichiometry do not affect the resulting permittivity noticeably. As a general observation, the maximum permittivity of the 15CZ compositions is always larger (ε_r' = 864 - 924) compared to the 20CZ compositions (ε_r' = 615 - 630). This, however, comes along with a larger temperature dependence of the permittivity.

Two local maxima for the dielectric losses are detectable for the Bi-excess $NB_{0.51}$T-6BT-20CZ composition (denoted by arrows in Figure 4.4.2 (f)). Those could be explained by the presence of two different types of PNRs (see also NBT-25ST in chapter 4.3.3).[117, 231, 336]

According to Zang *et al.*, the first local maximum (slightly below -110 °C at 1 MHz) corresponds to a transition from the non-ergodic to the ergodic relaxor state where rhombohedral low-temperature nano regions are generated.[231] The second local maximum (at 215 °C for 1 MHz) is therefore related to a coexistence of rhombohedral (low-temperature LT) and tetragonal (high-temperature HT) polar nano regions.[65, 117, 231, 336] The presence and the temperature-dependent overlap of LT- and HT-PNRs is claimed to be the reason for the pronounced temperature plateau at which the permittivity is almost temperature independent. This plateau forms in the stoichiometric as well as the Bi-excess NB_xT-BT-20CZ compositions.[117, 231, 336] By increasing the CZ content, the correlation length between the polar nano regions decreases and, as a consequence, the stability of the corresponding polar nano regions is reduced.[115, 228-230] Especially those compositions, exhibiting almost temperature-independent permittivity, are of major interest from an application point of view and is even more essential than the mere maximum value of the permittivity.[65] The typically used benchmark temperature for high-temperature capacitors is 150 °C.[333] For a so-called ferroelectric type II capacitor, the permittivity and so the capacitance must not vary more than ±15 % compared to the benchmark value (at 150 °C) and further defines the temperature range of application which should be from -55 °C to +125 °C.[65, 226, 329, 337] In Table 4.4-1, the application relevant values of the different NB_xT-BT-yCZ compositions are provided.

Table 4.4-1: Grain size, density, dielectric permittivity ε_r' at 1 kHz, temperature stability criteria for permittivity and dielectric loss $\tan\delta$ as well as recoverable energy W_{rec} and efficiency η of the NBxT-6BT-yCZ compositions.

Compo-sition	Grain size (µm)	Den-sity (%)	ε_r' (150 °C)	T (ε_r'±15%) (°C)	T (tanδ≤0.02) (°C)	ΔT (ε_r'±15%; tanδ≤0.02) (K)	W_{rec} (mJcm^{-3})	η (%)
$NB_{0.49}$T-BT-15CZ	3.7	89	829.4	69 - 321	125 - 200	75	52	84
$NB_{0.50}$T-BT-15CZ	2.4	97	896.3	63 - 459	23 - 365	302	64	88
$NB_{0.51}$T-BT-15CZ	2.2	97	882.6	60 - 476	106 - 356	250	56	89
$NB_{0.49}$T-BT-20CZ	3.4	95	617.2	<30 - >500	30 - 315	285	45	91
$NB_{0.50}$T-BT-20CZ	2.5	96	610.8	-87 - >500	-66 - 300	366	45	97
$NB_{0.51}$T-BT-20CZ	2.6	96	622.7	-72- >500	-67 - 362	429	44	97

The stoichiometric $NB_{0.50}$T-6BT-15CZ composition reaches a ΔT in which the permittivity criterion holds of about $\Delta T(\varepsilon_r' \pm 15\ \%) \approx 396$ K. By increasing the CZ content ($NB_{0.50}$T-6BT-20CZ), the temperature range further increases from -87 °C up to above 500 °C representing the measurement limit. Bi-excess only slightly changed this temperature region. Besides the permittivity at 150 °C and the temperature range in which the stable permittivity criterion is fulfilled, the temperature dependent dielectric losses are of major importance. A benchmark for the dielectric losses can be taken from literature and is set to a value of $tan\delta \leq 0.02$.[329] The corresponding parameters for the here investigated compositions can also be taken from Table 4.4-1.

The Bi-excess composition $NB_{0.51}$T-6BT-20CZ exhibits the largest temperature range where the loss criterion $T(\tan\delta) \leq 0.02$ holds (from -67 °C to 362 °C). It should be noted, that the dielectric loss $\tan\delta$ occasionally is even below 0.01 in the given temperature region. Those values are already considerably larger than what was reported in the literature about NBT-6BT-20CZ.[65, 329] Nevertheless, all compositions suffer increased dielectric losses with increasing temperature due to the contribution of temperature-dependent electrical conductivity.[5, 349] The frequency dispersion below 0 °C also leads to a decreased temperature window in which both criteria are fulfilled. As both criteria have to be fulfilled simultaneously, the best choice for a further investigation with $BiAlO_3$ addition was spotted to be the stoichiometric NBT-6BT-20CZ composition. A simple increase of the Bi content did not lead to significant improvements in the dielectric properties and might be detrimental with regards to higher chemical disorder when $BiAlO_3$ is added to the system. This result, however, highlights that a mere overcompensation of possible Bi loss not necessarily leads to better properties.

4.4.4 NB_xT-6BT-yCZ with BA Addition: Microstructure

To further decrease the dielectric losses at elevated temperatures, another approach based on Yang *et al.* was utilized. It was reported that forming a solid solution of NBT with $BiAlO_3$ (BA) leads to excellent high-temperature dielectric properties.[347] In the following, the effects of BA addition in the NBT-6BT-20CZ-yBA system will be discussed. For the system NBT, a solubility limit of 8.0 mol% BA was reported.[347] A secondary CZ-rich phase formation can be observed in the case of NBT-6BT-20CZ (see Figure 4.4.1). An addition of BA might influence the secondary phase formation as well. Figure 4.4.3 illustrates the XRD pattern of the NBT-6BT-20CZ-xBA (x= 0.0, 0.5, 1.0, 1.5, 2.0, 4.0 and 8.0 mol%).

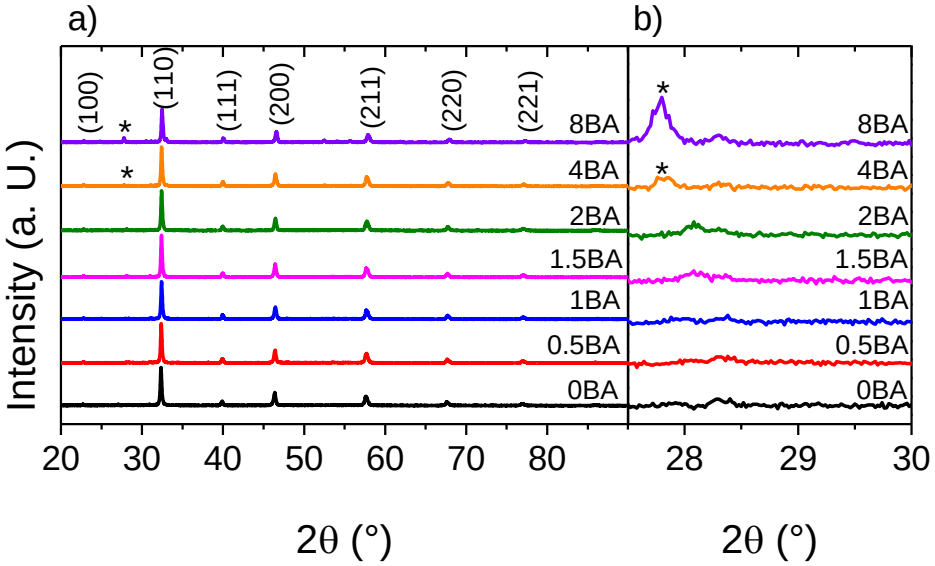

Figure 4.4.3: XRD-pattern of the NBT-6BT-20CZ-xBA compositions with x= 0.0, 0.5, 1.0, 1.5, 2.0, 4.0 and 8.0 mol%. A full scan from 2θ = 20° to 2θ = 90° is provided in (a). The peaks caused by secondary phases are denoted with a star and are shown in detail in (b).

The XRD pattern of the processed NBT-6BT-20CZ-xBA compositions represents a pseudo-cubic structure which is in good agreement with other NBT-based systems reported in the literature.[40, 62, 65, 342] Up to 2.0 mol% BA addition, no secondary phase is detectable in the XRD pattern. With regards to the 4.0 mol% and 8.0 mol% BA composition, an additional peak is observable at 2θ = 27.5° BA addition therefore reveals a significant effect on the tendency to form secondary phases. EDX analysis proved the secondary phases (bright regions in the BSE images in Figure 4.4.4) to be Bi-rich with a Bi content of about 90 %.

An annealing study of the processed samples revealed that BA further features a beneficial effect on the temperature stability of the composition. Representative SEM images in the BSE mode for NBT-6BT-20CZ ((a) and (b)) and NBT-6BT-20CZ-1.5BA ((c) and (d)) are provided in Figure 4.4.4.

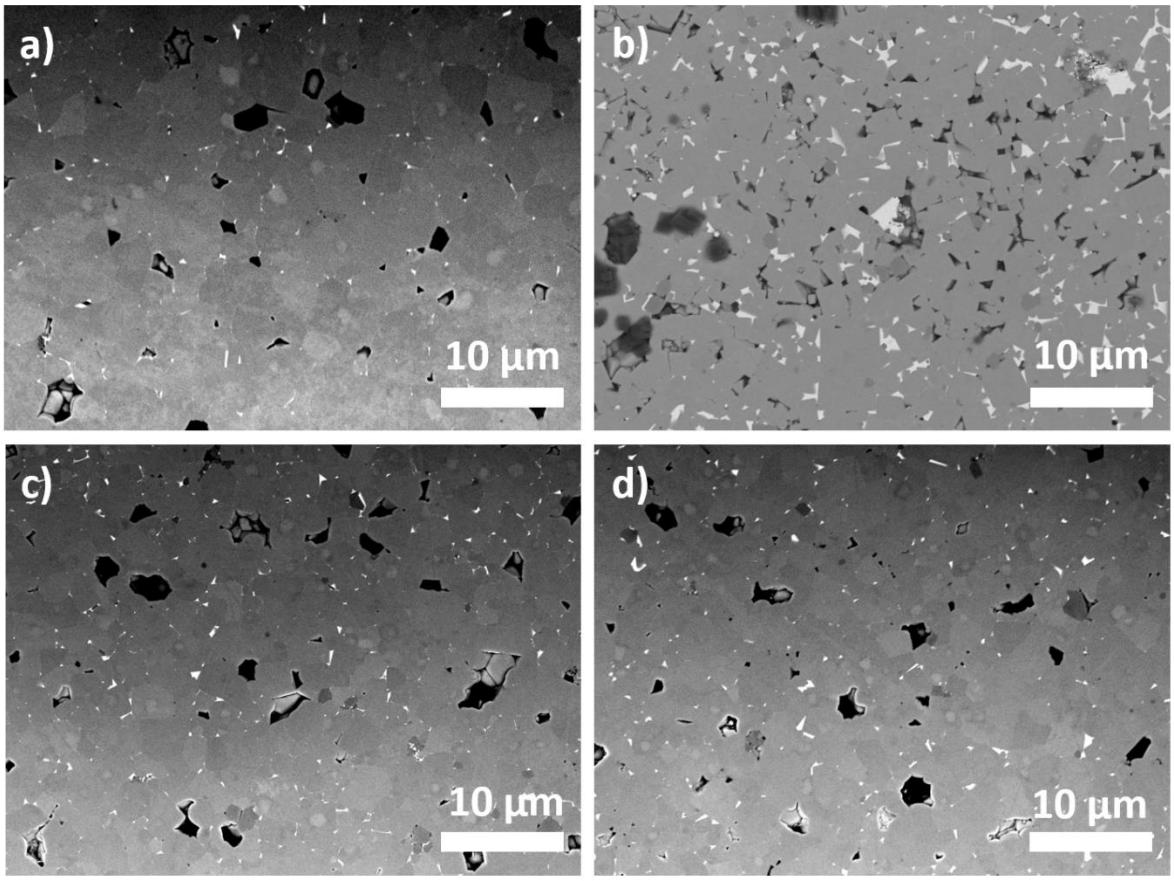

Figure 4.4.4: SEM-Images of pure NBT-6BT-20CZ after sintering (a) and an additional annealing at 750 °C for 12 h (b) compared to NBT-6BT-20CZ with 1.5 mol% BA addition after sintering (c) and an additional annealing step at 750 °C for 12 h (d) in the backscattered electron mode (BSE).

After annealing the samples for 12 h at 750 °C, a notable amount of secondary phases occurs in the NBT-6BT-20CZ without BA addition. The compositions with additional BA displayed increased temperature stability. Based on those results, low amounts of BA addition (up to 2.0 mol%) provide a beneficial effect on the temperature stability but exhibits a lower solubility limit in NBT-6BT-20CZ than compared to 8.0 mol% in NBT.[347]

4.4.5 NB_xT-6BT-yCZ with BA Addition: Dielectric Properties

Apart from the tendency to form secondary phases by BA addition, the main focus is set on the decrease of dielectric losses at elevated temperatures. Therefore, the temperature-dependent permittivity ε_r' as well as the dielectric loss $\tan\delta$ for the NBT-6BT-20CZ-xBA compositions are depicted in Figure 4.4.5 and Figure 4.4.6.

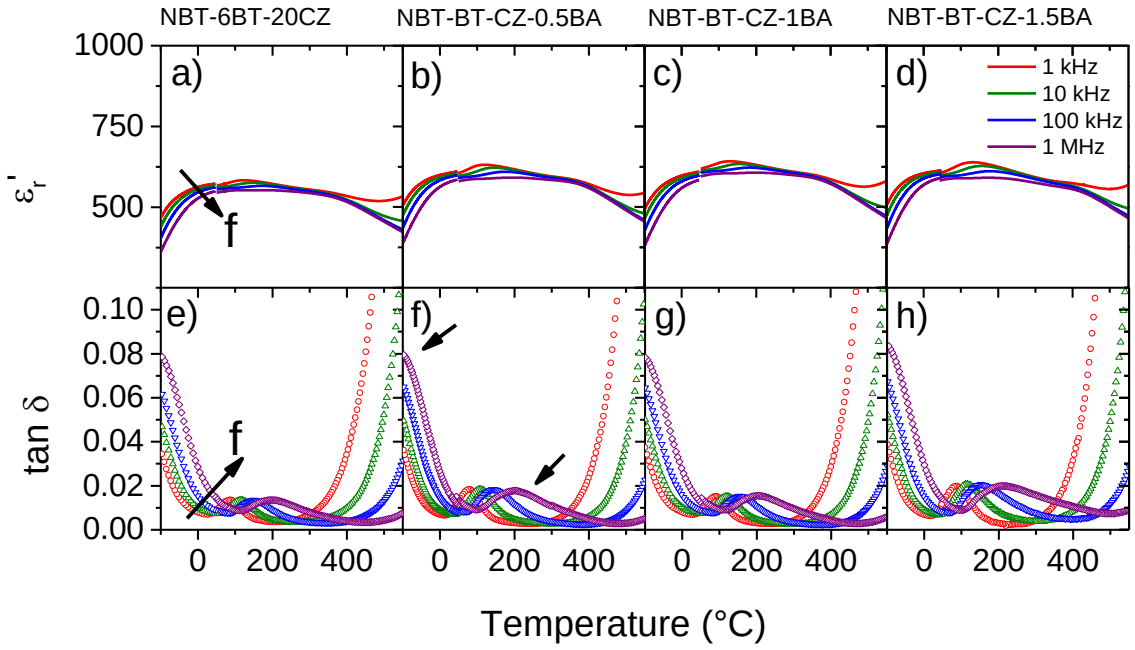

Figure 4.4.5: Temperature and frequency-dependent permittivity and dielectric loss factor for the NBT-6BT-20CZ-xBA compositions with x= 0.0 ((a) and (e)), 0.5 ((b) and (f)), 1.0 ((c) and (g)), and 1.5 ((d) and (h)) mol%. The frequency dispersion is depicted with an arrow in (a) and (e) exemplarily. The two local maxima in the dielectric loss are depicted with arrows in (f).

The NBT-6BT-20CZ-xBA compositions with x = 0.0, 0.5, 1.0 and 1.5 mol% exhibit a frequency dispersion in permittivity and dielectric loss (denoted with arrows in Figure 4.4.5 (a) and (e)). The frequency dispersion of the permittivity is more pronounced below 0 °C and above 400 °C. Within this temperature window, a frequency and also almost temperature-independent plateau is forming. It should be mentioned, that the maximum relative permittivity is only slightly affected by the addition of a low BA content. ε_r' slightly increases from 582 (NBT-6BT-20CZ) to 630 – 641 (for NBT-6BT-20CZ-xBA with x= 0.5, 1.0, 1.5 mol%) (see also Table 4.4-2). The temperature-independent permittivity plateau which was initially found for NBT-6BT-20CZ is also evident for the BA added compositions and can be regarded to the coexistence of low temperature (LT) and high temperature (HT) polar nano regions as already discussed for the NB_xT-6BT-yCZ compositions in chapter 4.4.3.[65, 117, 231, 336]

Small contents of BA up to 1.5 mol% lead to an increase in the range where the dielectric losses are below 0.02. The NBT-6BT-20CZ-0.5BA composition features an outstanding temperature range of -68 °C to 391 °C for 1 kHz where the dielectric losses are well below the desired value of 0.02. The losses are moreover almost frequency independent. Further increasing the BA content, however, reveals a detrimental effect on the dielectric permittivity and loss (see Figure 4.4.6).

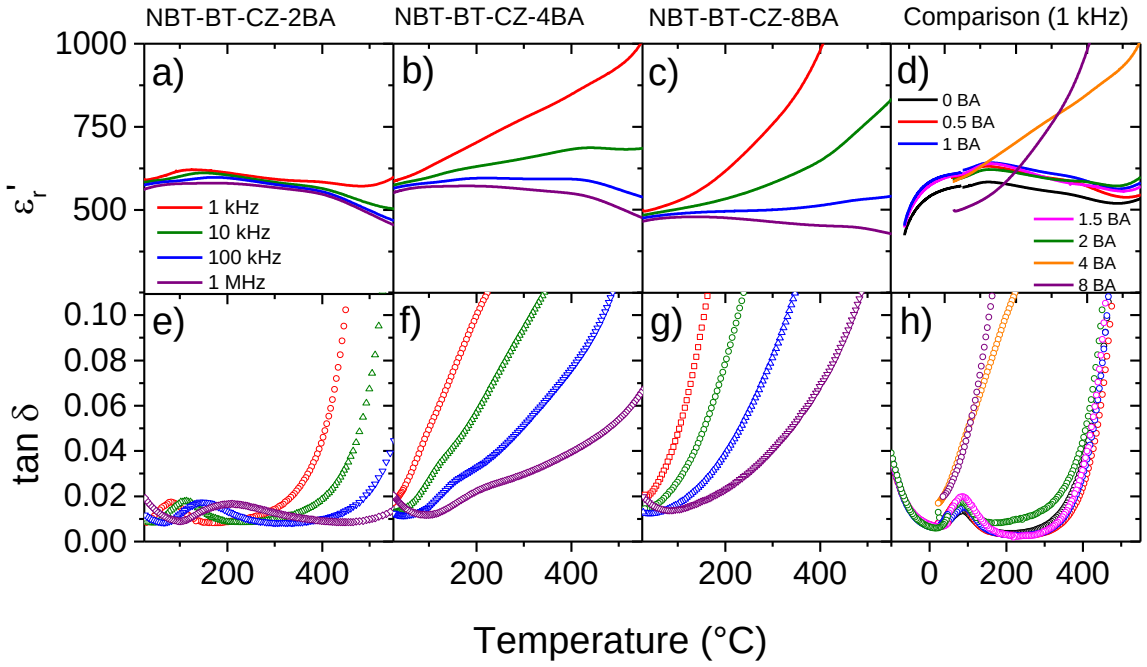

Figure 4.4.6: Temperature and frequency-dependent permittivity and dielectric loss factor for the NBT-6BT-20CZ-xBA compositions with x= 2.0 ((a) and (e)), 4.0 ((b) and (f)), 8.0 mol% ((c) and (g)), and a direct comparison for all processed compositions ((d) and (h)).

Above 2.0 mol% BA addition, the frequency dispersion of the permittivity increases paired with a systematic increase of the dielectric losses. In direct comparison at 1 kHz (see Figure 4.4.6 (d) and (h)), the detrimental effects of BA addition above 2.0 mol% become even more obvious. While the temperature invariant permittivity increases up to 1.5 mol% BA and the dielectric losses stay rather low, rapid degradation of the dielectric parameters can be detected by further increasing the BA content above 2.0 mol%. As already assumed by the presented microstructural analysis, the solubility limit of BA in NBT-6BT-20CZ is reached at about 2.0 mol% BA addition.

A combination of low dielectric losses and a stable permittivity is of major importance with regards to a possible application as a high-temperature capacitor. The application relevant parameters of the different NBT-6BT-20CZ-yBA compositions are summarized in Table 4.4-2.

Table 4.4-2: Relevant parameters for the processed NBT-6BT-20CZ-xBA compositions.

Composition NBT-6BT-20CZ-xBA	ε_r' (max)	ε_r' (150 °C; 1 kHz)	T (ε_r' ± 15 %) (°C)	T (tan $\delta \leq 0.02$) (°C)	ΔT (ε_r' ± 15 %; tan $\delta \leq 0.02$) (K)
0BA	582	581	-84 – 550	-68 – 368	436
0.5BA	630	628	-83 – 550	-68 – 391	459
1BA	641	640	-75 – 550	-71 – 381	452
1.5BA	639	637	-80 – 422	-67 – 375	442
2BA	620	620	23 – 550	23 – 336	313
4BA	-	666	53 – 243	23 – 36	-
8BA	-	563	23 – 202	33 – 37	4

The here presented results spot the NBT-6BT-20CZ-0.5BA composition to be the most suitable concerning an application. The temperature range, in which both criteria are fulfilled was determined to be $\Delta T(\varepsilon_r' \pm 15\ \%;\ \tan\delta \leq 0.02)$ = 459 K To reach better comparability, the permittivity normalized to ε_r' = 150 °C at 1 kHz and the dielectric loss are illustrated concerning the formerly defined benchmark values of ε_r' (150 °C) ± 15 % and $\tan\delta \leq 0.02$ [65, 226, 329, 350] in Figure 4.4.7 and Figure 4.4.8.

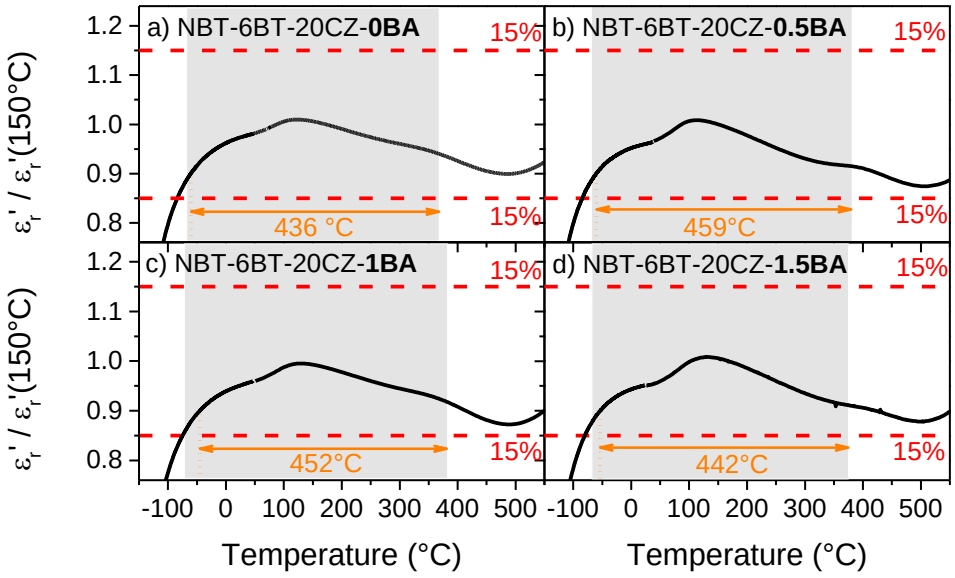

Figure 4.4.7: Comparison of $\Delta T(\varepsilon_r' \pm 15\ \%)$ (red dashed lines) and $\Delta T(\tan\delta \leq 0.02)$ (grey area) for the NBT-6BT-20CZ-xBA compositions (x= 0.0, 0.5, 1.0, 1.5 mol%). The orange arrows depict the temperature range in which both criteria are fulfilled simultaneously.

For the NBT-6BT-20CZ-xBA compositions up to 2.0 mol% BA content, the dielectric loss is determined to be the limiting factor for the temperature range of possible application with regards to the ε_r'(150 °C, 1 kHz) ± 15 % limit. In direct comparison, the NBT-6BT-20CZ-0.5BA composition exhibits overall superior properties with the largest determined operation window of 459 K paired with a permittivity of 628 which is stable up to 391 °C. This material already meets all industrial requirements and even exceeds the temperature stable dielectric properties of recently reported NBT-based high-temperature capacitor materials.[33, 66, 329, 341]

Nevertheless, a further increase in the BA content above 2.0 mol% is detrimental with regards to high-temperature dielectric properties (see Figure 4.4.8).

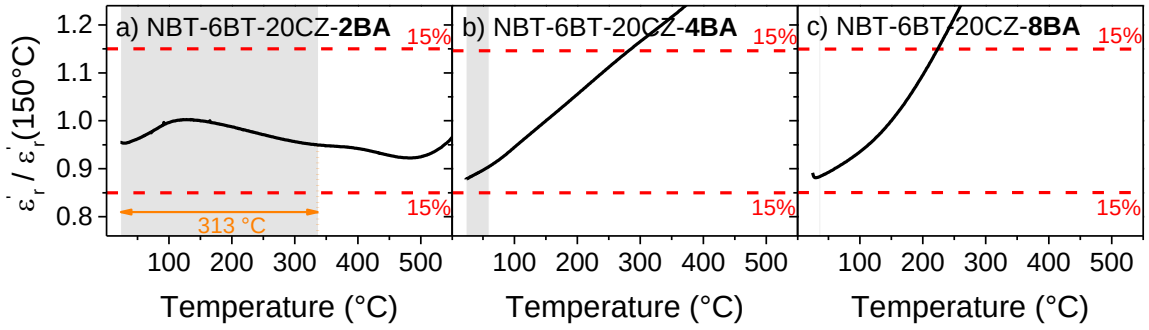

Figure 4.4.8: Comparison of $\Delta T(\varepsilon_r'$ ± 15 %) (red dashed lines) and $\Delta T(\tan\delta \leq 0.02)$ (grey area) for the NBT-6BT-20CZ-xBA compositions (x= 2.0, 4.0, 8.0 mol%). The orange arrow depicts the temperature range in which both criteria are fulfilled simultaneously.

To get an impression, how the key properties of NBT-6BT-20CZ evolve against the BA content, Figure 4.4.9 represents the evolution of the temperature range of stable permittivity ($\Delta T(\varepsilon_r'$ ± 15 %), orange curve) and loss ($\Delta T(\tan\delta \leq 0.02)$, blue curve) with respect to the BA concentration. The given values (orange) display the relative permittivity at 150 °C of the respective composition.

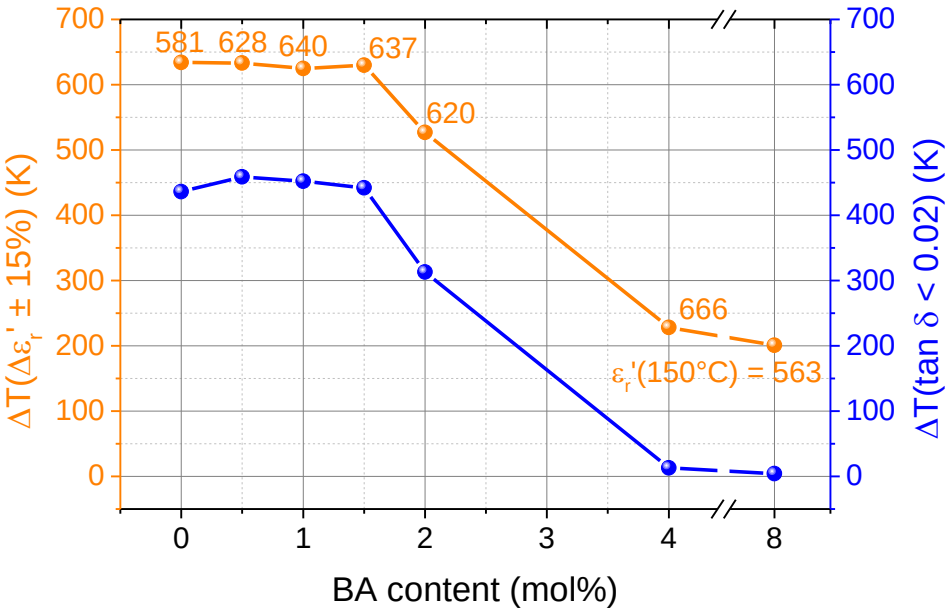

Figure 4.4.9: Comparison of $\Delta T(\varepsilon_r' \pm 15\ \%)$ (orange plot) and $\Delta T(\tan\delta \leq 0.02)$ (blue plot) for NBT-6BT-20CZ-xBA with respect to the BA content. The orange values represent ε_r'(150 °C).

The BA addition up to 1.5 mol% results in nearly BA concentration-independent dielectric properties. This is also crucial concerning a proper reproducibility on an industrial scale, as a too high sensitivity towards compositional changes could result in poor applicability. The here presented results highlight that the operational window for NBT-6BT-20CZ can further be enlarged by BA addition. The beneficial effects, however, vanish when a concentration of 2.0 mol% has overcome.

4.4.6 NB_xT-6BT-yCZ with BA Addition: Electrical Properties

As presented for the NB_xT-6BT-yCZ (see chapter 4.4.3) as well as for the NBT-6BT-20CZ-xBA compositions (see chapter 4.4.5), increased dielectric losses are observable for Bi-deficiency and high BA content, respectively. To address the remaining question about the effect of BA addition on the electrical properties and if possibly oxygen ionic conductivity is responsible for the increased loss at elevated temperatures, the thermal evolution of the electrical conductivity was measured with the help of temperature-dependent impedance spectroscopy.

Arrhenius-type plots for the temperature-dependent bulk conductivity the NB_xT-6BT-yCZ compositions are given in Figure 4.4.10 (a) and for the NBT-6BT-20CZ-xBA compositions in (b).

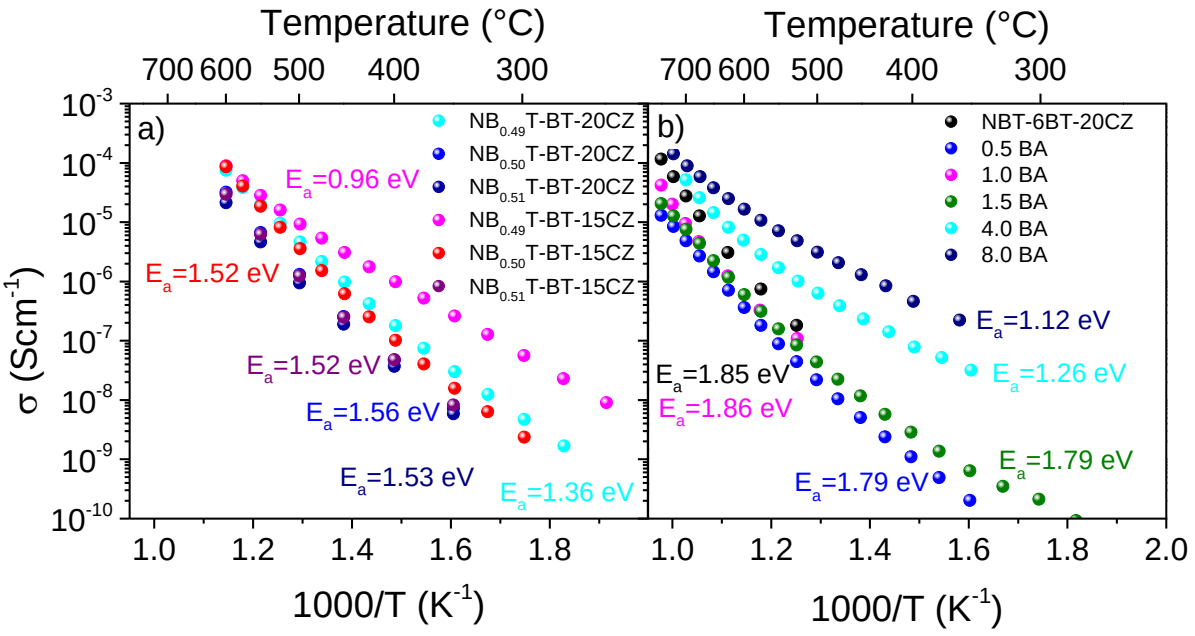

Figure 4.4.10: Arrhenius-type plots for the bulk conductivity σ_b for the A-site non-stoichiometric NB_xT-6BT-yCZ (a) and the BA added NBT-6BT-20CZ-xBA compositions.

All NB_xT-6BT-yCZ compositions exhibit a low bulk conductivity with comparable values over the measured temperature range. The Bi-deficient 15CZ composition shows a higher conductivity compared to the other compositions. This finding agrees well with the previously discussed permittivity values as this composition also exhibits the highest dielectric loss. At low temperatures, $NB_{0.49}$T-6BT-15CZ exhibits an activation energy of around 0.9 eV. Similar activation energies were found by Acosta *et al.* [65] and Dittmer *et al.*.[341] Acosta *et al.* predicted an oxygen vacancy dominated conductivity at low temperature, while the increased activation energies of 1.2 eV – 1.6 eV for NB_xT-6BT-yCZ at higher temperature could be explained by a dominant semiconducting behavior.

An increase of the CZ content leads to a decreased sensitivity concerning A-site non-stoichiometry and is therefore definitely more favorable from an application point of view. Bi-excess does not indicate a pronounced effect on the conductivity in both, the 15CZ and the 20CZ, compositions.

The presented Arrhenius plots for the BA added compositions (see Figure 4.4.10 (b)) also agree well with the permittivity data. The effects of BA addition on the electrical conductivity are more pronounced than the A-site non-stoichiometry. The addition of low BA content (up to 1.5 mol%) results in a decrease in the conductivity compared to NBT-6BT-20CZ. The activation energy is, however, only slightly affected by the BA content. The calculated activation energies are in the range of E_a ~ 1.79 eV – 1.86 eV for those particular compositions. It can be assumed that intrinsic semiconducting behavior is the dominant conductivity mechanism. By reaching a BA content above 2.0 mol%, the conductivity significantly increases. In particular, there is a discrepancy of about two orders of magnitude between the 0.5 mol% BA and the 8.0 mol% BA composition at 600 °C. Additionally, the activation energy is considerably lower for the NBT-6BT-20CZ-8BA composition (E_a ~ 1.12 eV). This value hints towards an extrinsic semiconducting behavior where additional defect states are present within the band gap. Mixed oxygen ionic/electronic conductivity can also not be ruled out completely at this point. [65, 341] The addition of BA should introduce trap states for oxygen ions without introducing additional oxygen vacancies like in the case of acceptor doping (see chapter 4.1.2). This is, however, only valid for low concentrations of BA. For higher concentrations, BA facilitates the formation of secondary phases (see chapter 4.4.4). A certain fraction of Al could, therefore, act as an acceptor dopant resulting in an increase of the oxygen vacancy concentration and oxygen ionic conductivity. Based on this consideration, BA addition in large amounts is detrimental for the desired high-temperature dielectric properties.

4.4.7 NB_xT-6BT-yCZ with BA Addition: Ferroelectric Energy Storage

Apart from the dielectric and electrical properties, the polarization response with an applied electric field is a crucial measure for capacitor applications. As already described in chapter 2.5.2, the recoverable energy storage density W_{rec} as well as the energy storage efficiency η are essential parameters that need to be determined. A low energy storage efficiency at high electric fields, thus, might limit the application range of a capacitor and therefore needs to be discussed in more detail.

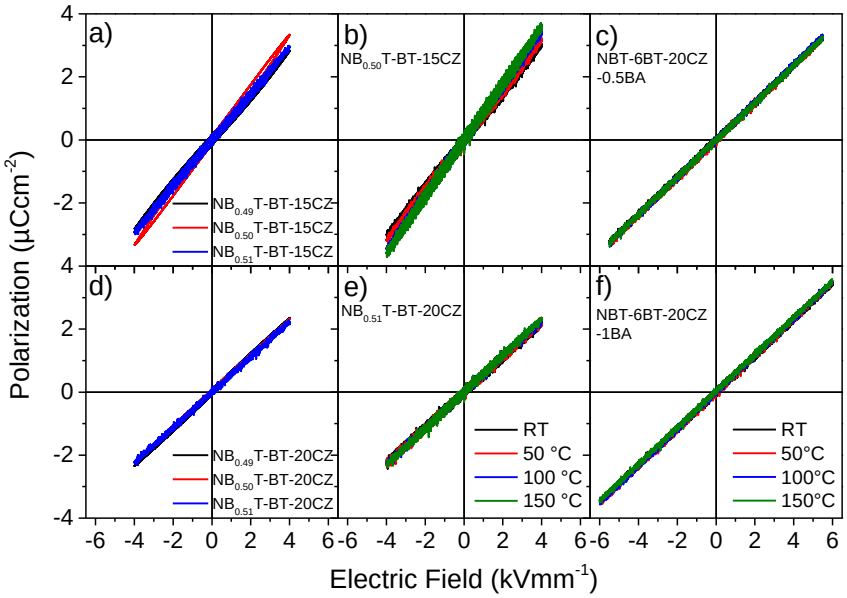

Figure 4.4.11: Polarization vs. Electric field for the different NB_xT-6BT-yCZ compositions ((a) and (d)) as well as temperature dependent polarization of the representative NB_xT-6BT-yCZ compositions ((b) and (e)) in comparison with the NBT-6BT-20CZ-xBA compositions ((c) and (f)) from room temperature to 150 °C.

In Figure 4.4.11, the polarization responses at room temperature for NB_xT-6BT-yCZ ((a) and (d)) and with temperature variation for NB_xT-6BT-yCZ ((b) and (e)) as well as for NBT-6BT-20-CZ-0.5BA (c) and NBT-6BT-20-CZ-1.0BA (f) with an applied electric field are given. The represented polarization responses for the A-site non-stoichiometric NB_xT-6BT-yCZ compositions have been measured at room temperature up to 4 $kVmm^{-1}$ at 1 Hz.

The polarization response of NBT-6BT-20CZ is nearly insensitive with regards to an occurring A-site non-stoichiometry and indicates an almost linear response without large polarization hysteresis. In contrast, NBT-6BT-15CZ features a more pronounced variation of the large field responses with a present A-site non-stoichiometry. Especially, for the Bi-deficient composition, a slightly larger polarization could be detected.

It should be noted, that the 15CZ composition exhibits a larger maximum polarization at the same applied electric field which would, of course, be beneficial concerning the energy storage density W. [351, 352] Nevertheless, the recoverable energy storage density will suffer from the broader hysteresis. The relevant material measures can be taken from Table 4.4-2.

To highlight the temperature stability of the large-signal properties, the temperature dependent polarization responses have been measured up to 150 °C. It can be observed that the NB_xT-6BT-20CZ compositions are also insensitive against temperature variation (see Figure 4.4.11 (e)).

Concerning the BA addition approach, the two most promising compositions NBT-6BT-20CZ-0.5BA and NBT-6BT-20CZ-1BA are presented in Figure 4.4.11 (c) and (f), respectively. The polarization responses are taken with an applied electric field of 6 $kVmm^{-1}$ at 1 Hz up to 150 °C. As already seen for the NB_xT-6BT-yCZ compositions, the BA added specimens also exhibit a linear polarization response with no pronounced hysteresis. Concerning increasing temperature, there is barely any change in the polarization response detectable for both discussed compositions which again illustrates the large temperature insensitivity of the investigated species. The recoverable energy storage density for the 0.5 mol% BA composition was calculated to be W_{rec} = 88 $mJcm^{-3}$ paired with an outstanding energy efficiency η of about 98 %. For the 1.0 mol% BA composition, W_{rec} is even larger with a value of ~ 104 $mJcm^{-3}$ with comparably high efficiency of η ~ 97 %.[5, 349]

4.4.8 NB_xT-6BT-yCZ with BA Addition: Summary

The here processed NB_xT-6BT-yCZ as well as the NBT-6BT-20CZ-xBA compositions feature outstanding temperature-dependent dielectric properties and exceed the even harshest industrial requirements by far. Apart from the excellent temperature stability of the permittivity, as well as the low dielectric losses and the resulting exceptionally broad operational temperature window, those materials also come up with a temperature-insensitive large recoverable energy storage density and efficiency. Moreover, especially the NB_xT-6BT-20CZ compositions exhibit large insensitivity towards non-stoichiometry and are therefore favorable in terms of reproducibility. The addition of BA further enhanced the operational window to function as a high-temperature capacitor material by about 25 K combined with larger temperature stability of the composition. The application of the gained defect chemical knowledge resulted in an excellent NBT-based high-temperature dielectric material which furthermore highlights the large property range of NBT and its solid solutions.

In detail, dielectric responses revealed a nearly temperature and frequency independent permittivity plateau in which the dielectric losses are below $\tan\delta \leq 0.02$ from -66 °C to 300 °C for the $NB_{0.50}$T-6BT-20CZ composition (see chapter 4.4.3). The dielectric properties of BA added compositions featured an even larger temperature range in which both criteria ($\Delta T(\tan\delta \leq 0.02)$ and $\Delta T(\varepsilon_r'(150\ °C) \pm 15\ \%)$) are fulfilled simultaneously. This temperature range was observed to be from -71 °C to 381 °C for the NBT-6BT-20CZ-1BA composition. It should be mentioned, that the resulting permittivity and loss values can only be enhanced until a BA concentration of 1.5 mol% BA is reached. Afterwards, the beneficial effects of BA addition vanish. Nevertheless, the resulting dielectric properties are almost constant between 0.5 mol% BA and 1.5 mol% BA making this approach suitable for industrial upscaling (see chapter 4.4.5).

Temperature-dependent polarization measurements delivered proof for an almost ideal dielectric behavior of NBT-6BT-20CZ-xBA (0.5 mol% and 1.0 mol% BA) up to temperatures of 150 °C resulting in an excellent recoverable energy storage density of W_{rec} = 104 mJcm^{-3} and an energy storage efficiency of η ~ 98 %(see chapter 4.4.7).

The electrical conductivity of the BA added compositions has been investigated with the help of temperature-dependent impedance spectroscopy. As assumed by the increased dielectric losses, the BA added compositions exhibited lower activation energies combined with higher bulk conductivities above a BA content of 2.0 mol%. It can be assumed, that mixed electronic/ionic conductivity is present (see chapter 4.4.6). These results highlight, that the formation of a solid solution with BA is limited to values of about 2.0 mol%. Additional BA is detrimental concerning the electrical properties.

This might be explainable by Al acting as an acceptor dopant (as described in chapter 4.1.2). Acceptor doping leads to an increase in the oxygen vacancy concentration and leads to increased conductivity. A detailed XRD analysis supported by SEM and EDX investigations revealed the formation of secondary phases in the NB_xT-6BT-yCZ compositions (see chapter 4.4.2). This is in agreement with existing literature. Forming an additional solid solution with bismuth aluminate $BiAlO_3$ (BA) led to a depression of the secondary phase formation for low concentrations. A secondary phase could, however, also be detected for BA contents above 4.0 mol%. An annealing study for 12 h at 750 °C further confirmed increased phase stability for NBT-6BT-20CZ-xBA (with $x \leq 2.0$ mol%) (see chapter 4.4.4).

5 Conclusion and Outlook

In this work, the impact of the A-site and B-site defect chemistry on the electrical, dielectric, piezoelectric and ferroelectric properties of $Na_{0.5}Bi_{0.5}TiO_3$ (NBT) and its solid solutions $0.94(Na_{0.5}Bi_xTiO_3)$-$0.06BaTiO_3$ (NB_xT-6BT), $0.75(Na_{0.5}Bi_xTiO_3)$-$0.25SrTiO_3$ (NB_xT-25ST) and $[(1-y)(0.94(Na_{0.5}Bi_xTiO_3)-0.06BaTiO_3)]$-$yCaZrO_3$ (NB_xT-6BT-yCZ) have been investigated.

The here presented results confirm that NBT and its solid solutions can be tuned towards excellent oxygen ion conductors by B-site acceptor doping. All the here investigated NBT-based solid solutions exhibited extremely high levels of oxygen ionic conductivity by choosing a B-site acceptor approach which are even competitive with the commercially most relevant oxygen ion conductor YSZ. The grain boundary conductivity represents the limiting factor for the total oxygen ionic conductivity which can further be enhanced by high doping concentrations. As compositionally tuning the electrical properties of the grain boundary was not part of this work, further enhancement of the total oxygen ionic conductivity in NBT can be expected.

It should be highlighted, that a systematic increase of B-site acceptor doping concentration resulted in a non-linear increase of the conductivity by about four orders of magnitude with a complete change of the conduction mechanisms from semiconducting to oxygen ionic conduction behavior. The induction of ionic conductivity followed the same defect chemical mechanisms for the NBT-based solid solutions as previously predicted by the in-depth investigation of the basic system NBT. With the help of the established analytical model, the oxygen ionic conductivity was confirmed to be dependent on the possible formation of defect complexes, the choice of the doping element, the doping element concentration as well as on the crystal structure and their coexistence of phases. The doping concentration-dependent formation of defect complexes by B-site acceptor doping in NBT could experimentally be confirmed by ^{27}Al NMR. Based on DFT calculations, a hierarchy of covalent, electrostatic Coulomb and mechanical interactions could be derived for their impact on the defect association energy. The mechanical contribution (caused by differences in the ionic radii) therefore delivers the largest fraction, followed by Coulomb interactions (based on the formal charge of the defect site) and covalent contributions (from antibonding and bonding states of the dopant elements). An increase of the doping concentration resulted in a decrease of the defect association energy which is the complete opposite of what would have been expected based on literature about defect complex formation in other systems.

The here obtained findings also highlight, that acceptor doping is not a valid approach to induce ferroelectric hardening in NBT-based systems. The polarization responses of NBT and NBT-6BT reveal that only a minor beneficial effect on the ferroelectric properties could be achieved. The high mobility of oxygen vacancies in NBT-based systems overwhelms the beneficial effects by far, resulting in aging and fatigue instead of ferroelectric hardening.

Controlling the A-site non-stoichiometry in NB_xT-6BT resulted in a tunability of the temperature-dependent relaxor behavior. The depolarization temperature T_d shifts to lower temperatures by increasing the Bi content from 120 °C for $N_{0.50}B_{0.49}T$-6BT towards 30 °C for the $N_{0.50}B_{0.53}T$-6BT. Additionally, the polarization and strain responses revealed a shift from non-ergodic towards ergodic relaxor behavior with increasing Bi content by disturbing the ferroelectric long-range order at room temperature. An interaction between occurring polar nano regions and induced oxygen vacancies could, therefore, be concluded.

For the solid solution NB_xT-25ST, the core-shell formation is also directly controllable by A-site non-stoichiometry and B-site acceptor doping. The formation of an NBT-rich core and an ST-rich shell results in a large strain which makes this solid solution attractive for piezoelectric applications. It could be revealed, that the oxygen vacancies have a larger impact on the formation or suppression of core-shell structures, compared to A-site vacancies. In detail, Bi-deficiency and acceptor doping (independent on additional A-site non-stoichiometry) result in homogeneous, large grains without core-shell formation. Bi-excess, as well as donor doping (as well independent on additional A-site non-stoichiometry), leads to a small-grained, core-shell microstructure. For the case of A-site non-stoichiometry, a close correlation between the occurrence of core-shell microstructures and the resulting ferroelectric and piezoelectric properties could be evidenced. Bi-deficiency leads to a shift of the mixed non-ergodic/ergodic behavior towards more non-ergodic behavior resulting in pinched polarization responses, paired with butterfly-shaped strain hysteresis at room temperature. Bi-excess results in a more ergodic behavior at room temperature. The effects of doping are more drastic. Fe-doping results in non-ergodic behavior, irrespective of the A-site non-stoichiometry, Nb-doping always results in ergodic behavior with slim polarization responses and sprout shaped strain responses. Those results reveal that the doping also affects the relaxor nature of the non-ergodic NBT core itself in such a way, that, even though core-shell structures are present, purely ergodic relaxor behavior can be achieved. The resulting strain values make NBT-25ST a suitable choice for actuator applications. With the help of the here obtained findings, the resulting strain values can further be modified.

Utilizing the findings regarding the defect chemistry in NBT furthermore resulted in an excellent NBT-based high-temperature dielectric material. NBT-6BT-20CZ exhibits an exceptionally large operating window where the industrial requirements for a temperature stable permittivity and low dielectric losses are fulfilled simultaneously. Temperature and frequency independent, stable permittivity was achieved between -84 °C and 550 °C. Additionally, the dielectric losses are below $\tan\delta \leq 0.02$ between -68 °C and 368 °C for NBT-6BT-20CZ. This high-temperature dielectric is, by far, better than every other yet reported NBT-based high-temperature capacitor material. The addition of $BiAlO_3$ further enhanced the temperature stability and is additionally insensitive towards compositional variations (stable properties between 0.5 mol% and 1.5 mol% BA addition) making this approach also suitable for industrial upscaling. With regards to a possible application as an energy storage device, temperature-dependent polarization measurements revealed a nearly ideal dielectric behavior resulting in a recoverable energy storage density of W_{rec} = 104 mJcm^{-3} combined with an energy storage efficiency of η ~ 98 % up to 150 °C for the NBT-6BT-20CZ-1.5BA composition.

To conclude all of the here obtained findings it was possible to elucidate the origin of oxygen ionic conductivity in NBT and its solid solutions. Oxygen ionic conductivity can be induced in all here investigated NBT-based systems. The uniqueness of the defect chemistry of NBT allows for precise control of the electrical, dielectric, piezoelectric and ferroelectric properties by the A-site and B-site related defect chemistry and can, therefore, be tuned towards the desired direction. The application range of NBT and its solid solutions is exceptionally large. The properties range from an excellent oxygen ionic conductor material e.g. for solid oxide fuel cells or oxygen sensors, to tunable piezo- and ferroelectric properties e.g. for actuators or pressure sensors, up to the best ceramic high temperature dielectrics combining a temperature and frequency stable permittivity with low losses making those NBT-based systems suitable for high temperature capacitors.

Appendix

Additional information to chapter 3.1:

An overview of the processing parameters for the here presented A-site non-stoichiometric and B-site doped NBT and NBT-based solid solutions is provided in Table A1.

Table A1: Powder processing parameters for the presented compositions

Composition	1st Ball Milling	1st Calcination	2nd Ball Milling	2nd Calcination	3rd Ball Milling
$Na_{0.5}Bi_{0.5}TiO_3$	6 h	800 °C; 2 h	4 h	850 °C; 2 h	6 h
$Na_{0.5}Bi_{0.501}Mg_xTi_{1-x}O_3$	"	"	"	"	"
x=0.001	"	"	"	"	"
x=0.002	"	"	"	"	"
x=0.005	"	"	"	"	"
x=0.01	"	"	"	"	"
x=0.02	"	"	"	"	"
x=0.03	"	"	"	"	"
x=0.04	"	"	"	"	"
$Na_{0.5}Bi_{0.501}Fe_xTi_{1-x}O_3$	"	"	"	"	"
x=0.001	"	"	"	"	"
x=0.003	"	"	"	"	"
x=0.01	"	"	"	"	"
x=0.02	"	"	"	"	"
x=0.04	"	"	"	"	"
$Na_{0.5}Bi_{0.501}Al_xTi_{1-x}O_3$	"	"	"	"	"
x=0.001	"	"	"	"	"
x=0.003	"	"	"	"	"
x=0.005	"	"	"	"	"
x=0.01	"	"	"	"	"
x=0.02	"	"	"	"	"
x=0.04	"	"	"	"	"
x=0.04	"	"	"	"	"
$0.94(Na_xBi_y)TiO_3$-0.06($BaTiO_3$)	24 h	800 °C; 3 h	24 h	-	-
x=0.50;y=0.49	"	"	"	"	"

x=0.50;y=0.50	"	"	"	"	"
x=0.50;y=0.51	"	"	"	"	"
x=0.50;y=0.52	"	"	"	"	"
x=0.50;y=0.53	"	"	"	"	"
x=0.51;y=0.50	"	"	"	"	"
0.94($Na_{0.5}Bi_{0.501}Fe_xTi_{1-x}O_3$)-0.06($BaTiO_3$)	6 h	800 °C; 2 h	4 h	850 °C; 2 h	6 h
x=0.01	"	"	"	"	"
x=0.02	"	"	"	"	"
x=0.03	"	"	"	"	"
x=0.04	"	"	"	"	"
0.75($Na_{0.5}Bi_xTiO_3$)-0.25($SrTiO_3$)	24 h	750 °C; 2 h	24 h	850 °C; 2 h	24 h
x=0.49	"	"	"	"	"
x=0.495	"	"	"	"	"
x=0.50	"	"	"	"	"
x=0.505	"	"	"	"	"
x=0.51	"	"	"	"	"
0.75($Na_{0.5}Bi_xTi_{0.97}Fe_{0.03}O_3$)-0.25($SrTiO_3$)	"	"	"	"	"
x=0.49	"	"	"	"	"
x=0.50	"	"	"	"	"
x=0.51	"	"	"	"	"
0.75($Na_{0.5}Bi_xTi_{0.97}Nb_{0.03}O_3$)-0.25($SrTiO_3$)	"	"	"	"	"
x=0.49	"	"	"	"	"
x=0.50	"	"	"	"	"
x=0.51	"	"	"	"	"
(1-y)[0.94($Na_{0.5}Bi_xTiO_3$)-0.06($BaTiO_3$)]-y($CaZrO_3$)	24 h	900 °C; 3 h	24 h	-	-
x=0.49; y=0.15	"	"	"	"	"
x=0.50; y=0.15	"	"	"	"	"
x=0.51; y=0.15	"	"	"	"	"
x=0.49; y=0.20	"	"	"	"	"
x=0.50; y=0.20	"	"	"	"	"

x=0.51; y=0.20	"	"	"	"	"
(1-x)[0.8(0.94$Na_{0.5}Bi_xTiO_3$)-0.06($BaTiO_3$)]-0.2($CaZrO_3$))-x($BiAlO_3$)	"	"	"	"	"
x=0.005	"	"	"	"	"
x=0.01	"	"	"	"	"
x=0.015	"	"	"	"	"
x=0.02	"	"	"	"	"
x=0.04	"	"	"	"	"
x=0.08	"	"	"	"	"

Additional information to chapter 4.2.7:

The SEM images of Fe-doped NBT and NBT-6BT in SE and BSE mode which not have been shown in chapter 4.2.7 are provided in Figure A1.

	SE (xFe-NBT)	SE (xFe-NBT-6BT)	BSE (x-Fe-NBT)	BSE (xFe-NBT-6BT)
0.1 % Fe	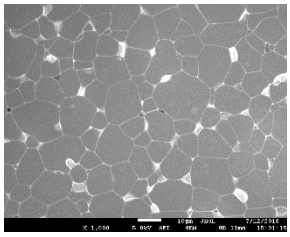	Not processed	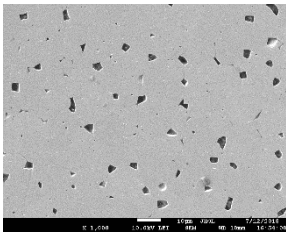	Not processed
0.3 % Fe	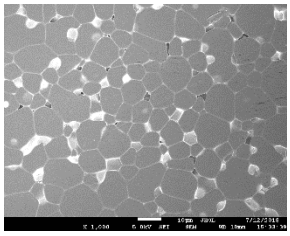	Not processed	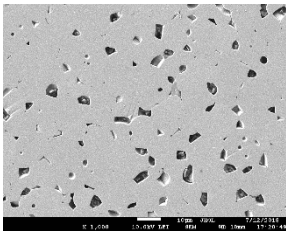	Not processed
1% Fe	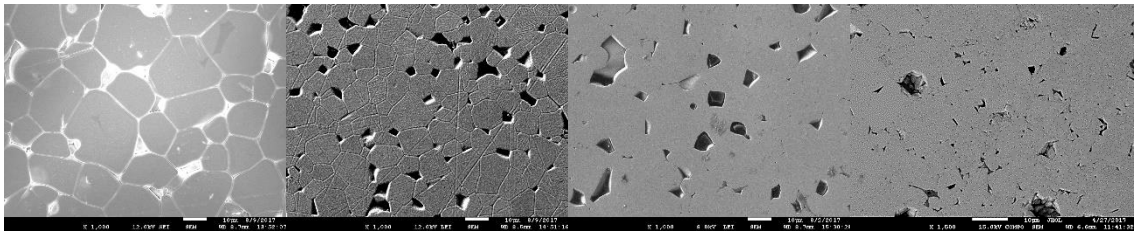			

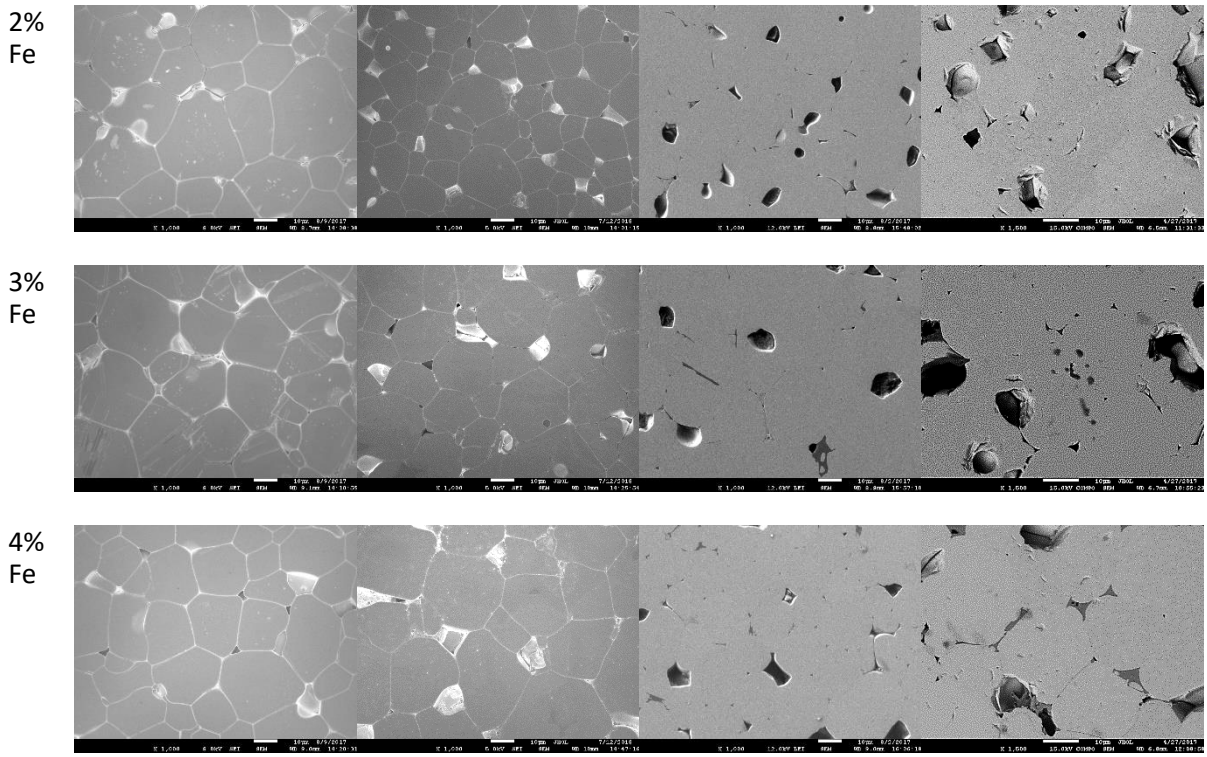

Figure A1: SEM images for the Fe-doped NBT and NBT-6BT compositions in the SE and BSE mode

Additional information to chapter 4.2.8:

To resolve the formation of a $(Fe'_{Ti} - V_O^{\bullet\bullet})^{\bullet}$ defect complex, electron paramagnetic resonance (EPR) measurements (see Figure A2) have been conducted by Dr. David Keeble at the University of Dundee, UK, for the 1 mol%, 2 mol% and 4 mol% Fe-doped NBT and NBT-6BT composition.

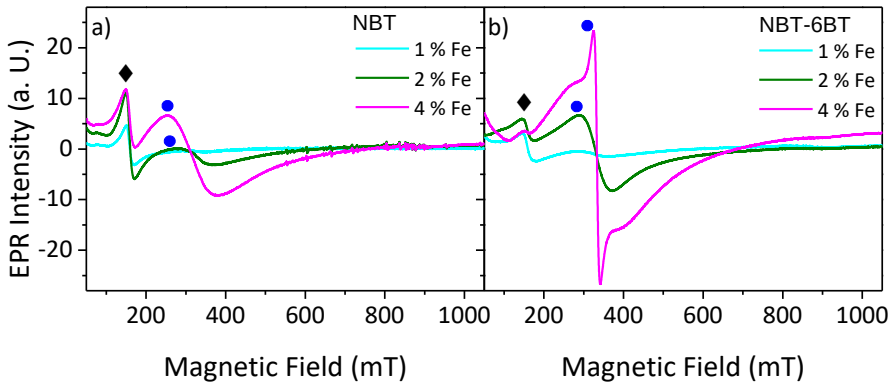

Figure A2: Electron paramagnetic resonance spectra measured at 9.39 GHz of Fe-doped NBT (a) and NBT-6BT (b) as a function of Fe-doping content. The spectral contributions attributed to Fe^{3+}-oxygen vacancy complexes (black diamond) and the Fe-containing impurity phase (blue circle) are marked.

The low field resonance line at round $150\ mT$ (marked as black diamonds) is characteristic for the formation of Fe^{3+} centers in a strongly axial crystal field which exhibits a large second order zero field splitting. This can be attributed to the defect complex $(Fe'_{Ti} - V_O^{\bullet\bullet})^{\bullet}$ which is formed by a Fe^{3+} ion and an oxygen vacancy at a nearest neighbor position.[140] All investigated compositions exhibit this resonance. The resonance at $330\ mT$ which is evident for the 1.0 mol% Fe-doped NBT can be attributed to Fe^{3+} occupying the B-site within a complete oxygen octahedron (marked as blue circles). A broadening of the $300\ mT$ line can be detected for increased Fe-doping concentrations. These broad EPR spectra are comparable to Fe_2O_3 and Fe containing impurity phases showing rather similar resonances.[296, 353] For the 2.0 mol% and 4.0 mol% Fe-doped compositions, this is in good agreement with the already seen secondary phases in the respective compositions. A similar broad line at $300\ mT$ can also be seen in the 2.0 mol% and 4.0 mol% Fe-doped NBT-6BT samples where the same secondary phases form. Moreover, the 4.0 mol% doped sample shows two contributions in this magnetic field range. The additional narrow line is likely caused by an impurity phase in which the Fe centers are exhibiting exchange narrowing. The secondary phase in the 2.0 mol% Fe-doped NBT sample which was also resolved by XRD is responsible for the onset of the detection of a broadened spectrum in the region of $300\ mT$. For the 4.0 mol% Fe-doped NBT-6BT sample, the formed secondary phase provides the dominant contribution to the measured EPR spectrum. For the 1.0 mol% and 2 mol% Fe-doped NBT samples, a contribution by the $(Fe'_{Ti} - V_O^{\bullet\bullet})^{\bullet}$ centers could be evidenced. The 4.0 mol% doped sample, however, does not show a further increase. In contrast, there is no significant contribution change evident in the Fe-doped NBT-6BT samples with increasing the doping content. Nonetheless, with respect to the grain size the presence and importance of oxygen vacancies in both systems was already highlighted. The EPR analysis provided, at least, qualitative evidence for the$(Fe'_{Ti} - V_O^{\bullet\bullet})^{\bullet}$ centers in both, Fe-doped NBT and NBT-6BT.

Additional information to chapter 4.3.3:

In Figure A3, an investigation of electrostriction for the A-site non-stoichiometric, B-site Nb-doped NB_xT-25ST compositions is provided:

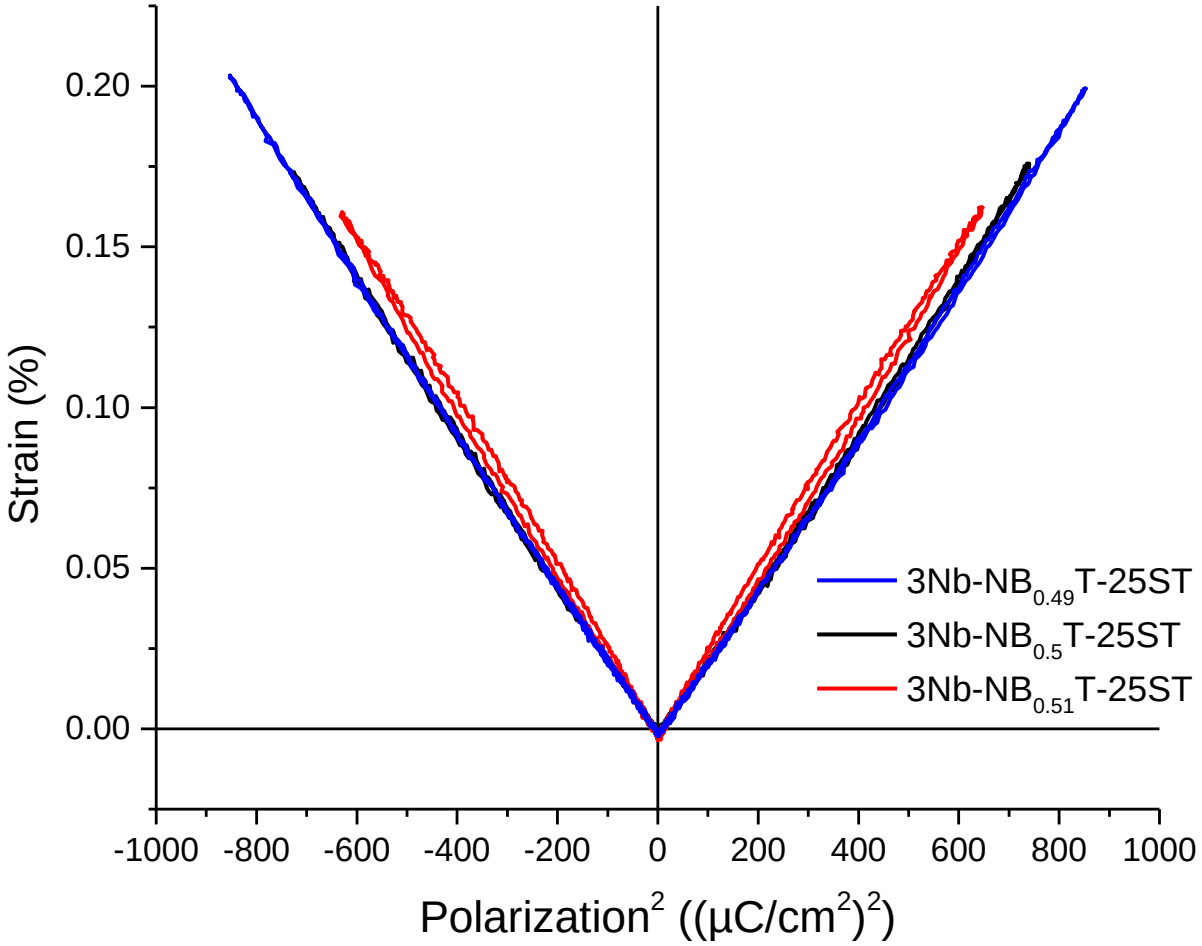

Figure A3: Strain versus the square of the polarization for the A-site non-stoichiometric, B-site Nb-doped NB_xT-25ST

Acknowledgement

First and foremost, I want to wholeheartedly thank my supervisor Dr. Till Frömling without him this thesis would not exist. Thank you for the very fruitful discussions and the great scientific guidance where own ideas and contributions were always welcomed and supported. Your advice greatly promoted my scientific knowledge and self-organization skills. No matter if, writing papers, planning experiments or supervising student, your feedback helped me a lot. Besides the work itself, you enabled a nice working surrounding with the exactly right balance between pressure and freedom. I really appreciated having you as my supervisor.

Additionally, my sincere gratitude goes to Prof. Dr. Jürgen Rödel giving me the opportunity to do my PhD in the NAW working group and further for the excellent organization and working climate. You are having kind of an intuition whom to hire to keep the group running as smoothly as it does at the moment. The working climate in this group definitely profits by this intuition a lot.

I want to address my gratitude also to the Deutsche Forschungsgesellschaft (DFG) under project Grants number FR 3718/1-1 for the financial support.

I also want to thank Prof. Dr. Karsten Albe and Prof. Dr. Barbara Albert for contributing as examiners. The discussions with Prof. Dr. Albe were highly appreciated and very often brought me back on the right track to find a solution for scientific problems.

Furthermore, I want to thank Prof. Dr. Kyle Grant Webber for being the second reviewer of this work. It was always a pleasure working on mutual publications where your scientific advice significantly increased the value of those works.

Further, I want to address my gratitude to all my collaborators. Without your help, this thesis would not exist in the present form. Your contributions remarkably increased the scientific wealth of this piece of work. In detail, I want to thank Leonie Koch for providing the presented DFT calculations in this work. Additionally, for the numerous discussions which always led to finding a solution for highly complex problems. I also want to thank Dr. In-Tae Seo, who really helped me performing plenty of measurements in the first year of my PhD. You were always calm and funny. It was a great time with you and I really enjoyed it. I further want to thank Jonas Heldt, who did his Master's thesis under my supervision. You have been a really focused scientist and very talented in performing the lab work. Supervising you was kind of an easy task. This is also true for Marion Höfling whom I also supervised in her Master's thesis. After you started your PhD in the NAW group you were even able to teach me things I didn't know. It was nice having you as office mate. You have the ability to let someone feel comfortable in your surrounding. This enabled an awesome working climate in our office.

I want to say thank you also to Dr. Ming Li for performing the electromotive force measurements of my samples, Dr. David Keeble for conducting the presented electron paramagnetic resonance

measurements and Dr. Pedro Groszewicz for doing the nuclear magnetic resonance experiments. Without your great support, this thesis would lack a lot of useful information.

Besides Jonas Heldt and Marion Höfling, I want to thank Daniel Bremecker, Dominik Weil, Benedikt Schaal and An-Phuc Hoang. You have done awesome work and it really was a pleasure to function as your supervisor in your Bachelor's or Master's theses. Sometimes it was not easy, but especially from that I learned a lot for the future.

With this, I want to further address my gratitude to the whole NAW working group. It was an awesome and rich time I was allowed to spend with all of you. Without Gila Völzke, the group would definitely not run as smoothly as it does currently. You always supported me in financial issues, vacation, bureaucracy etc.. Beyond, your ears were always open with regards to solving problems apart from the every-day working business. Also, Daniel Isaia and Patrick Breckner are mainly responsible for keeping the group running. You very often made the difference between nice results and a total catastrophe with respect to lab equipment and successful utilization. Without the handy lab-view programs from Patrick Breckner, life in lab would be much more time consuming and, of course, annoying.

Thank you Lukas Porz, Lovro Fulanovic, Qaisar Muhammad, Mao-Hua Zhang, Mihail Slabki, An-Phuc Hoang, Jurij Koruza, Lalitha Kodumudi-Venkataraman, Xuefei Fang, Daniel Bremecker and Andreas Wohninsland for keeping the working climate in the current NAW group so pleasant.

At this point I also want to thank the former PhD students of NAW Florian Schader, Jan Schultheiss, Florian Weyland, Peter Keil, Malte Vögler and Virginia Rojas who accompanied me during my time as a PhD. Thank you so much for the great time we could spend together not only at work but also beyond that. All of the hiking and skiing trips as well as the barbeques were amazing.

A special thanks goes out to my (almost) office mates Marion Höfling, Maximilian Gehringer and An-Phuc Hoang (who is such often in the office that one might think she belongs to it). You really supported me not only with numerous scientific discussions, but also to master every-day life. Not at least, finding the motivation to finish the upcoming tasks.

I will definitely miss you and the whole NAW group.

Dear Flo and Peter, without you I would not even be a material's scientist. I cannot really express how much I have enjoyed the awesome time together with you as my friends since the last ten years. Since the beginning of my Bachelor's studies in 2009, you two helped me finding my motivation when it appeared to be completely lost. Without your particular support, I would definitely not be where I am right now. Thank you so much for that.

Dear Gesche, thank you so much for your overwhelming support during the last five years. Especially, when I had hard times you were there with a helping hand. Thank you for the love you gave me to get through those times.

Last but not least, I want to thank my family for their love and sympathy. I want to say a big thank you to my parents Ursula and Rudolf for giving me the chance and all imaginable help and support one could wish for, to enjoy this section of my life in the way I did. I also want to address a big thank you to my brother Rudolf and his girlfriend Nelly who is, of course, also part of the family for their great support in tough times.

Bibliography

1 C. B. Carter and M. G. Norton, "Ceramic Materials: Science and Engineering . Springer Science & Business Media," (2007).

2 A. Testino, "Ceramics for Electronics and Energy: Issues and Opportunities," *International Journal of Applied Ceramic Technology,* 10[5] 723-30 (2013).

3 J. Valasek, "Piezo-electric and allied phenomena in Rochelle salt," *Physical review,* 17[4] 475 (1921).

4 J. Valasek, "Note on the piezo-electric effect in Rochelle salt crystals," *Science,* 65[1679] 235-36 (1927).

5 A. J. Moulson and J. M. Herbert, "Electroceramics: materials, properties, applications." Wiley, (2003).

6 E. Directive, "95/EC on the restriction of the use of certain hazardous substances in electrical and electronic equipment," *OJ L,* 37[13.2] (2002).

7 G. H. Haertling, "Ferroelectric ceramics: History and technology," *Journal of the American Ceramic Society,* 82 797-818 (1999).

8 K. Uchino, "Piezoelectric actuators and ultrasonic motors," Vol. 1. Springer Science & Business Media, (1996).

9 B. Jaffe, W. R. Cook Jr., and H. Jaffe, "Piezoelectric ceramics." Academic Press Inc.: London, (1971).

10 W. Jo, R. Dittmer, M. Acosta, J. Zang, C. Groh, E. Sapper, K. Wang, and J. Rödel, "Giant electric-field-induced strains in lead-free ceramics for actuator applications–status and perspective," *Journal of Electroceramics,* 29[1] 71-93 (2012).

11 IRAP, "Piezoelectronic Acuators and Motors - Global Markets and Market Trends," (2012).

12 GVE, "Piezoelectric Acutators and Motors Market Analysis, Market Size, Application Analysis, Regional Outlook, Competitive Strategies And Forecasts, 2015 To 2022," *Grand View Research, Inc. (San Francisco, USA)* (2015).

13 P. K. Panda, "Review: environmental friendly lead-free piezoelectric materials," *Journal of Materials Science,* 44[19] 5049-62 (2009).

14 G. S. Shukla and R. L. Singhal, "The present status of biological effects of toxic metals in the environment: lead, cadmium, and manganese," *Canadian journal of physiology and pharmacology,* 62[8] 1015-31 (1984).

15 W. H. O. (WHO), "Lead poisoning and health." in., www. who.int/en/news-room/fact-sheets/detail/lead-poisoning-and-health, (2016).

16 J. Rödel, W. Jo, K. T. Seifert, E. M. Anton, T. Granzow, and D. Damjanovic, "Perspective on the development of lead-free piezoceramics," *Journal of the American Ceramic Society,* 92[6] 1153-77 (2009).

17 J. Rödel, W. Jo, K. T. P. Seifert, E.-M. Anton, T. Granzow, and D. Damjanovic, "Perspective on the Development of Lead-free Piezoceramics," *Journal of the American Ceramic Society,* 92[6] 1153-77 (2009).

18 M. D. Maeder, D. Damjanovic, and N. Setter, "Lead free piezoelectric materials," *Journal of Electroceramics,* 13[1-3] 385-92 (2004).

19 Y. Guo, K.-i. Kakimoto, and H. Ohsato, "Phase transitional behavior and piezoelectric properties of $(Na_{0.5}K_{0.5})NbO_3$–$LiNbO_3$ ceramics," *Applied Physics Letters,* 85[18] 4121 (2004).

20 Y. Yuan, S. Zhang, X. Zhou, and J. Liu, "Phase Transition and Temperature Dependences of Electrical Properties of $[Bi_{0.5}(Na_{1-x-y}K_xLi_y)_{0.5}]TiO_3$Ceramics," *Jpn. J. Appl. Phys.,* 45[2A] 831-34 (2006).

21 Q. Chen, L. Chen, Q. Li, X. Yue, D. Xiao, J. Zhu, X. Shi, and Z. Liu, "Piezoelectric properties of $K_4CuNb_8O_{23}$ modified $(Na_{0.5}K_{0.5})NbO_3$ lead-free piezoceramics," *Journal of Applied Physics,* 102[10] 104109 (2007).

22 Y. Hiruma, K. Yoshii, H. Nagata, and T. Takenaka, "Phase transition temperature and electrical properties of $(Bi_{1/2}Na_{1/2})TiO_3$–$(Bi_{1/2}A_{1/2})TiO_3$ (A=Li and K) lead-free ferroelectric ceramics," *Journal of Applied Physics,* 103[8] 084121 (2008).

23 X. Liu, M. Zhu, Z. Chen, B. Fang, J. Ding, X. Zhao, H. Xu, and H. Luo, "Structure and electrical properties of Li-doped $BaTiO_3$–$CaTiO_3$–$BaZrO_3$ lead-free ceramics prepared by citrate method," *Journal of Alloys and Compounds,* 613 219-25 (2014).

24 A. Sasaki, T. Chiba, Y. Mamiya, and E. Otsuki, "Dielectric and piezoelectric properties of $(Bi_{0.5}Na_{0.5})TiO_3$–$(Bi_{0.5}K_{0.5})TiO_3$ systems," *Jpn. J. Appl. Phys.,* 38[9S] 5564 (1999).

25 J. Rödel, K. G. Webber, R. Dittmer, W. Jo, M. Kimura, and D. Damjanovic, "Transferring lead-free piezoelectric ceramics into application," *Journal of the European Ceramic Society,* 35[6] 1659-81 (2015).

26 A. Smolenskii, V. A. Isupv, A. I. Agranovskaya, and N. N. Krainik, "New Ferroelectrics of Complex Composition," *Sov. Phys. Solid St,* 4 2651 (1961).

27 R. Zuo, S. Su, Y. Wu, J. Fu, M. Wang, and L. Li, "Influence of A-site nonstoichiometry on sintering, microstructure and electrical properties of $(Bi_{0.5}Na_{0.5})TiO_3$ ceramics," *Materials Chemistry and Physics,* 110[2-3] 311-15 (2008).

28 Q. Xu, Y.-H. Huang, M. Chen, W. Chen, B.-H. Kim, and B.-K. Ahn, "Effect of bismuth deficiency on structure and electrical properties of $(Na_{0.5}Bi_{0.5})0.93Ba0.07TiO_3$ ceramics," *J. Phys. Chem. Solids,* 69[8] 1996-2003 (2008).

29 T. Takenaka, K. Sakata, and K. Toda, "Piezoelectric properties of $(Bi_{1/2}Na_{1/2})TiO_3$ based ceramics," *Ferroelectrics,* 106 375-80 (1990).

30 H. Nagata, N. Koizumi, and T. Takenaka, "Lead-free piezoelectric ceramics of $(Bi_{1/2}Na_{1/2})TiO_3$-$BiFeO_3$ system," pp. 37-40 in Key Engineering Materials. Vol. 169.

31 Y.-M. Li, W. Chen, Q. Xu, J. Zhou, H.-J. Sun, and M.-S. Liao, "Dielectric and Piezoelectric Properties of $Na_{0.5}Bi_{0.5}TiO_3$-$K_{0.5}Bi_{0.5}TiO_3$-$NaNbO_3$ Lead-Free Ceramics," *Journal of electroceramics,* 14[1] 53-58 (2005).

32 H. Yilmaz, S. Trolier-McKinstry, and G. L. Messing, "(Reactive) templated grain growth of textured sodium bismuth titanate ($Na_{1/2}Bi_{1/2}TiO_3$-$BaTiO_3$) ceramics - II dielectric and piezoelectric properties," *Journal of Electroceramics,* 11[3] 217-26 (2003).

33 R. Dittmer, E.-M. Anton, W. Jo, H. Simons, J. E. Daniels, M. Hoffman, J. Pokorny, I. M. Reaney, J. Rödel, and D. Damjanovic, "A High-Temperature-Capacitor Dielectric Based on $K_{0.5}Na_{0.5}NbO_3$-Modified $Bi_{1/2}Na_{1/2}TiO_3$-$Bi_{1/2}K_{1/2}TiO_3$," *Journal of the American Ceramic Society,* 95[11] 3519-24 (2012).

34 T. Takenaka, K.-i. Maruyama, and K. Sakata, "($Bi_{1/2}Na_{1/2}$) TiO_3-$BaTiO_3$ system for lead-free piezoelectric ceramics," *Jpn. J. Appl. Phys.,* 30[9S] 2236 (1991).

35 B.-J. Chu, D.-R. Chen, G.-R. Li, and Q.-R. Yin, "Electrical properties of $Na_{1/2}Bi_{1/2}TiO_3$–$BaTiO_3$ ceramics," *Journal of the European Ceramic Society,* 22[13] 2115-21 (2002).

36 J. Zang, W. Jo, H. Zhang, and J. Rödel, "$Bi_{1/2}Na_{1/2}TiO_3$–$BaTiO_3$ based thick-film capacitors for high-temperature applications," *Journal of the European Ceramic Society,* 34[1] 37-43 (2014).

37 E. A. Patterson, D. P. Cann, J. Pokorny, and I. M. Reaney, "Electromechanical strain in $Bi(Zn_{1/2}Ti_{1/2})O_3$–$(Bi_{1/2}Na_{1/2})TiO_3$–$(Bi_{1/2}K_{1/2})TiO_3$ solid solutions," *Journal of Applied Physics,* 111[9] 094105 (2012).

38 R. Dittmer, W. Jo, J. Rödel, S. Kalinin, and N. Balke, "Nanoscale insight into lead-free BNT-BT-xKNN," *Advanced Functional Materials,* 22[20] 4208-15 (2012).

39 X. Wang, X. Tang, and H. Chan, "Electromechanical and ferroelectric properties of ($Bi_{1/2}Na_{1/2}$) TiO_3–($Bi_{1/2}K_{1/2}$) TiO_3–$BaTiO_3$ lead-free piezoelectric ceramics," *Applied physics letters,* 85[1] 91-93 (2004).

40 S.-T. Zhang, A. B. Kounga, E. Aulbach, T. Granzow, W. Jo, H.-J. Kleebe, and J. Rödel, "Lead-free piezoceramics with giant strain in the system $Bi_{0.5}Na_{0.5}TiO_3$–$BaTiO_3$–$K_{0.5}Na_{0.5}NbO_3$. I. Structure and room temperature properties," *Journal of Applied Physics,* 103[3] 034107 (2008).

41 W. Jo, T. Granzow, E. Aulbach, J. Rödel, and D. Damjanovic, "Origin of the large strain response in ($K_{0.5}Na_{0.5}$)NbO_3-modified ($Bi_{0.5}Na_{0.5}$)TiO_3–$BaTiO_3$ lead-free piezoceramics," *Journal of Applied Physics,* 105[9] 094102 (2009).

42 Y. Hiruma, H. Nagata, and T. Takenaka, "Phase diagrams and electrical properties of ($Bi_{1/2}Na_{1/2}$) TiO_3-based solid solutions," *Journal of Applied Physics,* 104[12] 124106 (2008).

43 Y.-M. Chiang, G. W. Farrey, and A. N. Soukhojak, "Lead-free high-strain single-crystal piezoelectrics in the alkaline–bismuth–titanate perovskite family," *Applied Physics Letters,* 73[25] 3683-85 (1998).

44 H. Nagata, "Additive effect on electrical properties of ($Bi_{1/2}Na_{1/2}$)TiO_3 ferroelectric ceramics," *J. Eur. Ceram. Soc.,* 21 1299-302 (2001).

45 Y. Hiruma, H. Nagata, and T. Takenaka, "Thermal depoling process and piezoelectric properties of bismuth sodium titanate ceramics," *Journal of Applied Physics,* 105[8] 084112 (2009).

46 M. Davies, E. Aksel, and J. L. Jones, "Enhanced High-Temperature Piezoelectric Coefficients and Thermal Stability of Fe- and Mn-Substituted $Na_{0.5}Bi_{0.5}TiO_3$ Ceramics," *Journal of the American Ceramic Society,* 94[5] 1314-16 (2011).

47 C.-H. Hong, H.-P. Kim, B.-Y. Choi, H.-S. Han, J. S. Son, C. W. Ahn, and W. Jo, "Lead-free piezoceramics – Where to move on?," *Journal of Materiomics,* 2[1] 1-24 (2016).

48 M. Li, M. J. Pietrowski, R. A. De Souza, H. Zhang, I. M. Reaney, S. N. Cook, J. A. Kilner, and D. C. Sinclair, "A family of oxide ion conductors based on the ferroelectric perovskite $Na_{0.5}Bi_{0.5}TiO_3$," *Nature Materials,* 13[1] 31-5 (2014).

49 M. Li, H. Zhang, S. N. Cook, L. Li, J. A. Kilner, I. M. Reaney, and D. C. Sinclair, "Dramatic Influence of A-Site Nonstoichiometry on the Electrical Conductivity and Conduction Mechanisms in the Perovskite Oxide $Na_{0.5}Bi_{0.5}TiO_3$," *Chemistry of Materials,* 27[2] 629-34 (2015).

50 L. Koch, S. Steiner, K.-C. Meyer, I.-T. Seo, K. Albe, and T. Frömling, "Ionic conductivity of acceptor doped sodium bismuth titanate: influence of dopants, phase transitions and defect associates," *Journal of Materials Chemistry C,* 5[35] 8958-65 (2017).

51 P. Lacorre, F. Goutenoire, O. Bohnke, R. Retoux, and Y. Laligant, "Designing fast oxide-ion conductors based on $La_2Mo_2O_9$," *Nature,* 404[6780] 856-58 (2000).

52 E. D. Wachsman and K. T. Lee, "Lowering the temperature of solid oxide fuel cells.," *Science,* 334[6058] 935-39 (2011).

53 B. C. Steele and A. Heinzel, "Materials for fuel-cell technologies.," pp. 224-31. in Materials For Sustainable Energy: A Collection of Peer-Reviewed Research and Review Articles from Nature Publishing Group*,* Vol. 414**.** World Scientific, 2001.

54 Z. Shao and S. M. Haile, "A high-performance cathode for the next generation of solid-oxide fuel cells.," pp. 255-58. in Materials for Sustainable Energy: A Collection of Peer-Reviewed Research and Review Articles from Nature Publishing Group**.** World Scientific, 2011.

55 T. Ishihara, H. Matsuda, and Y. Takita, "Doped LaGaO3 perovskite type oxide as a new oxide ionic conductor.," *Journal of the American chemical society,* 116[9] 3801-03 (1994).

56 P. Singh and J. B. Goodenough, "$Sr_{1-x}K_xSi_{1-y}Ge_yO_{3-0.5x}$: a new family of superior oxide-ion conductors," *Energy & Environmental Science,* 5[11] 9626-31 (2012).

57 L. Malavasi, C. A. Fisher, and M. S. Islam, "Oxide-ion and proton conducting electrolyte materials for clean energy applications: Structural and mechanistic features.," *Chemical Society Reviews,* 39[11] 4370-87 (2010).

58 S. P. Badwal and F. T. Ciacchi, " Ceramic membrane technologies for oxygen separation. ," *Advanced materials,* 13[12-13] 993-96 (2001).

59 X. Kuang, M. A. Green, H. Niu, P. Zajdel, C. Dickinson, J. B. Claridge, L. Jantsky, and M. J. Rosseinsky, "Interstitial oxide ion conductivity in the layered tetrahedral network melilite structure.," *Nature materials,* 7[6] 498-504 (2008).

60 W. Weber, H. Tuller, T. O. Mason, and A. Cormack, "Research needs and opportunities in highly conducting electroceramics," *Materials Science and Engineering: B,* 18[1] 52-71 (1993).

61 B. Steele, "Oxygen ion conductors and their technological applications," *Materials Science and Engineering: B,* 13[2] 79-87 (1992).

62 I.-T. Seo, S. Steiner, and T. Frömling, "The effect of A site non-stoichiometry on $0.94(Na_yBi_x)TiO_3$-$0.06BaTiO_3$," *Journal of the European Ceramic Society,* 37[4] 1429-36 (2017).

63 M. Acosta, L. A. Schmitt, L. Molina-Luna, M. C. Scherrer, M. Brilz, K. G. Webber, M. Deluca, H. J. Kleebe, J. Rodel, and W. Donner, "Core-Shell Lead-Free Piezoelectric Ceramics: Current Status and Advanced Characterization of the $Bi_{1/2}Na_{1/2}TiO_3$-$SrTiO_3$ System," *Journal of the American Ceramic Society,* 98[11] 3405-22 (2015).

64 T. Frömling, S. Steiner, A. Ayrikyan, D. Bremecker, M. Dürrschnabel, L. Molina-Luna, H.-J. Kleebe, H. Hutter, K. G. Webber, and M. Acosta, "Designing properties of $(Na_{1/2}Bi_x)TiO_3$-based materials through A-site non-stoichiometry," *Journal of Materials Chemistry C,* 6[4] 738-44 (2018).

65 M. Acosta, J. Zang, W. Jo, and J. Rödel, "High-temperature dielectrics in $CaZrO_3$-modified $Bi_{1/2}Na_{1/2}TiO_3$-based lead-free ceramics," *Journal of the European Ceramic Society,* 32[16] 4327-34 (2012).

66 M. Höfling, S. Steiner, A.-P. Hoang, I.-T. Seo, and T. Frömling, "Optimizing the defect chemistry of $Na_{1/2}Bi_{1/2}TiO_3$-based materials: paving the way for excellent high temperature capacitors," *Journal of Materials Chemistry C,* 6[17] 4769-76 (2018).

67 M. E. Lines and A. M. Glass, "Principles and Applications of Ferroelectrics and Related Materials," *Oxford University Press* (1997).

68 R. Waser, U. Böttger, and S. Tiedke, "Polar Oxides: Properties, Characterization, and Imaging," (2005).

69 R. C. Buchanan, "Ceramic materials for electronics," pp. 9-10 Vol. 68. CRC press, (2004).

70 "Philips Research Reports, Defect Chemistry of Conductivity," 31 261-75 (1975).

71 L. Egerton and D. M. Dillon, "Piezoelectric and dielectric properties of ceramics in the system potassium—sodium niobate," *Journal of the American Ceramic Society,* 42[9] 438-42 (1959).

72 M. De Graef and M. E. McHenry, "Structure of materials: an introduction to crystallography, diffraction and symmetry." Cambridge University Press, (2012).

73 M. W. Barsoum, "Fundamentals of ceramics," *Institute of Physics Pub* 603 (2003).

74 R. J. Hemley and R. E. Cohen, "Silicate Perovskite," *Annu. Rev. Earth Planet. Sci.,* 20 553-600 (1992).

75 T. He, Q. Huang, A. P. Ramirez, Y. Wang, K. A. Regan, N. Rogado, M. A. Hayward, M. K. Haas, J. S. Slusky, K. Inumara, H. W. Zandbergen, N. P. Ong, and R. J. Cava, "Superconductivity in the non-oxide perovskite $MgCNi_3$," *Nature,* 411[6833] 54-56 (2001).

76 K. M. Rabe, M. Dawber, C. Lichtensteiger, C. H. Ahn, and J. M. Triscone, "Modern physics of ferroelectrics: Essential background," *Topics in Applied Physics,* 105 1-30 (2007).

77 V. M. Goldschmidt, "Geochemistry," *Quarterly Journal of the Royal Meteorological Society,* 82[354] 547 (1956).

78 A. Manbachi and R. S. Cobbold, "Development and application of piezoelectric materials for ultrasound generation and detection," *Ultrasound,* 19[4] 187 - 96 (2011).

79 J. Erhart, "Experiments to demonstrate piezoelectric and pyroelectric effects," *Physics Education,* 48 438 (2013).

80 R. E. Newnham, "Properties of materials: anisotropy, symmetry, structure." Oxford University Press on Demand, (2005).

81 D. Damjanovic, "Ferroelectric, dielectric and piezoelectric properties of ferroelectric thin films and ceramics," *Reports on Progress in Physics,* 61[9] 1267 (1998).

82 B. A. Strukov and A. P. Levanyuk, "Ferroelectric phenomena in crystals: physical foundations." Springer Science & Business Media, (2012).

83 C. Kittel, P. McEuen, and P. McEuen, "Introduction to solid state physics," Vol. 8. Wiley New York, (1996).

84 R. A. Levy, "Principles of solid state physics." Academic Press, (2012).

85 W. Cherry Jr and R. Adler, "Piezoelectric effect in polycrystalline barium titanate," *Physical Review,* 72[10] 981 (1947).

86 S. Roberts, "Dielectric and piezoelectric properties of barium titanate," *Physical Review,* 71[12] 890 (1947).

87 L. J. Gauckler, "Ingeneurskeramik 3 - Funktionskeramik," *Tech. rep. Swiss Federal Institute of Technology Zuerich* (2001).

88 G. Smolenskii and V. Isupov, "segnetoelekticheskie svoistva tverdykh restvorov stannata bariya v titanate bariya," *Zhurnal Tekhnicheskoi Fiziki,* 24[8] 1375-86 (1954).

89 L. E. Cross, "Relaxor ferroelectrics," *Ferroelectrics,* 76[1] 241-67 (1987).

90 G. A. Samara, "The relaxational properties of compositionally disordered ABO_3 perovskites," *J. Phys.-Condes. Matter,* 15[9] R367-R411 (2003).

91 G. Burns and B. Scott, "Index of refraction in 'dirty'displacive ferroelectrics," *Solid State Communications,* 13[3] 423-26 (1973).

92 G. Burns and F. Dacol, "Ferroelectrics with a glassy polarization phase," *Ferroelectrics,* 104[1] 25-35 (1990).

93 A. A. Bokov and Z. G. Ye, "Recent progress in relaxor ferroelectrics with perovskite structure," *Journal of Materials Science,* 41[1] 31-52 (2006).

94 I.-K. Jeong, T. Darling, J. Lee, T. Proffen, R. Heffner, J. Park, K. Hong, W. Dmowski, and T. Egami, "Direct observation of the formation of polar nanoregions in $Pb(Mg_{1/3}Nb_{2/3})O_3$ using neutron pair distribution function analysis," *Physical review letters,* 94[14] 147602 (2005).

95 O. Svitelskiy, J. Toulouse, G. Yong, and Z.-G. Ye, "Polarized Raman study of the phonon dynamics in $Pb(Mg_{1/3}Nb_{2/3})O_3$ crystal," *Physical Review B,* 68[10] 104107 (2003).

96 B. Mihailova, M. Bastjan, B. Schulz, M. Rübhausen, M. Gospodinov, R. Stosch, B. Güttler, T. Malcherek, and U. Bismayer, "Resonance Raman scattering of relaxors $PbSc_{0.5}Ta_{0.5}O_3$ and $PbSc_{0.5}Nb_{0.5}O_3$," *Applied physics letters,* 90[4] 042907 (2007).

97 R. Blinc, A. Gregorovič, B. Zalar, R. Pirc, and S. Lushnikov, "45 Sc NMR study of the relaxor transition in a lead scandotantalate single crystal," *Physical Review B,* 61[1] 253 (2000).

98 D. H. Zhou, G. L. Hoatson, R. L. Vold, and F. Fayon, "Local structure in perovskite relaxor ferroelectrics by ^{207}Pb NMR," *Physical Review B,* 69[13] 134104 (2004).

99 V. V. Shvartsman and D. C. Lupascu, "Lead-Free Relaxor Ferroelectrics," *Journal of the American Ceramic Society,* 95[1] 1-26 (2012).

100 D. Viehland, S. Jang, L. E. Cross, and M. Wuttig, "Freezing of the polarization fluctuations in lead magnesium niobate relaxors," *Journal of Applied Physics,* 68[6] 2916-21 (1990).

101 G. Smolenskii, V. Isupov, A. Agranovskaya, and S. Popov, "Ferroelectrics with diffuse phase transitions," *Soviet Physics-solid state,* 2[11] 2584-94 (1961).

102 T. Egami, E. Mamontov, W. Dmowski, and S. Vakhrushev, "Temperature Dependence of the Local Structure in Pb Containing Relaxor Ferroelectrics," pp. 48-54 in AIP Conference Proceedings. Vol. 677.

103 G. A. Samara, "Ferroelectricity revisited—advances in materials and physics," pp. 239-458. in Solid State Physics, Vol. 56**.** Elsevier, 2001.

104 H. Vogel, "The law of the relation between the viscosity of liquids and the temperature," *Phys. Z,* 22 645-46 (1921).

105 G. S. Fulcher, "Analysis of recent measurements of the viscosity of glasses," *Journal of the American Ceramic Society,* 8[6] 339-55 (1925).

106 G. Tammann and W. Hesse, "Die Abhängigkeit der Viscosität von der Temperatur bie unterkühlten Flüssigkeiten," *Zeitschrift für anorganische und allgemeine Chemie,* 156[1] 245-57 (1926).

107 E. Colla, E. Y. Koroleva, N. Okuneva, and S. Vakhrushev, "Long-time relaxation of the dielectric response in lead magnoniobate," *Physical review letters,* 74[9] 1681 (1995).

108 F. H. Schader, Z. Wang, M. Hinterstein, J. E. Daniels, and K. G. Webber, "Stress-modulated relaxor-to-ferroelectric transition in lead-free $(Na_{1/2}Bi_{1/2})TiO_3$−$BaTiO_3$ ferroelectrics," *Physical Review B,* 93[13] 134111 (2016).

109 V. Westphal, W. Kleemann, and M. Glinchuk, "Diffuse phase transitions and random-field-induced domain states of the ‘‘relaxor’’ferroelectric $PbMg_{1/3}Nb_{2/3}O_3$," *Physical Review Letters,* 68[6] 847 (1992).

110 Z. Kutnjak, C. Filipič, R. Pirc, A. Levstik, R. Farhi, and M. El Marssi, "Slow dynamics and ergodicity breaking in a lanthanum-modified lead zirconate titanate relaxor system," *Physical Review B,* 59[1] 294 (1999).

111 A. Levstik, Z. Kutnjak, C. Filipič, and R. Pirc, "Glassy freezing in relaxor ferroelectric lead magnesium niobate," *Physical Review B,* 57[18] 11204 (1998).

112 O. Noblanc, P. Gaucher, and G. Calvarin, "Structural and dielectric studies of $Pb(Mg_{1/3}Nb_{2/3})O_3$–$PbTiO_3$ ferroelectric solid solutions around the morphotropic boundary," *Journal of applied physics,* 79[8] 4291-97 (1996).

113 M. Algueró, B. Jiménez, and L. Pardo, "Transition between the relaxor and ferroelectric states for $(1- x)Pb(Mg_{1/3}Nb_{2/3})O_3$–$xPbTiO_3$ with x=0.2 and 0.3 polycrystalline aggregates," *Applied Physics Letters,* 87[8] 082910 (2005).

114 Z.-G. Ye, Y. Bing, J. Gao, A. Bokov, P. Stephens, B. Noheda, and G. Shirane, "Development of ferroelectric order in relaxor $(1-x)Pb(Mg_{1/3}Nb_{2/3})$ O_3–$xPbTiO_3$ (0<~x<~0.15)," *Physical review B,* 67[10] 104104 (2003).

115 X. H. Dai, Z. Xu, and D. Viehland, "The spontaenous relaxor to normal ferroelectric transofrmation in La-modified lead-zirconate-titanate," *Philos. Mag. B-Phys. Condens. Matter Stat. Mech. Electron. Opt. Magn. Prop.,* 70[1] 33-48 (1994).

116 X. Dai, A. DiGiovanni, and D. Viehland, "Dielectric properties of tetragonal lanthanum modified lead zirconate titanate ceramics," *Journal of applied physics,* 74[5] 3399-405 (1993).

117 J. Zang, M. Li, D. C. Sinclair, W. Jo, and J. Rödel, "Impedance Spectroscopy of $(Bi_{1/2}Na_{1/2})TiO_3$–$BaTiO_3$ Ceramics Modified with $(K_{0.5}Na_{0.5})NbO_3$," *Journal of the American Ceramic Society,* 97[5] 1523-29 (2014).

118 J. E. Daniels, W. Jo, J. Rödel, and J. L. Jones, "Electric-field-induced phase transformation at a lead-free morphotropic phase boundary: Case study in a $93\%(Bi_{0.5}Na_{0.5})TiO_3$–$7\%BaTiO_3$ piezoelectric ceramic," *Applied Physics Letters,* 95[3] 032904 (2009).

119 M. Acosta, W. Jo, J. Rödel, and D. C. Lupascu, "Temperature- and Frequency-Dependent Properties of the $0.75Bi_{1/2}Na_{1/2}TiO_3$-$0.25SrTiO_3$ Lead-Free Incipient Piezoceramic," *Journal of the American Ceramic Society,* 97[6] 1937-43 (2014).

120 H. Simons, J. Daniels, W. Jo, R. Dittmer, A. Studer, M. Avdeev, J. Rodel, and M. Hoffman, "Electric-field-induced strain mechanisms in lead-free 94%($Bi_{1/2}Na_{1/2}$)TiO_3-6%$BaTiO_3$," *Applied Physics Letters,* 98[8] 3 (2011).

121 W. Jo and J. Rödel, "Electric-field-induced volume change and room temperature phase stability of ($Bi_{1/2}Na_{1/2}$) TiO_3-x mol.% $BaTiO_3$ piezoceramics," *Applied Physics Letters,* 99[4] 042901 (2011).

122 Y. Zhao, X. H. Hao, and Q. Zhang, "Energy-Storage Properties and Electrocaloric Effect of $Pb_{(1-3x/2)}La_xZr_{0.85}Ti_{0.15}O_3$ Antiferroelectric Thick Films," *Acs Applied Materials & Interfaces,* 6[14] 11633-39 (2014).

123 K. Yao, S. T. Chen, M. Rahimabady, M. S. Mirshekarloo, S. H. Yu, F. E. H. Tay, T. Sritharan, and L. Lu, "Nonlinear Dielectric Thin Films for High-Power Electric Storage With Energy Density Comparable With Electrochemical Supercapacitors," *Ieee T Ultrason Ferr,* 58[9] 1968-74 (2011).

124 M. Chandrasekhar and P. Kumar, "Synthesis and characterizations of BNT–BT and BNT–BT–KNN ceramics for actuator and energy storage applications," *Ceramics International,* 41[4] 5574–80 (2015).

125 W. Jia, Y. Hou, M. Zheng, Y. Xu, X. Yu, M. Zhu, K. Yang, H. Cheng, S. Sun, and J. Xing, "Superior temperature-stable dielectrics for MLCC s based on $Bi_{0.5}Na_{0.5}TiO_3$-$NaNbO_3$ system modified by $CaZrO_3$," *Journal of the American Ceramic Society,* 101[8] 3468-79 (2018).

126 H. Yang, F. Yan, Y. Lin, T. Wang, F. Wang, Y. Wang, L. Guo, W. Tai, and H. Wei, "Lead-free $BaTiO_3$-$Bi_{0.5}Na_{0.5}TiO_3$-$Na_{0.73}Bi_{0.09}NbO_3$ relaxor ferroelectric ceramics for high energy storage," *Journal of the European Ceramic Society,* 37[10] 3303-11 (2017).

127 X. Hao, "A review on the dielectric materials for high energy-storage application," *Journal of Advanced Dielectrics,* 3[01] 1330001 (2013).

128 W. Cai and W. D. Nix, "Imperfections in Crystalline Solids," pp. 1-519. Cambridge Univ Press: Cambridge, (2016).

129 J. Maier, "Physical chemistry of ionic materials: ions and electrons in solids." John Wiley & Sons, (2004).

130 A. R. West, "Basic solid state chemistry." John Wiley & Sons Inc, (1999).

131 Y.-M. Chiang, D. P. Birnie, and W. D. Kingery, "Physical Ceramics: Principles for Ceramic Science and Engineering." John Wiley & Sons, (1996).

132 D. M. Smyth, "The defect chemistry of metal oxides," *The Defect Chemistry of Metal Oxides, by DM Smyth, pp. 304. Foreword by DM Smyth. Oxford University Press, Jun 2000. ISBN-10: 0195110145. ISBN-13: 9780195110142* 304 (2000).

133 S. Lee, G. A. Rossetti Jr, Z.-K. Liu, and C. A. Randall, "Intrinsic ferroelectric properties of the nonstoichiometric perovskite oxide $Ba_{1-x}Ti_{1-y}O_{3-x-2y}$," *Journal of Applied Physics,* 105[9] 093519 (2009).

134 F. Kröger and H. Vink, "Relations between the concentrations of imperfections in crystalline solids," pp. 307-435. in Solid state physics, Vol. 3. Elsevier, 1956.

135 F. Yang, M. Li, L. Li, P. Wu, E. Pradal-Velázquez, and D. C. Sinclair, "Defect chemistry and electrical properties of sodium bismuth titanate perovskite," *Journal of Materials Chemistry A,* 6[13] 5243-54 (2018).

136 R. K. Willardson and A. C. Beer, "Semiconductors and semimetals," Vol. 12. Academic press, (1977).

137 K. Carl and K. H. Hardtl, "Electrical after-effects in Pb(Ti, Zr)O_3 ceramics," *Ferroelectrics,* 17[1] 473-86 (1977).

138 G. Arlt and H. Neumann, "Internal bias in ferroelectric ceramics: Origin and time dependence," *Ferroelectrics,* 87[1] 109-20 (1988).

139 P. V. Lambeck and G. H. Jonker, "Ferroelectric domain stabilization in $BaTiO_3$ by bulk ordering of defects," *Ferroelectrics,* 22[1] 729-31 (2011).

140 E. S. Kirkpatrick, K. A. Müller, and R. S. Rubins, "Strong Axial Electron Paramagnetic Resonance Spectrum of Fe^{3+}in $SrTiO_3$ Due to Nearest-Neighbor Charge Compensation," *Physical Review,* 135[1A] A86-A90 (1964).

141 R. Merkle and J. Maier, "Defect association in acceptor-doped $SrTiO_3$: case study for $Fe'_{Ti}V^{\cdot\cdot}_O$ and $Mn''_{Ti}V^{\cdot\cdot}_O$," *Phys. Chem. Chem. Phys.,* 5[11] 2297-303 (2003).

142 M. Schie, R. Waser, and R. A. De Souza, "A Simulation Study of Oxygen-Vacancy Behavior in Strontium Titanate: Beyond Nearest-Neighbor Interactions," *The Journal of Physical Chemistry C,* 118[28] 15185-92 (2014).

143 G. Arlt and U. Robels, "Aging and fatigue in bulk ferroelectric perovskite ceramics," *Integrated Ferroelectrics,* 3[4] 343-49 (2006).

144 M. Suzuki, A. Morishita, Y. Kitanaka, Y. Noguchi, and M. Miyayama, "Polarization and Piezoelectric Properties of High Performance Bismuth Sodium Titanate Single Crystals Grown by High-Oxygen-Pressure Flux Method," *Jpn. J. Appl. Phys.,* 49[9] 5 (2010).

145 N. W. Ashcroft and N. D. Mermin, "Solid State Physics." Saunders College Pbulishing, (1976).

146 S. M. Sze and K. K. Ng, "Physics of semiconductor devices." John wiley & sons, (2006).

147 R. A. Matula, "Electrical resistivity of copper, gold, palladium, and silver," *Journal of Physical and Chemical Reference Data,* 8[4] 1147-298 (1979).

148 S. Arrhenius, "Über die Dissociationswärme und den Einfluss der Temperatur auf den Dissociationsgrad der Elektrolyte," *Zeitschrift für physikalische Chemie,* 4[1] 96-116 (1889).

149 K. Funke, "Jump relaxation in solid electrolytes," *Progress in Solid State Chemistry,* 22[2] 111-95 (1993).

150 P. Debye and H. Falkenhagen, "Dispersion of the Conductivity and Dielectric Constants of Strong Electrolytes," *Phys. Z.,* 29 121 (1928).

151 P. Debye and H. Falkenhagen, "Dispersion der Leitfähigkeit und der Dieletrizitätskonstante starker Elektrolyte," *Phys. Z.,* 29 401 (1928).

152 H. Mehrer, "Diffusion in solids: fundamentals, methods, materials, diffusion-controlled processes," Vol. 155. Springer Science & Business Media, (2007).

153 P. Manning, J. Sirman, R. De Souza, and J. Kilner, "The kinetics of oxygen transport in 9.5 mol% single crystal yttria stabilised zirconia," *Solid State Ionics,* 100[1-2] 1-10 (1997).

154 J. Irvine, D. C. Sinclair, and A. R. West, "Electroceramics: Characterization by Impedance Spectroscopy," *Advanced Materials,* 3 132-38 (1990).

155 J. V. Stewart, "Intermediate electromagnetic theory." World Scientific Publishing Company, (2001).

156 Y. S. Sung, J. M. Kim, J. H. Cho, T. K. Song, M. H. Kim, and T. G. Park, "Effects of Bi nonstoichiometry in $(Bi_{0.5+x}Na)TiO_3$ ceramics," *Applied Physics Letters,* 98[1] 012902 (2011).

157 Y. S. Sung, J. M. Kim, J. H. Cho, T. K. Song, M. H. Kim, H. H. Chong, T. G. Park, D. Do, and S. S. Kim, "Effects of Na nonstoichiometry in $(Bi_{0.5}Na_{0.5+x})TiO_3$ ceramics," *Applied Physics Letters,* 96[2] 022901 (2010).

158 M. Spreitzer, M. Valant, and D. Suvorov, "Sodium deficiency in $Na_{0.5}Bi_{0.5}TiO_3$," *Journal of Materials Chemistry,* 17[2] 185-92 (2007).

159 D. D. Macdonald, "Reflections on the history of electrochemical impedance spectroscopy," *Electrochimica Acta,* 51[8-9] 1376-88 (2006).

160 H. D. Park and D. A. Payne, "Microstructure-property relations for internal boundary-layer capacitors," *Am. Ceram. Soc. Bull.,* 60[3] 402-02 (1981).

161 D. Williams and A. Hilger, "Solid state gas sensors," *Adam Hilger, Bristol* 71 (1987).

162 P. A. Tippler, "Physik." Spectrum Verlag, (1994).

163 V. F. Lvovich, "Impedance spectroscopy: applications to electrochemical and dielectric phenomena." John Wiley & Sons, (2012).

164 H. Lindner, "Taschenbuch für Elektronik und Elektrotechnik." Carl Hanser Verlag, (2004).

165 E. Barsoukov and J. R. Macdonald, "Impedance spectroscopy: theory, experiment, and applications." John Wiley & Sons, (2018).

166 D. C. Sinclair, "Characterization of Electro-materials using ac Impedance Spectroscopy," *Boletín de la Sociedad Española de Cerámica y Vidrio,* 34[2] 55-65 (1995).

167 T. Van Dijk and A. Burggraaf, "Grain boundary effects on ionic conductivity in ceramic $Gd_xZr_{1-x}O_{2-(x/2)}$ solid solutions," *physica status solidi (a),* 63[1] 229-40 (1981).

168 S. Song and F. Placido, "The influence of phase probability distributions on impedance spectroscopy," *Journal of Statistical Mechanics: Theory and Experiment,* 2004[10] P10018 (2004).

169 P. G. Bruce and A. R. West, "The ac conductivity of polycrystalline LISICON, $Li_{2+2X}Zn_{1-x}GeO_4$, and a model for intergranular constriction resistances," *J. Electrochem. Soc.,* 130[3] 662-69 (1983).

170 J. Fleig and J. Maier, "Finite-element calculations on the impedance of electroceramics with highly resistive grain boundaries: I, laterally inhomogeneous grain boundaries," *Journal of the American Ceramic Society,* 82[12] 3485-93 (1999).

171 J. T. S. Irvine, M. Lacerda, and A. R. West, "Oxide ion conduction in $Ca_{12}Al_{14}O_{33}$," *Materials Research Bulletin,* 23[7] 1033-38 (1988).

172 I. Raistrick, C. Ho, and R. A. Huggins, "Ionic conductivity of some lithium silicates and aluminosilicates," *J. Electrochem. Soc.,* 123[10] 1469-76 (1976).

173 C. F. Buhrer, "Some properties of bismuth perovskites," *The Journal of Chemical Physics,* 36[3] 798-803 (1962).

174 S. B. Vakhrushev, V. A. Isupov, B. E. Kvyatkovsky, N. M. Okuneva, I. P. Pronin, G. A. Smolensky, and P. P. Syrnikov, "Phase transitions and soft modes in sodium bismuth titante," *Ferroelectrics,* 63[1-4] 153-60 (1985).

175 I. Levin and I. M. Reaney, "Nano- and Mesoscale Structure of $Na_{1/2}Bi_{1/2}TiO_3$: A TEM Perspective," *Advanced Functional Materials,* 22[16] 3445-52 (2012).

176 M. Gröting, S. Hayn, and K. Albe, "Chemical order and local structure of the lead-free relaxor ferroelectric," *Journal of Solid State Chemistry,* 184[8] 2041-46 (2011).

177 G. O. Jones and P. A. Thomas, "Investigation of the structure and phase transitions in the novel A-site substituted distorted perovskite compound $Na_{0.5}Bi_{0.5}TiO_3$," *Acta Crystallographica Section B,* B58 168-78 (2001).

178 V. Dorcet, G. Trolliard, and R. Boullay, "Reinvestigation of Phase Transitions in $Na_{0.5}Bo_{0.5}TiO_3$ by TEM. Part I: First Order Rhombohedral to Orthorhombic Pahse Transition," *Chemistry of Materials,* 20[15] 5061-73 (2008).

179 V. Dorcet and G. Trolliard, "A transmission electron microscopy study of the A-site disordered perovskite $Na_{0.5}Bi_{0.5}TiO_3$," *Acta Materialia,* 56[8] 1753-61 (2008).

180 K. Sakata and Y. Masuda, "ferroelectric and antiferroelectric properties of $(Na_{0.5}\ Bi_{0.5})TiO_3$-$SrTiO_3$ solid solution ceramics," *Ferroelectrics,* 7[1-4] 347-49 (1974).

181 G. Trolliard and V. Dorcet, "Reinvestigation of Phase Transitions in $Na_{0.5}Bi_{0.5}TiO_3$ by TEM. Part II: Second Order Orthorhombic to Tetragonal Phase Transition," *Chemistry of Materials,* 20[15] 5074-82 (2008).

182 M. Gröting, S. Hayn, and K. Albe, "Chemical order and local structure of the lead-free relaxor ferroelectric $Na_{1/2}Bi_{1/2}TiO_3$," *Journal of Solid State Chemistry,* 184 2041-46 (2011).

183 E. Aksel, J. S. Forrester, J. L. Jones, P. A. Thomas, K. Page, and M. R. Suchomel, "Monoclinic crystal structure of polycrystalline $Na_{0.5}Bi_{0.5}TiO_3$," *Applied Physics Letters,* 98[15] 152901 (2011).

184 D. S. Keeble, E. R. Barney, D. A. Keen, M. G. Tucker, J. Kreisel, and P. A. Thomas, "Bifurcated Polarization Rotation in Bismuth-Based Piezoelectrics," *Advanced Functional Materials,* 23[2] 185-90 (2013).

185 E. Aksel, J. S. Forrester, J. C. Nino, K. Page, D. P. Shoemaker, and J. L. Jones, "Local atomic structure deviation from average structure of $Na_{0.5}Bi_{0.5}TiO_3$: Combined x-ray and neutron total scattering study," *Physical Review B,* 87[10] 10 (2013).

186 A. Mishra, D. K. Khatua, A. De, B. Majumdar, T. Frömling, and R. Ranjan, "Structural mechanism behind piezoelectric enhancement in off-stoichiometric $Na_{0.5}Bi_{0.5}TiO_3$ based lead-free piezoceramics," *Acta Materialia,* 164 761-75 (2019).

187 L. Li, M. Li, H. Zhang, I. M. Reaney, and D. C. Sinclair, "Controlling mixed conductivity in $Na_{1/2}Bi_{1/2}TiO_3$ using A-site non-stoichiometry and Nb-donor doping," *Jorunal of Materials Chemistry C,* 4[24] 5779-86 (2016).

188 J. Zvirgzds, P. Kapostin, J. Zvirgzde, and T. Kruzina, "X-ray study of phase transitions in efrroelectric $Na_{0.5}Bi_{0.5}TiO_3$," *Ferroelectrics,* 40[1] 75-77 (1982).

189 K. Roleder, J. Suchanicz, and A. Kania, "Time dependence of electric permittivity in $Na_{0.5}Bi_{0.5}TiO_3$ single crystals," *Ferroelectrics,* 89[1] 1-5 (1989).

190 T. Takenaka, "Piezoelectric properties of some lead-free ferroelectric ceramics," *Ferroelectrics,* 230[1] 87-98 (1999).

191 F. Yang, P. Wu, and D. C. Sinclair, "Enhanced bulk conductivity of A-site divalent acceptor-doped non-stoichiometric sodium bismuth titanate," *Solid State Ionics,* 299 38-45 (2017).

192 J. Huang, F. Zhu, D. Huang, B. Wang, T. Xu, X. Li, P. Fan, F. Xia, J. Xiao, and H. Zhang, "Intermediate-temperature conductivity of B-site doped $Na_{0.5}Bi_{0.5}TiO_3$-based lead-free ferroelectric ceramics," *Ceramics International,* 42[15] 16798-803 (2016).

193 X. Liu, H. Fan, J. Shi, L. Wang, and H. Du, "Enhanced ionic conductivity of Ag addition in acceptor-doped $Bi_{0.5}Na_{0.5}TiO_3$ ferroelectrics," *RSC Advances,* 6[36] 30623-27 (2016).

194 G. Lewis and C. Catlow, "Defect studies of doped and undoped barium titanate using computer simulation techniques," *J. Phys. Chem. Solids,* 47[1] 89-97 (1986).

195 B. A. Boukamp, M. T. Pham, D. H. Blank, and H. J. Bouwmeester, "Ionic and electronic conductivity in lead–zirconate–titanate (PZT)," *Solid State Ionics,* 170[3-4] 239-54 (2004).

196 F. Yang, H. Zhang, L. Li, I. M. Reaney, and D. C. Sinclair, "High Ionic Conductivity with Low Degradation in A-Site Strontium-Doped Nonstoichiometric Sodium Bismuth Titanate Perovskite," *Chemistry of Materials,* 28[15] 5269-73 (2016).

197 K. Reichmann, A. Feteira, and M. Li, "Bismuth Sodium Titanate Based Materials for Piezoelectric Actuators," *Materials (Basel),* 8[12] 8467-95 (2015).

198 E. Aksel, J. S. Forrester, B. Kowalski, M. Deluca, D. Damjanovic, and J. L. Jones, "Structure and properties of Fe-modified $Na_{0.5}Bi_{0.5}TiO_3$at ambient and elevated temperature," *Physical Review B,* 85[2] (2012).

199 K.-C. Meyer, M. Gröting, and K. Albe, "Octahedral tilt transitions in the relaxor ferroelectric $Na_{1/2}Bi_{1/2}TiO_3$," *Journal of Solid State Chemistry,* 227 117-22 (2015).

200 C.-M. Wang, L. Zhao, Y. Liu, R. L. Withers, S. Zhang, and Q. Wang, "The temperature-dependent piezoelectric and electromechanical properties of cobalt-modified sodium bismuth titanate," *Ceramics International,* 42[3] 4268-73 (2016).

201 D. J. Ruth, M. Muneeswaran, N. Giridharan, and B. Sundarakannan, "Enhanced electrical properties in Rb-substituted sodium bismuth titanate ceramics," *Applied Physics A,* 122[5] 502 (2016).

202 S. Supriya, A. J. Dos santos-García, C. You, and F. Fernández-Martinez, "Analysis of single and binary phases in cerium doped sodium bismuth titanate-$Na_{0.5}Bi_{0.5}TiO_3$ materials," *Energy Procedia,* 84 190-96 (2015).

203 R. Ranjan, V. Kothai, R. Garg, A. Agrawal, A. Senyshyn, and H. Boysen, "Degenerate rhombohedral and orthorhombic states in Ca-substituted $Na_{0.5}Bi_{0.5}TiO_3$," *Applied Physics Letters,* 95[4] 3 (2009).

204 X. F. He and Y. F. Mo, "Accelerated materials design of $Na_{0.5}Bi_{0.5}TiO_3$ oxygen ionic conductors based on first principles calculations," *Physical Chemistry Chemical Physics,* 17[27] 18035-44 (2015).

205 J. A. Dawson, H. R. Chen, and I. Tanaka, "Crystal structure, defect chemistry and oxygen ion transport of the ferroelectric perovskite, $Na_{0.5}Bi_{0.5}TiO_3$: insights from first-principles calculations," *Journal of Materials Chemistry A,* 3[32] 16574-82 (2015).

206 B. Y. R. D. Shannon, M. H, N. H. Baur, O. H. Gibbs, M. Eu, and V. Cu, "Revised Effective Ionic Radii and Systematic Studies of Interatomie Distances in Halides and Chaleogenides," (1976).

207 S. T. Zhang, A. B. Kounga, E. Aulbach, and Y. Deng, "Temperature-dependent electrical properties of 0.94 $Bi_{0.5}Na_{0.5}TiO_3$–0.06 $BaTiO_3$ ceramics," *Journal of the American Ceramic Society,* 91[12] 3950-54 (2008).

208 Q. Xu, S. Chen, W. Chen, S. Wu, J. Zhou, H. Sun, and Y. Li, "Synthesis and piezoelectric and ferroelectric properties of $(Na_{0.5}Bi_{0.5})$ 1− xBa_xTiO_3 ceramics," *Materials Chemistry and Physics,* 90[1] 111-15 (2005).

209 M. Chen, Q. Xu, B. H. Kim, B. K. Ahn, J. H. Ko, W. J. Kang, and O. J. Nam, "Structure and electrical properties of $(Na_{0.5}Bi_{0.5})$ 1− xBa_xTiO_3 piezoelectric ceramics," *Journal of the European Ceramic Society,* 28[4] 843-49 (2008).

210 B. Wylie-van Eerd, D. Damjanovic, N. Klein, N. Setter, and J. Trodahl, "Structural complexity of $(Na_{0.5}Bi_{0.5})$ TiO_3-$BaTiO_3$ as revealed by Raman spectroscopy," *Physical Review B,* 82[10] 104112 (2010).

211 C. Ma, X. Tan, E. Dul'kin, and M. Roth, "Domain structure-dielectric property relationship in lead-free (1−x)$(Bi_{0.5}Na_{0.5})TiO_3$-$xBaTiO_3$ ceramics," *Journal of Applied Physics,* 108[10] 104105 (2010).

212 W. Jo, J. E. Daniels, J. L. Jones, X. Tan, P. A. Thomas, D. Damjanovic, and J. Rödel, "Evolving morphotropic phase boundary in lead-free $(Bi_{1/2}Na_{1/2})TiO_3$–$BaTiO_3$ piezoceramics," *Journal of Applied Physics,* 109[1] 014110 (2011).

213 W. Jo, S. Schaab, E. Sapper, L. A. Schmitt, H.-J. Kleebe, A. J. Bell, and J. Rödel, "On the phase identity and its thermal evolution of lead free $(Bi_{1/2}Na_{1/2})TiO_3$-6 mol% $BaTiO_3$," *Journal of Applied Physics,* 110[7] 074106 (2011).

214 M. Guennou, P. Bouvier, J. Kreisel, and D. Machon, "Pressure-temperature phase diagram of $SrTiO_3$ up to 53 GPa," *Physical Review B,* 81[5] 10 (2010).

215 D. Rout, K. S. Moon, S. J. L. Kang, and I. W. Kim, "Dielectric and Raman scattering studies of phase transitions in the (100-x)$Na_{0.5}Bi_{0.5}TiO_3$-$xSrTiO_3$ system," *Journal of Applied Physics,* 108[8] 7 (2010).

216 W. Krauss, D. Schutz, F. A. Mautner, A. Feteira, and K. Reichmann, "Piezoelectric properties and phase transition temperatures of the solid solution of (1-x)$(Bi_{0.5}Na_{0.5})TiO_3$-$xSrTiO_3$," *Journal of the European Ceramic Society,* 30[8] 1827-32 (2010).

217 Y. Hiruma, Y. Imai, Y. Watanabe, H. Nagata, and T. Takenaka, "Large electrostrain near the phase transition temperature of $(Bi_{0.5}Na_{0.5})TiO_3$-$SrTiO_3$ ferroelectric ceramics," *Applied Physics Letters,* 92[26] 3 (2008).

218 M. Acosta, L. A. Schmitt, C. Cazorla, A. Studer, A. Zintler, J. Glaum, H. J. Kleebe, W. Donner, M. Hoffman, J. Rödel, and M. Hinterstein, "Piezoelectricity and rotostriction through polar and non-polar coupled instabilities in bismuth-based piezoceramics," *Sci Rep,* 6 8 (2016).

219 J. Koruza, V. Rojas, L. Molina-Luna, U. Kunz, M. Duerrschnabel, H. J. Kleebe, and M. Acosta, "Formation of the core-shell microstructure in lead-free $Bi_{1/2}Na_{1/2}TiO_3$-$SrTiO_3$ piezoceramics and its influence on the electromechanical properties," *Journal of the European Ceramic Society,* 36[4] 1009-16 (2016).

220 S. Kim, H. Choi, S. Han, J. S. Park, M. H. Lee, T. K. Song, M. H. Kim, D. Do, and W. J. Kim, "A correlation between piezoelectric response and crystallographic structural parameter

observed in lead-free (1-x)($Bi_{0.5}Na_{0.5}$)TiO_3-x$SrTiO_3$ piezoelectrics," *Journal of the European Ceramic Society,* 37[4] 1379-86 (2017).

221 J. K. Lee, K. S. Hong, C. K. Kim, and S. E. Park, "Phase transitions and dielectric properties in A-site ion substituted ($Na_{1/2}Bi_{1/2}$)TiO_3 ceramics (A=Pb and Sr)," *Journal of Applied Physics,* 91[7] 4538-42 (2002).

222 N. Liu, M. Acosta, S. Wang, B. X. Xu, R. W. Stark, and C. Dietz, "Revealing the core-shell interactions of a giant strain relaxor ferroelectric 0.75$Bi_{1/2}Na_{1/2}TiO_3$-0.25$SrTiO_3$," *Sci Rep,* 6 9 (2016).

223 M. Naderer, T. Kainz, D. Schütz, and K. Reichmann, "The influence of Ti-nonstoichiometry in $Bi_{0.5}Na_{0.5}TiO_3$," *Journal of the European Ceramic Society,* 34[3] 663-67 (2014).

224 X. Liu, F. Li, P. Li, J. W. Zhai, B. Shen, and B. H. Liu, "Tuning the ferroelectric-relaxor transition temperature in NBT-based lead-free ceramics by Bi nonstoichiometry," *Journal of the European Ceramic Society,* 37[15] 4585-95 (2017).

225 P. Patnaik, "Handbook of inorganic chemicals," Vol. 529. McGraw-Hill New York, (2003).

226 Y. Yuan, X. H. Zhou, C. J. Zhao, B. Li, and S. R. Zhang, "High-Temperature Capacitor Based on Ca-Doped $Bi_{0.5}Na_{0.5}TiO_3$-$BaTiO_3$ Ceramics," *J. Electron. Mater.,* 39[11] 2471-75 (2010).

227 T. K. Song, J. Park, S. Lee, M. Lee, D. Kim, Y. Sung, M. Kim, J. Cho, B. Choi, and S. Kim, "Effects of Zr Doping on the Depolarization Temperature and the Piezoelectric Properties in ($Bi_{0.5}Na_{0.5}$)TiO_3-$BaTiO_3$ Lead-free Ceramics," *Journal of Korean Physical Society,* 57 1905 (2010).

228 X. Dai, Z. Xu, and D. Viehland, "The spontaneous relaxor to normal ferroelectric transformation in La-modified lead zirconate titanate," *Philosophical Magazine Part B,* 70[1] 33–48 (2006).

229 H. Qian and L. A. Bursill, "Phenomenological theory of the dielectric response of lead magnesium niobate and lead scandium tantalate," *International Journal of Modern Physics B,* 10[16] 2007–25 (1996).

230 R. Dittmer, W. Jo, J. Daniels, S. Schaab, J. Rödel, and D. W. Johnson, "Relaxor Characteristics of Morphotropic Phase Boundary ($Bi_{0.5}Na_{0.5}$)TiO_3-($Bi_{0.5}K_{0.5}$)TiO_3 Modified with Bi($Zn_{0.5}Ti_{0.5}$)O_3," *Journal of the American Ceramic Society,* 94[12] 4283–90 (2011).

231 J. Zang, M. Li, D. C. Sinclair, T. Frömling, W. Jo, J. Rödel, and D. Johnson, "Impedance Spectroscopy of ($Bi_{1/2}Na_{1/2}$)TiO_3-$BaTiO_3$ Based High-Temperature Dielectrics," *Journal of the American Ceramic Society,* 97[9] 2825-31 (2014).

232 M. N. Rahaman, "Ceramic Processing and Sintering," 2 ed. CRC press, (2017).

233 J. Carter, E. Aksel, T. Iamsasri, J. S. Forrester, J. Chen, and J. L. Jones, "Structure and ferroelectricity of nonstoichiometric ($Na_{0.5}Bi_{0.5}$)TiO_3," *Applied Physics Letters,* 104[11] (2014).

234 Sartorius, "YDK 01-0D, YDK 01 LP, Betriebsanleitung," pp. 35-40. in., 2001.

235 W. Göpel and C. Ziegler, "Struktur der Materie: Grundlagen, Mikroskopie und Spektroskopie." Springer, (1994).

236 Y. Jung, S. Choi, and S. Kang, "Effect of oxygen partial pressure on grain boundary structure and grain growth behavior in $BaTiO_3$," *Acta Materialia,* 54[10] 2849-55 (2006).

237 J. G. Fisher and S. J. L. Kang, "Microstructural changes in ($K_{0.5}Na_{0.5}$)NbO_3 ceramics sintered in various atmospheres," *Journal of the European Ceramic Society,* 29[12] 2581-88 (2009).

238 "Alpha-A High Resolution Dielectric , Conductivity , Impedance and Gain Phase Modular Measurement System," (2005).

239 C. B. Sawyer and C. Tower, "Rochelle salt as a dielectric," *Physical review,* 35[3] 269 (1930).

240 J.-P. Amoureux, C. Fernandez, and S. Steuernagel, "ZFiltering in MQMAS NMR," *Journal of Magnetic Resonance, Series A,* 1[123] 116-18 (1996).

241 G. Kresse and J. Furthmüller, "Efficiency of ab-initio total energy calculations for metals and semiconductors using a plane-wave basis set," *Computational materials science,* 6[1] 15-50 (1996).

242 G. Kresse and J. Furthmüller, "Efficient iterative schemes for ab initio total-energy calculations using a plane-wave basis set," *Physical review B,* 54[16] 11169 (1996).

243 G. Kresse and D. Joubert, "From ultrasoft pseudopotentials to the projector augmented-wave method," *Physical Review B,* 59[3] 1758 (1999).

244 P. E. Blöchl, "Projector augmented-wave method," *Physical review B,* 50[24] 17953 (1994).

245 J. P. Perdew and A. Zunger, "Self-interaction correction to density-functional approximations for many-electron systems," *Physical Review B,* 23[10] 5048 (1981).

246 J. P. Perdew, J. A. Chevary, S. H. Vosko, K. A. Jackson, M. R. Pederson, D. J. Singh, and C. Fiolhais, "Atoms, molecules, solids, and surfaces: Applications of the generalized gradient approximation for exchange and correlation," *Physical review B,* 46[11] 6671 (1992).

247 J. P. Perdew, K. Burke, and M. Ernzerhof, "Generalized gradient approximation made simple," *Physical review letters,* 77[18] 3865 (1996).

248 J. P. Perdew and W. Yue, "Accurate and simple density functional for the electronic exchange energy: Generalized gradient approximation," *Physical review B,* 33[12] 8800 (1986).

249 S. Maintz, V. L. Deringer, A. L. Tchougréeff, and R. Dronskowski, "LOBSTER: A tool to extract chemical bonding from plane-wave based DFT," *Journal of computational chemistry,* 37[11] 1030-35 (2016).

250 V. L. Deringer, A. L. Tchougréeff, and R. Dronskowski, "Crystal orbital Hamilton population (COHP) analysis as projected from plane-wave basis sets," *The journal of physical chemistry A,* 115[21] 5461-66 (2011).

251 J. Maier, "Mass Transport in the Presence of Internal Defect Reactions- Concept of Conservative Ensembles: I I I, Trapping Effect of Dopants on Chemical Diffusion," *journal of the American Ceramic Society,* 76[5] 1223-27 (1993).

252 R. A. De Souza, "Oxygen Diffusion in $SrTiO_3$ and Related Perovskite Oxides," *Advanced Functional Materials,* 25[40] 6326-42 (2015).

253 J. Maier, "Mass-Transport in the presence of internal defect reactions- concept of conservative ensembles .1. Chemical diffusion in pure compounds," *Journal of the American Ceramic Society,* 76[5] 1212-17 (1993).

254 P. Erhart and K. Albe, "Thermodynamics of mono- and di-vacancies in barium titanate," *Journal of Applied Physics,* 102[8] 8 (2007).

255 V. Dorcet, G. Trolliard, and P. Boullay, "Reinvestigation of Phase Transitions in $Na_{0.5}Bi_{0.5}TiO_3$ by TEM. Part I: First Order Rhombohedral to Orthorhombic Phase Transition," *Chemistry of Materials,* 20[15] 5061-73 (2008).

256 G. Trolliard and V. Dorcet, "Reinvestigation of Phase Transitions in $Na_{1/2}Bi_{1/2}TiO_3$ by TEM. Part II: Second Order Orthorhombic to Tetragonal Phase Transition," *Chemistry of Materials,* 20[15] 5074-82 (2008).

257 R. A. Maier and C. A. Randall, "Low-Temperature Ionic Conductivity of an Acceptor-Doped Perovskite: I. Impedance of Single-Crystal $SrTiO_3$," *Journal of the American Ceramic Society,* 99[10] 3350-59 (2016).

258 B. Parija, "Study of Structural, Electrical and Optical Properties of Lead-Free $(Bi_{0.5}Na_{0.5})TiO_3$ Based Ceramic Systems." in., 2012.

259 K.-C. Meyer and K. Albe, "Influence of phase transitions and defect associates on the oxygen migration in the ion conductor $Na_{1/2}Bi_{1/2}TiO_3$," *J. Mater. Chem. A* (2017).

260 D. Park, J. Griffith, and A. Nowick, "Oxygen-ion conductivity and defect interactions in yttria-doped ceria," *Solid State Ionics,* 2[2] 95-105 (1981).

261 N. Hainovsky and J. Maier, "Simple phenomenological approach to premelting and sublattice melting in Frenkel disordered ionic crystals," *Physical Review B,* 51[22] 15789-97 (1995).

262 R. Dronskowski and P. E. Blöchl, "Crystal orbital Hamilton populations (COHP): energy-resolved visualization of chemical bonding in solids based on density-functional calculations," *The Journal of Physical Chemistry,* 97[33] 8617-24 (1993).

263 J. F. Stebbins, "Aluminum substitution in rutile titanium dioxide: New constraints from high-resolution ^{27}Al NMR," *Chemistry of Materials,* 19[7] 1862-69 (2007).

264 A. Escudero, L. Delevoye, and F. Langenhorst, "Aluminum incorporation in TiO_2 rutile at high pressure: An XRD and high-resolution ^{27}Al NMR study," *The Journal of Physical Chemistry C,* 115[24] 12196-201 (2011).

265 J. Kim, A. J. Ilott, D. S. Middlemiss, N. A. Chernova, N. Pinney, D. Morgan, and C. P. Grey, "^{2}H and ^{27}Al solid-state NMR study of the local environments in Al-doped 2-line ferrihydrite, goethite, and lepidocrocite," *Chemistry of Materials,* 27[11] 3966-78 (2015).

266 D. Rettenwander, J. Langer, W. Schmidt, C. Arrer, K. J. Harris, V. Terskikh, G. R. Goward, M. Wilkening, and G. Amthauer, "Site Occupation of Ga and Al in Stabilized Cubic $Li_{7-3(x+y)}Ga_xAl_yLa_3Zr_2O_{12}$ Garnets As Deduced from ^{27}Al and ^{71}Ga MAS NMR at Ultrahigh Magnetic Fields," *Chemistry of materials,* 27[8] 3135-42 (2015).

267 E. Lippmaa, A. Samoson, and M. Magi, "High-resolution aluminum-^{27}NMR of aluminosilicates," *Journal of the American Chemical Society,* 108[8] 1730-35 (1986).

268 D. Coster and J. J. Fripiat, "Memory effects in gel-solid transformations: coordinately unsaturated aluminum sites in nanosized aluminas," *Chemistry of materials,* 5[9] 1204-10 (1993).

269 C. A. Fyfe, J. L. Bretherton, and L. Y. Lam, "Solid-state NMR detection, characterization, and quantification of the multiple aluminum environments in US-Y catalysts by ^{27}Al MAS and MQMAS experiments at very high field," *Journal of the American Chemical Society,* 123[22] 5285-91 (2001).

270 H. J. Jakobsen, J. Skibsted, H. Bildsøe, and N. C. Nielsen, "Magic-angle spinning NMR spectra of satellite transitions for quadrupolar nuclei in solids," *Journal of Magnetic Resonance (1969),* 85[1] 173-80 (1989).

271 M. Cherry, M. S. Islam, and C. Catlow, "Oxygen ion migration in perovskite-type oxides," *Journal of Solid State Chemistry,* 118[1] 125-32 (1995).

272 J. C. Fisher, "Calculation of diffusion penetration curves for surface and grain boundary diffusion," *Journal of Applied Physics,* 22[1] 74-77 (1951).

273 R. Whipple, "CXXXVIII. Concentration contours in grain boundary diffusion," *The London, Edinburgh, and Dublin Philosophical Magazine and Journal of Science,* 45[371] 1225-36 (1954).

274 Y. Mishin, C. Herzig, J. Bernardini, and W. Gust, "Grain boundary diffusion: fundamentals to recent developments," *International materials reviews,* 42[4] 155-78 (1997).

275 A. Le Claire, "The analysis of grain boundary diffusion measurements," *British Journal of Applied Physics,* 14[6] 351 (1963).

276 S. Badwal, "Electrical conductivity of single crystal and polycrystalline yttria-stabilized zirconia," *Journal of materials science,* 19[6] 1767-76 (1984).

277 X. X. Wang, X. G. Tang, K. W. Kwok, H. L. W. Chan, and C. L. Choy, "Effect of excess Bi_2O_3 on the electrical properties and microstructure of $(Bi_{1/2}Na_{1/2})TiO_3$ ceramics," *Applied Physics A,* 80[5] 1071-75 (2003).

278 H. Yan, D. Xiao, P. Yu, J. Zhu, D. Lin, and G. Li, "The dependence of the piezoelectric properties on the differences of the A-site and B-site ions for $(Bi_{1-x}Na_x)TiO_3$-based ceramics," *Materials & Design,* 26[5] 474-78 (2005).

279 M. Ehmke, J. Glaum, W. Jo, T. Granzow, and J. Rödel, "Stabilization of the Fatigue-Resistant Phase by CuO Addition in $(Bi_{1/2}Na_{1/2})TiO_3$-$BaTiO_3$," *Journal of the American Ceramic Society,* 94[8] 2473-78 (2011).

280 J. Anthoniappen, C. H. Lin, C. S. Tu, P. Y. Chen, C. S. Chen, S. J. Chiu, H. Y. Lee, S. F. Wang, C. M. Hung, and H. J. Kleebe, "Enhanced Piezoelectric and Dielectric Responses in 92.5%$(Bi_{0.5}Na_{0.5})TiO_3$-7.5%$BaTiO_3$ Ceramics," *Journal of the American Ceramic Society,* 97[6] 1890-94 (2014).

281 R. Cheng, Z. Xu, R. Chu, J. Hao, J. Du, W. Ji, and G. Li, "Large piezoelectric effect in $Bi_{1/2}Na_{1/2}TiO_3$-based lead-free piezoceramics," *Ceramics International,* 41[6] 8119-27 (2015).

282 D. Pérez-Mezcua, M. L. Calzada, I. Bretos, J. Ricote, R. Jiménez, L. Fuentes-Cobas, R. Escobar-Galindo, D. Chateigner, and R. Sirera, "Influence of excesses of volatile elements on structure and composition of solution derived lead-free $(Bi_{0.50}Na_{0.50})_{1x}Ba_xTiO_3$ thin films," *Journal of the European Ceramic Society,* 36[1] 89-100 (2016).

283 Q. Xu, D.-P. Huang, M. Chen, W. Chen, H.-X. Liu, and B.-H. Kim, "Effect of bismuth excess on ferroelectric and piezoelectric properties of a $(Na_{0.5}Bi_{0.5})TiO_3$–$BaTiO_3$ composition near the morphotropic phase boundary," *Journal of Alloys and Compounds,* 471[1-2] 310-16 (2009).

284 X. Chen, H. Ma, W. Pan, M. Pang, P. Liu, and J. Zhou, "Microstructure, dielectric and ferroelectric properties of $(Na_xBi_{0.5})0.94Ba0.06TiO_3$ lead-free ferroelectric ceramics: Effect of Na nonstoichiometry," *Materials Chemistry and Physics,* 132 368-74 (2012).

285 X.-S. Qiao, X.-M. Chen, H.-L. Lian, W.-T. Chen, J.-P. Zhou, and P. Liu, "Microstructure and Electrical Properties of Nonstoichiometric $0.94(Na_{0.5}Bi_{0.5+x})TiO_3$–$0.06BaTiO_3$ Lead-Free Ceramics," *Journal of the American Ceramic Society,* 99[1] 198-205 (2016).

286 E. Subbarao, "Crystal Chemistry of Mixed Bismuth Oxides with Layer-Type Structure," *Journal of the American Ceramic Society,* 45[4] 166-69 (1962).

287 M.-L. Zhao, Q.-Z. Wu, C.-L. Wang, J.-L. Zhang, Z.-G. Gai, and C.-M. Wang, "Dielectric and piezoelectric properties of $Na_{0.5}Bi_{4.5}Ti_4O_{15}$–(x−1)$Na_{0.5}Bi_{0.5}TiO_3$ composite ceramics," *Journal of Alloys and Compounds,* 476[1-2] 393-96 (2009).

288 R. Beanland and P. A. Thomas, "Imaging planar tetragonal sheets in rhombohedral $Na_{0.5}Bi_{0.5}TiO_3$ using transmission electron microscopy," *Scripta Mater,* 65[5] 440-43 (2011).

289 S.-M. An and S.-J. L. Kang, "Boundary structural transition and grain growth behavior in $BaTiO_3$ with Nd_2O_3 doping and oxygen partial pressure change," *Acta Materialia,* 59[5] 1964-73 (2011).

290 W. Jo, J. B. Ollagnier, J. L. Park, E. M. Anton, O. J. Kwon, C. Park, H. H. Seo, J. S. Lee, E. Erdem, R. A. Eichel, and J. Rodel, "CuO as a sintering additive for $(Bi_{1/2}Na_{1/2})TiO_3$-$BaTiO_3$-$(K_{0.5}Na_{0.5})NbO_3$ lead-free piezoceramics," *Journal of the European Ceramic Society,* 31[12] 2107-17 (2011).

291 W. Jo, R. Dittmer, M. Acosta, J. Zang, C. Groh, E. Sapper, K. Wang, and J. Rödel, "Giant electric-field-induced strains in lead-free ceramics for actuator applications – status and perspective," *Journal of Electroceramics,* 29[1] 71-93 (2012).

292 Y. P. Guo, Y. Liu, R. L. Withers, F. Brink, and H. Chen, "Large Electric Field-Induced Strain and Antiferroelectric Behavior in (1-x)$(Na_{0.5}Bi_{0.5})TiO_3$-x$BaTiO_3$ Ceramics," *Chemistry of Materials,* 23[2] 219-28 (2011).

293 S. S. Sundari, B. Kumar, and R. Dhanasekaran, "Synthesis, dielectric and relaxation behavior of lead free NBT-BT ceramics," *Ceramics International,* 39[1] 555-61 (2013).

294 Y. A. Genenko, J. Glaum, M. J. Hoffmann, and K. Albe, "Mechanisms of aging and fatigue in ferroelectrics," *Materials Science and Engineering: B,* 192 52-82 (2015).

295 T. R. Shrout and S. J. Zhang, "Lead-free piezoelectric ceramics: Alternatives for PZT?," *Journal of Electroceramics,* 19[1] 113-26 (2007).

296 E. Aksel, E. Erdem, P. Jakes, J. L. Jones, and R.-A. Eichel, "Defect structure and materials "hardening" in Fe_2O_3-doped $[Bi_{0.5}Na_{0.5}]TiO_3$ ferroelectrics," *Applied Physics Letters,* 97[1] 012903 (2010).

297 O. Boser, "Statistical theory of hysteresis in ferroelectric materials," *Journal of Applied Physics,* 62[4] 1344-48 (1987).

298 U. Robels and G. Arlt, "Domain wall clamping in ferroelectrics by orientation of defects," *Journal of Applied Physics,* 73[7] 3454-60 (1993).

299 S. Prasertpalichat, W. Schmidt, and D. P. Cann, "Effects of A-site nonstoichiometry on oxide ion conduction in $0.94Bi_{0.5}Na_{0.5}TiO_3$–$0.06BaTiO_3$ ceramics," *Journal of Advanced Dielectrics,* 06[02] 1650012 (2016).

300 E. Sapper, R. Dittmer, D. Damjanovic, E. Erdem, D. J. Keeble, W. Jo, T. Granzow, and J. Rödel, "Aging in the relaxor and ferroelectric state of Fe-doped (1-x)$(Bi_{1/2}Na_{1/2})TiO_3$-x$BaTiO_3$ piezoelectric ceramics," *Journal of Applied Physics,* 116[10] 104102 (2014).

301 S. Prasertpalichat and D. P. Cann, "Hardening in non-stoichiometric $(1 - x)Bi_{0.5}Na_{0.5}TiO_3$–x$BaTiO_3$ lead-free piezoelectric ceramics," *Journal of Materials Science,* 51[1] 476–86 (2016).

302 J. Koruza, A. J. Bell, T. Frömling, K. G. Webber, K. Wang, and J. Rödel, "Requirements for the transfer of lead-free piezoceramics into application," *Journal of Materiomics,* 4[1] 13-26 (2018).

303 Y. S. Sung, J. M. Kim, J. H. Cho, T. K. Song, M. H. Kim, and T. G. Park, "Effects of Bi nonstoichiometry in $(Bi_{0.5+x}Na_{0.5-x})TiO_3$ ceramics," *Applied Physics Letters,* 98[1] 012902 (2011).

304 F. Yang, M. Li, L. Li, P. Wu, E. Pradal-Velázque, and D. C. Sinclair, "Optimisation of oxide-ion conductivity in acceptor-doped $Na_{0.5}Bi_{0.5}TiO_3$ perovskite: approaching the limit?," *Journal of Materials Chemistry A,* 5[41] 21658-62 (2017).

305 H. Zhang, A. H. H. Ramadan, and R. A. De Souza, "Atomistic simulations of ion migration in sodium bismuth titanate (NBT) materials: towards superior oxide-ion conductors," *Journal of Materials Chemistry A,* 6[19] 9116-23 (2018).

306 W. L. Warren, D. Dimos, G. E. Pike, K. Vanheusden, and R. Ramesh, "Alignment of defect dipoles in polycrystalline ferroelectrics," *Applied Physics Letters,* 67[12] 1689-91 (1995).

307 H. Meštrić, R. A. Eichel, T. Kloss, K. P. Dinse, S. Laubach, S. Laubach, P. C. Schmidt, K. A. Schönau, M. Knapp, and H. Ehrenberg, "Iron-oxygen vacancy defect centers in$PbTiO_3$: Newman superposition model analysis and density functional calculations," *Physical Review B,* 71[13] (2005).

308 D. Schütz, M. Deluca, W. Krauss, A. Feteira, T. Jackson, and K. Reichmann, "Lone-Pair-Induced Covalency as the Cause of Temperature- and Field-Induced Instabilities in Bismuth Sodium Titanate," *Advanced Functional Materials,* 22[11] 2285-94 (2012).

309 R. Lohkämper, H. Neumann, and G. Arlt, "Internal bias in acceptor-doped $BaTiO_3$ ceramics: Numerical evaluation of increase and decrease," *Journal of Applied Physics,* 68[8] 4220-24 (1990).

310 R. Waser, "Bulk Conductivity and Defect Chemistry of Acceptor-Doped Strontium-Titanate in the Quenched State," *Journal of the American Ceramic Society,* 74[8] 1934-40 (1991).

311 W. L. Warren, K. Vanheusden, D. Dimos, G. E. Pike, and B. A. Tuttle, "Oxygen Vacancy Motion in Perovskite Oxides," *Journal of the American Ceramic Society,* 79[2] 536-38 (1996).

312 A. Mishra, D. K. Khatua, A. De, B. Majumdar, T. Frömling, and R. Ranjan, "Structural mechanism behind piezoelectric enhancement in off-stoichiometric $Na_{0.5}Bi_{0.5}TiO_3$ based lead-free piezoceramics," *Acta Materialia,* 164 761-75 (2019).

313 J. Glaum, H. Simons, M. Acosta, and M. Hoffman, "Tailoring the Piezoelectric and Relaxor Properties of $(Bi_{1/2}Na_{1/2})TiO_3$-$BaTiO_3$ via Zirconium Doping," *Journal of the American Ceramic Society,* 96[9] 2881-86 (2013).

314 L. Molina-Luna, S. Wang, Y. Pivak, A. Zintler, H. H. Perez-Garza, R. G. Spruit, Q. Xu, M. Yi, B. X. Xu, and M. Acosta, "Enabling nanoscale flexoelectricity at extreme temperature by tuning cation diffusion," *Nat. Commun.,* 9 8 (2018).

315 S. Y. Choi, S. J. Jeong, D. S. Lee, M. S. Kim, J. S. Lee, J. H. Cho, B. I. Kim, and Y. Ikuhara, "Gigantic Electrostrain in Duplex Structured Alkaline Niobates," *Chemistry of Materials,* 24[17] 3363-69 (2012).

316 J. H. Cho, S. J. Jeong, S. W. Kim, C. J. Jeon, Y. H. Jeong, J. S. Yun, Y. W. Hong, and J. H. Paik, "Effect of chemical inhomogeneity on domains and ferroelectric properties of Fe-modified $0.77Bi_{0.5}Na_{0.5}TiO_3$-$0.23SrTiO_3$," *Journal of the American Ceramic Society,* 101[10] 4669-76 (2018).

317 M. Li, L. Li, J. Zang, and D. C. Sinclair, "Donor-doping and reduced leakage current in Nb-doped $Na_{0.5}Bi_{0.5}TiO_3$," *Applied Physics Letters,* 106[10] 102904 (2015).

318 R. Zuo, H. Wang, B. Ma, and L. Li, "Effects of Nb^{5+} doping on sintering and electrical properties of lead-free $(Bi_{0.5}Na_{0.5})TiO_3$ ceramics," *Journal of Materials Science: Materials in Electronics,* 20[11] 1140-43 (2009).

319 M. Kizilyalli, J. Corish, and R. Metselaar, "Definitions of terms for diffusion in the solid state," *Pure and Applied Chemistry,* 71[7] 1307-25 (1999).

320 J. Heldt, "Control of the core-shell structure in $Na_{0.5}Bi_{0.5+-x}TiO_3$-$SrTiO_3$ solid solutions." in Nichtmetallisch Anorganische Werkstoffe (NAW). Technische Universität Darmstadt, 2018.

321 S. Sayyed, S. A. Acharya, P. Kautkar, and V. Sathe, "Structural and dielectric anomalies near the MPB region of $Na_{0.5}Bi_{0.5}TiO_3$-$SrTiO_3$ solid solution," *Rsc Advances,* 5[63] 50644-54 (2015).

322 J. R. Gomah-Pettry, P. Marchet, A. Salak, V. M. Ferreira, and J. P. Mercurio, "Electrical properties of $Na_{0.5}Bi_{0.5}TiO_3$-$SrTiO_3$ ceramics," *Integrated Ferroelectrics,* 61 159-62 (2004).

323 W. P. Cao, W. L. Li, X. F. Dai, T. D. Zhang, J. Sheng, Y. F. Hou, and W. D. Fei, "Large electrocaloric response and high energy-storage properties over a broad temperature range in lead-free NBT-ST ceramics," *Journal of the European Ceramic Society,* 36[3] 593-600 (2016).

324 Y. S. Sung and M. H. Kim, "Effects of B-site donor and acceptor doping in Pb-free $(Bi_{0.5}Na_{0.5})TiO_3$ ceramics." in Ferroelectrics**.** IntechOpen, 2010.

325 K. van Benthem, C. Elsasser, and R. H. French, "Bulk electronic structure of $SrTiO_3$: Experiment and theory," *Journal of Applied Physics,* 90[12] 6156-64 (2001).

326 L. H. Li, M. Li, and D. C. Sinclair, "The influence of excess K_2O on the electrical properties of $(K,Na)_{1/2}Bi_{1/2}TiO_3$ ceramics," *Applied Physics Letters,* 112[18] 5 (2018).

327 S. Praharaj, D. Rout, S. Anwar, and V. Subramanian, "Polar nano regions in lead free $(Na_{0.5}Bi_{0.5})TiO_3$-$SrTiO_3$-$BaTiO_3$ relaxors: An impedance spectroscopic study," *Journal of Alloys and Compounds,* 706 502-10 (2017).

328 R. Dittmer, "Lead-Free Piezoelectrics Ergodic and Nonergodic Relaxor Ferroelectrics Based on Bismuth Sodium Titanate." in Nichtmetallisch-Anorganische Werkstoffe (NAW). Technische Universität Darmstadt, 2013.

329 A. Zeb and S. J. Milne, "High temperature dielectric ceramics: A review of temperature-stable high-permittivity perovskites," *Journal of Materials Science: Materials in Electronics,* 26[12] 9243–55 (2015).

330 J. Bultitude, J. McConnell, and C. Shearer, "High temperature capacitors and transient liquid phase interconnects for Pb-solder replacement," *Journal of Materials Science: Materials in Electronics,* 26[12] 9236–42 (2015).

331 R. W. Johnson, J. L. Evans, P. Jacobsen, J. R. Thompson, and M. Christopher, "The changing automotive environment: high-temperature electronics," *Electronics Packaging Manufacturing, IEEE Transactions on,* 27[3] 164-76 (2004).

332 C. Buttay, D. Planson, B. Allard, D. Bergogne, P. Bevilacqua, C. Joubert, M. Lazar, C. Martin, H. Morel, D. Tournier, and C. Raynaud, "State of the art of high temperature power electronics," *Materials Science and Engineering: B,* 176[4] 283-88 (2011).

333 J. Watson and G. Castro, "A review of high-temperature electronics technology and applications," *Journal of Materials Science: Materials in Electronics,* 26[12] 9226–35 (2015).

334 X. Zhong, X. Wu, W. Zhou, and K. Sheng, "An All-SiC High-Frequency Boost DC-DC Converter Operating at 320 °C Junction Temperature," *IEEE Transactions on Power Electronics,* 29[10] 5091-96 (2014).

335 H. Wang and F. Blaabjerg, "Reliability of Capacitors for DC-Link Applications in Power Electronic Converters-An Overview," *IEEE Transactions on Industry Applications,* 50[5] 3569-78 (2014).

336 J. Zang, M. Li, D. C. Sinclair, T. Frömling, W. Jo, and J. Rödel, "Impedance Spectroscopy of $(Bi_{1/2}Na_{1/2})TiO_3$–$BaTiO_3$ Based High-Temperature Dielectrics," *Journal of the American Ceramic Society,* 97[9] 2825-31 (2014).

337 M.-J. Pan and C. A. Randall, "A brief introduction to ceramic capacitors," *IEEE Electrical Insulation Magazine,* 26[3] 44–50 (2010).

338 H. Ogihara, C. A. Randall, and S. Trolier-McKinstry, "Weakly Coupled Relaxor Behavior of $BaTiO_3$-$BiScO_3$ Ceramics," *Journal of the American Ceramic Society,* 92[1] 110–18 (2009).

339 Q. Zhang, Z. Li, F. Li, Z. Xu, and S. Zhang, "Structural and Dielectric Properties of $Bi(Mg_{1/2}Ti_{1/2})O_3$-$BaTiO_3$ Lead-Free Ceramics," *Journal of the American Ceramic Society,* 94[12] 4335–39 (2011).

340 A. Zeb, Y. Bai, T. Button, and S. J. Milne, "Temperature-Stable Relative Permittivity from-70 °C to 500 °C in $(Ba_{0.8}Ca_{0.2})TiO_3$-$Bi(Mg_{0.5}Ti_{0.5})O_3$-$NaNbO_3$ Ceramics," *Journal of the American Ceramic Society,* 97[8] 2479-83 (2014).

341 R. Dittmer, W. Jo, D. Damjanovic, and J. Rödel, "Lead-free high-temperature dielectrics with wide operational range," *Journal of Applied Physics,* 109[3] 034107 (2011).

342 C. Groh, K. Kobayashi, H. Shimizu, Y. Doshida, Y. Mizuno, E. A. Patterson, and J. Rödel, "High-Temperature Multilayer Ceramic Capacitors Based on $100-x(94Bi_{1/2}Na_{1/2}TiO_3–6BaTiO_3)–xK_{0.5}Na_{0.5}NbO_3$," *Journal of the American Ceramic Society,* 99[6] 2040-46 (2016).

343 A. Zeb, S. u. Jan, F. Bamiduro, D. A. Hall, and S. J. Milne, "Temperature-stable dielectric ceramics based on $Na_{0.5}Bi_{0.5}TiO_3$," *Journal of the European Ceramic Society,* 38[4] 1548-55 (2018).

344 S. Prasertpalichat, W. Schmidt, and D. P. Cann, "Effects of A-site nonstoichiometry on oxide ion conduction in $0.94Bi_{0.5}Na_{0.5}TiO_3$ –$0.06BaTiO_3$ ceramics," *Journal of Advanced Dielectrics,* 06[02] 1650012 (2016).

345 X.-s. Qiao, X.-m. Chen, H.-l. Lian, J.-p. Zhou, and P. Liu, "Dielectric, ferroelectric, piezoelectric properties and impedance analysis of nonstoichiometric $(Bi_{0.5}Na_{0.5})0.94+xBa0.06TiO_3$ ceramics," *Journal of the European Ceramic Society* (2016).

346 M. A. Beuerlein, N. Kumar, T.-M. Usher, H. J. Brown-Shaklee, N. Raengthon, I. M. Reaney, D. P. Cann, J. L. Jones, G. L. Brennecka, and D. J. Green, "Current Understanding of Structure-Processing-Property Relationships in $BaTiO_3$-$Bi(M)O_3$ Dielectrics," *Journal of the American Ceramic Society,* 99[9] 2849-70 (2016).

347 F. Yang, P. Wu, and D. C. Sinclair, "Suppression of electrical conductivity and switching of conduction mechanisms in 'stoichiometric' $(Na_{0.5}Bi_{0.5}TiO_3)1-x$ $(BiAlO_3)x$ $(0\leq x\leq 0.08)$ solid solutions," *Journal of Materials Chemistry C,* 5[29] 7243-52 (2017).

348 S.-T. Zhang, A. B. Kounga, E. Aulbach, H. Ehrenberg, and J. Rödel, "Giant strain in lead-free piezoceramics $Bi_{0.5}Na_{0.5}TiO_3$–$BaTiO_3$–$K_{0.5}Na_{0.5}NbO_3$ system," *Appl. Phys. Lett.,* 91[11] 112906 (2007).

349 A. J. Moulson and J. M. Herbert, "Electroceramics: Materials, Properties, Applications," pp. 576. Wiley: West Sussex PO19 8SQ, England, (2003).

350 E. Standard, "Ceramic dielectric capacitors classes I, II, III and IV–part I: characteristics and requirements." in. EIA-198-1-F, November, 2002.

351 Q. Li, J. Wang, Y. Ma, L. Ma, G. Dong, and H. Fan, "Enhanced energy-storage performance and dielectric characterization of $0.94Bi_{0.5}Na_{0.5}TiO_3$–$0.06BaTiO_3$ modified by $CaZrO_3$," *Journal of Alloys and Compounds,* 663 701-07 (2016).

352 Y. Pu, M. Yao, H. Liu, and T. Frömling, "Phase transition behavior, dielectric and ferroelectric properties of $(1-x)(Bi_{0.5}Na_{0.5})TiO_3$-$xBa_{0.85}Ca_{0.15}Ti_{0.9}Zr_{0.1}O_3$ ceramics," *Journal of the European Ceramic Society,* 36[10] 2461-68 (2016).

353 H.-J. Kleebe, S. Lauterbach, L. Silvestroni, H. Kungl, M. J. Hoffmann, E. Erdem, and R.-A. Eichel, "Formation of magnetic grains in ferroelectric $Pb[Zr_{0.6}Ti_{0.4}]O_3$ ceramics doped with Fe^{3+} above the solubility limit," *Applied Physics Letters,* 94[14] 142901 (2009).

Curriculum Vitae

Personal Details:

Name	Sebastian Andre Steiner
Date of Birth	02.04.1990
Place of Birth	Offenbach am Main
Nationality	German

Education:

02/2016-08/2019	Nichtmetallisch-Anorganische Werkstoffe, Prof. Dr. Jürgen Rödel, Technische Universität Darmstadt: PhD student in materials science
10/2009-01/2016	Material- und Geowissenschaften, Technische Universität Darmstadt (Degree: B.Sc. in 2013, M.Sc. in 2015)
08/2006-07/2009	Gymnasiale Oberstufe, Clauss-von-Stauffenberg Schule, Rodgau, Dudenhofen (Abitur)

Work Experience:

02/2016-08/2019	Nichtmetallisch-Anorganische Werkstoffe, Prof. Dr. Jürgen Rödel, Technische Universität Darmstadt: Research associate and PhD student Co-Supervisor for three Bachelor's and three Master's Theses Supervisor for lab course: "Bruchfestigkeit und Bruchzähigkeit von Keramik und Glas") Industrial work for Siemens

Publications:

Koch, L., **Steiner, S.**, Meyer, K. C., Seo, I. T., Albe, K., & Frömling, T. (2017). Ionic conductivity of acceptor doped sodium bismuth titanate: influence of dopants, phase transitions and defect associates. *Journal of Materials Chemistry C*, *5*(35), 8958-8965.

Seo, I. T., **Steiner, S.**, & Frömling, T. (2017). The effect of A site non-stoichiometry on 0.94 (Na_yBi_x) TiO_3-0.06 $BaTiO_3$. *Journal of the European Ceramic Society*, *37*(4), 1429-1436.

Srikanth, K. S., Patel, S., **Steiner, S.**, & Vaish, R. (2017). Engineered microstructure for tailoring the pyroelectric performance of $Ba_{0.85}Sr_{0.15}Zr_{0.1}Ti_{0.9}O_3$ ceramics by 3BaO-3TiO_2-B_2O_3 glass addition. *Applied Physics Letters*, *110*(23), 232901.

Ayrikyan, A., Weyland, F., **Steiner, S.**, Duerrschnabel, M., Molina-Luna, L., Koruza, J., & Webber, K. G. (2017). Multilayer lead-free piezoceramic composites: Influence of co-firing on microstructure and electromechanical behavior. *Journal of the American Ceramic Society*, *100*(8), 3673-3683.

Frömling, T., **Steiner, S.**, Ayrikyan, A., Bremecker, D., Dürrschnabel, M., Molina-Luna, L., & Acosta, M. (2018). Designing properties of ($Na_{1/2}Bi_x$)TiO_3-based materials through A-site non-stoichiometry. *Journal of Materials Chemistry C*, *6*(4), 738-744.

Höfling, M., **Steiner, S.**, Hoang, A. P., Seo, I. T., & Frömling, T. (2018). Optimizing the defect chemistry of $Na_{1/2}Bi_{1/2}TiO_3$-based materials: paving the way for excellent high temperature capacitors. *Journal of Materials Chemistry C*, *6*(17), 4769-4776.

Weyland, F., Eisele, T., **Steiner, S.**, Frömling, T., Rossetti Jr, G. A., Rödel, J., & Novak, N. (2018). Long term stability of electrocaloric response in barium zirconate titanate. *Journal of the European Ceramic Society*, *38*(2), 551-556.

Srikanth, K. S., Patel, S., **Steiner, S.**, & Vaish, R. (2018). Pyroelectric signals in (Ba,Ca)TiO_3-x$Ba(Sn,Ti)O_3$ ceramics: a viable alternative for lead-based ceramics. *Scripta Materialia*, *146*, 146-149.

Patel, S., Srikanth, K. S., **Steiner, S.**, Vaish, R., & Frömling, T. (2018). Pyroelectric and impedance studies of the 0.5$Ba(Zr_{0.2}Ti_{0.8})O_3$-0.5$(Ba_{0.7}Sr_{0.3})TiO_3$ ceramics. *Ceramics International*, *44*(17), 21976-21981.

Steiner, S., Seo, I. T., Ren, P., Li, M., Keeble, D. J., & Frömling, T. (2019). The effect of Fe-acceptor doping on the electrical properties of $Na_{1/2}Bi_{1/2}TiO_3$ and $0.94(Na_{1/2}Bi_{1/2})TiO_3$–$0.06BaTiO_3$. *Journal of the American Ceramic Society*.

Riess, K., Geiger, P. T., Khansur, N. H., **Steiner, S.**, Frömling, T., Hinterstein, M., & Webber, K. G. (2019). Influence of the annealing conditions on temperature-dependent ferroelastic behavior of LSCF. *Materialia*, *6*, 100297.

Conference Contributions:

International Symposium on the Applications of Ferroelectrics (ISAF) 08/2016 (Darmstadt, Germany) (oral)

S. Steiner, I.-T. Seo, L. Koch, K.C. Meyer, K. Albe, T. Frömling (2016). Defect chemistry and conduction mechanisms in B-site doped and A-site non-stoichiometric $Na_{0.5}Bi_{0.5}TiO_3$

Materials Science and Engineering (MSE) 09/2016 (Darmstadt, Germany) (Poster)

S. Steiner, I.-T. Seo, T. Frömling (2016). $Na_{0.5}Bi_{0.5}TiO_3$-based ceramics as high performance oxygen ion conductors?

Bunsenkolloquium 11/2016 (Aachen, Germany) (Poster)

S. Steiner, L. Koch, I.-T. Seo, K. C. Meyer, T. Frömling, K. Albe (2016). Conductivity Mechanisms in B-site Mg-Doped $Na_{0.5}Bi_{0.5}TiO_3$–Based Ceramics

Conference of the European Ceramic Society (ECERS) 07/2017 (Budapest, Hungary) (oral)

S. Steiner, L. Koch, I.-T. Seo, K. Albe, T. Frömling (2017). Defect chemistry and conductivity mechanisms in B-site acceptor doped and A-site non-stoichiometric $Na_{0.5}Bi_{0.5}TiO_3$

SIMS Conference 09/2017 (Krakow, Poland) (Poster)

S. Steiner, O. Sobol, K. Albe, T. Frömling, W. E. S. Unger (2017). The characterization of oxygen diffusion in $Na_{0.5}Bi_{0.5}TiO_3$ piezo-ceramics by Time-of-Flight secondary ion mass spectrometry (ToF-SIMS)

Annual Spring Meeting 03/2018 (Manchester, UK) (oral)

S. Steiner, L. Koch, K. C. Meyer, I.-T. Seo, K. Albe, T. Frömling (2018). Ionic conductivity in sodium bismuth titanate and its solid solutions: The impact of dopants, phase transitions and defect associates

International Symposium on the Applications of Ferroelectrics (ISAF) 05/2018 (Hiroshima, Japan) (oral)

S. Steiner, L. Koch, K. C. Meyer, I.-T. Seo, K. Albe, T. Frömling (2018). Ionic conductivity of acceptor doped sodium bismuth titanate: Influence of dopants, phase transitions, and defect associates

European Materials Research Society Spring Meeting (E-MRS) 06/2018 (Strasbourg, France) (oral)

S. Steiner, L. Koch, K. C. Meyer, I.-T. Seo, K. Albe, T. Frömling (2018). Ionic conductivity of acceptor doped sodium bismuth titanate (NBT): Influence of dopants, phase transitions, and defect associates

Materials Science and Engineering (MSE) 09/2018 (Darmstadt, Germany) (Invited Talk)

S. Steiner, L. Koch, K. C. Meyer, I.-T. Seo, K. Albe, T. Frömling (2018). Ionic conductivity of acceptor doped sodium bismuth titanate (NBT) and its solid solutions